# UNIVERSITY OF SOUTHAMPTON

FACULTY OF ENGINEERING, SCIENCE & MATHEMATICS

School of Engineering Sciences

# Development of Carbon-Based Atomic Oxygen Sensors

by

**Carl Barry White**

Thesis for the degree of Doctor of Philosophy

June 2007

UNIVERSITY OF SOUTHAMPTON

# ABSTRACT

FACULTY OF ENGINEERING, SCIENCE & MATHEMATICS
SCHOOL OF ENGINEERING SCIENCES

Doctor of Philosophy

# DEVELOPMENT OF CARBON-BASED ATOMIC OXYGEN SENSORS

by Carl Barry White

This work focuses on the development of a hyperthermal, neutral atomic oxygen (AO) sensor that can be used on a wide variety of spacecraft platforms and in ground-based atomic oxygen environment simulators. Carbon has been identified as the sensitive medium for sensing the AO and one of the most important aspects of this work was selecting the most appropriate type of carbon for a particular AO dose.

This work fabricates carbon films by physical vapour deposition (PVD) and screen-printing techniques to provide different thicknesses and erosion rates, which affect the sensitivity and life of the sensor. Screen-printed films provided a useful means of detecting large AO doses (fluences), whilst the thinner PVD films provide a more sensitive film for smaller AO fluences. Attempts are also made at interpreting the data to measure the rate of AO (flux).

A combination of characterisation techniques confirm that the carbon films react by chemical removal of the carbon, which is also detected by measuring changes in electrical resistance. This work also postulates that the disorder of the carbon films (measured by Raman spectroscopy) can have an effect on the erosion rate of the material.

Results from this work will eventually be compared with two low Earth orbiting spacecraft experiments: STORM on the International Space Station and CANX-2. These experiments are described and engineering details relevant to the sensors are also included.

# TABLE OF CONTENTS

# LIST OF FIGURES

# LIST OF TABLES

# AUTHORS DECLARATION

I, Carl White declare that this report entitled *Development of Carbon-Based Atomic Oxygen Sensors* and the work presented in it, are my own.
I confirm that:

- This work was done wholly or mainly while in the candidature for a research degree at this University;
- Where any part of this thesis has previously been submitted for a degree or any other qualification at this university or any other institution, this has clearly been stated;
- Where I have consulted the published work of others, this is always clearly attributed;
- Where I have quoted from the work of others, the source is always given. With the such quotations, this thesis is entirely my own work;
- I have acknowledged all main sources of help;
- Where the thesis is based on work done by myself jointly with others, I have made clear exactly what was done by others and what I have contributed myself.

**Name:**

**Signature:**

**Date:**

# ACRONYMS

| | |
|---|---|
| a-C | Amorphous Carbon |
| a-C: H | Hydrogenated Amorphous Carbon |
| a-C: Si: H | Hydrogenated Amorphous Carbon-Silicon alloy |
| ADC | Analogue to Digital Converter |
| ANLE | Actinometer Non-Linearity Error |
| AO | Atomic Oxygen |
| AOE | Atomic Oxygen Experiment |
| ATOX | ATomic OXygen test rig (hyperthermal source) |
| BREMSAT | University of BREMen SATellite |
| CANX | Canadian Advanced Nanospace Experiment |
| CCD | Charge-Coupled Device |
| CHDI | trans-CycloHexane DiIsocyanate |
| CONCAP | CONsortium for materials development in space Complex Autonomous Payload |
| CNES | Centre National D'Etudes Spatiales |
| C-QCM | Carbon-coated QCM |
| CVD | Chemical Vapour Deposition |
| DC | Direct Current |
| DLC | Diamond-Like Carbon |
| DMM | Digital Multimeter |
| DS | Deposition Session |
| E-Beam | Electron Beam |
| EDS | Energy Dispersive x-ray Spectroscopy |
| EDX | Energy Dispersive X-ray spectroscopy |
| ESA | European Space Agency |
| ESTEC | European Space research and Technology Centre |
| EUTEF | European Technology Exposure Facility |
| EUV | Extreme Ultraviolet |
| FEGSEM | Field Emission Gun Scanning Electron Microscope |
| FIPEX | Flux Probe EXperiment |
| FWHM | Full Width Half Maximum |

| | |
|---|---|
| GPS | Global Positioning System |
| GTO | Geostationary Transfer Orbit |
| HOPG | Highly Orientated Pyrolytic Graphite |
| HPIB | Hewlett-Packard Instrument Bus |
| IPA | IsoPropyl Alcohol |
| IR | Infrared |
| IRDT | Inflatable Re-entry and Descent Technology |
| ISAC | International Solar Array Coupon |
| ISS | International Space Station |
| ITL | Integrity Testing Laboratories |
| KWS | Kapton Witness Sample |
| LANL | Los Alamos National Laboratory |
| LDCE | Limited Duration space environment Candidate materials Exposure payload |
| LDEF | Long Duration Exposure Facility |
| LED | Light Emitting Diode |
| LEO | Low Earth Orbit |
| MACOR | Machinable glass ceramic |
| MEDET | Materials Exposure and Degradation Experiment on EuTEF |
| MEMS | Micro Electro-Mechanical System |
| MSERD | Mono-Substituted Epoxide Ring Deformation |
| NASA | National Aeronautics and Space Administration |
| ONERA | Office National d’Etudes et de Recherches Aerospatiales |
| PA | Polyacetylene |
| PC | Personal Computer |
| PCB | Printed Circuit Board |
| PL | PhotoLuminescence |
| PPDI | Para-Phenylene DiIsocyanate |
| PSU | Pennsylvania State University |
| PTF | Polymer Thick Film |
| PTFE | PolyTetraFluoroEthylene |
| PU | Polyurethane |
| PVD | Physical Vapour Deposition |
| QCM | Quartz Crystal Microbalance |

| | |
|---|---|
| RF | Radio Frequency |
| SAA | South Atlantic Anomaly |
| SAE | Systematic Actinometer Error |
| SCD | Semi-Conducting Detector |
| SEM | Scanning Electron Microscope |
| SESAM | Surface Effects SAmple Monitor |
| SiC | Silicon Carbide |
| SIMS | School of Industrial and Manufacturing Science (Cranfield University) |
| STORM | Southampton Transient Oxygen and Radiation Monitor |
| STRV | Space Technology Research Vehicle |
| STM | Scanning Tunnelling Microscopy |
| STS | Space Transportation System (the Space Shuttle) |
| SXR | Soft X-Ray |
| ta-C | Tetrahedral Amorphous Carbon |
| ta-C:H | Hydrogenated Tetrahedral Amorphous Carbon |
| TEA | Transversely Excited Atmospheric |
| TEAMSAT | Technology, science and Education experiments Added to MaqSAT |
| TEXUS | Unknown, sounding rocket missions |
| TEY | Theoretical Erosion Yield |
| TQCM | Temperature controlled QCM |
| UTIAS | University of Toronto Institute of Aerospace Studies |
| UV | UltraViolet |
| VUV | Vacuum UltraViolet |
| XPS | X-ray Photoelectron Spectroscopy |
| YSZ | Yttria-Stabilised Zirconia |
| ZnO | Zinc Oxide |

# ACKNOWLEDGMENTS

Firstly, I think it is best to thank my supervisors Graham Roberts and Alan Chambers for providing the exciting opportunities, financial wizardry, their valuable time…and patience.

The Engineering and Physical Sciences Research Council, World Universities Network and the Royal Academy of Engineering should also be noted for their invaluable financial contributions.

This PhD would have not have been possible without the help of the following people:

- Marc van Eesbeek, Adrian Tighe and the others at ESTEC who offered their time, hospitality and use of the ATOX facility.
- John Badding, Bryan Jackson and Neil Baril of PSU who provided the facilities and substantial expertise for Raman spectroscopy.
- Ken Lawson and Jeff Rao of Cranfield University SIMS, who deposited the carbon films and provided tasty pizzas every time I visited.
- John Atkinson and Zhige (Gary) Zhang of the Thick Film Unit, who were once again invaluable to the fabrication of the sensor substrates.
- Jacob Kleiman and Zelina Iskanderova of ITL Inc for their plasma asher work.
- Duncan Goulty for all the hard work designing, building, testing and integrating the Southampton Transient Oxygen and Radiation Monitor with the MEDET module.

During the course of my research I have spent substantial periods on my own; either in my office or in far away lands. So thanks to Martijn, Dave, Paolo (the 'Bulk'), Christoph, Thomas, Ian W and the others for the office distractions and to Steven, Ian H, Jürgen and Stuart for when the office just got too quiet. I should also note the conversations with Juan Carlos.

Finally, a special thanks to Mum, Dad and Lauren for their encouragement and support.

# 1 INTRODUCTION

## 1.1 The Spacecraft Environment

Regardless of the mission, spacecraft operate in harsh environments. Perhaps the most influential body to the spacecraft environment is the sun, which (excluding planetary decay processes) provides 99.9% of the energy in the solar system[1]. Energy is emitted across the whole electromagnetic spectrum, but particularly in the form of infra-red (IR), visible, ultra violet (UV) and X-rays. The sun not only emits massive amounts of energy but also matter, predominantly in the form of electrons and protons. This stream of matter from the sun is called the solar wind.

Van Allen radiation belts contain energetic protons and electrons from the solar wind that are trapped inside the Earth's magnetic field. These trapped particles are known to degrade electronic parts due to high-energy particle impact, affecting both the energy structure and lattice structure of semiconductors [2]. Normally, low Earth orbits (those below 1000km) are too low for the Van Allen belt to cause concern, however asymmetry in the Earth's magnetic field reduces the altitude of this belt above the South Atlantic Ocean in a region called the South Atlantic Anomaly (SAA), which can at times be troublesome [3].

The Earth's gravitational field is not only essential for describing why the Earth is like it is, but is very significant for orbiting bodies, whether they are spacecraft or meteoroids. Meteoroids are solid objects that range in size and mass over many orders of magnitude and originate from natural and man-made sources. Due to the large relative impact velocities of these bodies, they can cause significant damage even when they are very small particles [4]. Very small particles can affect thermo-optical surface properties whilst larger particles can cause a catastrophic loss of a satellite. Meteoroid impacts create yet more particles and debris, increasing the risk of future impacts.

The orbit of a satellite alone can greatly influence its environment, particularly with respect to temperature. The thermal environment of a spacecraft is influenced predominantly by direct heating from the Sun. As a low Earth orbit (LEO) satellite enters or exits the Earth's shadow, very high heating or cooling rates can occur that can warp or fatigue materials to the point of failure [5].

Last but by no means least, it is important to describe the contributions made by Earth's atmosphere. In the upper atmosphere, vacuum (10-200nm) and extreme (1-30nm) ultra-violet light (VUV and EUV) from the Sun interact with atmospheric species to create the ionosphere, an atmospheric layer of heated plasma. Orbiting spacecraft passing through the ionosphere may suffer rapid electrical discharges that can damage instrumentation and material surfaces should charging effects not be accounted for in the spacecraft design [6].

Solar energy also affects the density of the thermosphere, a region of Earth's atmosphere between 90–600 kilometres altitude. Although the density of the thermosphere is low, the drag forces present greatly affect the orbits and trajectories of passing spacecraft due to the relative speed of impact with atmospheric species. Drag should be countered by an appropriate propulsion system to prevent re-entry into the Earth's lower atmosphere and the obvious loss of the spacecraft [7]. More importantly for this thesis, important chemical processes are occurring as a spacecraft impacts the thermosphere. The most abundant species in the thermosphere is atomic oxygen (AO).

AO is formed by the UV dissociation of molecular oxygen and is therefore a process driven by solar emissions. As AO strikes forward (ram) facing spacecraft surfaces at high relative velocities, several important phenomena occur. One of the effects is to degrade these surfaces, often by erosion.

The modification of surfaces by AO is an extremely important consideration for spacecraft developers. Modified surfaces can lead to changes in thermo-optical properties and electrical properties that in turn affect other design considerations such as spacecraft charging and spacecraft heating as discussed above [8].

## 1.2 Atomic Oxygen Detection

To aid spacecraft designers select and develop appropriate materials to be exposed to an AO environment, it is important to assess the concentration or typical doses of the species in a particular orbital regime, or a man-made simulator.

The University of Southampton has developed sensors that are suitable for measuring the concentration of atomic oxygen at different Earth orbits[9]. In the past, the university has developed silver sensors (or actinometers) that measure AO flux by monitoring changes in electrical resistance across an eroding silver film [10-12]. Unfortunately, the effectiveness of these sensors is restricted by the development of an oxide film as the silver reacts with AO, making sensor response dependent on a diffusion-based mechanism. These silver actinometers also have a limited life, as eventually the film will react completely.

More recently, the university has been developing semi-conducting films, made from n-type zinc oxide (ZnO), for the purposes of AO detection [13-15]. These sensors do not erode, but exhibit a change in resistance as the zinc oxide adsorbs AO. When heated, the zinc oxide expels the adsorbed AO, restoring the resistance to approximately the ‘pre-exposure’ values. This so-called ‘regeneration’ gives a much-extended sensor lifetime, over the silver actinometers.

Despite the advantages of the zinc oxide sensor there remain some difficulties. The zinc oxide sensors have a complex response to AO exposure, and suffer electrically conductive hysteresis effects when regenerated. Whilst some of these difficulties may be overcome by suitable development, these sensors are inherently unsuitable for continuous material characterisation purposes, as AO measurement is interrupted as the sensor is regenerated [9].

Carbon has been identified as another suitable sensing material. The material is known to produce volatile oxides so offers a lifetime advantage over the silver actinometers, as they are not passivated by the development of an oxide layer [9].

The response from carbon sensors is known to be much simpler than ZnO sensors, so offering an advantage.

An interesting aspect of carbon is that it is commonly available in two different allotropes and many other different forms, as will be highlighted in a later chapter. The many possible variants could mean that a wide range of different responses to AO are also available, which have not yet been researched. This work will focus on developing suitable carbon materials for AO sensing in a wide range of orbital applications.

## 1.3 Spaceflight Opportunity

During the course of the research presented here, there have been two flight opportunities to test the carbon materials.

A package, named the European Technology Exposure Facility (EuTEF), is due to fly aboard the International Space Station (ISS), a manned low Earth orbiting experimental platform. EuTEF will contain a variety of experimental platforms that are directly exposed to the LEO environment for a period of 3 years. The Materials Exposure and Degradation Experiment on EuTEF (MEDET) is one such experiment [16].

MEDET is a project run jointly between the European Space Agency (ESA), Centre National d'Etudes Spatiales (CNES), Office National d'Etudes et de Recherches Aerospatiales (ONERA) and the University of Southampton. MEDET will be used primarily to monitor the effects of the LEO environment (such as solar energy emission, space debris and AO fluxes) on a selection of materials.
The Southampton Transient Oxygen and Radiation Monitor (STORM) aboard MEDET will be used to monitor X-ray, UV and AO fluxes and will house the developed AO sensor [17].

Recently, there has been much focus on developing very small micro (<100kg), nano (<10kg) and more recently pico-satellites (<1kg) [18-20], which can be launched and operated at significantly less cost than more traditional platforms. The advantage of actinometers over other existing AO sensing techniques is that they are very simple, lightweight and use only very small amounts of power, so they lend themselves well to such an application [9].

An opportunity to fly aboard a nano-satellite has also arisen during the course of this work. The Canadian Advanced Nanospace Experiment (CANX) program is an initiative set up by the University of Toronto Institute for Aerospace Studies Space Flight Laboratory (UTIAS/SFL) [21]. The second experiment of the program, CANX-2 is a 3.5kg nanosatellite used as a test-bed for future formation flying missions. The experimental package consists of an atmospheric spectrometer, a dual band GPS receiver/antenna and an atomic oxygen degradation experiment.

The orbital parameters for this nano-satellite are much less defined than the ISS mission. In order to save launch costs, the satellite orbit is defined by the requirements of a larger satellite to which the nano-satellite is ‘piggy-backed’ or simply by the chosen launch vehicle capabilities. The CANX-2 mission is designed to orbit Earth for a period of 1 year before undertaking a de-orbit manoeuvre. The type of orbit and altitude were not defined during satellite constuction, but was later set for a 600km LEO. This will naturally impact the AO dose and the thermal environment of the spacecraft.

It should be noted that the anticipated total AO dose of each orbital platform is much greater than that of previous AO detector flights [22]. The emphasis of this work is to therefore develop carbon films that can measure these greater doses.

## 1.4 Project Aims

The aims of this project are:

- To investigate the nature of the carbon/AO interaction including reaction characteristics and rates, with a wide variety of carbon materials.
- To analyse the data acquired from carbon-based sensors and how it relates to AO dose.
- To develop carbon-based films suitable for a variety of atomic oxygen sensing missions, including the long duration MEDET mission and the shorter duration CANX2 mission.

## 1.5 Manuscript Layout

This document begins with a literature review of AO, its simulation and measurement. The literature review then continues, covering actinometer research to date before describing carbon and its various reactions with AO.

The experimental phase of this work is then described. Chapter 5 describes the general design of the actinometer devices used in this work and their integration with the ISS and CANX2.

Chapters 6 and 7 provide details of the experimental design, AO simulation facilities and characterisation methods. Chapter 7 also gives some detail on the latest research into interpretation of Raman spectra, as the understanding of this technique has improved significantly in recent years [23-27].

Three different ways of producing carbon films for actinometers were investigated. The results and some discussion of each deposition method are given their own chapter. Chapter 8 covers the evaporated films, Chapter 9 the sputtered and Chapter 10 the screen-printed film results.

In Chapter 11 each deposition method is compared in terms of the reactions with AO and the use of each film as a sensing material. The work is concluded and suggestions for further work are made in Chapter 12.

## 1.6 Publications

As a result of the work described here, six conference contributions have been published in proceedings[28-33]. Additionally, one journal paper has been published and others are currently work in progress [34].

# 2 THERMOSPHERIC ATOMIC OXYGEN, ITS SIMULATION AND MEASUREMENT

## 2.1 Introduction

This chapter will be used to summarise the processes by which atomic oxygen is formed, both by natural and man made processes. This chapter will then go on to summarise the effects of atomic oxygen and the techniques used to measure it. It should be noted that these topics are very comprehensive subjects that could each demand a stand-alone chapter. However, Harris [35] and Osborne [15] have reviewed this work extensively, so without repeating these works, each topic is summarised and reviewed in a single chapter for completeness.

## 2.2 Atomic Oxygen Formation

Atomic oxygen is commonly formed by the dissociation of molecular oxygen. Dissociation occurs when sufficient energy is provided to the oxygen molecule, where the sources of energy can vary greatly.

### *2.2.1 Atmospheric AO formation*

Five distinct layers based on thermal characteristics, chemical composition, movement and density identify the Earth's neutral atmosphere. These layers are called the troposphere (0-15km above Earth's surface), stratosphere (15-50km), mesosphere (50-85km), the thermosphere (85-600km), where most low Earth orbits take place and the exosphere (>600km) [36].

Oxygen is present in all these layers, but in different quantities and forms. Molecular oxygen is the dominant oxygen in the troposphere and is formed at the Earth's surface by biological photosynthesis and UV dissociation of surface water.

By a process of convection and diffusion, oxygen is found in the stratosphere. At these altitudes atmospheric density is much lower and UV solar energy becomes strong enough to split oxygen molecules into neutral atomic oxygen, a process called photo-dissociation. In the stratosphere, these oxygen atoms are free to recombine into a variety of molecules, the most important one of which is ozone ($O_3$). The ozone layer lies within the stratosphere [37].

At greater altitudes atmospheric species become excited as they absorb the Sun's energy until the thermosphere is reached. Like the stratosphere, photo-dissociation of molecular oxygen takes place within the thermosphere. Atomic oxygen (AO) is not the main constituent in the stratosphere because mean free paths allow sufficient particle collisions to form new molecules. However, the lower density of the thermosphere does not allow such collisions to take place and so neutral AO becomes the dominant species. In fact, as altitude increases the relative concentrations of AO continue to increase due to a reduction in recombination probability [8]. Figure 1 shows the typical compositional variation of the major atmospheric constituents over the altitude range 100 - 800 km.

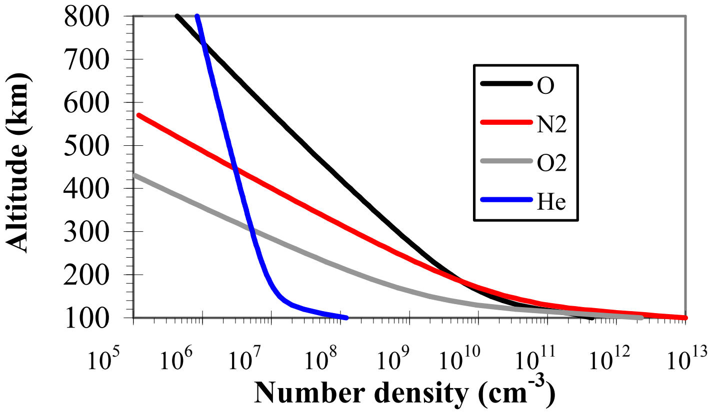

**Figure 1: Compositional variation of the thermosphere [15]**

Given the formation of AO is reliant on solar UV, it is perhaps unsurprising that the rate of AO formation is dependant on solar illumination, especially at VUV and EUV wavelengths. A consequence of this is that AO number density is influenced by the intensity variations associated with the (11 year) solar cycle. Variation of AO number density with solar activity is demonstrated in Figure 2, which shows curves for solar minimum, maximum and mean irradiation levels. Clearly, the effect of solar activity is most significant at the higher altitudes, where AO density may alter by as much as two orders of magnitude between solar minimum and maximum. Near the bottom of the thermosphere, in comparison, the density varies by much less than one order of magnitude.

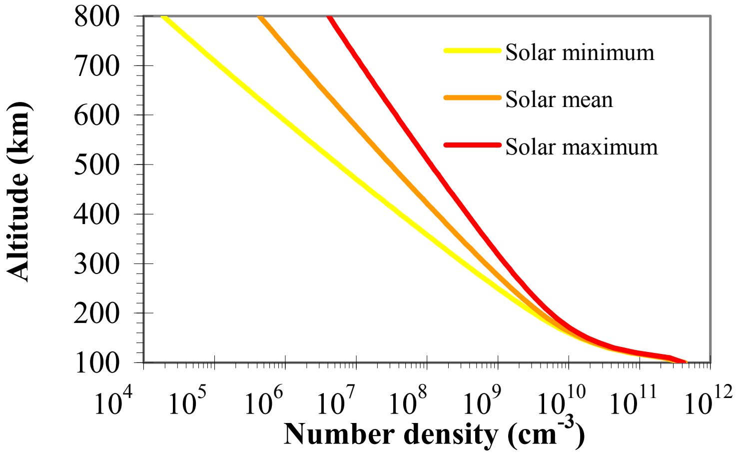

**Figure 2: Variation of AO abundance within the thermosphere [15]**

It should be noted that AO is free to move within the thermosphere, and between atmospheric layers. However, the speed of these species relative to an impacting spacecraft is sufficiently low to be considered zero. Although the atoms have nominally zero translational energy, they are at a temperature above zero Kelvin so have a thermal energy described by the following equation of an ideal monatomic gas:

$$Energy(eV) = \frac{3k_B T}{2e}$$ **Equation 1**

where

*$k_B$=Boltzmanns constant ( $1.38x10^{-23}$ J/atom/K), T = gas temperature (K) and e=electron charge ($1.6x10^{-19}$C).*

At typical LEO altitudes the mean thermospheric temperature is ~1000K, which gives an AO thermal energy of ~0.14eV.

Spacecraft pass through the Earth's atmosphere at very high velocities, LEO spacecraft travel at approximately 8 km/s [38] and some elliptical orbits like that of geo-stationary transfer orbits (GTO) can reach speeds of 11km/s or more at perigee [11]. The oxygen atoms have some thermal energy, but this is usually neglected because of the high relative speeds between the atoms and the spacecraft. The high velocities give the atoms a high translational or kinetic energy, as defined by the equation below.

$$Energy(eV) = \frac{m_{o1} v_{s/c}^2}{2e} \qquad \textbf{Equation 2}$$

where

$m_{o1}$=O atom mass, $v_{s/c}$=spacecraft velocity, $e$=electron charge ($1.6x10^{-19}C$).

### 2.2.2 Ground-based, man-made AO

Spaceflight experiments are inherently expensive and can sometimes be impractical to assess AO effects on materials. For fundamental AO research such as the:

1) determination and prediction of erosion yields,
2) calibration of sensors and
3) investigation of synergistic effects,

AO induced effects need to be separated from other parameters such as UV and micrometeoroid degradation at lower costs than spacecraft experiments.

Several researchers have tried to produce an AO environment in ground based simulation facilities [39]. The fundamental difference between the formation of atmospheric AO and that simulated on the ground is that ground based sources may need to adopt a method of accelerating AO to speeds comparable to that of impacting spacecraft. When accelerating AO additional energy, surplus to dissociation, is required. A risk with providing this additional energy is that some energy will be used to strip off electrons and form oxygen ions rather than fast neutral AO. This statement somewhat summarises why there are a variety of AO sources with different beam energies and ion/neutral species content. Another factor that complicates AO simulation is that in some cases testing needs to be accelerated. Accelerated tests require yet more energy to dissociate greater concentrations of molecular oxygen, and so care must be taken to ensure that energy is distributed equally to each molecule, otherwise beam content could be somewhat more variable.

Table 1 lists some of the various methods by which atomic oxygen is created. Perhaps the most curious omission from the table is that UV photo-dissociation is not currently used to break-down molecular oxygen, as evident in the LEO environment. There is no documentation found explaining why this is so. Also included are two methods that produce predominantly oxygen ions and are commonly used in the AO community. Whilst these sources do not strictly produce neutral AO, they provide a simple means to accelerate oxygen erosion, when it is not possible to use existing AO simulation technology.

| **AO Formation Method** | **Beam Acceleration/ Delivery** | **Mode** | **Beam Energy (eV)** | **Flux (species/ $cm^2$/s)** | **Flux Composition (%)** | **Reference** |
|---|---|---|---|---|---|---|
| RF Plasma | Electrostatic | Pulsed | 5 | $5x10^{15}$ | (1/99) $O^+$/O (+VUV) | [41, 42] |
| Pulsed Laser Breakdown of $O_2$ | Detonation Wave in Supersonic Nozzle | Pulsed | 1-16 | $10^{15}$-$10^{17}$ | (10/90) $O_2$ /O (+VUV) | [43, 44] |
| Pulsed Laser Breakdown of $O_2$ | Detonation Wave in Supersonic Nozzle | Pulsed | 5 | $10^{14}$ | (60/40) $O_2$ /O | [39] |
| Laser Breakdown of $O_2$ in Ar | Supersonic Expansion | Continuous | 1-3 | $10^{16}$ | (90/7/3) Ar/ $O_2$ /O | [38, 45] |
| Microwave Breakdown of $O_2$ in He | Supersonic Expansion | Continuous | 1-3 | $10^{17}$ | (97/1/2) He/ $O_2$ /O | [46] |
| Arc discharge | Electrostatic | Continuous | 30-50 | $10^{14}$ | ~(100) $O^+$ | [39] |
| $O_2$ dissociation/ diffusion through Ag foil | Electron-stimulated desorption | Continuous | 5 | $5x10^{13}$ | ~(100) O | [47] |

**Table 1: A sample of modern AO simulation methods**

## 2.3 AO effects

The most significant effects of AO on a spacecraft are drag, shuttle glow and surface modification.

### *2.3.1 Drag*

As a spacecraft passes through the Earth's atmosphere there will be a reaction force from the oxygen atoms that will collectively slow the spacecraft. Drag is an important problem because as a spacecraft slows down, it will gradually de-orbit. The Long Duration Exposure Facility (LDEF) is an example of how drag can affect the performance of a satellite. Launched in 1984 by the Challenger Space Shuttle, the LDEF was an orbital platform that exposed a wide range of candidate spacecraft materials to the LEO environment for a period of 2114 days [48]. During the course of its mission, LDEF had slowed to such an extent that its retrieval date was brought forward to prevent a dangerous de-orbit [49]. Although AO does contribute to drag forces, so do a number of other effects such as micrometeoroid impacts that are beyond the scope of this work.

### *2.3.2 Shuttle glow*

Shuttle glow is a phenomenon where atomic oxygen atoms interact with nitrogen-based species around a spacecraft, creating an optical emission [50]. Nitrogen atoms, molecules and nitrous oxide molecules that are present in the thermosphere, the spacecraft materials or mass ejections (like reaction thruster firings) can be found on or surrounding spacecraft surfaces and in the wake of the vehicle. The AO reacts to form vibrationally excited species, which then relax to the ground state by photon emission, thereby producing an optical emission, or glow (Figure 3). The glow has emissions in the infra-red, visible and UV wavelengths and can interfere with the operation of optical devices, especially those operating in these spectral bands [50]. Shuttle glow is so termed because its presence was first confirmed by optical photography on the STS-3 space shuttle mission [51].

**Figure 3: Solar illuminated shuttle tail-fin (left) and shuttle glow during eclipse (right). Image courtesy of NASA.**

### *2.3.3 Surface modification*

As a spacecraft collides with high-energy AO atoms, susceptible materials on the forward facing (ram) surfaces can react with the oxygen if there is sufficient energy to break the chemical bonds. Table 2 shows some important bonds and their associated energies found in a variety of spacecraft polymers. The chemical reactions that can take place have different effects on different materials. The oxides that form during these reactions can be classed into two kinds: gaseous (volatile) or solid (stable).

| Bond | Energy (eV) |
|---|---|
| C-C | 3.58 |
| C-H | 4.24 |
| C-O | 3.70 |
| C-N | 3.16 |
| C=C | 6.24 |
| C=O | 8.27 |
| AO Energy | LEO ~ 5<br>GTO ~ 9 |

**Table 2: Common chemical bond strengths[52]**

Gaseous oxides are often found in the reaction with polymers and usually leave the surface of the parent material, causing it to recede. Typical oxides are CO, $CO_2$ and $NO_2$. Figure 4 shows a scanning electron microscope (SEM) image of a Kapton-H polymer post AO exposure. Kapton-H is a common spacecraft material used on thermal blankets to help maintain steady temperatures. The image shows that a debris particle inadvertently left on the surface has protected the underlying material from AO attack. It can be seen that the material exposed to AO has eroded somewhat, leaving a rough grass, or rug-like texture. The texturing seen here is typical for many kinds of carbon-based materials.

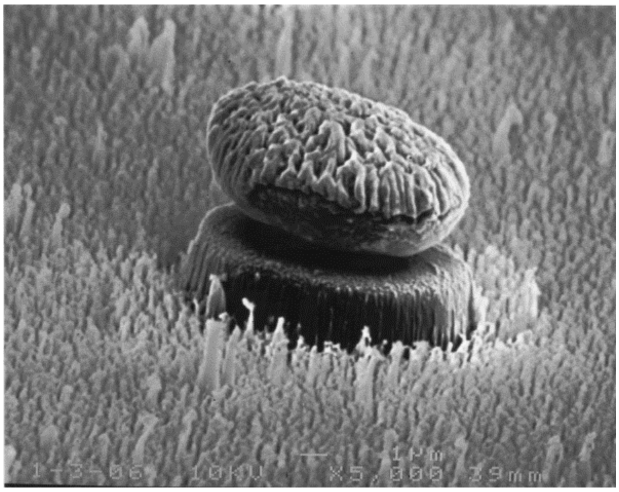

**Figure 4: SEM image of particle on Kapton exposed to ~1.4x10$^{20}$ atoms/cm$^{-2}$, x5000 taken from [53]**

AO may also react with certain materials to form a solid oxide, causing the mass of the sample to increase. Solid oxides may be porous to AO and other species, as in the case of silver oxides or form a protective barrier, as with aluminium.

Irrespective of the type of oxide, the standard method of defining reaction rates of *virgin* material is the erosion yield, as defined by equation 3 [48].

$$Y = \frac{\Delta m}{\rho F A} = \frac{\Delta \tau}{F}$$ **Equation 3**

*Y=yield (cm$^3$/atom), $\Delta m$ =mass loss of virgin material (g), A=affected area (cm$^2$), $\rho$=density (g/cm$^3$), $\Delta\tau$ = thickness loss (cm) and F=AO fluence (atoms/cm$^2$)*

Another way of expressing reaction rate, but not as commonly used is the reaction probability, P [54].

$$P = \frac{y}{f} \qquad \textbf{Equation 4}$$

*where y = rate of material loss (atoms/cm$^2$/s), f = AO flux (atoms/cm$^2$/s).*

In some cases, UV illuminating on material surfaces is known to enhance the erosive effect of AO. This effect, termed ‘AO-UV synergism’, has undergone many studies on various materials [55, 56]. Under certain conditions, one study has shown that the erosion rate increases by up to 400% over non-illuminated Kapton samples [57].

## 2.4 AO measurement

There are a wide variety of AO sensing techniques as reviewed by Osborne *et al* [9], which are described under the headings of 1) witness samples, 2) mass spectrometry, 3) catalytic probes, 4) optical methods, 5) crystal microbalances, or 6) actinometers. A brief summary of each method is provided in this section.

### *2.4.1 Witness Samples*

Presently the accepted reference standard for AO measurement is by Kapton witness sample (KWS) erosion [58, 59]. Witness samples are the simplest form of AO measurement. Samples of material with a known erosion yield, which in the case of Kapton is assumed to be 3x10$^{-24}$cm$^3$/atom, are exposed to the AO fluence. During exposure the surface erodes, causing a change in surface profile and mass; measuring these changes and using the data with equation 3 provide a fluence estimate.

The main advantages of this method are that it is small, light and does not require power. This method is also very low cost provided mass and profile measurement facilities are available. The simplicity of this method means that it can be applied to any AO simulation facility and it is for this reason that it is useful as a common reference standard.

The inherent problems with this method are that:

1. It is susceptible to contamination errors,
2. It does not provide in-situ measurements (it only provides post exposure measurement of fluence)
3. The erosion yield of Kapton is very variable and
4. Accuracy is generally poor for low fluences.

The most significant disadvantage of this method is that the erosion yield of Kapton is not always 3 $\times 10^{-24}$ $cm^3$/atom. This value was derived from the early LEO space shuttle missions [60], but subsequent ground based testing has revealed that the erosion rate is proportional to beam energy, sample temperature and the relative intensity of UV light and AO [57, 61]. In the latter case, for extremely high intensities of UV (albeit unrealistic) the erosion rate is increased by 400%.

### *2.4.2 Mass Spectrometers*

Contrasting greatly with witness sample measurement, mass spectrometers are one of the most frequently used and sophisticated instruments for thermospheric investigations. The main benefits of mass spectrometers are that they are able to provide direct, time resolved measurements of thermospheric densities. They can also make measurements of other neutral and charged species [62]. Disadvantages include mass, power and cost budgets. With the ever-increasing use of small satellite technology, this approach to AO measurement may be used less frequently. The sophisticated nature of this technique also means it would be difficult to use as a measurement standard for ground based applications, as different AO facilities would require different systems.

### *2.4.3 Catalytic Probes*

Catalytic probes measure AO flux via the energy released during a recombination reaction on a catalytic surface [63]. Thermocouples attached to the surface of the catalyst are used to measure the heat energy released during recombination. The amount of heat released, and hence the temperature, is proportional to the amount of AO impinging the surface. These sensors are simple, low mass, low size and low power instruments, but are only useful in steady thermal conditions, and so are generally unsuited for orbital applications and many ground based AO facilities where temperatures are known to vary significantly.

### *2.4.4 Optical Methods*

Optical methods are based on the measurement of the emission, scattering or absorption of visible, infrared or ultraviolet radiation caused by atomic oxygen. Optical methods vary significantly, but in general they are more complex systems that consume more power and mass than many of the methods discussed above. However, there are two recent exceptions to this general rule.

The first of these optical techniques measures the AO induced reflectance changes of an optically thin metal film deposited on the end of an optical fibre [64-66]. As the film is oxidised by AO, the reflectance of the fibre-film interface alters, thus the change of reflectance can be associated with the accumulated AO exposure. Reflectance changes are measured by passing the radiation from a light emitting diode (LED) along the fibre and comparing the intensity of the back reflection to that of the LED output.

A technique using the change in transmission of a polymethylmethacrylate (Perspex ®) optical fibre subject to AO attack has also been proposed for a micro-satellite application [9]. AO erosion of the fibre alters its transmissivity, which is measured by shining LED light along the fibre and comparing intensities before and after transmission.

Neither of the two optical methods described have flown successfully in space, but their simplicity, low mass and power mean that these methods are promising for the increasing numbers of small satellite missions. The main limitations of these techniques are that once the reacting film becomes fully consumed, no further measurements can be made.

### *2.4.5 Quartz Crystal Microbalances*

Quartz-crystal microbalances (QCM) consist of essentially a piezo-excited quartz crystal coated with a material sample that reacts with AO. Depending on the kind of oxides developed, the mass of the crystal will either increase or decrease giving a measurable change in resonant frequency.

This method is able to provide high resolution, in-situ measurements and can therefore measure both flux and fluence. The sensors themselves are light, compact and consume relatively small amounts of power. The other advantages of QCMs are that a wide variety of materials can be deposited onto the crystal and if no coating is applied have the ability to measure contamination [67]. These advantages mean that QCMs have been used for a wide variety of sensing applications, both in orbit and in ground based testing applications [68-71].

The QCM has moving parts, resonating by the order of $10^6$ Hz, so there can be reliability issues for the sensor. The electronics used to measure these high frequencies are also moderately complex; detrimentally affecting cost and reliability. Unless two QCMs are used, one coated and one uncoated, one of the side effects of measuring mass changes is that the sensor is unable to discriminate contaminants and absorbed species from AO erosion, which could lead to underestimates in the AO flux readings.

### *2.4.6 Actinometers*

Actinometers are electrically conducting films that experience a change in ohmic resistance when exposed to AO. Either erosion of the conducting film or oxygen absorption/adsorption into the film brings about the change in resistance [9]. These devices are inexpensive, lightweight and consume relatively low amounts of power.

They can provide in-situ measurements of flux and fluence and require very simple electronics to do so. This makes the actinometer ideal for small satellite applications where such issues are vitally important [11, 12, 14].

As actinometers are exposed directly to the space environment, there is the possibility that the AO sensitive element becomes coated to some degree by contaminants. Obviously this will have an effect on sensor response if the contaminant is not easily removed by AO, leading to an underestimate in AO fluence. However, all the other sensing methods described here have this problem except for mass spectrometers. Another common problem shared with many other sensing methods is that the eroding actinometers have a limited lifetime, although using thicker or less sensitive materials to AO attack can increase this.

Actinometers that use adsorption as the sensing mechanism have the advantage of being reused upon heating, but this consequently increases the power consumption and complexity of the device. Adsorption devices also require disruption of the AO measurement when being heated for re-use.

### *2.4.7 Summary*

The measurement techniques summarised here span a wide range of operating parameters and each technique has different advantages and disadvantages. The ideal system would utilise the least amount of mass and power, have an infinite lifetime, be simple to activate and have the ability to monitor fluxes of AO and other species to a high-resolution, without being effected by contamination. Unfortunately there is no such system and so measurement techniques have to be selected by the constraints of the mission. As will be reviewed in the next chapter, actinometers have been applied to a wide range of space missions, from micro-satellite applications to space shuttle missions, as they are simple, inexpensive and have low mass and power budgets. Most importantly of all, the lifetime of the actinometer can be adjusted to meet the needs of a particular mission by using films of different materials. This thesis will now describe how different actinometer materials respond to the AO environment.

# 3 A REVIEW OF ATOMIC OXYGEN ACTINOMETERS

## 3.1 Introduction

As highlighted in the previous section, actinometers are a highly versatile and inexpensive solution to atomic oxygen measurement. They offer a number of advantages over other sensing techniques, particularly for space flight experiments with low mass and power budgets [72]. The AO sensitive material used for the actinometer greatly affects its response and its method of operation.

Actinometers are available in essentially two different forms: those that have a limited useable lifetime (non-renewable) and those that do not (renewable).

- Non-renewable actinometers usually depend on a degrading chemical reaction of some sort to measure atomic oxygen flux. Typical examples are carbon film actinometers and silver film actinometers. Although the reaction mechanisms of these two materials are different, material degradation plays a fundamental sensing role in both cases. As AO reacts with the material the volume of electrically conducting material falls and in most cases cannot be recovered.

- Renewable actinometers do not depend on a degradation mechanism to measure AO flux. Instead the exposed sensor material will typically absorb or adsorb the oxygen atoms in some way, creating a resistance change. The “renewable” aspect occurs when these oxygen atoms can be desorbed later in the sensors life to return the actinometer back to (ideally) its original condition.

Almost all the work carried out on actinometers has been on three types of film material. These materials are silver, carbon and zinc oxide. Of these materials zinc oxide is the only material researched that can provide renewable properties. Other materials, like osmium can also be used as the sensing element, but for various reasons have not been studied thoroughly. This section will provide a comprehensive review of previous work undertaken to develop these sensors, with particular emphasis on the AO sensitive material.

## 3.2 Silver Actinometers

Before discussing the use of silver as a non-renewable actinometer, it is appropriate to begin with a description of how the material reacts with AO.

### *3.2.1 Reactions with AO*

Silver reactions with AO are:

$$2Ag\ (s) + O\ (g) \rightarrow Ag_2O\ (s)$$

$$Ag\ (s) + O\ (g) \rightarrow AgO\ (s)$$

Under AO exposure $Ag_2O$ is formed when an excess of silver exists and AgO is formed with an excess of AO. Some properties of silver and its oxides are given in Table 3:

| Property | Ag | $Ag_2O$ | AgO |
|---|---|---|---|
| **Density, g cm$^{-3}$** | 10.49 | 7.14 | 7.44 |
| **Molar volume, cm$^{-3}$** | 10.25 | 16.25 | 16.6 |
| **Resistivity at 20°C, Ω.cm** | $1.587 \times 10^{-6}$ | $10^{8}$ | 14 |
| **High temperatures (@1 bar)** | Melts at 960.8°C | Reduces to silver ~250°C | Decomposes to $Ag_2O$ at ~110°C |

**Table 3:Properties of silver and its oxides from [73] and [11]**

Investigations by Oakes [74] involving the in-situ measurement of film mass during AO exposure show that for the first 250 angstroms of film oxidation, the mass increase is linear. After this, the oxide layer becomes diffusion limiting; the reaction rate begins to slow because the oxygen atoms are diffusing through the oxide layer before arriving at the virgin material. Over time the diffusing oxygen atoms may recombine to form molecular oxygen, which being less reactive contributes to a reduction in the reaction rate of the material [72, 75]. Additionally as less and less silver atoms are available for reaction so the probability of an oxygen atom reacting reduces [74].

Oakes [74] found that during the diffusion-limiting period, silver reacts to form the peroxide AgO preferentially to $Ag_2O$ at an AO flux equivalent to $1x10^{15}$atoms/ $cm^2$/s and a sample temperature of 20°C. Unfortunately, this work was not able to comment on the reaction products during the initial linear phase of reaction. The preceding work of Moore [76] states that this initial layer also consists of AgO, but unfortunately the flux used to obtain this result is not clear from the paper.

The linear reaction rate has been reported by many authors as independent of temperature and sample thickness between 0°C and 85°C [74, 77, 78]. This offers some advantage over materials that do have temperature dependence, as a temperature sensor or temperature controlling device may not need to be incorporated into the design of the AO sensor, thus giving any sensor package greater mass and power economy.

At temperatures above 80°C, the reaction rate of silver increases to a point where, at 150°C, the erosion rate is six times greater[38]. At this temperature, the oxides formed were found to be predominantly $Ag_2O$ rather than the AgO observed at room temperature. Unfortunately no flux values are quoted for comparison with Oakes [74].

The linear reaction rate has also been reported as independent of AO energy between 1 and 12eV [74, 77, 79] using ground based simulation techniques. This means that sensors flying on very different orbits can be compared easily, for example data from LEO sensors could be compared with GTO sensors assuming a constant temperature.

It is interesting to note from Table 3 that as the silver oxides are heated they can reduce back to silver. For AO measurement, this is a useful characteristic, as it would appear the silver could act as a renewable AO sensor by the application of temperature. The works of [80] and [76] have identified and demonstrated this effect, stating that oxidised films can be recycled many times and will assimilate as much oxygen as the original film. Whilst this system of operation adds an additional power requirement and complexity to the actinometer, the benefits of having a sensor with a nominally infinite lifetime could out-weigh the disadvantages. Indeed, if a small single crystal of silver were used, the additional power requirement may be very small. The main practical limitation to this idea is the potential of oxide layer flaking, as described below.

Table 3 shows that the molar volumes of the oxides are approximately 60% greater than the original silver material. Consequently, as the oxide layer builds up, stresses develop between the metal and oxide causing the oxide layer to flake away; a phenomenon that has been observed by a variety of space flight experiments and ground based simulations[81-83]. Flaking of the oxide layer means that virgin material will continually be exposed to atomic oxygen and react, unlike the protective oxides formed on other metals such as aluminium or copper. If flaking is allowed to occur, it will provide a mass loss and silver films will be unsuited to the renewable approach mentioned above, because after regeneration the film will be different to its pre-exposure condition. However, if the sensor is heated before oxides detach (within the 250 angstrom oxide thickness limit, mentioned above) then there could be some potential for silver as a renewable sensor material. Unfortunately there is little other research investigating this aspect of silver.

### *3.2.2 Silver Actinometer Performance*

Silver is perhaps the most frequently used actinometer material to date because silver is well suited for sounding rocket missions that pioneered the use of actinometers in the early nineteen seventies[84, 85]. Sounding rockets are not orbital platforms and as such have very little time to react with AO. Silver is well suited for this purpose because its high reaction rate with AO ensures readings are sensitive to low fluences.

A number of flight experiments have used silver actinometers for AO measurement as listed in Table 4.

| Flight | Film Thickness | Reference |
|---|---|---|
| Sounding Rockets | 380-570 angstroms<br>10-100 angstroms | [85]<br>[73] |
| STS-4 | 2250 angstroms | [86] |
| STS- 41 (ISAC) | 1.1 micrometers | [87] |
| STS- 46 (CONCAP-II) | 220 angstroms | [88, 89] |
| STRV-1a | 1836-2839 angstroms | [11] |
| STS80 & STS85 (SESAM) | 100 nanometres | [90] |

**Table 4: Summary of silver actinometer flights**

Upon AO exposure, the silver film initially erodes in a linear fashion until a point where the response becomes parabolic with fluence due to the continued growth of the oxide layer. This point occurs when thicknesses are between 250 and 350 angstroms. As the oxide layer thickens, the time for the oxygen atoms to reach the conducting virgin substrate increases and so a time lag between AO flux and sensor response is observed. This phenomenon is called coasting [72]. These trends are seen by all the experiments referenced above.

It is pertinent to point out that because the useful (linear) life of the sensor always occurs within the first few hundred angstroms, no matter how much thicker the films are than this, AO measurement is limited by a maximum measurable fluence dictated by these first few hundred angstroms. Assuming an erosion yield of $141\text{x}10^{-25}\text{cm}^3/\text{atom}$ [72] and a thickness of 350 angstroms, this maximum fluence can be calculated as being $2.5\text{x}10^{16}\text{atoms/cm}^2$.

An important aspect of silver actinometer calibration is the need to associate a resistance value with a thickness value. The change of thickness can then be associated to an AO fluence, assuming that erosion yield is constant. Therefore an understanding of film electrical properties is essential. The work of Harris [10] has reviewed this topic in great detail for thin silver films.

At any given temperature the resistivity of bulk silver, or any metallic conductor, is assumed constant. However as the film thickness reduces so that it approaches the mean free path of electrons, the movement of free electrons becomes impaired, so reducing the effective mean free path and increasing resistivity.

The mean free path of silver is found experimentally and theoretically to lie within the range of 500 to 530 angstroms[10, 91, 92]. Since the useful, linear life of silver actinometers lies somewhere within the first 250 angstroms of film thickness, the effect of mean free path must be considered. If the effect of resistivity change is not accounted for, then estimated film thickness would be artificially high.

The most useful way with which to take account of the above effect is by experiment, as there are differences between theoretical and practical resistivity trends, brought about by contact effects, island formation and substrate roughness [53]. Figure 5 shows the variation of silver film thickness and resistivity obtained by evaporation depositing 172 silver films with different thicknesses onto a glass substrate. Figure 5 also shows the curve used to fit this data, the equation being:

$$R = \frac{4.1x10^9}{\tau^3} - \frac{4.4x10^6}{\tau^2} + \frac{15000}{\tau} - 1.4 \qquad \textbf{Equation 5}$$

*where thicknesses (τ) are in angstroms.*

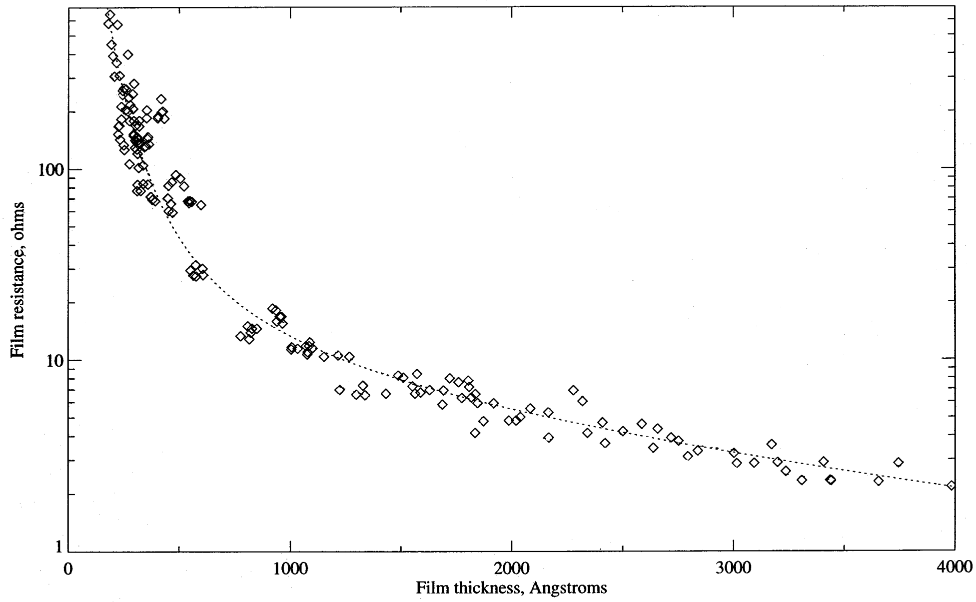

**Figure 5: Silver film resistance-thickness variation [10]**

A description of how silver films are used to detect AO has now been given and it is perhaps worthwhile to comment on the validity of measuring resistance to ascertain levels of silver mass loss. A direct comparison between the oxidation of a silver coated QCM and a silver actinometer is made by Oakes [74]. In general measurements made by each device exhibited similar behaviour and produced similar estimates of the AO flux. However, the silver actinometers in this study were found to be four times more variable than the silver coated QCMs.

The reasons for this variability are:

- Resistivity was assumed constant and equal to that of bulk silver. Obviously, if this study had considered the thickness dependence of resistivity, like the work of Harris [10, 11, 53], then variability could be reduced somewhat.

- Contact resistance. The film contact resistances were found to be a major source of variability.

- Uncertainty in stoichiometry. In order to calculate the oxygen atom flux from the resistance data of a silver film, Oakes has stated that stoichiometry of the oxide layer must be known to obtain a measurement of AO flux. This statement is true, if absolute values of flux are to be determined independently of other measurement techniques. However flux can still be determined if the response of silver films to AO are repeatable and the results from the actinometers are calibrated against results from other measurement techniques exposed to the same conditions. The silver reaction investigations in the above section would appear to show that the oxide is mostly AgO up to temperatures of 80°C anyway.

Provided consideration is given to the potential problems listed above, it would appear that the silver actinometer is a useful and appropriate method for determining silver mass loss and hence AO flux, particularly for low fluence spacecraft missions.

## 3.3 Zinc Oxide Actinometers

The use of zinc oxide (ZnO) as an AO sensitive material is perhaps the most recent development in actinometry and as such not much literature, apart from that produced by Osborne [13-15, 93]is currently available on the subject.

Instead of the sensing material becoming permanently oxidized, ZnO or any other semiconducting detectors (SCD) rely on the influence that an adsorbed species has on the electronic structure of the semiconductor. AO removes free electrons from the material and in the process the adsorbed atoms become charged. If the semiconductor has electron charge carriers (n-type material), the action of the oxidising species is to reduce the charge carrier concentration and therefore reduce sample conductivity. If the material carriers are positively charged holes (p-type), then conductivity increases.

The change of semiconductor surface conductivity is proportional to the change of adsorbed atoms, molecules, or radicals on the surface. Bulk conductivities are neglected, as they are generally insensitive to surface effects like AO attack [94]. Additionally, if the surface is free of adsorbed species, the conductivity change is also proportional to the flux of atoms impinging on the surface at a constant temperature and thus the rate of change of conductivity can be used as the measurand of the flux. Osborne shows this for low fluxes [14]:

$$f = \frac{1}{\alpha(1-\gamma)}\frac{dN_s}{dt}$$ **Equation 6**

where *$f$ = AO flux ($cm^{-2}s^{-1}$), $N_s$ = surface charge carrier concentration ($cm^{-2}$), $\alpha$ = ratio of ionised to total number of particles on the semiconductor surface, $\gamma$ = scattering coefficient of AO on ZnO.*

Surface conductivity of the sensor is given by:

$$\sigma_s = N_s e \mu_s$$ **Equation 7**

where *e is the electron charge of* $1.6x10^{-19}$*C and* $\mu_s$ *is the surface electron mobility (*$cm^2/V/s$*).*

The surface resistance, $R_s$, of the sensor of breadth b, distance between contacts l, thickness $\tau$, and surface resistivity $\rho_s$ is given by:

$$R_s = \frac{\rho_s l}{\tau b} \qquad \textbf{Equation 8}$$

Equations 7 and 8 with $\sigma = 1/\rho$ give:

$$N_s = \frac{l}{R_s \tau b e \mu_s} \qquad \textbf{Equation 9}$$

Dimensions are constant throughout, and by assuming $\mu_s$=constant:

$$\frac{dN_s}{dt} = \left(\frac{l}{\tau b e \mu}\right)\frac{d}{dt}\left(\frac{1}{R_s}\right) \qquad \textbf{Equation 10}$$

Substituting for $dN_s/dt$ in Equation 6 and defining surface conductance as $g_s = 1/R_s$ gives:

$$f = \left(\frac{l}{\tau b e \mu}\right)\left(\frac{1}{\alpha(1-\gamma)}\right)\left.\frac{dg_s}{dt}\right|_{t=0} \qquad \textbf{Equation 11}$$

Therefore it can be seen that at a constant sensor temperature, flux is proportional to the initial rate of change of surface conductance and this result has also been demonstrated experimentally [14]. Over time, as the ZnO is exposed to AO, more and more oxygen atoms populate the surface until all sites able to hold an adsorbed atom have become full or the number of new atoms arriving on the surface is balanced by the number leaving through desorption mechanisms such as recombinations and collisions. This is seen as a decrease in the rate of change of conductivity until it falls monotonically towards zero (when $dg_s/dt=0$); a condition called saturation.

One of the benefits of using ZnO is that, in the ideal case, the adsorbed oxygen can be desorbed and the original electronic properties of the material recovered or regenerated. Desorption is achieved by providing sufficient energy, typically by heating, to overcome the forces holding the oxygen to the surface. Figure 6 shows the ideal response of an n-type zinc-oxide sensor to atomic oxygen and heating.

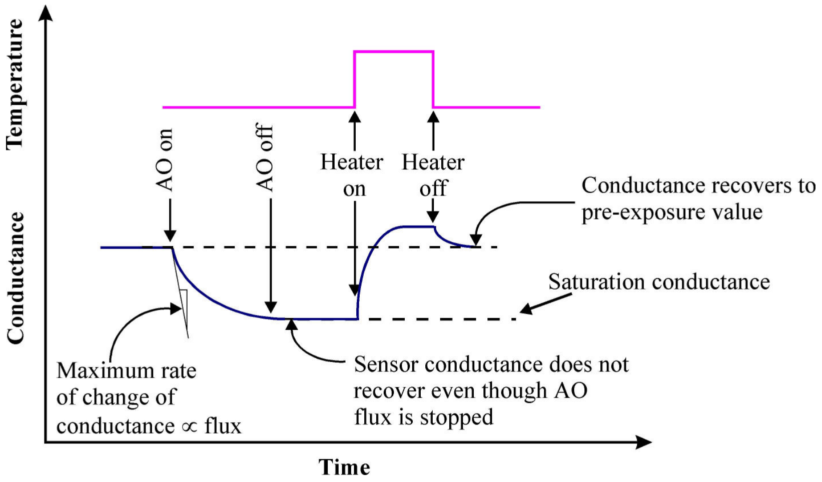

**Figure 6: Ideal ZnO actinometer characteristics [15]**

It is worth pointing out that the ZnO senor has only been shown to correlate to AO flux during the first moments of AO exposure. This is an obvious limitation, particularly if the total AO dose (or fluence) is the item of interest, or if the AO environment changes faster than the time it takes to regenerate the sensor.

A flight instrument incorporating zinc oxide sensors was developed for a Space Technology Research Vehicle (STRV-1c) micro-satellite and has been tested in the laboratory. Unfortunately data from the STRV-1c mission is not available as the satellite was lost shortly after launch. Figure 7 shows from [93] the response of a ZnO sensor exposed to a 5eV ground simulation facility.

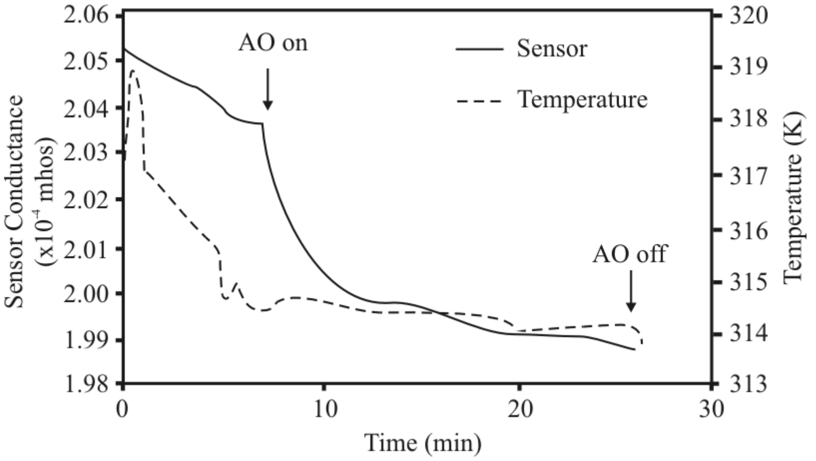

Figure 7: Actual ZnO actinometer response to AO [93]

During this run, there was a slight fall in temperature as the sample was moved into a position of AO exposure, which is observed as a fall in sensor conductance. Upon exposure to AO, the sensor conductance fell in a similar manner expected for an n-type semiconductor. Unfortunately the data does not show whether or not conductance remains constant post-AO exposure. Figure 8 shows the complete exposure and regeneration cycle for one sensor, although there is insufficient time between the AO beam switching off and regeneration to assess whether resistances remain constant during this interval.

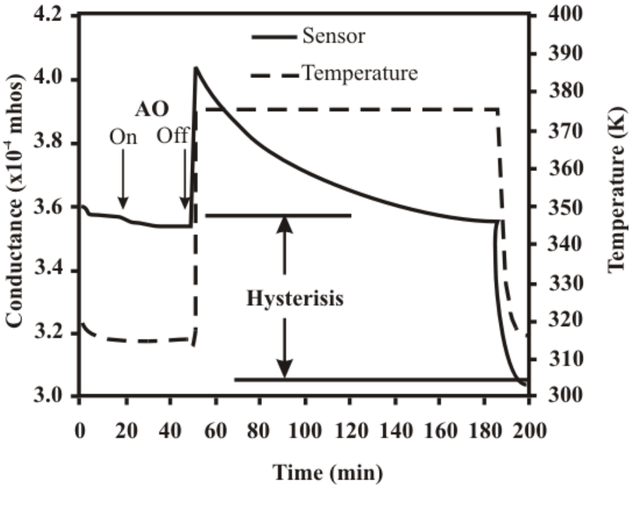

Figure 8: Actual ZnO actinometer regeneration performance [15]

One of the most striking aspects of the regeneration cycle is the permanent change of conductance upon heating. It is postulated that the hysteresis is caused by the irreversible oxidation of zinc atoms and/or mechanical damage of the material.

However, it should be noted that the work of Osborne did not carry out any characterisation of the films to prove any of the suggestions made.

## 3.4 Carbon Actinometers

As already mentioned, silver is an actinometer material most suited to low fluence missions, like those performed on sounding rockets or geostationary transfer orbit (GTO). Contrasting with this, ZnO actinometers can theoretically provide long term AO flux measurement but with some interruption as the sensor is regenerated. For applications where large fluences are to be measured continuously, or as simply as possible, then an alternative material should be considered.

Various tests performed in the LEO environment and in ground based simulation facilities have shown that carbon reacts with AO by at least an order of magnitude less than silver [54, 89, 95], suggesting that it could be used as a longer duration actinometer material. Furthermore, carbon is believed to produce volatile reaction products that dissipate into the surrounding environment [96]. Volatile reaction products are advantageous because virgin carbon material is continuously exposed to the AO environment, which means:

- Thicker films can be used because an oxide layer does not stop the use of the same actinometer after a given AO dose.

- Provided the erosion yield is constant throughout the material thickness, AO response of the actinometer will be the same throughout its entire life, making flux correlation easier.

Although carbon has been exposed to AO in many different experiments (as will be discussed in Chapter 4), not much work has been specifically carried out on carbon actinometers. The two most significant works have been performed on the CONCAP-II experiment carried out on the STS-46 shuttle mission [89, 97] and during a brief ground based experiment on diamond films [98].

CONCAP-II was a 20 hour-long exposure in LEO at an altitude of 228km. The experiment consisted of two silver films with a thickness of 220nm, two screen-printed carbon films of 28μm thickness and two vitreous carbon films with thicknesses of 290nm and 380nm. Each film was deposited between gold pads on a quartz substrate.

To account for temperature, platinum resistance thermometers were placed inside a base plate to which the actinometers were mounted. The temperature dependence of the reaction rate, r, was estimated using the Arrhenius equation

$$r = Ae^{(-\Delta E / RT)} \qquad \textbf{Equation 12}$$

where the *activation energy* $\Delta E$ was assumed to be 0.29kJ/mole, $T$ is *temperature (°K)* and $R$ is the *universal gas constant* $(8.31x10^{-3}\ kJ\ mol^{-1}K^{-1})$. $A$, the *pre-exponential factor*, is assumed to be a constant.

Presumably by taking a reciprocal, this equation found that with temperatures ranging from 15°C to 45°C, the reaction rate was affected by less than 3% and so temperature effects on erosion yield were considered negligible. This perhaps explains why no attempt was made to control temperature. As will be shown in Chapter 4, the assumption of constant activation energy is perhaps naïve given the wide range of carbon materials that are in existence.

To simplify data interpretation resistance measurements were normalised by dividing the initial resistance $R_0$ by measured resistance R. This method ensures that all sensors can be compared together on the same plot irrespective of their actual resistance values. Rather than calibrating the response of the sensor against a reference material, like Kapton-H, a material reaction rate is assumed and assigned to the actinometers. Reaction probability was assumed as 1 for silver and 0.1 for the carbon. Carbon reaction rates have appeared to be very variable in past experiments (as will be highlighted in the next chapter), and so the assumption made is perhaps dangerous because, based on the available literature, the thick film carbon has never been exposed to an AO environment before.

When exposed to AO, the vitreous carbon samples of different thickness had eroded completely after approximately the same AO exposure (around 380 minutes). The fact that the thicknesses of the two vitreous carbon films were different suggests that a temperature dependent erosion rate could have been significant, contrary to the assumption that temperature effects were negligible. The paper explains that the thicker sample could have been hotter than the thinner sample due to a heat leak from a hot plate used on the mission but does not comment on the differences with the Arrhenius prediction. Actinometer response to atomic oxygen appeared repeatable over each orbit but small disturbances are observed and associated with solar heating effects that are not removed from the data.

Results from the screen-printed carbon were found to be noisy due to problems with the electronics used to measure film resistances and a slight resistance increase was also noted when the actinometer was heated. However, the general response of the film appears to be a linear reduction of the $R_0/R$ ratio. One important difference with the vitreous carbon response is that the screen-printed film appears to be significantly more durable. At the same time the vitreous actinometer had completely eroded ($R_0/R=0$), the screen-printed actinometers showed a $R_0/R$ ratio of 0.97, suggesting the screen printed material is well suited for higher AO fluence missions, by virtue of its increased thickness.

With a view to increasing sensor lifetime, the brief work of Haenni and co-workers [98] deposited boron-doped diamond and exposed the material to a simulated AO environment. It is presumed that the diamond has been doped to increase the conductivity of the material so resistances can be measured easily. Some of these samples were covered by a silicon dioxide/nitride double layer to allow the effects of temperature to be isolated from the effects of AO. Results showed that the resistance of the films increased linearly during the duration of the exposure to a fluence of approximately $5x10^{20}$ atoms/cm$^2$. The energy of the AO beam is not stated, but exposures were conducted at the ESA-ESTEC facility that typically produces beam energies similar to that of LEO (5eV)[99].

Besides the apparent absence of an oxide layer, another important difference between carbon films compared with silver is that a resistance-thickness calibration does not need to be made. All forms of carbon are semiconductors so there are some potential risks in making the assumption that electrical conduction is metallic, like silver. This means an assessment of carbon’s mean-free path of electrons may not indicate when resistivity changes occur as the film become thinner.

From experiment it appears that resistivity changes occur only when the film is very thin. A study investigating the conduction properties of ion-sputtered amorphous carbon films measured thickness and resistivity during the deposition process[100]. There are no details of how these measurements were made but the results (Figure 9) show that resistivity only begins to shift from bulk values at a thickness of around 20nm (200 Angstroms); a value less than half that for the silver films. Given that the resistivity of carbon is at least two orders of magnitude greater than silver, a greater thickness will be required to achieve the same resistance value as a silver film. This means the film can be easily designed to erode when resistivity is equal to the bulk value.

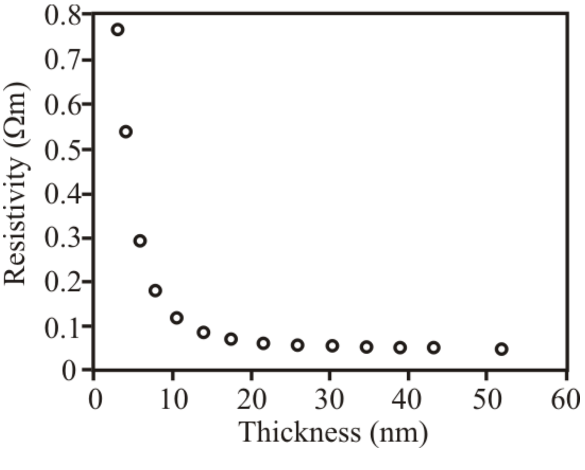

**Figure 9: Variation of resistivity as a function of thickness for an amorphous carbon film[100]**

Finally, like in the case of silver, it is useful to assess whether or not a resistance change is representative of AO induced thickness loss. Unfortunately there are no direct comparisons, but many carbon samples have been deposited onto QCM devices and exposed to an AO environment [99, 101-103]. In each case the erosion was found to be essentially linear, except for cases when mass approached a zero value; slowing the erosion rate. This trend is thought to be a consequence of a reduction in the available material for erosion, so reducing the probability of AO reaction. If a constant density and even erosion across the face of the material is assumed, the linear mass loss can be equated to a linear loss in thickness. On the basis of the information provided here, so long as thicknesses are above the 20nm thickness-resistivity limit (see above) a predictable resistance increase will be observed. More details on AO reactions with carbon can be found in Chapter 4.

### *3.4.1 Theoretical Aspect*

From all of the literature work carried out, there has been little mathematical description of erosive actinometer response. A proposed theory is given below, which is based on a film erosion mechanism and constant resistivity.

To easily compare sensor materials with different AO responses, the ratio of initial resistance and measured resistance is taken.

$$\frac{R_0}{R} = \frac{\rho \frac{L}{A_0}}{\rho \frac{L}{A}}$$ **Equation 13**

where $R_0$ *= initial resistance (Ω), R = resistance (Ω),* $A_0$ *=initial cross sectional area (cm$^2$),* $A$ *=cross sectional area (cm$^2$), L=length of carbon film (cm), ρ=film resistivity (Ω.cm).*

By assuming a constant resistivity it can be shown that:

$$\frac{R_0}{R} = \frac{A}{A_0} = \frac{\tau W}{\tau_0 W} = \frac{\tau}{\tau_0}$$ **Equation 14**

where $\tau_0$ *=initial thickness (cm),* $\tau$ *= thickness (cm), W=film width (cm).*

The eroded volume can be estimated from:

$$\Delta V = WL(\tau_0 - \frac{R_0 \tau_0}{R})$$ **Equation 15**

where $\Delta V$ = *volume change by erosion (cm$^3$)*

Erosion yield is then described by:

$$Y = \frac{\Delta V}{FWL}$$ **Equation 16**

where $F$ = *AO fluence (atoms/cm$^2$) and* $Y$ = *erosion yield (cm$^3$/atom).*

It can be shown from above that, if the erosion yield and initial thickness are known, fluence is given by:

$$F = -\frac{\tau_0}{Y}\frac{R_0}{R} + \frac{\tau_0}{Y}$$ **Equation 17**

or, if fluence and initial thickness are known, erosion yield can be determined theoretically:

$$Y = -\frac{\tau_0}{F}\frac{R_0}{R} + \frac{\tau_0}{F}$$ **Equation 18**

Equation 18 can also be resolved for time:

$$F = ft$$ **Equation 19**

where $f$ = *AO flux (atoms/cm$^2$/s) and* $t$ = *time (s).*

### *3.4.2 Errors and Differences*

The theoretical erosion yield (TEY) equation (Equation 18) can be used in two ways. Firstly, resistance measurements can be compared with actual thickness measurements. In the ideal case:

$$\frac{R_0}{R} = \frac{\tau}{\tau_0}$$ **Equation 20**

By rearranging Equation 20, to give:

$$0 = \frac{\tau}{\tau_0} - \frac{R_0}{R}$$ **Equation 21**

Expressing any differences relative to a final thickness measurement, errors can be quantified:

$$error = \frac{\frac{\tau}{\tau_0} - \frac{R_0}{R}}{\frac{\tau}{\tau_0}}$$ **Equation 22**

Which simplifies to:

$$error = 1 - \frac{R_0 \tau_0}{R\tau}$$ **Equation 23**

Any differences will indicate that the theory is not accurately describing the erosion and conduction mechanisms taking place, but will also help explain how the real material is responding to the AO environment. This measurement will be called the systematic actinometer error (SAE).

SAE can be reduced by fitting a straight line to the data, giving an effective TEY rather than an actual TEY; this is the second use of the equation. If the resistance measurements deviate from the fitted straight line, the differences will be called the actinometer non-linearity error (ANLE). The ANLE can be derived in a similar manner to the SAE, to give:

$$ANLE = 1 - \frac{R_0 R_F}{R R_{F0}} \qquad \textbf{Equation 24}$$

where *fitted resistance* $R_F$ and *fitted initial resistance* $R_{F0}$ substitute thickness measurements.

Having quantified the performance of a sensor against its desired performance, the next task is to assess what is an acceptable margin of error. This is a somewhat contentious issue that will depend on individual applications. Hyperthermal AO sensors are by no means commonplace and little comment has been made about existing precision and accuracies, so it is difficult to draw comparisons with the same type of sensor. However, it is possible to draw comparisons with other sensors to be flown on the same experiment. Typical errors for temperature sensing devices used for the STORM package are listed in Table 5 to provide the reader with an impression of typical values for commercial sensors.

| Device | Systematic Error (%) | Non-linearity (%) |
|---|---|---|
| AD590 K | ±5.5 | ±1 |
| PT100 | <\|0.09\| | ±0.8 |

**Table 5: Typical errors of commercial sensors**

## 3.5 Other Materials

So far this review has concentrated on the most commonly used materials for AO actinometers. This section will summarise some of the less commonly used materials based on the few publications available.

There are three suitable materials for non-renewable actinometers based on their ability to conduct electricity and to produce non-conducting oxides on AO attack. These are silver and carbon, that have already been discussed, and osmium. Presently osmium has not been used as an actinometer, but the material has undergone some AO exposure. The first exposure was during the STS-4 mission where a passive sample of 15nm thickness was exposed to the LEO environment [96]. Upon retrieval the material was completely removed with no trace of oxide. The second exposure was aboard the STS-8 mission, where an osmium film was deposited onto a temperature controlled QCM [101]. Unfortunately there is very little data on this experiment, but the QCM response appears to show a linear fall in mass over the duration of the exposure. The erosion yield of the material was found to be approximately $0.03\text{x}10^{-24}$ $\text{cm}^3$/atom, suggesting that osmium would be suitable for the detection of AO over a larger fluence than those detected by silver and many carbons. Unfortunately osmium is a hazardous material, it is an irritant, noxious and creates a flammable powder so these are probably the reasons for the lack of literature on the use of this material as an AO sensor.

Yttria-stabilized zirconia (YSZ) is another material that can be used as an AO actinometer, but applied in a different manner to other actinometers [9]. Platinum electrodes are attached to an element of YSZ and a voltage is applied. The platinum catalyses reactions with the ambient oxygen as follows:

$$O + 2e^- \rightarrow O^{2-}$$

$$O_2 + 4e^- \rightarrow 2O^{2-}$$

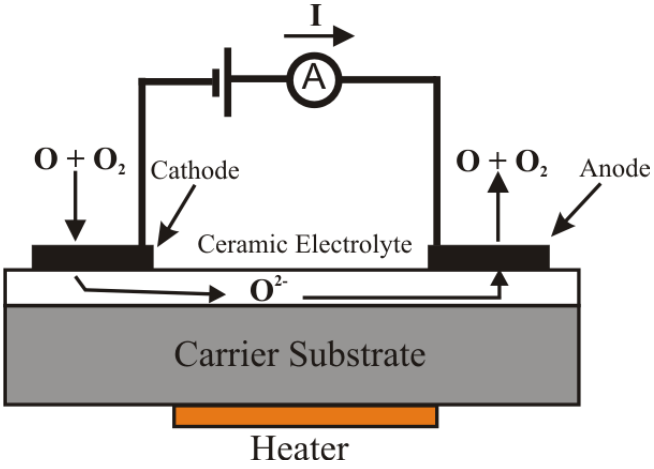

**Figure 10: Schematic of yttria-stabilised zirconia (YSZ) actinometer [9]**

The yttria doping introduces oxygen vacancies into the zirconia lattice thereby allowing the oxygen ions formed by the platinum electron to migrate from the sensor cathode to the anode producing a measurable current. The current generated can then be calibrated to become a measure of oxygen flux. The YSZ element must be heated to ≥600°C to provide sufficient conductivity for this technique to be effective, requiring a warm-up period before sensor operations.

This sensor clearly has many advantages as AO flux can be measured:

- Continuously without disturbing the measurement, like silver and carbon actinometers.
- For long periods, like the ZnO actinometer.

Whilst this system does have some of the benefits of both a renewable and a non-renewable sensor, there are some potential problems with the device. The most significant problem is the sample temperature required for measurement. To heat the sensor to such high temperatures will require much more power than the other devices described and a high degree of thermal isolation.

Another potential problem of this sensor is that it is sensitive to both molecular and atomic oxygen. Whilst in orbit such a characteristic may prove trouble free, the use of YSZ sensors in ground based simulation facilities may be unsuitable, as many of these systems are known to produce $O_2$ fluxes to some degree. This naturally creates difficulties with the calibration of the sensor.

Five YSZ sensors have been flown as part of the flux probe experiment (FIPEX), which was flown on the TEXUS 34 sounding rocket and later on the TEAMSAT microsatellite [104]. Further experimentation is presently being conducted on the IRDT (Inflatable Re-entry and Descent Technology) demonstrator where electrodes have been developed to exclude the measurement of molecular oxygen. Unfortunately, apart from the information presented by Osborne *et al* [9], there is little other information on these sensors.

## 3.6 Summary, Discussion and Conclusions

This section has summarised the use of candidate materials as an AO sensitive element in an actinometer. Most of the research undertaken has been on silver films where six orbital experiments have been performed. Silver is well suited to short fluence missions like those on geostationary transfer orbits (GTO), short term LEO and sounding rockets. However, many materials experiments are now being performed aboard the International Space Station (ISS) to assess the effects of larger AO doses [16]. Such experiments will require sensors that are less resistant to AO attack to ensure that measurement is possible for the entirety of the mission. Table 6 summarises some of the properties of the materials discussed in this section.

The longevity of the sensor, of a given film thickness, can be assessed by comparing the erosion yield with other materials. Zinc-oxide and YSZ have an ideally infinite lifetime which would suggest that these sensors are best suited to sensing large doses of AO. However, there are some limitations to these materials, most notably the requirement for heating that places additional power requirements and sometimes complexity on the mission. The additional limitation of the zinc-oxide sensor is that measurement is periodically disturbed by regeneration. The regeneration cycle has also led to hysteresis issues that significantly lower the lifetime of the sensor and increase measurement uncertainty.

From a low mass, low power and simplicity of operation standpoint the non-renewable sensors appear to be most desirable. The non-renewable sensors can easily monitor flux or fluence by a simple two-point resistance measurement without the need for heating, unless a steady temperature is required. Out of these it would appear that either osmium or a diamond carbon would be well suited for detecting large doses of AO.

Unfortunately there are some difficulties with using osmium. Osmium is a hazardous material and could therefore be difficult for spacecraft operators to authorise its use. There is also very limited information on its use in a space environment.

Alternatively, diamond is a much safer material than osmium and has a similar erosion yield. The most significant problem with diamond is that it has a very high resistivity, making resistance measurements difficult, although some rather brief work has managed to reduce resistivity by doping the material with boron atoms [98].

Carbon materials in general are very interesting due to the capability of measuring a variety of different fluences. Whilst a film with a low erosion yield can measure large and small AO doses, it may not be sensitive enough to detect small changes in flux and will not have optimum accuracy at lower doses. Carbon offers the potential advantage that the erosion yield can be varied to suit a particular application.

Overall the use of carbon actinometers for AO detection appeared to be promising, as the research carried out on these devices show that no oxide layer limitations are seen and the lifetime of the sensor appears to be modifiable. Unfortunately in the CONCAP-II experiment accurate measurement of AO fluence was not possible due to the assumption of a single reaction probability value. Calibration in a ground based simulation facility or comparison with a reference material, which can provide more reliable estimates of the reaction rates and possibly indicate temperature dependencies, would have helped resolve these issues.

Given the relatively small amount of research published for carbon AO actinometers and given the potential advantages of using such devices, it seems appropriate to perform some new research on these devices.

| **Material** / **Property** | **Silver** | **Osmium** | **Carbon** | **Zinc Oxide** | **Yttria-stabilized zirconia** |
|---|---|---|---|---|---|
| **Erosion Yield ($\times10^{-24}$cm$^3$/atom)** | 10-100 | 0.03 | 0-0.02 (diamond)<br>0.1-1.7 (Various forms) | ~0 | ~0 (assumed) |
| **Resistivity @ 20°C ($\times10^{-6}\Omega$cm)** | 1.59 | 8.80 | $10^{20}$(diamond)<br>1375 (graphite) | 0.01-3225 | - |
| **Oxides** | Solid | Volatile (in vacuum) | Volatile | - | - |
| **Hazards** | Few | Irritant, noxious, flammable powder | Few | Few | High temperatures |

**Table 6: Summary of actinometer material properties**

# 4 CARBON

## 4.1 Introduction

Carbon can differ in many ways, making the description of some carbon materials non-trivial. For example carbon atom hybridisation, bonding between each atom, atomic arrangement and crystallinity can all have a great effect on the properties of the bulk material. Further complexity is added to this problem when one considers the possible variation of these factors in a single sample and the use of any additives such as hydrogen.

The carbon actinometers described in the previous section rely on an erosion mechanism of some kind to measure atomic oxygen, so it is important to highlight how different carbon materials respond to atomic oxygen. Although there are few published accounts of carbon as an actinometer, there is rather more literature describing the exposure of passive carbon samples to AO. The information gained from the passive experiments will provide some insight on the lifetime and sensitivities of an actinometer utilising the same material samples. This section will therefore provide an overview of the many forms of carbon available and explain how they vary, with particular emphasis on erosion by AO attack.

## 4.2 Atomic Hybridisations

Carbon has atomic orbitals that can hybridise, and is perhaps the most important factor to identify in carbon materials. Orbitals represent a volume of space within which an electron would have a certain probability of existing, based on particular energy states and atoms. In the simplest case the electrons are most likely to be found within a sphere around the nucleus of an atom; hydrogen is an example of this. In higher energy states the shapes become deformed due to the interaction of quantum effects between different atomic particles. Hybridisation is possible because the single s-orbital and three p-orbitals of the carbon atoms second electronic shell have similar energies (s-orbital –19.2eV and p-orbital –11.8eV). As a result carbon can adapt to form chemical bonds with different energies.

Carbon atoms can take three principal forms: $sp^1$, $sp^2$ and $sp^3$. Other kinds of carbon do exist, such as the recently discovered Buckminster Fullerenes and carbon nanotubes, but these are essentially deformed networks of $sp^2$ atoms. By far the most common of these hybridisations (or allotropes) are $sp^2$ and $sp^3$.

In the $sp^3$ configuration, the s-orbital and all three p-orbitals undergo an $sp^3$ hybridisation, where their energies equalise at –13.64eV. In terms of the atoms' geometry each of the carbons four valence electrons is assigned to a tetrahedrally directed $\sigma$ orbital as shown in Figure 11, with equal bond angles of 109.5° [105]. In the $sp^2$ configuration, the s-orbital and two p-orbitals undergo an $sp^2$ hybridisation to an energy level of –14.26eV, forming a triagonal, 3-electron arrangement. The remaining electron is assigned to an orbit perpendicular to this plane; an orbit termed the $\pi$ orbital.

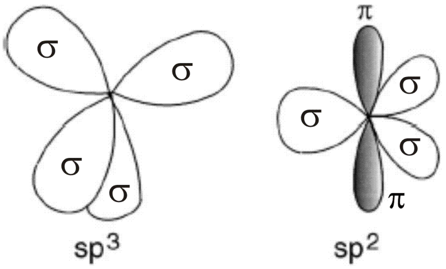

**Figure 11: Schematic of $sp^3$ and $sp^2$ hybridised carbon atoms.**

In both hybridisations, a covalent chemical bond is formed between two atoms when their orbitals overlap and share a pair of electrons. When the orbitals overlap along an axis between the atoms (inter-nuclear axis) they form a $\sigma$ bond. In addition to this $\pi$ orbitals allow sideways overlapping, creating a $\pi$ bond, which is weaker than the $\sigma$ bond. Multiple covalent bonds between atoms contain a $\sigma$ bond and one or more $\pi$ bonds, as shown in Table 7. Triple bonds are a unique condition of $sp^1$ hybridisations and are only included for completeness.

| Type of Bond | Symbol | Number of σ bonds | Number of π bonds | Bond Energy, kJ/mole |
|---|---|---|---|---|
| Single | C-C | 1 | 0 | 348 |
| Double | C=C | 1 | 1 | 614 |
| Triple | C≡C | 1 | 2 | 839 |

**Table 7: The bonds of carbon**

## 4.3 Diamond and Graphite

The structure of graphite is shown in Figure 12a. The $sp^2$ hybridised atoms form continuous hexagons in stacked basal planes (a-b direction). Within each basal plane, the carbon atom is strongly bonded to its three neighbours with a covalent bond. The π orbitals overlap sideways to neighbouring atoms, thus forming an alternating (conjugated) network of C-C and C=C bonds. The π orbitals are delocalised, so the C-C/C=C sequence alternates effectively forming a 'sea of electrons', similar to that seen in metallic bonding.

The basal planes of graphite are bonded together by weak Van der Waals forces with energy of 7kJ/mol. In bulk samples many layers can be built up into an ABAB stacking sequence. The spacing between basal planes is larger than the spacing between atoms in the plane, which together with the different bonding types, results in anisotropic properties. Pure, manufactured graphite is often termed highly orientated pyrolytic graphite (HOPG) to indicate the manufacturing process.

In contrast, diamond has a very different structure and properties. The four orbitals of an $sp^3$ atom form single covalent bonds with the orbitals of four other carbon atoms. The structure of diamond is more isotropic than graphite and in the polycrystalline form is largely considered as fully isotropic. Each diamond tetrahedron combines with four other tetrahedrons to form a strongly bonded, three-dimensional and entirely covalent crystalline structure.

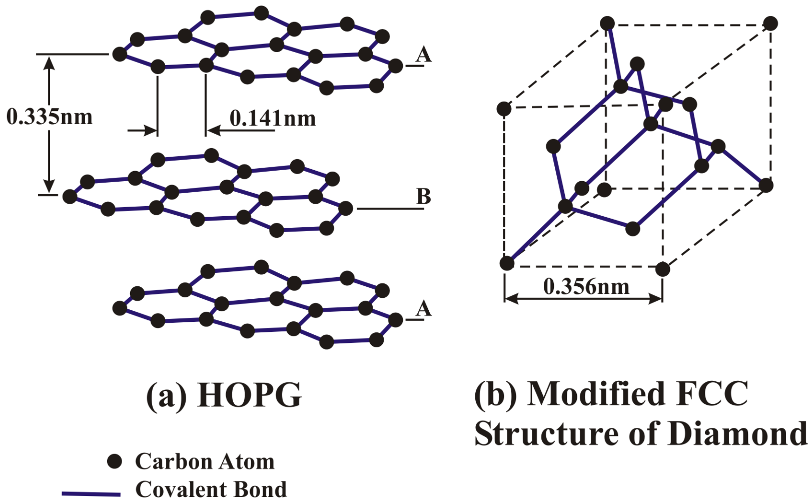

(a) HOPG

(b) Modified FCC Structure of Diamond

**Figure 12: Diamond and graphite atomic arrangement**

Diamond and graphite contrast greatly in chemical, mechanical, thermal and electrical properties and are perhaps the most representative of carbon property extremes. Given that the engineering properties of the polycrystalline materials do not differ greatly from single crystals and the fact that it is generally more difficult to produce large single crystals of diamond and graphite, both diamond and graphite are more commonly used in a polycrystalline form. Diamond is typically used for applications that require high thermal conductivity, electrical insulating properties or high hardness [106]. Polycrystalline graphite is often used in applications that make use of its low shear strength (lubricants for example), electrical conductivity or anisotropic properties [106].

## 4.4 Amorphous Carbons

When addressing the amorphous state of a material it is important to state the degree of order. Order can be classed as short-range order (up to a few angstroms) or long-range order [107]. A perfectly crystalline material possesses both long range and short-range order. A solid that has all bonds occupied (with perhaps the exception of surface bonds) but with some distortion possesses short-range order, but the solid as a whole has an irregular arrangement of atoms. The absence of long-range order in these materials means that they are a kind of amorphous carbon (a-C). However, to avoid confusion with materials lacking both short range and long-range order, this type of solid will be referred to as a carbon glass rather than an amorphous carbon (not to be confused with glassy or vitreous carbon, which is described later).

A solid of this kind with zero defects is termed an ideal covalent glass [107]. In most cases defects and voids are inherent to most amorphous materials and these structures are the ones most commonly given an association to the term “amorphous carbon” or a-C.

The critical point determining the transition from a crystalline to an amorphous state can be difficult to define. Whilst it is simple to define an average minimum crystal size before amorphousness begins, this method cannot work for composite systems that have, for example an arbitrary 50% diamond crystal and 50% amorphous $sp^2$ content, because the properties between the components are known to contrast greatly. Similarly it is difficult to define a point when crystals become deformed to become glass-like structures as defined above. The distinctions usually arise from characterisation techniques that shall be explained in Chapter 7.

This chapter provides a more general overview of the material properties. For the purposes of this section, materials will be defined by the fractions of $sp^2$ to $sp^3$, hydrogen content or process of manufacture. These rather simplified distinctions are made here because the same distinctions are made by other authors later in this literature review. As yet there have been no investigations on crystallinity/amorphousness influence on AO performance, so there appears to be some novelty in performing such a study.

Most carbons can be mapped onto a ternary phase diagram showing levels of hydrogen, $sp^2$ and $sp^3$ content. Figure 13 shows the different kinds of amorphous carbon produced so far by a variety of deposition techniques. There are many different kinds of carbon that have an entirely disordered $sp^2$ network for example: soot, chars, vitreous carbon and evaporated carbon. These all lie in the lower left hand corner.

The addition of hydrogen leads to significant differences in properties - in concentrations where hydrogen content is dominant either polyethylene or polyacetylene will form, as these are essentially long chains of carbon atoms with hydrogen atoms bonded to them. These hydrocarbon polymers define the limits of the triangle in the right hand corner.

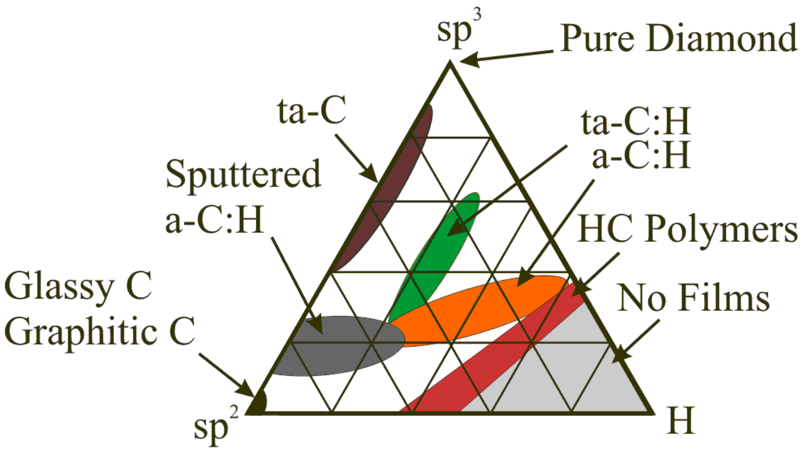

**Figure 13: Amorphous carbon ternary phase diagram from [108]**

It can be seen that deposition methods also allow a-Cs with increasing degrees of $sp^3$ fraction. If the fraction of $sp^3$ reaches a high level, then the material is given the description of tetrahedral amorphous carbon (ta-C) [108] to indicate more diamond-like carbon (DLC) properties.

| **Material** | **$sp^3$ (%)** | **H (%)** | **Density ($g/cm^3$)** | **Hardness (GPa)** | **Reference** |
|---|---|---|---|---|---|
| Diamond | 100 | 0 | 3.515 | 100 | [113] |
| Graphite | 0 | 0 | 2.267 | - | [114] |
| Polycrystalline Diamond | ~100 | 0 | ~3.5 | 140 | [115-117] |
| Polycrystalline Graphite | 0 | 0 | ~2.25 | - | [118, 119] |
| Vitreous carbon | 0 | 0 | 1.3-1.55 | 3 | [120] |
| Evaporated a-C | 0 | 0 | 1.9 | 3 | [120] |
| Sputtered a-C | 5 | 0 | 2.2 | - | [121] |
| ta-C | 80-88 | 0 | 3.1 | 80 | [121-123] |
| a-C:H (Hard) | 40 | 30-40 | 1.6-2.2 | 10-20 | [124] |
| a-C:H (Soft) | 60 | 40-50 | 1.2-1.6 | <10 | [124] |
| ta-C:H | 70 | 30 | 2.4 | 50 | [125] |
| Polyethylene | 100 | 67 | 0.92 | 0.01 | [126] |

**Table 8: Sample properties of some different kinds of carbon and carbon-based materials**

Certain deposition methods [109, 110]are able to produce hydrogenated amorphous carbons (a-C:H) and tetrahedral amorphous carbons (ta-C:H). From the available literature [111, 112], both these carbons are considered DLC, even if the $sp^3$ content is relatively low in some cases. Table 8 compares some properties of the materials shown on the ternary phase diagram and other carbon materials.

## 4.5 Vitreous carbon

Another significant type of amorphous carbon used in AO experiments is glassy (vitreous) carbon. Vitreous carbon consists of entangled ribbons of graphitic polymeric molecules [127].These entangled ribbons are thought to be responsible for the materials inherent strength, porosity and low density. Carbon fibres used for structural applications are considered to be a form of glassy carbon [127]. Vitreous carbons are typically made by heating a polymer or carbon based-resin to very high temperatures, thereby removing non-carbon atoms. This process is named pyrolysis.

## 4.6 AO erosion

The precise reactions and mechanisms involved during the AO attack on carbon can be rather complex and require a wide range of characterisation techniques to determine them. This section will focus on the most fundamental aspects of AO reactions with carbon, these being the erosion yields or reaction rates of different carbon films versus other fundamental parameters, such as temperature, AO flux or beam energy.

AO reacts with carbon to form gaseous oxides with predominantly the following reaction [54]:

$$C\ (s) + O\ (g) \rightarrow CO\ (g)$$

However it is possible, but a lot less likely, to have the following reactions [54, 128].

$$C\ (s) + 2O\ (g) \rightarrow CO_2\ (g)$$

$$2C(s) + O\ (g) \rightarrow CO\ (g) + C\ (g)$$

$$3C(s) + O\ (g) \rightarrow CO\ (g) + C_2\ (g)$$

It is also possible for impinging oxygen atoms to recombine at the surface and not react with the material [128]:

$$C\ (s) + O\ (g) + O\ (g) \rightarrow C(s) + O_2\ (g)$$

For the purposes of this work, like the work of many others, only the first reaction will be assumed to be taking place and eroding the carbon material [54, 129]. If an atom does not react, then it shall be assumed that recombination has occurred.

### *4.6.1 Graphite*

Graphite was exposed to the LEO environment during the STS-8 space shuttle mission [95, 130]. AO flux was maximised by lowering the shuttle altitude to 225km and maintaining the sample surfaces in direct ram conditions throughout a 40-hour exposure. These conditions provided a fluence of 3.5 $\times 10^{20}$ atoms/cm$^2$ [60].

Both edge orientated and basal orientated HOPG was exposed to the AO environment. The edge-orientated graphite was found to be slightly more reactive to the AO environment than the basal orientated sample. There were also differences in the surface appearance after AO exposure. Basal orientated graphite appeared smooth, with what is described as an orange peel effect on the surface, whilst edge orientated graphite had a rough, separated and striated structure. Unfortunately there are no available images of these surfaces.

Further work performed by Gregory [130] compared the erosion yields of HOPG for two missions in LEO: STS-8 and LDEF. The LDEF experiment exposed materials to much greater fluences than the STS-8 mission (see Table 9 at the end of this chapter). The erosion yields were found to be 0.6 $\times 10^{-24}$ cm$^3$/atom and 1.04 $\times 10^{-24}$

$cm^3$/atom for STS-8 and LDEF respectively, suggesting a fluence dependence on erosion yield.

A fluence dependent erosion yield of HOPG is also suggested by another space shuttle exposure [71, 131], this time performed on the STS-46 mission. Six samples were exposed at the end of an extended arm outside the shuttle for 43 hours, giving an estimated fluence of $2x10^{20}$ atoms/$cm^2$. On returning to Earth, the surface profile of the material was measured where the average amount of graphite removed was found to be $2.2\pm0.1\mu$, equivalent to an erosion yield of $1.1\ x10^{-24}$ $cm^3$/atom. Compared with the STS-8 and LDEF experiments, this is the greatest erosion yield with the least fluence so conflicts with the idea of a fluence dependant erosion yield.

Microscopy performed on the samples revealed a very rough surface of mounds that (at higher magnifications) appeared to have terraces, steps and islands on them. The appearance of these samples post-exposure was then compared to a mathematical model that normally describes the growth of epitaxial films, but in this case applies the theory to an eroding film by reversing constants.

The mathematical model is not outlined completely and in any case is beyond the scope of this thesis. However, calculated surface roughness scaling is reported as being significantly less than the results of AO exposures, and consequently the authors suggest an alternative erosion mechanism that might reduce these errors.

After an O atom impinges the graphite surface [131]:

1. the O atom diffuses until it reaches a step or defect site,
2. the O atom reacts with a site on the graphite basal plane, forming CO or $CO_2$ which then desorbs OR
3. the atom recombines with another O atom and then desorbs from the surface,
4. as the surface is etched it becomes rougher, eventually forming isthmuses, and then isolated islands of graphite sheet,
5. due to weak van der Waals forces between sheets and the inter colation of

oxygen between these sheets, some of these islands are removed easily.

The result of this mechanism is that the erosion yield of the material is a function of fluence. As the surface roughness increases, so does the surface area and number of defects exposed to AO, thereby increasing the etch rate. Each step defined here is not fully justified in the paper, and requires further proof before becoming accepted.

Although a pure HOPG crystal may potentially have a fluence dependent erosion yield, polycrystalline graphite would appear not to. The work of Gregory on HOPG is repeated for two polycrystalline graphite samples [130], one sample being flown on the STS-8 mission and another on the LDEF experiment. In general, the erosion yield found for both samples were comparable to one another, indicating that the polycrystalline graphite erosion is less dependent on fluence. Both erosion yields also fell closer to the values of HOPG at the lower STS-8 fluence.

So far not much has been said about ground-based testing of graphite materials. A variety of exposures were co-ordinated by Banks and co-workers [132], in what is termed as a "round robin" test. In 1986 a round robin programme was initiated to improve understanding of the simulation facilities available at the time and their effect on a variety of materials, including a single crystal of HOPG and pyrolytic graphite. Test samples were sent to 30 different facilities for evaluation, but judging by the number of references only a small proportion of these provided results.
The erosion yields for both graphite materials are tabulated to fall between 0.9-$1.7 \times 10^{-24}$ cm$^3$/atom. From this range a "commonly agreed upon" value is quoted as being $1.2 \times 10^{-24}$ cm$^3$/atom. Unfortunately individual exposure conditions are not indicated, nor are particular erosion yield values assigned to a particular facility, which makes these results hard to understand. It is worth considering whether or not the authors were aware of the fluence dependent erosion yield at the time, because to quote a single value without quoting a fluence value would be careless given this information.
The work of Koontz *et al* [133] associates the above erosion yield range to "various forms of carbon" which is in turn compared against a value derived from a ground based facility, thought to be that of the Los Alamos National Laboratory (LANL). Whether or not the carbon sample tested in the LANL facility was the same as that

used in the investigation by Banks is unclear, but an erosion yield of 1 x$10^{-24}$ $cm^3$/atom is quoted. The precise exposure conditions are also unclear, but the LANL facility typically produces fast (1-5eV) beams of AO at LEO fluxes.

### *4.6.2 Diamond*

One shuttle experiment intended to assess the reactivity of a variety of diamond and diamond-like films was an STS-46 payload named the Limited Duration Space Environment Candidate Materials Exposure Payload (LDCE)-2 and 3[134]. The fluence was measured nominally as 2.2x$10^{20}$ atoms/$cm^2$ by a mass spectrometer and Kapton witness samples. The experiment exposed two CVD polycrystalline diamond films, which contained very small amounts of graphite at the grain boundaries. It was expected that the small graphitic component would be preferentially etched by the AO leaving behind the diamond crystals, but upon retrieval the films showed no measurable change in mass or composition. There is no explanation for this result.

Therefore, it is perhaps useful to compare the results of a similar material in ground-based simulations. The work of Joshi [135] exposed a variety of carbon materials to an oxygen plasma. The samples were exposed to a flux of 6x$10^{15}$ ions/$cm^2$/s for 30 hours. Unfortunately the energy of the oxygen ions is not given, but it is assumed that the beam is not hyperthermal. CVD was used to deposit two different kinds of diamond film. One of the films showed a “cauliflower-like” morphology of fine diamond grains with small amounts of $sp^2$. The other film had a more faceted structure to the diamond grains and had no $sp^2$ content.

A comparison of the two diamond films before and after ion exposure indicated little or no change in thickness, with only minor surface roughening. The film containing pure $sp^3$ facets was attacked uniformly at all crystal facets, leaving the surfaces acicular with a very fine needle size. The “cauliflower-like” film showed damage to be preferential to the grain boundaries and other defect regions which, contrasting with the experiments performed on STS-46 [134], was attributed to preferential $sp^2$ erosion. It is worth noting that the work of Joshi [135] does not positively locate the

$sp^2$ on their films, but would appear to assume its location by other work on high temperature molecular oxygen attack.

If atomic oxygen had been eroding $sp^2$ sites preferentially, reasons for the differences between [135] and [134] cannot be clearly defined, but some inference can be made with the type of exposures. The ground based results use oxygen plasma at a much lower translational energy than that found in LEO, possibly increasing the time for the oxygen atoms to react with the surface of the material. Other possible reasons for the difference could be related to the sample temperatures or the ionic nature of the oxygen. Sample temperatures are not mentioned for the STS-46 paper, whilst Joshi estimates sample temperatures to be 80-120°C. At the present time it is unclear what effects the ionic nature of oxygen has on diamond materials [133].

The only account of natural diamond being exposed to hyperthermal AO is reported by Peters [95] where a face of a natural stone was exposed to the space environment during the STS-8 mission. The exposed surface was etched by 75nm and coated with an uncharacterised greyish-white solid, much softer than diamond. Surrounding surfaces did not have the same coating, eliminating the possibility of contamination; thereby suggesting diamond is susceptible to attack from the space environment.

### *4.6.3 Vitreous carbon*

Vitreous carbon was exposed on STS-5, which was one of the earliest materials science shuttle missions. A polished sample was exposed to the LEO environment for a total of 47 hours, resulting in a fluence of $0.99\pm0.3 \times 10^{20}$ atoms/cm$^2$[136]. Post-exposure, an unprotected area of the material was visibly roughened; peak to valley depth of the eroded area was 1.09 microns with a root-mean-square depth of 0.3 microns. The reaction probability for the material is calculated as $2.3\pm0.7\times10^{-2}$ [54], which given a material density of 1.538g/cm$^3$ can be converted to an erosion yield of $0.3\times10^{-24}$ cm$^3$/atom. The temperature of the vitreous carbon sample was not controlled or monitored. However it is believed that the experiment tray to which the sample was mounted did not exceed 350K in the course of the flight [54].

Vitreous carbon samples were flown again on the STS-8 mission, where exposed surfaces were etched by about 4500nm [95]. These surfaces also had a rough surface with a reported grass-like profile. If erosion yield is calculated on the quoted etch depth, this gives a value of about 1.3 $\times 10^{-24}$ $cm^3$/atom, which is very different to that of STS-5 ($0.3 \times 10^{-24}$ $cm^3$/atom).

A material sample identical to that flown aboard the STS-5 mission was tested in a ground based arc-jet type AO simulator [129], in which a dc arc heats a flowing stream of helium at atmospheric pressure. A small quantity of $O_2$ is injected into the flow downstream of the arc, where it is thermally dissociated into oxygen atoms. This system produced an AO flux of 5-$7 \times 10^{15}$$cm^2$/s with a beam energy of 1eV (4eV less than that of LEO AO). The total exposure time was 5 hours, producing a fluence of $1 \pm 0.5 \times 10^{20}$ atoms/$cm^2$. Temperature in this instance was controlled to 299K.

The exposed area of the sample was visibly roughened in a similar way to the flight sample. The erosion yield is also reported as comparable to that obtained from the STS-5 mission, where a value of $0.27 \pm 0.16 \times 10^{-24}$ $cm^3$/atom can be calculated. Whilst the error bands for both experiments are large, comparing each result with one another it is clear that the erosion is not a strong function of beam energy between 1-5eV. The errors do, however make comparisons with results from different materials more difficult.

### *4.6.4 Amorphous carbon*

A wide variety of amorphous carbons have been flown in LEO and tested in ground-based simulators. The STS-8 mission provided an active measurement experiment on amorphous carbon that is largely unpublished. A temperature controlled QCM (TQCM) coated with 240nm of amorphous carbon was exposed to AO in the payload bay of the space shuttle. The temperature of the TQCM was maintained at 308K. The two papers briefly describing the experiment provide two different results. The paper of Leger [60] simply quotes the erosion yield as being approximately $0.35 \times 10^{-24}$$cm^3$/atom, whilst the paper of Arnold [54]is more descriptive. The mass loss rate ranged from 6-$8 \times 10^{13}$ carbon atoms/$cm^2$/s, and a reaction probability of 0.026±0.005 is quoted. The density of the film was 2g/cm$^{-3}$, so the erosion yield is calculated here as 0.26±0.05x10$^{-24}$cm$^{3}$/atom. The difference between the two papers' values cannot be explained given the limited data available. Similarly the composition and/or deposition method are not indicated.

Perhaps the most definitive work performed on amorphous carbon so far is that carried out by Tennyson [102], Bourdon and their co-workers [103, 137]. A wide range of amorphous carbons were deposited onto QCM devices and exposed to a ground-based AO beam. The simulation facility uses microwave energy to dissociate molecular oxygen into a stream of neutral AO atoms, which is seeded into a helium carrier gas. This process produces a steady stream of AO with energy of approximately 2.5eV. The first investigation exposed a QCM with two layers of different amorphous carbon[102, 103]. The first layer deposited was unhydrogenated (a-C) whilst the layer deposited on top of this was hydrogenated (a-C:H). The precise levels of hydrogen in the a-C:H film are not stated.

The QCM was then exposed to an AO flux of approximately 5.6x10$^{16}$ atoms/cm$^{2}$/s as measured by Kapton witness sample mass loss. During exposure, the outer layer of a-C:H was removed first before a slower reaction rate was observed from the QCM. The change in erosion rate was attributed to the removal of a-C:H and subsequent exposure of a-C. The in-situ measurement provided by the QCM indicates that both types of amorphous carbon erode in a linear fashion.

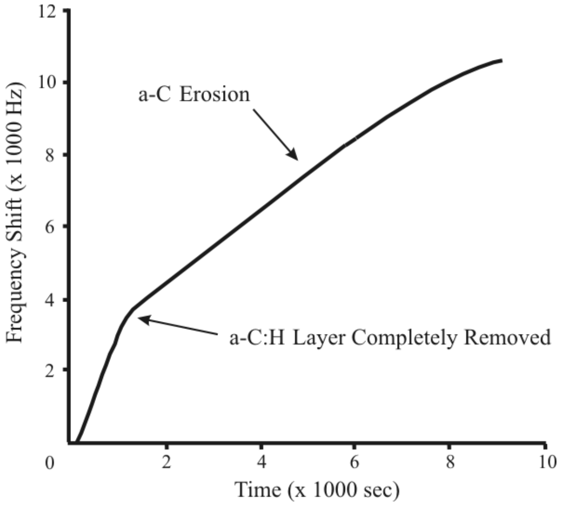

**Figure 14: Measurements from a QCM coated with two different carbon films and exposed to an AO environment [103]**

The ratio of reaction rates (a-C:H : a-C) were then calculated as being 3.4. Assuming that the AO strips off C atoms to form volatile CO, a reaction probability of 0.01 and 0.03 were calculated for a-C and a-C:H respectively. Unfortunately the density values are not given, so it is difficult to convert the reaction probability into an erosion yield. However, results can be compared to those of vitreous carbon [54, 129]. Taking account of error bounds, a-C has a reaction probability less than vitreous carbon (P=0.01 compared to a lower limit for vitreous carbon of P=0.016), whilst a-C:H has a reaction probability equivalent to the upper limit of vitreous carbon. The authors suggest the increased reactivity for a-C:H is due to the presence of H atoms.

The second investigation provides a more focussed study of a-C:H hydrogenation levels [137]. Again a-C:H was deposited onto QCMs, which measured the reaction rates. The same AO simulation facility was used to generate AO at 2.5eV but this time with a flux of approximately $1\text{x}10^{16}$atoms/cm$^2$/s. This work shows the typical data from two QCMs each coated with a different kind of a-C:H. It appears that the etch rate is thickness dependent to some degree, with the fastest erosion occurring at the beginning of the AO exposure before slowing. This result is very important for a sensing application because a variable erosion yield must be accounted for in the calibration of the sensors. A thickness dependent characterisation was not performed so the authors do not state the reasons for this variable erosion yield, which could be attributed to a change in microstructure, composition, defects, density or a combination of these factors.

Generally speaking, the etch rate of the films increased with hydrogen content, although there is rather a lot of scatter in these results when hydrogen content falls between 20 and 35% of film composition. The greatest reaction rate of 20ng/cm$^2$s was observed for the film with greatest hydrogen content (47 at.%). Assuming the mass of a carbon atom is $2\text{x}10^{-23}$g, the equivalent reaction probability is 0.1. The lowest reaction rate was 1 ng/ cm$^2$s, which is equivalent to a reaction probability of 0.005.

In order to investigate the degree of scatter in the results, films with 25 at.%

hydrogen were characterised for bonded hydrogen content. It was found that the etch rate increased linearly with bonded hydrogen. The lowest erosion yield was obtained from a film with a very densely packed carbon network with a large amount of unbonded hydrogen. These films were found to have a smooth surface, a high hardness and an erosion yield only 3 times greater than CVD crystalline diamond.

With such an in-depth analysis of a-C:H response to 2.5eV AO it would be useful to compare the results with an experiment performed in LEO to find any beam energy dependencies. One experiment was performed aboard the STS-46 mission alongside the polycrystalline diamond films described above [134]. Different CVD DLC films of different thicknesses were exposed to a fluence of $2.2x10^{20}$atoms/$cm^2$. Differences in composition are not highlighted but the thicknesses used were 100nm, 500nm and 1000nm. Unfortunately the films were completely eroded upon retrieval, so only the minimum erosion yield of each material can be derived and is given in Table 9.

The only remaining study of a-C film erosion in an LEO equivalent beam energy is the work of Singh *et al* [138]. Unfortunately the precise nature of the carbon films is unknown as they are only referred to as “carbon-films”. However, the deposition process and material properties would suggest that the carbon is amorphous. Films of 600 to 1000 angstroms in thickness were deposited onto QCMs by the sublimation of carbon rods, as used in preparing films for electron microscopy applications. The films were then exposed to a simulated oxygen beam with a nominal energy of 5eV. The beam content was completely ionic, with approximately half the oxygen being atomic ($O^+$) and the rest being molecular.

The data from the QCM shows that mass loss is a linear function of time. The rate eventually becomes slower as less and less material is available for oxidation. The erosion yields were found to fall between 17 to $56x10^{-24}$ $cm^3$/atom depending on flux. Apart from the flux dependent erosion yield that is discussed in the next section, the most apparent result is the very high erosion yield that is some 10-50 times greater than results from other experiments. The authors attribute this result to differences in density, microstructure and beam content, although apart from beam content no characterisation is performed on these factors.

It may be beneficial to compare the results from other materials exposed in the same experiment. Kapton films were exposed to the same beam where a fluence dependent erosion yield was evident. Erosion yield values fell in the range of 56 – 170x10$^{-24}$ cm$^3$/atom, which again contrasts massively with the values of approximately 3x10$^{-24}$ cm$^3$/atom found in many other experiments.

### *4.6.5 Dependencies on AO fluence, flux, beam energy and sample temperature*

So far a discussion of the erosion yields for a variety of carbon types has been made. Apart from some comments on graphite orientation and the fluence dependence of HOPG erosion, few comments have been made on how the erosion yield can vary for the same material. For a sensing application this is of particular importance, as a variable erosion yield will inevitability influence sensor output.

The severe erosion yields obtained by Singh, although unrealistically high, showed that there is some evidence of a flux dependent yield for amorphous carbons [138]. As flux increased, so did the erosion yield as demonstrated in Figure 15. Here the erosion yield is normalised to remove the high values from the data and possibly allowing comparison with results from elsewhere. It can be seen that the erosion yield is a linear function of AO flux, however it should be noted that the flux in LEO and in other simulation facilities could be several orders of magnitude greater than the fluxes shown here, and that this result was obtained from an amorphous carbon film in a positively charged 5eV ion beam with some molecular oxygen ions. There is no other evidence suggesting the presence of this trend either for a-C or any other form of carbon.

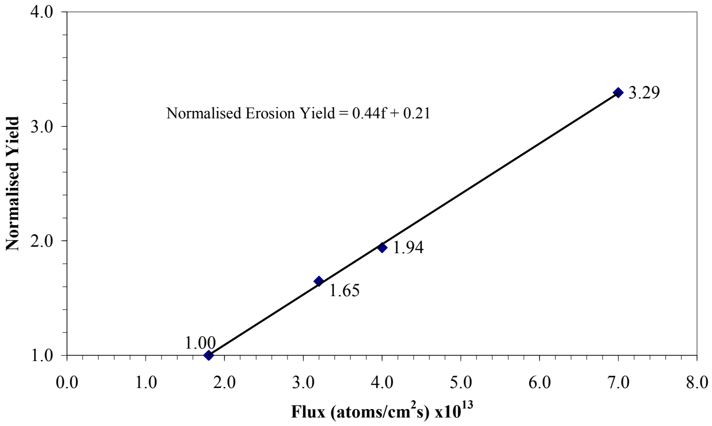

**Figure 15: Flux dependent erosion yield of an amorphous carbon film, data plotted from [138]**

Purposeful investigations into the temperature dependence on erosion yield are performed by Arnold and Peplinski [54, 129], Park [128] and Caledonia [99]. Arnold and Peplinski exposed amorphous films to a 1eV AO beam and varied sample temperatures above ambient up to 393K. In general, as temperature increased so did the reaction rate. However, it should be noted that as temperature was increased the authors also increased the AO flux, which could also influence the erosion rate obtained. The data was fitted to an Arrhenius plot to give the equation:

$$P=4.2e^{-1800/T}$$ **Equation 25**

*Where P=reaction probability and T is temperature (K)*. This gives an activation energy value of approximately 15kJ/mole.

The work of Park [128] analysed a wide range of data taken from previous AO studies on various graphite materials. It should be noted that the majority of data were taken from low energy facilities, but in some cases very high temperatures (up to 4000K), during a time before the effects on spacecraft materials became fully apparent. The Arrhenius expression is this time:

$$P=0.63e^{-1160/T}$$ **Equation 26**

Giving an activation energy of 10kJ/mole. Despite the differences in conditions and subsequent expressions, Arnold *et al* [54] comments that the precision of each experiment is not sufficient to suggest that the differences between Arnold *et al* and Park are significant. Consequently the latter expression is used to fit the data of vitreous as well as amorphous carbon [129].

One other investigation of note on the temperature dependence of erosion yield is that performed by Caledonia *et al* [99]. Microcrystalline carbon films were deposited onto a QCM to a thickness of 1 micron and then exposed to a simulated neutral AO beam of 5eV. Sample temperature was varied from 273K to 360K and mass loss measured. At 273K, the reaction probability was 0.033 and increased linearly with temperature to 0.145, a 430% increase in erosion rate (Figure 16). Although the hybridisation of the microcrystalline carbon is not clearly defined, based on the reaction probability at room temperature it is fair to assume that the material is graphitic in nature. The same study also assessed the reaction rate as a function of beam energy. Beam kinetic energies were varied from 5eV (LEO energies) to approximately 11eV (equivalent to 12km/sec) at an unspecified temperature. The etch rate was found to increase up to 250% of LEO energy equivalent etch rates. These results are plotted in Figure 17, with etch rates normalised to aid comparison.

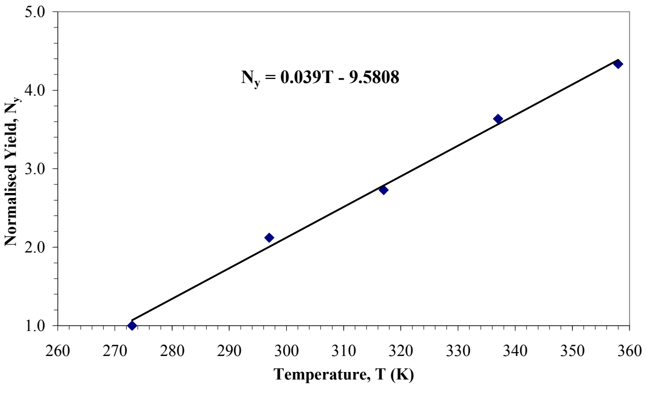

**Figure 16: Temperature dependent erosion yield of microcrystalline carbon [99]**

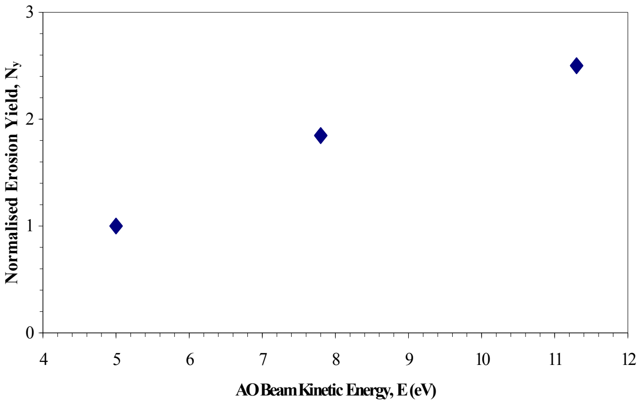

**Figure 17: Beam energy dependent erosion yield of microcrystalline carbon [99]**

Exactly how the erosion yield develops as a function of beam energy is not clear from the plot in Figure 17 because there are too few data points. Work on amorphous films exposed to lower beam energies of 1.88-2.5eV also suggest an energy dependence on erosion yield [103]. By introducing greater proportions of inert carrier gas, beam energy of the simulation facility was reduced by 25% which resulted in 25% reduction in the erosion yield. The only work to suggest that carbon materials erosion yield is independent of AO beam energy is that by Arnold and co-workers[54, 129]. The results from two identical vitreous carbon samples revealed no significant difference in erosion yield between the sample flown in a 5eV LEO environment and that exposed to a 1eV AO source.

### *4.6.6 Summary*

The different kinds of carbon are almost limitless. Carbon can be produced as diamond, graphite or a composite of these two allotropes in either a crystalline or amorphous form. Additionally, hydrogen can be added to amorphous films to change the properties of the material.

In general erosion yields can be grouped into three different categories. The first category is material erosion yields that are between 0 and 0.05 $\times 10^{-24}$ $cm^3$/atom that have a high $sp^3$ content with little or no hydrogen content. The second category can be defined as being $1.7 \geq$ yield $\geq 0.3 \times 10^{-24}$ $cm^3$/atom which is the typical response of graphite and graphite-like carbon films (either crystalline or amorphous) that are not hydrogenated. Finally, the third category appears to have yields approximately 3 times the second category and is reserved for mostly hydrogenated amorphous carbon materials.

Table 9 and Table 10 summarise the various AO experiments undertaken with carbon. Much of this work was carried out before Kapton was accepted as a common reference sample, so AO dose is estimated from thermospheric AO models. The errors of this technique are also highlighted. These errors are often ascribed to measurement errors associated with the input data, and the inability to account for all the drivers of AO density [15]. Therefore, all thermospheric models require absolute composition measurement to improve the accuracy of their predictions, so highlighting the need for suitable AO sensors.

The assumption of constant erosion yield may be inappropriate in certain situations. There is some evidence to suggest that certain carbon materials are sensitive to flux, fluence, beam energy and temperature. These results come from a variety of different carbons with a mostly graphitic nature and more research must be undertaken to find out how erosion yields of less graphitic films are influenced by these parameters. It is particularly worth noting that the reactivity of diamond and a-C: H as a function of temperature or energy has not been undertaken in any way.

Any temperature dependencies must be determined when sensing AO in LEO, as this environment has particularly aggressive heating and cooling rates if not accounted for in the instrument design. It is also worth noting that AO flux energy dependence is not of particular concern when operating in LEO, as the flux energy remains approximately constant. Concerns do arise when:

- Simulating the effects of AO on the ground, as facilities with lower beam energies could incorrectly estimate the thickness of material required for a particular mission.
- Using the material as an actinometer in an elliptical orbit, such as GTO where energies can vary. In these cases energy dependence will somehow

need to be removed from the results.

Any carbon actinometer will require some kind of calibration in a ground-based facility if it is to be used for AO measurement. Therefore such a device will have to be characterised for temperature and energy dependencies or alternatively a carbon material may arise that is insensitive to these factors.

It is somewhat interesting to see that there is little understanding of how the film content can affect the AO response of the material. It is worth considering whether new carbon materials can be developed that have erosion yields between diamond and graphite-like, or between graphite-like and hydrogenated films. If this could be achieved, carbon would be a very valuable actinometer material, as a film could be designed and manufactured to meet the specific needs of a particular mission.

To fully understand the relationship between film content and AO response any carbon film will require characterisation. From the literature review presented here crystallinity, $sp^2/sp^3$ content and hydrogen inclusion appear to be the main factors that can potentially affect AO response.

| **Material** | **Spacecraft flown** | **Exposed AO fluence (atoms/cm$^2$) x10$^{20}$** | **Fluence measurement technique** | **AO reactivity coefficient (cm$^3$/atom) x10$^{-24}$** | **Reference** |
|---|---|---|---|---|---|
| Graphite | STS-3 (temperatures unknown) | >2.16 | Unknown | >1.4 | [54] |
| Carbon film | STS-4 | 0.65 | Calculated estimate (±20% error) | 1.4 | [96, 136] |
| Vitreous carbon | STS-5 (no temperature control or measurement) | 0.99±0.3 | | 0.3 (Assuming density=1.538 g/cc) | [129] |
| Vitreous carbon (identical to above) | Ground simulation (1eV) | 1±0.5 | Mass spectrometer | 0.27±0.16 (Assuming density=1.538 g/cc) | [129] |

**Table 9: Summary of AO reaction with carbon**

| Material | Spacecraft flown | Exposed AO fluence (atoms/cm$^2$) x10$^{20}$ | Fluence measurement technique | AO reactivity coefficient (cm$^3$/atom) x10$^{-24}$ | Reference |
|---|---|---|---|---|---|
| CVDDLC (100nm) | STS-46 | 2.2 | Mass spectrometer + Kapton witness samples + calculated estimate | ≥0.045 | [134] |
| CVDDLC (500nm) | STS-46 | 2.2 | | ≥0.23 | [134] |
| CVDDLC (1000nm) | STS-46 | 2.2 | | ≥0.45 | [134] |
| CVD Diamond | STS-46 | 2.2 | | ~0 | [134] |
| HOPG | STS-46 | 2.2 | | 1.1 | [131] |
| HOPG | LDEF | 100 | Calculated estimate (±20% error) | 1.04 | [88] |
| HOPG | STS-8 | 3.5 | | 0.6 | [88] |
| Graphite (pyrolytic polycrystalline) | LDEF | 100 | | 0.61 | [88] |
| Graphite (pyrolytic polycrystalline) | STS-8 | 3.5 | | 0.58 | [88] |
| Natural diamond | STS-8 | 3.5 | | 0.02 | [95] |
| Graphite (basal orientated) | STS-8 | 3.5 | | 0.63 | [95] |
| Graphite (edge orientated) | STS-8 | 3.5 | | 0.66 | [95] |
| Vitreous carbon | STS-8 | 3.5 | | 1.3 | [95] |
| CVD DLC | Ground simulation (O plasma) | 6.5 | Unknown | 3.66 | [135] |
| CVD polycrystalline diamond (pure sp3) | Ground simulation (O plasma) | 6.5 | | 0.02 | [135] |
| CVD polycrystalline diamond | Ground simulation (O plasma) | 6.5 | | 0.04 | [135] |
| a-C | Ground simulation (2.5 eV) | - | | P=0.01 | [103] |
| a-C:H | Ground simulation (2.5 eV) | - | | P=0.005-0.1 | [103, 137] |

**Table 10: Summary of AO reaction with carbon (continued)**

# 5 ACTINOMETER DESIGN AND FABRICATION

## 5.1 Introduction

So far various AO sensing techniques and actinometers have been reviewed and some fundamental carbon concepts highlighted. The next phase is to develop suitable carbon based films for testing, and ultimately, spacecraft experiments. This chapter details the design and fabrication of films to be tested in a ground-based simulation facility and their eventual integration with the STORM and CANX-2 space experiments.

## 5.2 Spaceflight Experiments

### *5.2.1 STORM*

The Southampton Transient Oxygen and Radiation Monitor (STORM) provides detectors for observing the atomic oxygen (AO) flux and fluence, the solar soft-x-ray (SXR) flux and the solar vacuum ultraviolet (VUV) flux, to complement the other environmental and materials observation instrumentation within MEDET, an ISS experiment [29]. MEDET forms part of an experiment called the European Technology Exposure Facility (EuTEF).

Figure 18 shows how MEDET is located with respect to other EuTEF experiments. With the exception of the zenith facing X-ray and UV detectors, all of the MEDET instruments are ram facing. EuTEF is mounted to an EXPRESS pallet, which is mounted to the end of the European Columbus module.

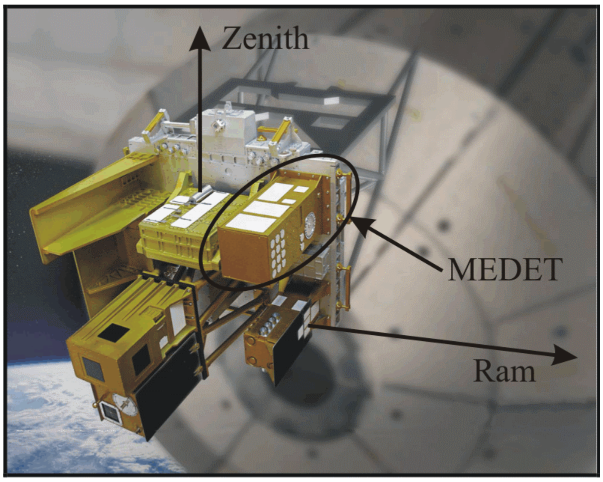

**Figure 18: MEDET on EuTEF [29]**

The volume, mass and power limits for STORM were all dictated by the MEDET design and final values are given in Table 11. The output from all signal lines will cover a range from 0-10V and be acquired by the MEDET analogue-to-digital converter (ADC) at 12-bit resolution.

| | |
|---|---|
| **Mass of mechanical components** | 437.5g |
| **Mass of electronic components** | 530.2g |
| **Total Mass** | 967.7g |
| **Width** | 130mm |
| **Height** | 105mm |
| **Depth** | 85mm |
| **Power (nominal)** | 2.1W |
| **Power (peak)** | 5W |
| **Operating temperature range** | -20º to +40ºC |
| **Stay-alive/storage temp. range** | -50º to +85ºC |
| **Data output** | 732.3 kB/day |

**Table 11: STORM system characteristics**

The electronics within STORM are encased within six panels of aluminium alloy 6063. These structural plates are 2mm thick, with the internal faces thinned to 1mm in a cross-ribbed pattern to conserve mass on panels not exposed to the space environment.

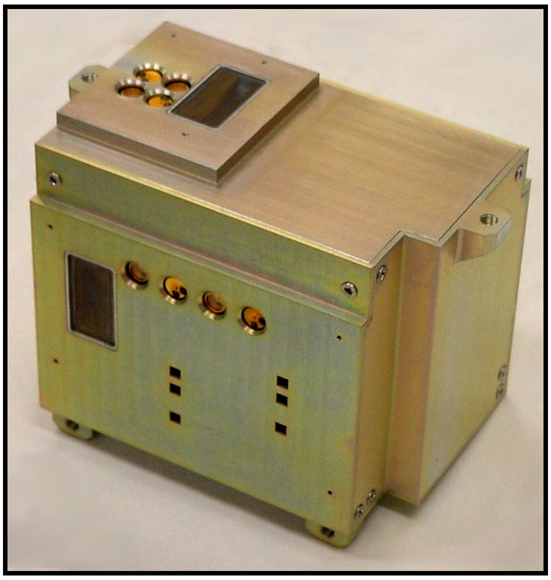

**Figure 19: The STORM module**

There are eight printed circuit-boards (PCBs) inside STORM, two of which contain the various detectors while the remaining six contain the amplification, heater control and signal multiplexing electronics. The PCBs are arranged into a major stack of six along the ram-wake axis, supported by stainless steel studs and PTFE spacers, and a minor stack of two against the zenith panel.

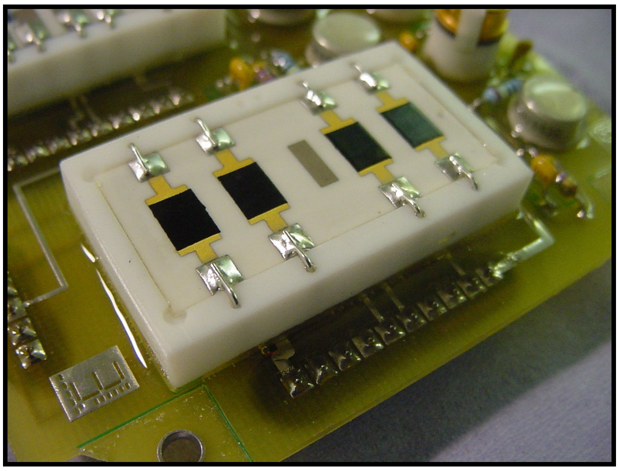

**Figure 20: Carbon actinometers on ram face PCB**

Figure 20 shows the carbon thick-film actinometer substrate in its mounted position on the ram face PCB. The alumina substrate is mounted onto a PTFE sensor holder, which minimises heat leak from the substrate heater into the PCB and the rest of the

STORM module. Details of the holder design are given in appendix A1. The substrate is secured in place by copper wire that passes from the PCB, through the PTFE holder and bent onto the surface of the substrate. An AD590 temperature sensor is potted directly to the heater on the reverse side of the substrate.

Heating rates in the ISS LEO can be very severe due to instantaneous direct solar illumination as the satellite orbits out of eclipse and shadow. To minimise thermal fluctuations, the surface of the actinometer substrate is mounted 1mm below the aluminium faceplate, which is in good thermal contact with the MEDET module. Further to this, the substrate heater is activated 18 minutes after entering eclipse (as measured by the UV sensors). After 29 minutes and 10 seconds, the heaters are switched off.

It should be noted that although there is a degree of thermal control, temperature is not kept constant but is rather kept within a safe range of temperatures. This means that changes in actinometer resistance could be the result of the thermal environment and not just AO. To isolate the effect of AO one of the actinometers is covered by the aluminium faceplate. This reference sensor will detect the effect of temperature variation without AO exposure. The AO response can then be isolated as follows:

For the reference sensor,

$$\left(\frac{R_0}{R}\right)_{ref} = \frac{\rho_0}{(\rho_0 + \Delta\rho)} \qquad \textbf{Equation 27}$$

*$R_0$ = initial electrical resistance ($\Omega$), $R$ = electrical resistance ($\Omega$), $\rho_0$ = initial resistivity ($\Omega$cm)* and *$\Delta\rho$ = resistivity difference from initial condition.*

For the sensor exposed to AO,

$$\left(\frac{R_0}{R}\right)_{ex} = \frac{\rho_0\tau_0}{(\rho_0 + \Delta\rho)(\tau_0 - \Delta\tau)} \qquad \textbf{Equation 28}$$

*$\tau_0$= initial thickness (cm), $\Delta\tau$ = thickness change from initial condition.*

The AO isolated response is then:

$$\left(\frac{R_0}{R}\right)_{isol} = \left(\frac{R_0}{R}\right)_{ref} \div \left(\frac{R_0}{R}\right)_{ex} = \frac{\tau_0 - \Delta\tau}{\tau_0}$$ **Equation 29**

This represents the ideal case when all data channels are recorded simultaneously. In cases when this is not possible, time must be accounted for by replacing ($\rho_0$+$\Delta\rho$) with a time dependent resistivity, where $t_{ref}$ is the *time when the reference sensor resistance is measured* and $t_{ex}$ is the *time when the exposed sensor resistance is measured*.

$$\left(\frac{R_0}{R}\right)_{isol} = \frac{\rho(t_{ex})\ (\tau_0 - \Delta\tau)}{\rho(t_{ref})\tau_0}$$ **Equation 30**

It can be seen that if resistivity changes are large over one time increment, then an offset in the resistance ratio will result. For the STORM instrument, 5 measurements are made in 10 seconds, one for each carbon sensor and another for a temperature measurement. Therefore, a resistance measurement is repeated every 10 seconds. The cycle is repeated 6 times during each eclipse pass.

### *5.2.2 CANX-2*

The CANX-2 nanosatellite (Figure 21) has been designed to test important technologies for future formation flying applications, including a GPS positioning system, sun sensors, a magnetometer and a 3-axis reaction wheel system. A paper by Sarda and co-workers provides more details on these systems [21].

In addition to the above, CANX-2 also carries 3 atmospheric experiments, including a materials degradation monitor. As this experiment is a secondary mission objective and given the size of the satellite the mass, size and power limits imposed on the experimental module design were much more limiting than the STORM package.

The whole satellite weighs 3.5kg and is 10 x 10 x 34cm. Depending on solar illumination, the power available to the satellite is within 2-7W. Attitude will be controlled to within ±10° during certain periods but not necessarily for the entire mission. The implication of this is that a rate change in response may occur during periods when the sensor passes through the AO field at different angles. The measurand for this experiment should therefore be total AO dose (fluence), rather than the AO flux.

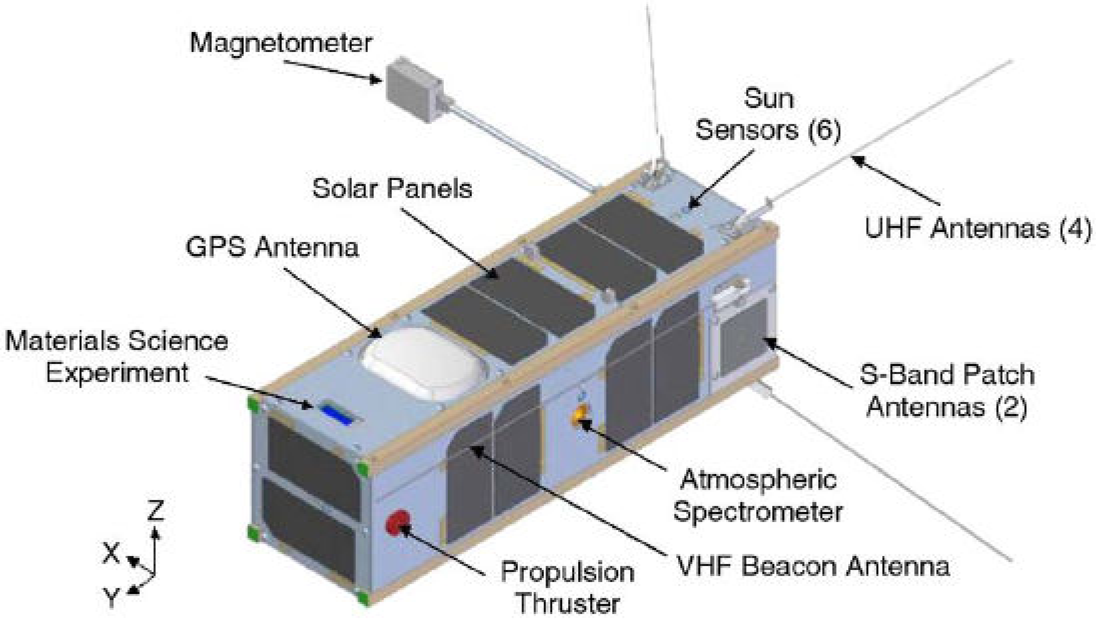

**Figure 21: Computer generated model of the CANX-2 nanosatellite [21]**

During periods of solar eclipse, the maximum available power to the entire satellite will be 2W. This power will be needed for 'housekeeping' purposes and will be unavailable to the AO experiment. Therefore, unlike STORM, it will not be possible to heat the substrate during periods when temperatures are at their lowest.

As the precise orbit of CANX-2 was not fixed during its manufacture, the anticipated temperature extremes could not be determined, leaving the possibility that the sensors could get too hot or cold. To help characterise any adverse temperature effects, an AD590 temperature sensor has been included in the design of the experiment. Additionally, one sensor is covered by an aluminium faceplate in a similar manner to the STORM experiment (Figure 22). This will allow any temperature-induced effects to be isolated from the rest of the space environment and the temperature recorded. It should be noted that all of the experiment is covered by the structure of CANX-2 except for the actinometer substrate and its aluminium cover shown in Figure 22. Like the STORM experiment, one sensor is protected from AO exposure to provide a reference for normalisation.

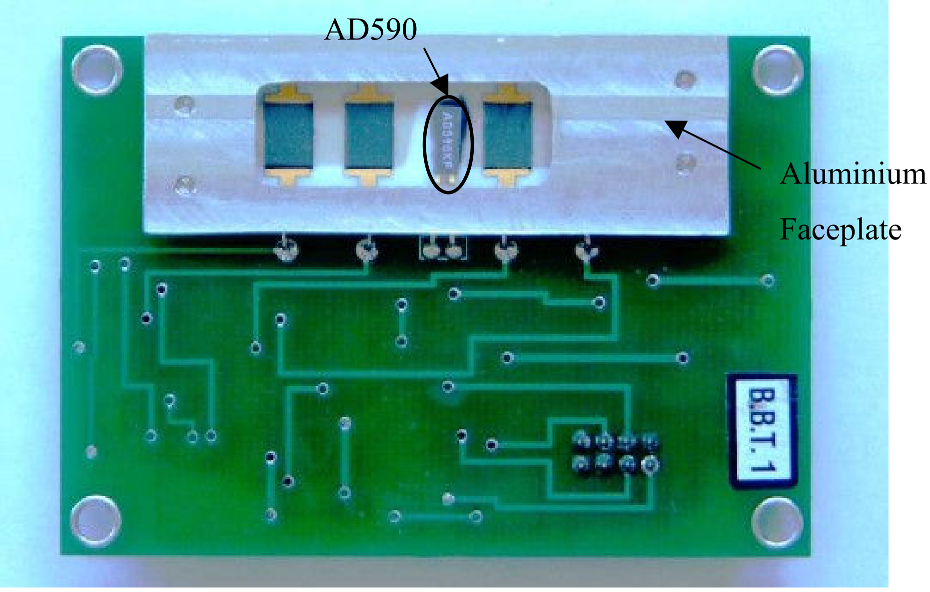

**Figure 22: CANX-2 AO experiment module**

### *5.2.3 Fluence Estimates*

The International Space Station can perhaps provide the worst-case scenario for fluence exposure, as it will follow a LEO over many years. After a period of three years, the STORM/MEDET package will be retrieved for ground-based analysis. AO concentration is dependant on levels of solar activity and the orbital altitude, so maximum and minimum estimates of fluence are given in Table 12 below.

| | **AO concentration (atoms/cm$^3$)** | **3 year AO fluence, with velocity at 8km/s (atoms/cm$^2$)** |
|---|---|---|
| 360 km orbit (solar maximum) | $2.25 \times 10^9$ | $1.7 \times 10^{23}$ |
| 440 km orbit (solar minimum) | $9.85 \times 10^6$ | $7.5 \times 10^{20}$ |

**Table 12: Fluence estimates for STORM based on figures from CEPF [22]**

The CANX2 mission is designed to orbit earth for a period of approximately one year before ending its life in a de-orbit maneuver. At the time a suitable sensor had to be selected, the orbital altitude was not decided and was subject to launch opportunities. The orbit was thought to be a high LEO, which significantly reduces the total anticipated fluence. As shown in Table 13, the initial estimates for fluence covered a wide range of fluences, which overlaps with the fluence requirements of the ISS. As discussed in Chapter 11, the selected sensor had to be designed for the maximum worst-case fluence of $1.3\text{x}10^{21}$ atoms/cm$^2$. Subsequently, the orbit was fixed to a 600km LEO giving an anticipated fluence range of $6.5\text{x}10^{18}$ to $6.5\text{x}10^{20}$ atoms/cm$^2$.

| | **AO concentration (atoms/cm$^3$)** | **1 year AO fluence, with velocity at 8km/s (atoms/cm$^2$)** |
|---|---|---|
| 500 km orbit (solar maximum) | $5\text{x}10^7$ | $1.3\ \text{x}10^{21}$ |
| 700 km orbit (solar minimum) | $5\text{x}10^4$ | $1.3\ \text{x}10^{18}$ |

**Table 13: Fluence estimates for CANX2 based on figures from CEPF**

## 5.3 Device Design

### *5.3.1 Substrates*

An important aspect in the design of the actinometer device is the substrate material onto which the carbon films are deposited. The substrate material must:

- be stable at its highest operational temperature,
- be electrically insulating to allow reliable resistance measurements,
- be immune to AO attack,
- chemically inert to the deposited film material,
- have adequate roughness for the film to adhere,
- have adequate smoothness for accurate thickness measurement,
- have a good thermal conductivity to ensure a more efficient use of any heating power.

Following on from the work of Osborne and Harris[9, 10, 14, 52, 93, 139, 140], alumina was deemed the most appropriate substrate material. This decision is in part related to the fabrication of the electrical contacts and a substrate-mounted heater, which are discussed later. Two different alumina types were used: Coors 96% (with an average surface roughness, Ra, of ~0.7μm) and 97% alumina (with Ra ~ 0.07μm).

### *5.3.2 Electrical Contacts*

The architecture of the actinometers in this work is derived from a previous AO experiment from STRV-1d, where 4 films are deposited onto a single 36x17mm substrate [15]. To measure the resistance of the films, it is necessary to have contacts that can be soldered into spacecraft electronics.

Following on from the work of Osborne, the films were deposited onto gold tracks due to its high electrical conductivity and inertness to AO attack[52]. The gold tracks are not solder compatible so silver-palladium contacts were overlaid onto the gold tracks. The contacts and tracks were fabricated using the screen-printing process.

Many of the carbon films were deposited onto a simple two point contact layout, as shown in Figure 23. Some of the deposited carbon films had very low electrical conductance, to a point where the resistances could not be measured using simple multimeter devices. To address this issue, a new contact layout was fabricated that would lower the measured electrical resistance for subsequent depositions by lowering the length/width ratio of the film. The layout of this ‘interdigitated array’ is given in Figure 24.

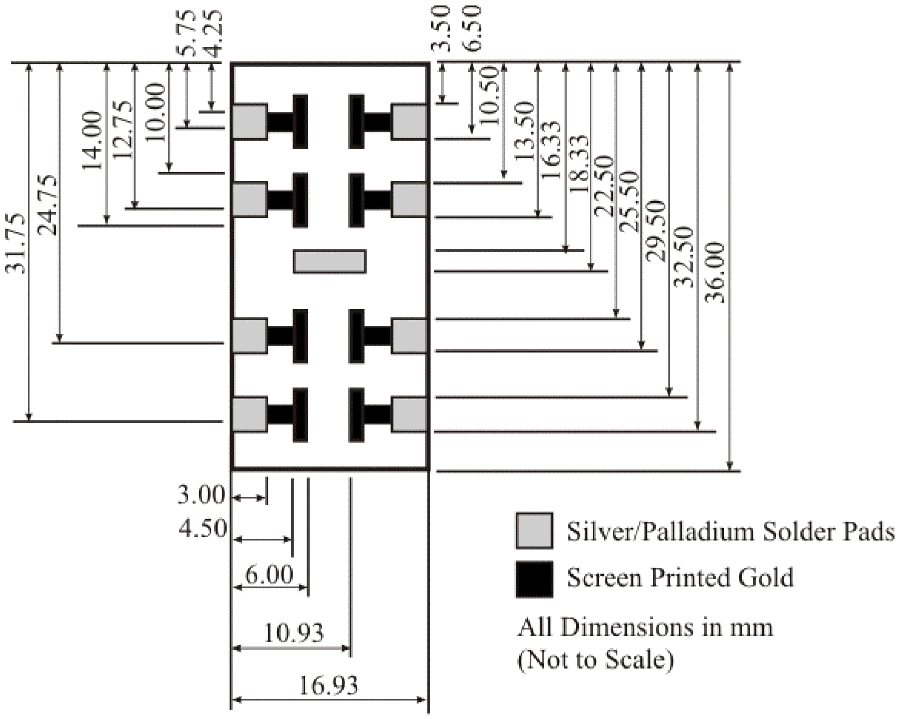

**Figure 23: Two point contact layout**

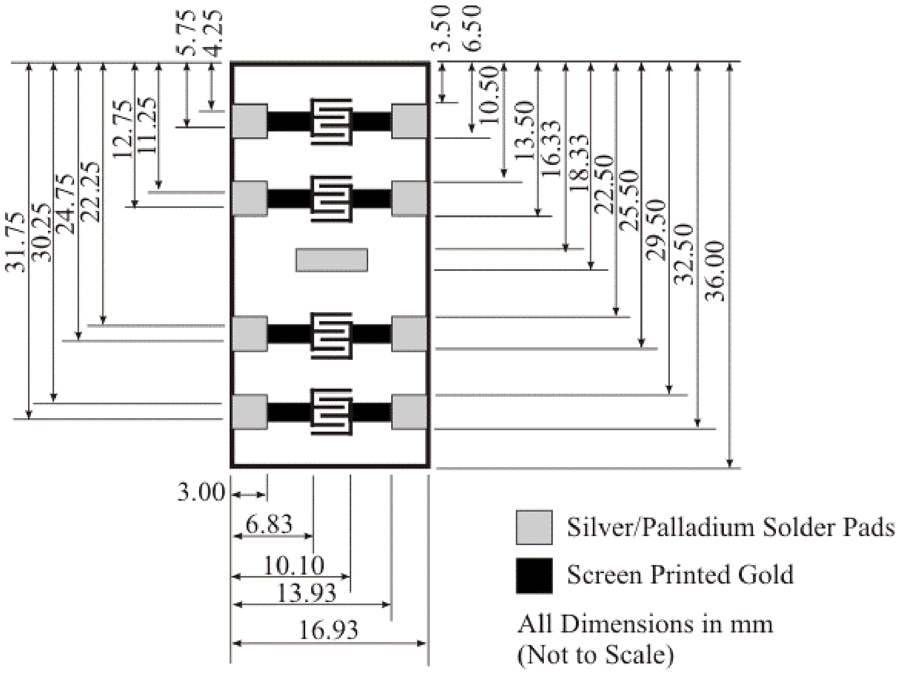

**Figure 24: Interdigitated array layout**

### *5.3.3 Heater*

In LEO the transitions between solar illumination and eclipse can cause very high heating and cooling rates if not accounted for in the design process. The AO devices on STORM are protected as much as possible from direct solar illumination by an aluminium plate, which helps keep temperatures as low as possible. In situations when the device may get too cold, such as an eclipse period, a heater is required.

The style of heater adopted is a screen-printed (thick film) resistive element, formed directly onto the rear face of the sensor substrate. The advantages of this technique are:

- No adhesives are required. The heater material is directly bonded to the substrate, so reducing the risk of contamination.
- Excellent thermal contact. There is no thermally insulating layer, such as an adhesive, between the heater and the substrate.

A schematic of the heater can be found in Figure 25. The heating element consists of a ruthenium oxide in a glass frit whilst electrical contacts are printed from a silver palladium alloy. The silver palladium contacts are known to erode in the atomic oxygen environment but can be protected using shielding and the solder used on the pads.

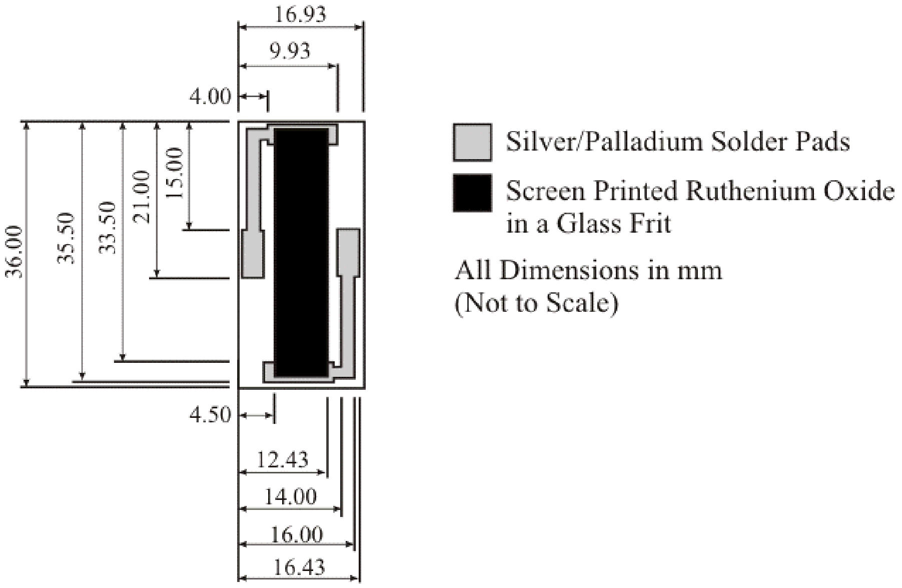

**Figure 25: Screen printed heater layout**

The silver palladium contacts were the first to be deposited onto the substrate and dried for approximately 10 minutes before one hour of firing at 850°C. The heater material was then screen printed onto the substrate, overlapping with the silver palladium contacts before a second firing interval. Resistances are then measured and trimmed to the design requirement by removing some of the heater material with a precision shot-blasting tool.

### *5.3.4 Sensor Designation*

The alumina material is delivered as a 50.8x50.8 mm coupon. From the coupon, three substrates and a test section were scribed into the material using a laser, as shown in Figure 26. All the contacts, heaters and carbon film depositions were carried out with the coupon in this condition. After deposition the coupons were broken along the scribe lines to produce a substrate. A total of four sensors, or films, were deposited onto each substrate.

Each coupon, substrate and sensor was identified by a number, as shown in Figure 26. For example, if the coupon is designated 20, the film labelled ‘4’ immediately above the test piece is designated 20-02-04 and the substrate can be labeled 20-02 to indicate that all sensors are included in the description. The coupon numbering is based on the order in which they were deposited with carbon films.

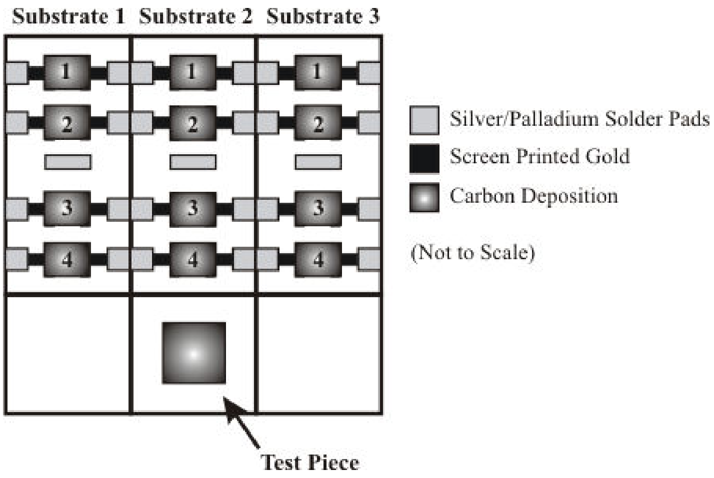

**Figure 26: Coupon and sensor designation**

## 5.4 Film Deposition Methods

Chapter 3 provided a theoretical model for carbon actinometers. An important aspect of this model was that erosion was assumed to take place uniformly across the surface of the carbon film. From the literature review, it was apparent that the AO erosion of carbon initiates at defect sites, which could lead to a rather pitted and uneven surface post exposure. To ensure that the films erode as evenly as possible, it will be necessary to deposit a material with a high number of defects that is typical of amorphous carbon.

Currently there is a wide range of deposition methods used to deposit amorphous carbon [105]. Very thin films (less than 100nm) can be manufactured using a variety of nano-deposition methodologies, but the inherent structure of the deposited films will be significantly different from those deposited using more conventional techniques such as PVD and CVD, that provide more practical, thicker films.

For a given erosion yield, thickness should be increased if a greater lifetime is required. However, film stresses limit the maximum thicknesses of typical physical and chemical vapour deposition (PVD and CVD) techniques to around 1-3μm [69, 141]. With typical erosion rates of graphite-like materials being around $0.5 \times 10^{-24}$ $cm^3$/atom, these thicknesses equate to a life of ~$1 \times 10^{20}$ atoms/$cm^2$, which falls below the minimum annual fluence for the ISS [22]. Therefore, any alternative deposition methods that can provide a greater thickness should be investigated. The work reviewed on the CONCAP II mission exposed a composite ‘thick film’ carbon [79, 80, 88]. This material showed some promise as an actinometer and can be deposited to a greater thickness than PVD or CVD techniques.

In addressing the above issues, the following deposition processes were selected:

- DC magnetron sputtering, a PVD technique.
- Electron Beam (E-beam) Evaporation, a PVD technique.
- Thick film screen-printing.

### *5.4.1 Magnetron Sputtering*

DC magnetron sputtering involves the following processes:

Substrate material is placed in a vacuum chamber below a DC coupled magnetron, to which the source material (in this case carbon) is attached (Figure 27). Argon is then introduced at a low pressure, which is then ionised by the DC induced electric field. The argon ions are then accelerated towards the surface of the target, causing target atoms to break off in vapour form (sputter) and condense on all surfaces including the substrate. The magnetron is effectively a permanent magnet that enhances ion acceleration and density.

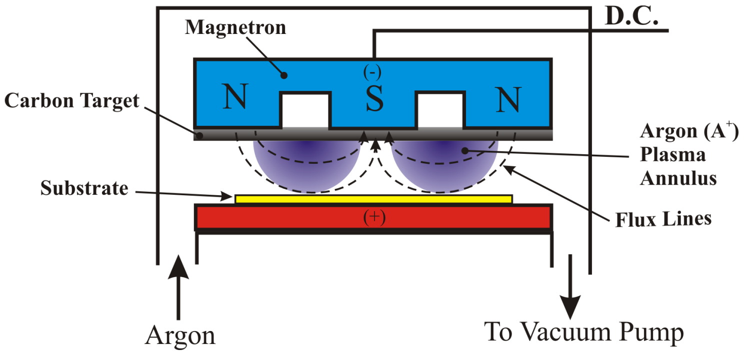

**Figure 27:DC magnetron sputtering setup**

DC magnetron sputtering is a widely used technique in the deposition of many kinds of a-C film. Its versatility has led such facilities to be widespread. The deposition conditions can be controlled and are relatively independent of substrate geometry or condition [142-144]. This technique was selected because of its relative abundance in industry, ease of control and can produce carbon films with a wide variety of contents. By controlling the amount of 'disorder' and $sp^3$ in a carbon film, it was thought that the technique could produce a carbon film with a particular erosion response.

### 5.4.2 *Electron Beam Evaporation*

In electron beam (e-beam) evaporation, an e-beam is used to heat a graphite target so that it evaporates. As the carbon cloud cools, it deposits itself onto all the surrounding surfaces of the sample chamber. Figure 28 shows a schematic diagram of the e-beam evaporation method.

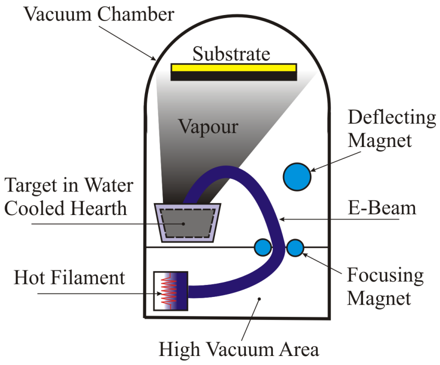

**Figure 28: Electron beam evaporation facility**

E-beam evaporation is another commonly used technique and is used to produce a-C films of a generally more graphitic nature [145, 146]. The advantage of this technique is that it can provide greater deposition rates, so producing thicker films faster than the sputtering technique.

### 5.4.3 *Screen Printing*

The screen-printing process involves the application of ink onto a porous fabric screen. A rubber squeegee is used to make contact with an underlying substrate and force the ink through the screen onto the substrate. The basic film geometry is defined by use of a non-permeable mask. The substrate then undergoes a drying and baking process to polymerise the film material.

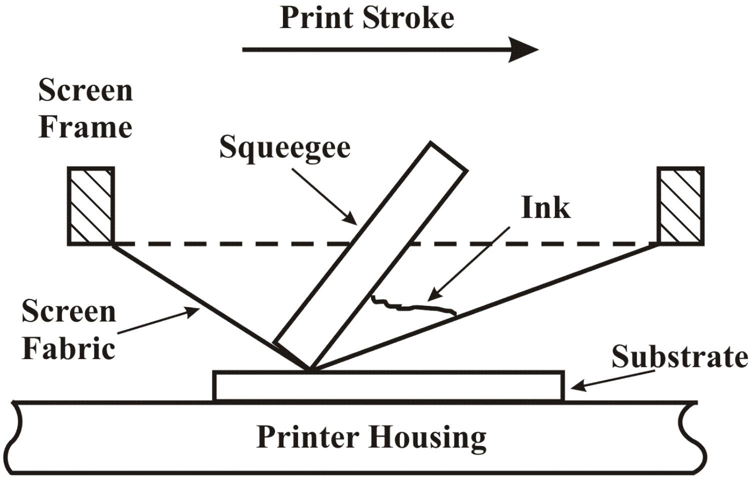

Figure 29: Screen printing technique

The screen-printing process has been used in many sensing and microelectronic applications and has been found to produce sensitive instruments at a low cost [147, 148]. Polymer Thick Films (PTF) are known to be a particulate composite of carbon particles in a polymer matrix. The polymer matrix increases the resistivity, allowing thicker films to be deposited with a similar resistivity to the above two techniques [149]. PTFs are commonly used as microcircuit resistors, where many resistors can be printed in one run rather than having to solder individual components.

## 5.5 Carbon Depositions

The e-beam and sputtered depositions were carried out in two deposition sessions at the Cranfield University School of Industrial and Manufacturing Sciences. The first deposition session (DS1) was undertaken during October 2002, whilst the second deposition session (DS2) was undertaken during February 2004. Screen-printing was carried out at the University of Southampton School of Engineering Sciences Thick Film Unit. Before each deposition, each substrate was dusted clean using pressurised dry air before a 5-minute IPA rinse in a sonic bath.

An important aspect of this work is to understand the relationship between film content and AO performance. The work of Besold has shown that by heating evaporated carbon to 700°C for 15 minutes, the films should undergo a graphitisation and densification process [133]. To provide further variation in content, some of the evaporated samples were heat-treated to this regime.

Following DS1, the sputtered films were found to have open loop resistances. In this case heat treatment was necessary if the films were to be used as an actinometer. All thermal treatment was carried out in an inert argon atmosphere.

Following deposition and any heat treatment, the thickness of each film was measured using a Rank Taylor talysurf. The thickness measurements of DS2 sensors were consolidated by measurements of films on SiO test wafer substrates, which were deposited alongside the actinometer substrates. Details of each deposition are tabulated in the results of Chapters 8, 9 and 10.

# 6 AO EXPERIMENTS

## 6.1 Introduction

Before the actinometers can be used to measure the AO environment they need to be calibrated. Chapter 2 has highlighted the wide range of facilities available for calibration. It is important to select which one of these will give the most accurate representation of the LEO environment. In the case of the ISS and CANX-2, the AO environment will have a constant energy at approximately 5eV. The literature review of Chapter 4 has highlighted a possible carbon erosion energy dependence, so it is appropriate to select a source of similar energy to the LEO environment. The ATOX source at ESTEC is one such source that can also provide an accelerated flux of atoms, which is useful when designing sensors for a large fluence mission such as the ISS or CANX-2. This system was used for the majority of the AO exposures.

In cases where achievable simulated fluences are still much lower than anticipated exposures, plasma ashers are required. Plasma ashers typically ionise air with an RF source to give a thermal (<0.1eV) source of oxygen plasma. Whilst materials react with significantly reduced erosion yields at thermal energies, the reaction rate is significantly greater because of the very high flux. Whilst these systems are by no-means an accurate representation of LEO AO attack, they can provide a useful means of assessing variations in the erosion rate of thicker and more durable materials. A sample of screen-printed sensors were sent for testing in the plasma asher facility located at ITL Incorporated

Testing took place in two exposure sessions. Exposure session 1 (ES1) was used to test the sensors of deposition session 1 (DS1), whilst exposure session 2 (ES2) was used to test sensors from both DS1 and DS2. Both experiments have been conducted in ATOX. The plasma asher exposure is not defined as part of an exposure session and are discussed separately.

## 6.2 AO Simulation Facility (ATOX)

The ATOX facility is comprised of three vacuum chambers, the first of which is the sample compartment (Figure 30). This chamber is used as a "load lock", so that the samples to be exposed to AO may be loaded onto a sample tray without destroying the vacuum in the other chambers, thereby reducing the time for pump down between experiments. The sample compartment is evacuated by a turbo molecular pump and typically reaches base pressures of $\sim 10^{-6}$ mbar.

Adjacent to the sample compartment is the main chamber, which is pumped simultaneously by turbo molecular and cryo-pumps. When the sample compartment is evacuated a gate valve is opened, allowing the sample tray to be moved inside the main chamber for greater AO exposure. Base pressures are $\sim 10^{-9}$ mbar, but during AO exposures, the pressure fluctuates around $10^{-6}$ mbar due to the gas load brought about by injection of molecular oxygen into the nozzle chamber.

The nozzle chamber contains a copper nozzle used in the AO formation process and has its own pumping system for operation from atmospheric pressure. When the nozzle has been evacuated, a gate valve is opened to allow oxygen to flow into the main chamber. When the gate valve is opened, the main chamber pumps regulate nozzle chamber pressure.

Molecular oxygen is pulsed through a PTFE valve into the copper nozzle of the nozzle chamber, creating a cloud of gas. A pulsed, transversely-excited atmospheric (TEA) carbon dioxide laser is then fired at a point inside the nozzle where its energy is absorbed by the oxygen molecules, which dissociate to form a hot (>20000K) plasma. The initiation of the plasma creates a blast wave that accelerates the oxygen ions and electrons through the (supersonic) nozzle. During acceleration, the plasma cools at an optimum rate to allow ion-electron recombination, but preventing atom-atom recombination, thereby forming a beam of fast, neutral atomic oxygen. The expansion of the beam from the nozzle provides an AO flux that is inversely proportional to the square of the distance travelled [150]. The AO beam strikes a moveable sample tray, which can be located between 55-130cm from the nozzle, providing flux variations if required.

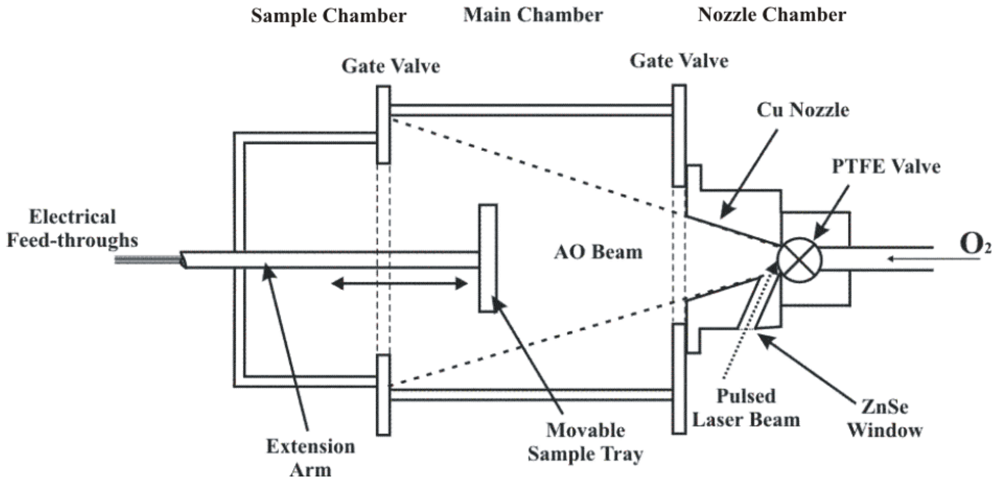

**Figure 30: Schematic of ATOX facility**

Flux can also be changed by altering the amount of oxygen processed per pulse, but this typically produces additional changes in beam velocity, which can be controlled over the range of 6-10km/s. Hence if the effect of beam velocity is to be evaluated, this would require a proportional change in the nozzle to sample distance to maintain flux levels.

Another method of controlling flux levels is by changing the pulse rate of the laser, which can operate to a maximum frequency of 7Hz. It has been shown that the time-averaged AO flux changes linearly with the repetition rate [15].

The ATOX is capable of producing high levels of neutral AO flux at LEO energies. However, ATOX does have some limitations:

The pulsed nature of the AO beam is not an ideal simulation of the LEO environment. The limitations of the pulsed beam technique are not yet fully understood, however it can be postulated that the pulses of high density AO followed by periods of zero flux (and possibly recovery) could lead to different equilibrium conditions of the exposed materials [39, 44].

Neutral AO is not the only species to which the samples under test are exposed. There remains a small amount of excited molecular oxygen and possibly oxygen ions and electrons. Perhaps most significantly, one side effect of producing fast atomic oxygen in the way described is that significant amounts of ultra-violet (UV) and vacuum ultra-violet (VUV) radiation are also produced, due to the high plasma temperature. Although UV does exist in LEO, its proportions with respect to AO differ from those of ground-based simulators, which are several orders of magnitude higher [151]. Therefore, the effects of UV degradation must also be considered.

## 6.3 AO Calibration

An important part of developing accurate sensors is the methods used to calibrate them. Ideally, a calibrating device should have a greater sensitivity to AO than the sensors being developed, to maximize the precision and accuracy. Kapton witness samples (KWS) were the main method of calibration used here. The type of Kapton used was Kapton-HN, which has an assumed constant erosion yield of $3x10^{-24}cm^{-3}atom^{-1}$. This value is approximately twice the currently accepted maximum erosion yield of carbon and approximately the same as a-C:H. It should be noted that Kapton-HN is the replacement material of the now obsolete Kapton-H (used in early experiments) and has an erosion yield 93.7% of Kapton-H [152].

A minimum of three samples were placed in the sample tray of ATOX and the mass of each was recorded in a humidity-controlled environment in air, before and after AO exposure. Using the erosion yield of $3x10^{-24}cm^{3}atom^{-1}$, fluence of the exposure was then calculated and averaged.

To complement the KWS a single carbon coated quartz crystal microbalance (CQCM) was used to measure fluence in-situ. A limitation of the KWS technique used here is that it cannot measure fluence in-situ. In-situ methods are useful if a parameter, such as temperature or flux is varied during the exposure, so that the effect of their change can be recorded. Table 14 gives details of the QCM used.

| **Type** | Stablix A 02 |
|---|---|
| **Nominal Output Frequency** | 11 MHz |
| **Mass Sensitivity** | -255Hz/µg/cm$^2$ |
| **Operating Temperature** | 0-70°C |
| **Nominal Power Requirement** | 0.2W |
| **Mass** | 3.5g |
| **Coating** | 2µm Magnetron Sputtered Amorphous Carbon |

**Table 14: CQCM specification**

As stated previously, it is possible that changes in temperature can also lead to a change in resistance measurements, which may lead to inaccurate AO flux estimates. The temperature compensation technique detailed in Chapter 5 was therefore used to isolate AO effects. Two of the four sensors on each substrate were covered with an alumina plate of 0.6mm thickness to prevent AO exposure. Figure 31 shows the general layout of the substrates, KWS and QCM used for the exposures.

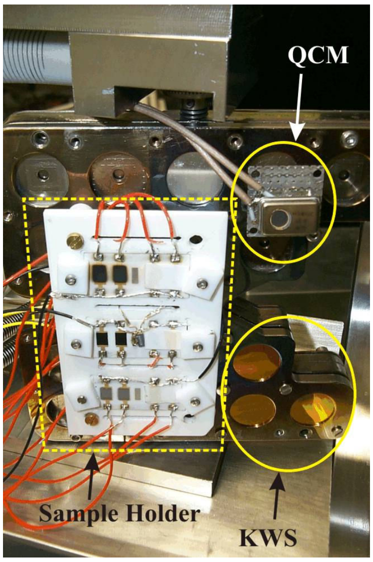

**Figure 31: Samples in ATOX before closure and pump down**

## 6.4 The Sample Holder

The substrates used for carbon sensor deposition are dimensionally identical to those used by Osborne [52], so the same jig (or sample holder) designed and manufactured by Osborne was used to hold substrates in these experiments.

The sample holder is designed to hold three sensor substrates, with a 1cm elevation in order to maintain tidy wiring to the vacuum feed through lines. The holder is fabricated from a machinable glass ceramic (MACOR) that is highly resistant to AO attack and is also vacuum compatible, even at high temperatures under the influence of UV irradiation.

## 6.5 Data Acquisition System

The ATOX facility also includes a data acquisition system. A PC controls a switch unit via a LabVIEW ™ based programme. The switch unit can be configured with up to 12 separate input channels and is essentially no more than a relay-based multiplexer. The output from the switch unit can be directed either to a Hewlett Packard Digital Multimeter (DMM), or to a frequency counter manufactured by the same company.

When the computer commands the switch unit to send a particular input to the measurement device, it also instructs either the frequency counter or the DMM to take a measurement. In the case of the DMM, the measurement may either be a resistance, voltage or current. The frequency counter is used to interpret the CQCM signal. Communication between the computer, the switch unit, the DMM and the frequency counter is through HPIB cables and protocols.

## 6.6 AO Exposures

### *6.6.1 Exposure Session 1*

AO simulator use was restricted by time constraints, so it was necessary to test the widest variety of sensors in as few exposures as possible. ES1 consisted of 4 individual runs as outlined by Table 15. The results from this exposure session had to be used to select an appropriate material for the ISS flight. Therefore, to assess the maximum erosion rate of the material temperatures were elevated up to 76°C. Details of the temperature conditions are given in Table 16.

| **Exposure Run No.** | **Exposure Session** | **Nozzle to Sample Tray Distance (cm)** | **Kapton Witness Sample Mass Losses (mg)** | **Average Witness Sample Fluence (x$10^{19}$ atoms/cm$^2$)** | **Time of Run (minutes)** |
|---|---|---|---|---|---|
| 1 | ES1 | 55 | 1.11, 1.13, 1.09 | 7.9 | 360 |
| 2 | ES1 | 55 | 0.58, 0.56, 0.51 | 3.9 | 330 |
| 3 | ES1 | 55 | 1.23, 1,23, 1.16, 1.14 | 8.8 | 688 |
| 4 | ES1 | 55→65→55 | 0.05, 0.06, 0.06 | 0.5 | 185 |
| 5 | ES2 | 55 | 0.22, 0.20, 0.14 | 0.85 | 145 |
| 6 | ES2 | 55 | 0.10, 0.94, 0.68 | 6.93 | 507 |

**Table 15: Atomic oxygen exposure data**

| **Run Number** | **Temperature Setting (°C)** | **Elapsed Time of Setting (min)** | **Average Sample Temperature (°C)** |
|---|---|---|---|
| 1 | 76<br>53<br>24 | 0<br>50<br>200 | 44.6 |
| 2 | 65 | 0 | 65 |
| 3 | 25<br>70<br>49 | 0<br>218<br>502 | 49.7 |
| 4 | 25 | 0 | 25 |

**Table 16: Temperature settings for first exposure session**

The ATOX facility produced an unusually high AO flux for run 1 and over the course of the exposures the AO flux decreased. Figure 32 shows the decay of observed average AO flux over ES1 time. Flux was determined by dividing the Kapton witness sample fluence by the exposure time. Zero minutes indicate the commencement of run 1.

A C-QCM reading taken mid-way through exposure run 1 (interval 1 in Figure 32) suggests that the average flux reduced with time, and fell to about 80% of its initial value after a fluence of approximately 4.8x$10^{19}$ atoms/cm$^2$ (as calibrated against the Kapton witness samples). The reduction in flux was also apparent from the observation of plasma glow intensity from the ATOX nozzle.

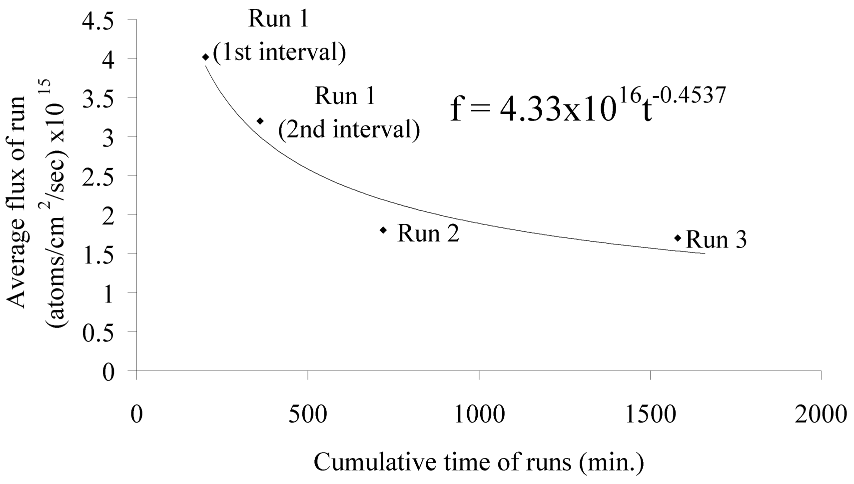

**Figure 32: ATOX facility flux decay over ES1**

A line of best fit is made to indicate the level of average flux decay over the course of the exposure session. By assuming that the flux decay is continuous between runs, it will be possible to plot the resistance measurements from the sensors versus the fluence of the run. Of course by assuming that the flux decay is continuous, there is no guarantee that plotted fluence will be a true value, but it will help assess whether or not the sensor is responding to a change in flux.

The curve fit from Figure 32 shows that:

$$flux = 4.33 \times 10^{16} t_{cum}^{-0.4537} \qquad \textbf{Equation 31}$$

where $t_{cum}$ is the *cumulative time of the exposure session*. Expressing $t_{cum}$ in seconds this converts to:

$$flux = 4.33 \times 10^{16} \left( \frac{t_{cum}}{60} \right)^{-0.4537} = 2.78 \times 10^{17} t_{cum}^{-0.4537} \qquad \textbf{Equation 32}$$

Integrating this expression gives:

$$fluence = 5.08 \times 10^{17} t_{cum}^{0.5463} + const$$ **Equation 33**

Using the above equation and subtracting the fluence from previous runs will determine the fluence accumulated over a run of interest. This new fluence value shall then be plotted against the sensor resistance measurements.

From the first exposure it was learned that the screen-printed and sputtered films had an apparent high oxidation resistance relative to the evaporated films. These observations were considered in the design of the third and fourth exposures.

The third exposure tested only screen-printed sensors and the duration of the exposure was increased to provide a greater fluence. Additionally, the screen printed substrate exposed during the first run (substrate 02-01) was re-exposed, but with the sensors covered in such a way that one sensor was fresh before exposure and another exposed to the full fluence of the first run (Figure 33). After exposure to run three this substrate had four sensors each exposed to different fluence levels to ensure a fluence dependent characterisation could be carried out.

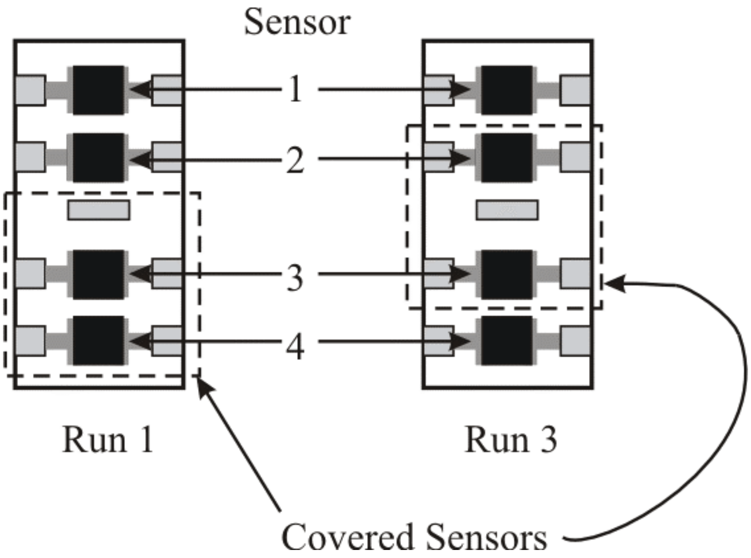

**Figure 33: Sensor masking regime of coupon 02-01 for each AO exposure**

During the course of the 1st and 2nd exposure runs, both evaporated films completely eroded, which did not leave any material for subsequent characterisation. The fourth run was designed to have relatively low fluence to provide some degree of characterisation for this type of film. The sample tray was also moved to understand any potential response to AO flux.

### *6.6.2 Exposure Session 2*

The purpose of this exposure session was to expose a variety of films, from all deposition sessions, to an AO environment at constant (room) temperature. This was done so that more reliable erosion rate estimates could be made. The temperatures of the samples were kept at ambient (25°C) for all the exposures.

The first run of this session (run 5) tested a wide range of sensitive or potentially sensitive sensors. An evaporated substrate from DS1, a sputtered substrate and an evaporated substrate from DS2 were exposed to a low AO fluence to ensure sufficient material remained for subsequent characterisation. Identical samples deposited onto a smooth $SiO_2$ substrate were also exposed to provide a better measure of thickness changes, but they were not electrically connected to the data acquisition system.

One sensor from the evaporated substrate of DS1 had a magnesium fluoride cover to prevent AO attack, but allowing UV penetration (>90% transmissivity for 200-6500nm). This test helped assess the AO-UV synergy effects on the film reactively as well as checking for actinometer UV sensitivity.

The second run of the session, run 6, was originally designed to be a high fluence experiment that would induce a greater resistance change in the more durable sensors. Unfortunately, a problem with the vacuum system meant that only a relatively short exposure run could be completed. Run 6 exposed sputtered sensors from DS1 and DS2, a screen-printed sensor and a thick evaporated sensor from DS2.

### *6.6.3 Plasma Asher*

As part of another study, two screen-printed substrates were exposed to a plasma asher environment [28]. The study assessed the response of screen-printed films through to the end of life condition. The two substrates were placed inside a low temperature, inductively coupled radio frequency (RF) plasma asher. The asher operated at 13.56 MHz, with an RF power of 200W and an oxygen pressure of 100mTorr ±5%. Kapton HN was used to calibrate the oxygen plasma fluence, which measured ~$4.8 \times 10^{20}$ atoms/cm$^2$ by the end of the exposure run.

# 7 FILM CHARACTERISATION

## 7.1 Introduction

The literature review has highlighted that there are many forms of carbon, based on $sp^2/sp^3$ content, disorder and hydrogenation. As well as calibrating sensors, it is therefore important to know precisely what sort of carbon is being tested. This is only possible by selecting appropriate characterisation methods for the material. Appendix A2 gives a summary of the potential techniques that can detect the various aspects of carbon in combination with other techniques or by themselves.

This chapter selects the appropriate characterisation methods for this study, before describing the equipment used. The understanding of Raman spectroscopy has seen significant development over recent years, so sections have been included that describe the interpretation of the data obtained [23-27, 153-163].

## 7.2 Technique Selection

The key characterisation requirements are to measure $sp^3$ content, disorder, hydrogenation and other elemental content of the films, as these are the factors that define the type of carbon. Additional characterisation requirements are to observe how the surface morphology of the films changes with AO exposure.

A combination of visible and UV Raman spectroscopy was chosen as the principal characterisation method because together they can assess $sp^3$ content, disorder and hydrogenation, as well as detect other bonding regimes that may be present. To support the Raman spectroscopy, a combination of scanning electron microscopy (SEM) and energy dispersive X-ray spectroscopy (EDS or EDX) was used. The SEM provides a means of assessing topological changes, whilst EDS helps detect non-carbon elements, other than hydrogen (and elements of a lower mass than beryllium), that may exist in the film.

An important consideration in technique selection is the depth of the analysis. Many studies investigating the reactions of AO with spacecraft materials have used techniques that can only penetrate the 'top surface' layer of the material, such as X-Ray Photoelectron Spectroscopy (XPS) or Scanning Tunnelling Microscopy (STM) [70, 164]. One reason for this is that most of the reactions are believed to occur at the surface of the material.

This study differs from others because film resistivity is also an important consideration in the design of an actinometer, which is mostly influenced by the bulk properties of the material. Raman spectroscopy appears to be a very useful technique, as it can characterise many of the aspects of interest throughout the bulk thickness [23, 26, 165, 166]. Whilst it is difficult to comment on precise interrogation depths, especially when the properties of the sample of interest are unknown, Raman spectroscopy generally has deeper interrogation depths than other contemporary techniques (Appendix A2).

## 7.3 Raman Spectroscopy Theory

When monochromatic radiation of frequency $f_0$ is incident on a surface some of the energy is absorbed, some may be transmitted and a small amount is scattered. Most of this scattered light is at the same frequency as the incident radiation (elastic or Raleigh scattering) whilst a very small amount (typically $10^{-3}$ to $10^{-4}$ of the Raleigh intensity) is scattered at a frequency higher or lower than that of the incident radiation. This is called inelastic or Raman scattering.

A classical explanation of Raman scattering is based on the polarisability $\alpha$ of molecules [167]. Consider a molecule placed in an electric field. In this situation the electron cloud will be displaced relative to the nuclear framework. This distortion, or polarisation, produces an induced dipole moment. The magnitude and direction of this moment varies in accordance with:

$$\mu = \alpha . E$$ **Equation 34**

where $\alpha$ is the polarisability, $\mu$ is the induced electric moment and E is the electric field in which the molecule is placed. $\mu$ and E are vectors and $\alpha$ is a second order tensor, so the above equation can be expanded as:

$$\mu_x = \alpha_{xx} E_x + \alpha_{xy} E_y + \alpha_{xz} E_z$$ **Equation 35**

$$\mu_y = \alpha_{yx} E_x + \alpha_{yy} E_y + \alpha_{yz} E_z$$ **Equation 36**

$$\mu_z = \alpha_{zx} E_x + \alpha_{zy} E_y + \alpha_{zz} E_z$$ **Equation 37**

where (x,y,z) are the axes of a coordinate system fixed in the molecule.

In order to understand the concept of polarisability, it may be helpful to recall that the units of polarisability are volume units. Thus the magnitude of polarisability is related to the volume of the “bag of loose electrons” which are free to move or to be polarised. The greater the volume of “loose” electrons, the greater the polarisability and hence the more the molecule can contribute to the scattering process.

It is useful to develop this theory by placing the same molecule in the oscillating field of a monochromatic light beam. If the light is of a frequency $f_0$, we may express the associated electric field as:

$$E = E_0 \sin(2\pi f_0 t)$$ **Equation 38**

and so the induced electric moment is:

$$\mu = \alpha E_0 \sin(2\pi f_0 t)$$ **Equation 39**

This oscillating induced dipole can now radiate electromagnetic radiation of frequency $f_0$ (Raleigh scattering).

However, if some internal changes take place during this process (i.e. the molecule vibrates or rotates as a consequence of light excitation) the polarisability periodically changes and the oscillation of the induced dipole has vibrational oscillations superposed upon it (i.e. a frequency modulation effect occurs).

Consider an internal vibration (or energy level, E=hf) with frequency $f_{vib}$, where $f_{vib}<f_0$, then:

$$\alpha = \alpha_0 + \alpha_1 \sin(2\pi f_{vib} t)$$ **Equation 40**

where $\alpha_0$ is the equilibrium polarisability and $\alpha_1$ is the rate of change of polarisability with the vibration. Equation 32 becomes:

$$\mu = \alpha E = [\alpha_0 + \alpha_1 \sin(2\pi f_{vib} t)] E_0 \sin(2\pi f_0 t)$$ **Equation 41**

and can be rearranged as:

$$\mu = \alpha_0 E_0 \sin(2\pi f_0 t) + \frac{1}{2}\alpha_1 E_0 [\cos(2\pi(f_0 - f_{vib})t) - \cos(2\pi(f_0 + f_{vib})t)]$$

**Equation 42**

Hence the induced oscillating dipole, and the scattered radiation has three components: ($f_0$-$f_{vib}$) called the Stokes scatter, ($f_0$+$f_{vib}$) called the Anti-Stokes scatter and the exciting (Elastic/Raleigh) frequency $f_0$.

A photon of energy $hf_0$ colliding with a molecule can either be scattered elastically or inelastically. In the latter case, the collision with the photons induces the molecule to undergo a transition between two vibrational energy levels of the molecule and the resulting scattered radiation has a different frequency than the incident photon. If during the collision, the molecule gains some energy $hf_{vib}$, the photon will be scattered at the frequency $f_0$-$f_{vib}$ (Stokes). Conversely, if the molecule loses some energy by relaxing from an excited vibrational level to the ground state, then the scattered frequency will be at $f_0+f_{vib}$ (Anti-Stokes).

Individual molecular bonds will have a particular scattered radiation frequency. Whilst many of the same molecular bonds will have nominally the same scatter, variations such as bond length and angle will alter the polarisability and produce a different spectral response.

## 7.4 Curve Fitting

Once a raw spectrum is obtained a number of statistical curves are used to collectively produce a data fit. Each curve will correspond to a particular bonding regime. There is a certain degree of trial and error in the curve fitting process. First a predetermined number of statistical curves and their approximate positions are assigned to the spectra. Then the location, height, width and shape of each assigned curve are iteratively calculated to produce a best fit to the spectrum. If this does not appear to be a close enough fit, the process is repeated with either a different number of curves or a new location and/or height. The curve fitting process was carried out using the Renishaw WiRE™ 2.0 curve fit tool that used a composite curve of Lorentzian and Gaussians.

## 7.5 Raman Spectral Features

### *7.5.1 Peak identification*

A summary of the major carbon peaks and their spectral position is given in Table 17.

| **Peak I.D.** | **Approximate Position in UV (cm-1)** | **Assignment** |
|---|---|---|
| G-peak | 1580-1630 | $Sp^2$ stretch |
| D-peak | 1380-1450 | $Sp^2$ ring breathing |
| T Peak | 960-1100 | Amorphous $sp^3$ stretch |
| Diamond peak | 1332 | Crystalline $sp^3$ |

**Table 17: Raman peak assignments for carbon**

Irrespective of excitation frequency pure, single crystal diamond has a single Raman mode at 1332cm$^{-1}$, whilst single crystal graphite has a single mode at 1580cm$^{-1}$. The former peak is labeled the diamond peak and the latter the G-peak. These are stretching vibrational modes. The $\pi$ bonds in sp$^2$ carbon lie at a lower energy than $\sigma$ bonds and are therefore more polarisable by an excitation laser. This means that sp$^2$ bonds produce a much stronger (x50-230) Raman signal than that produced by sp$^3$ bonding. The result is that composite sp$^2$/sp$^3$ systems have very weak and sometimes untraceable diamond peaks. Increasing the laser excitation frequency (and hence energy) to UV levels is known to reduce this disproportionate effect, enabling reliable quantification of sp$^3$ content [27, 159].

Sp$^3$ content in UV excited spectra is determined by the T-peak, which typically occurs between 960cm$^{-1}$ and 1100cm$^{-1}$ [26]. To quantify the levels of sp$^3$, the ratio of G-peak and T-peak intensities are compared with other experiments, most notably the work of Adamopoulos [159].

Figure 34 shows how the sp$^3$ content in a-C films increases with the ratio of intensities of the T and G-peak ($I_T/I_G$). The trend is most useful for intermediate sp$^3$ content, such as ta-C films because it cannot quantify sp$^3$ levels below 20at.% (as there is no available data), or above 80at.% where there is a significant degree of scatter.

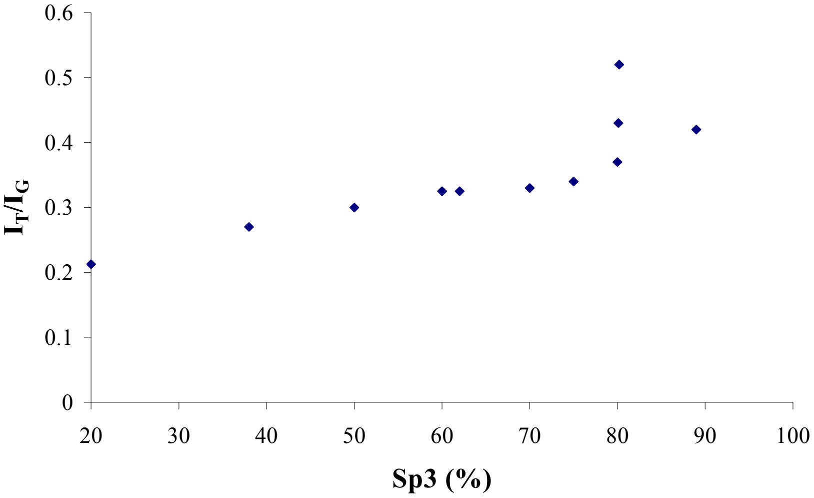

**Figure 34: $I_T/I_G$ variation with sp3 content[27]**

As carbon films become more disordered by multi-crystallinity, a peak in the range of 1350-1450cm$^{-1}$ emerges. This peak is the result of a carbon ring-breathing mode, as shown in Figure 35. This peak does not occur in single crystal HOPG because the outer rings, not excited by the laser, constrain the structure. As a result this peak is often referred to as the D-peak, where D is for 'disorder'. The position of the D-peak typically increases with excitation frequency [154, 157].

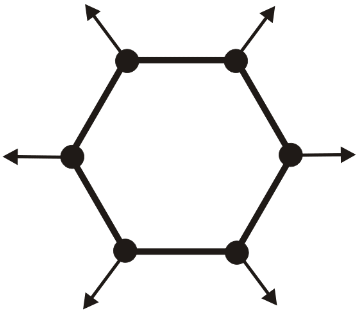

**Figure 35: D-peak breathing mode**

Figure 36 shows how the D-peak and the G-peak vary with excitation wavelength for a microcrystalline graphite sample. The trends shown are valid for graphite and glassy carbon. The D-peak trend is also the same in a-Cs [26, 158, 168, 169].

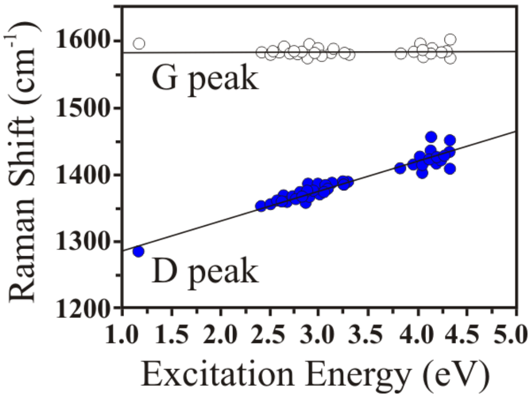

**Figure 36: Variation of the D and G-peaks with excitation energy[161]**

### *7.5.2 Detection of Disorder*

Raman spectroscopy was chosen partly for its ability to characterise disorder. An important aspect to remember is that it is rare to have a fully amorphous system. In carbon materials it is more usual to have islands of crystalline-like material (called clusters) surrounded by a more amorphous network [120].

As clusters become more dispersed throughout the analysed area, the spectral features will widen to form a statistical distribution centred on the modal frequencies. Therefore the width of a fitted curve will help determine the levels of this dispersal [105]. In visibly excited systems, if the full width half maximum (FWHM) of the peak equals or exceeds 50cm$^{-1}$, the material is considered to be amorphous; this is where the in-plane correlation length, La (which correlates to cluster size) is approximately 20Å [170]. In the amorphous condition, the ratio of D-peak and G-peak intensity $I_D/I_G$ is known to vary proportionally to the square of La, as shown in Figure 37 [105].

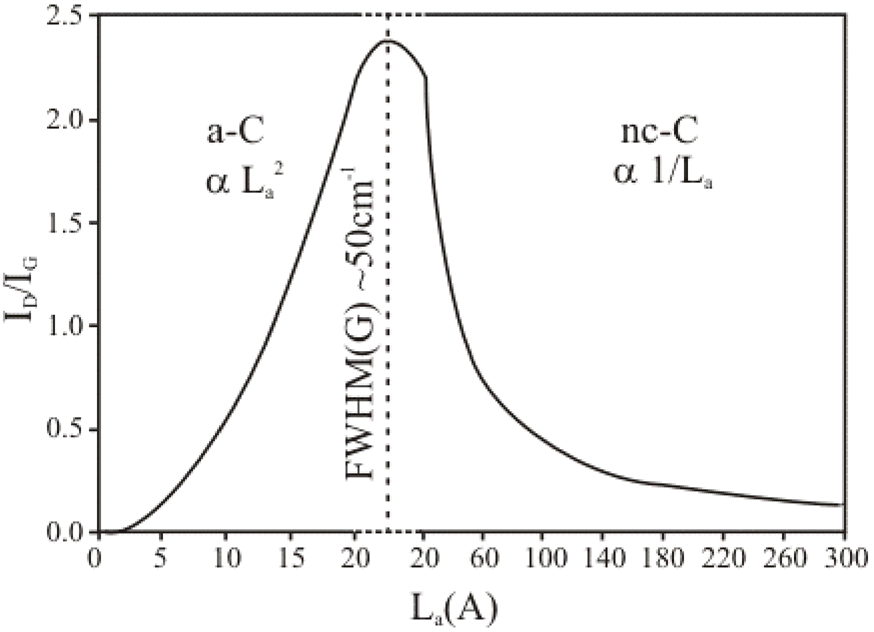

**Figure 37: $I_D/I_G$ variation with in-plane correlation length, La [105].**

Further to this trend, the position of the G-peak shifts within 3 defined stages of increasing disorder, as defined by Ferrari [26, 154, 157]. The three stages are:

2. Perfect HOPG to nC graphite. The G position increases from 1580cm$^{-1}$ to 1600cm$^{-1}$, within this range.
3. nC graphite to predominantly sp$^2$ a-C. Here the G-peak begins to fall from 1600cm$^{-1}$, down towards 1520cm$^{-1}$.
4. sp$^2$ a-C to predominantly sp$^3$ a-C. Greater sp$^3$ content shortens bond length and so increases the position of the G-peak.

This type of analysis has been applied successfully to only visibly excited spectra so far. Therefore to accurately determine both the sp$^3$ content and the levels of disorder, both visible and UV excitation lasers must be used.

### *7.5.3 Detection of Hydrogen*

A recent development in the analysis of visibly excited carbon Raman spectra is the quantification of hydrogen content [23-25, 171]. When a material is optically excited to create electron-hole pairs, these can either recombine radiatively with the emission of light as photoluminescence (PL) or non-radiatively to give lattice vibrations (phonons) and heat. A typical signature of hydrogenated samples in visible Raman spectra is the increasing PL background as hydrogen content increases.

The ratio between the slope *m* of the fitted linear background and the intensity of the G-peak, m/I(G), can empirically measure the bonded hydrogen content by Equation 40 [23, 24] for 20%<H [at%]<45%. This relationship has been utilised on PVD/CVD thin film depositions with different levels of sp$^3$ content, but has not been used on polymeric/carbon composites.

$$H[at\%] = 21.7 + 16.6\log\left\{\frac{m}{I(G)}[\mu m]\right\} \qquad \textbf{Equation 43}$$

For hydrogen contents over 40-45 %, the PL background obscures the Raman signal and the method is no longer valid [24].

## 7.6 Characterisation Equipment

### *7.6.1 Raman*

Two different UV Raman systems and one visible system were used. The first UV system was a home built facility developed by Pennsylvania State University (PSU), whilst the remaining systems are commercial Renishaw inVia products (Figure 38).

**Figure 38: The Renishaw inVia Raman spectrometer**

The PSU home built facility consisted of a single stage model 1400 SPEX spectrometer equipped with a Princeton Instruments Model 1340-PB back thinned CCD detector. A Coherent Innova 300 FreD frequency doubled argon ion laser was used for excitation at 257nm (4.82eV). After passing through a Pellin-Broca prism and spatial filter, the laser light was focussed at an angle of 35° through a cylindrical lens, which created a laser line approximately 1mm x 15µm. The scatted light was collected with a Coherent Ealing 0.5NA 15x reflecting objective. The Rayleigh scattered light was rejected by a pair of Omega Optical dielectric edge filters. As the investigations were primarily focussed on the analysis of carbon films, the range of analysis covered was fixed to 0-2000cm$^{-1}$.

To obtain wider spectral ranges the Renishaw systems were used. Both the visible and UV systems are essentially the same with the exception of the excitation laser. The UV systems employed the same laser as the PSU home built system, whilst the visible system used a Renishaw 514nm green laser.

#### 7.6.1.1 Control Samples

Taking spectra of control samples allows a good assessment of sample purity and an indication of measurement error. The control samples used here are HOPG graphite and CVD diamond. CVD diamond is commonly polycrystalline and generally of a low purity when compared with natural diamond, but budget restraints has meant a natural diamond sample was not practical for this study.

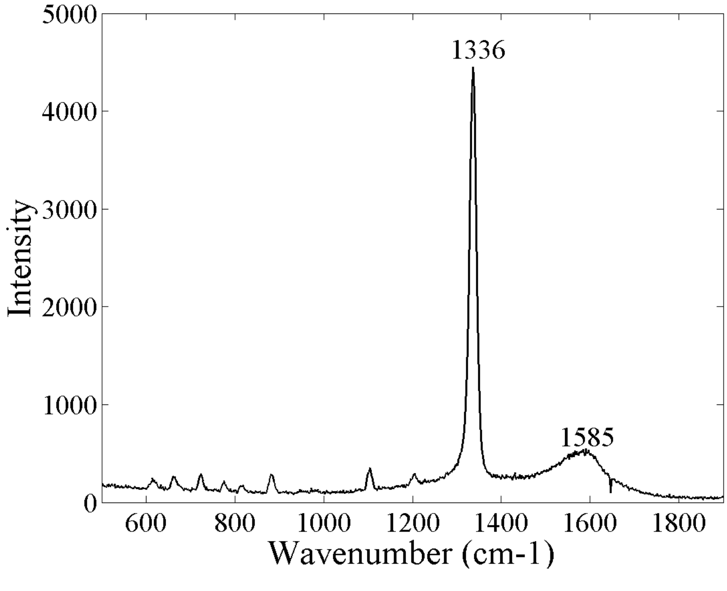

**Figure 39: Raman spectrum of polycrystalline diamond reference**

Figure 39 shows the UV Raman spectrum of a CVD diamond reference film. The diamond peak can clearly be seen at 1336cm$^{-1}$, whilst a broad G-peak can also be seen at 1585cm$^{-1}$. It is commonly known that the diamond peak is found at 1332cm$^{-1}$ and the G-peak at 1580cm$^{-1}$. It can be seen here that a shift of approximately 5cm$^{-1}$ is possible from the ideal case.

The strong and narrow diamond peak indicates a predominantly crystalline $sp^3$ content with small amounts of $sp^2$. There is little sign of a D-peak, suggesting that most of the $sp^2$ is fully amorphous. The broadness of the G-peak suggests that the $sp^2$ content is well dispersed. Many authors that have analysed these films have suggested that the $sp^2$ content is found at the grain boundaries of the $sp^3$ crystals [135, 172-174].

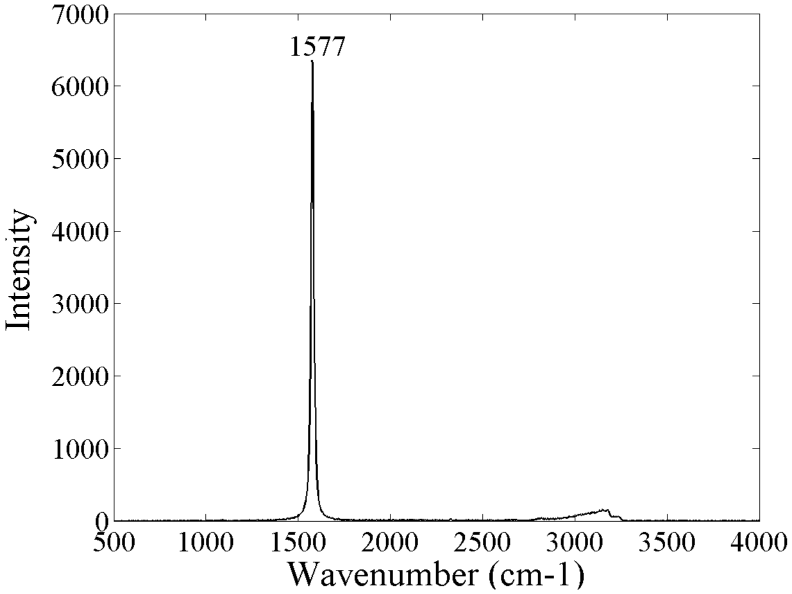

**Figure 40: Raman spectrum of HOPG reference**

Figure 40 shows a UV Raman spectrum from a HOPG sample. Pure HOPG spectra should have only one peak (the G-peak) at around $1580cm^{-1}$ and it can be seen that the calibration sample is very close to this ideal, but a shift of $-3cm^{-1}$ has occurred [175].

The sampling range has been extended to $4000cm^{-1}$ to show the presence of weak features around $3100cm^{-1}$ that indicate the presence of some hydrogen bonding [176]. The hydrogen bonding is a possible side effect of the deposition process used to fabricate the sample, as this may involve cracking methane [106]. The hydrogen quantities must be very small, as the rest of the spectrum is that of pure HOPG with insufficient defects for bonding to other elements. This result demonstrates the difficulty in completely avoiding hydrogenation, given this is supposed to be an ideal sample.

An important consideration in the interpretation of the Raman spectra is the contribution from the underlying substrate. Raman spectroscopy is known to have an analysis depth of the order of a few microns (Appendix A2) and given that the carbon film thicknesses are similar to the Raman analysis depth, there is a possibility that the substrate could be interrogated as well as the carbon. Figure 41 shows a typical Raman spectrum of an alumina sample. It can be seen that there are 6 distinct peaks, with the most dominant peak occurring at 395cm$^{-1}$. These signature signals can then be removed from the spectrum should they be detected.

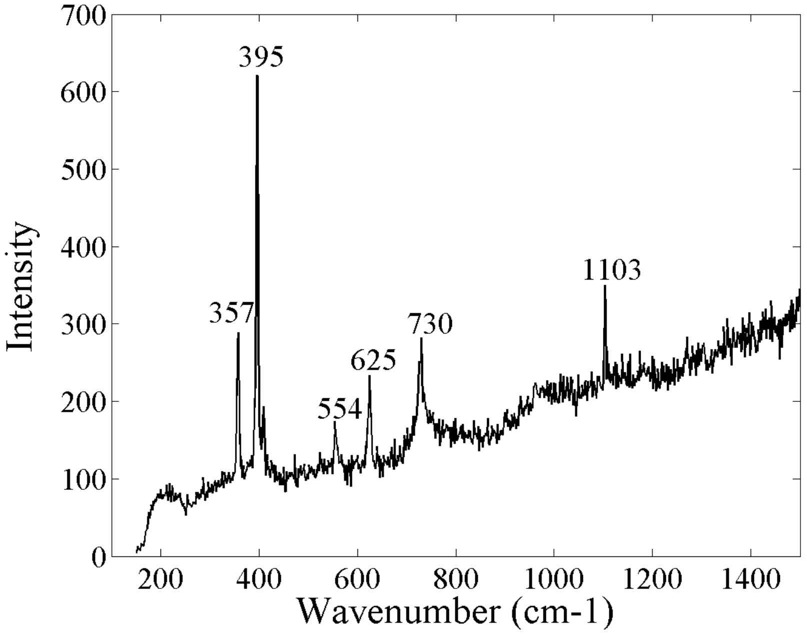

**Figure 41: Alumina Raman spectrum**

### *7.6.2 SEM and EDS*

SEM and EDS work was carried out on a JOEL FEG SEM 6500F with an integrated Inca Energy 300 system, manufactured by Oxford Instruments. Most SEM imaging was undertaken with beam energies of 5keV or less to minimise beam induced heating and subsequent damage of the sample. Once SEM imaging of a sample was complete, electron beam energies were increased to values of 15KeV for EDS analysis. These higher energy levels are a requirement for reliable EDS data. Whilst the higher energies increase the possibility of sample damage post imaging, the elemental content should not change.

### *7.6.3 Damage Prevention*

It is known that high beam energies and intensities can damage the material being analysed, either by mechanical bombardment forces or heating effects [177]. Since a variety of characterisation techniques were to be used, it is important to define a sequence of analysis so that the changes induced by one technique are not detected by another. Films were characterised in order of the beam energies used, as shown in Table 18.

| **Characterisation Method** | **Typical Electron/Photon Energies** |
|---|---|
| Raman | <5eV |
| FEG-SEM | 1-10keV |
| EDS | 10-15keV |

**Table 18: Order of characterisation beam energies**

Unfortunately, even UV Raman is known to damage some materials in the region of analysis, which could potentially affect AO response. All films were analysed post-exposure to prevent this problem. Pre-exposure characterisation was carried out by analysing covered portions of the film material.

# 8 EVAPORATED FILM RESULTS

## 8.1 Fabrication

E-beam evaporation was carried out using an Airco Temescal VES-2550 evaporator and CV14-A electron gun, coupled to a CTI Cryotorr 8 cryopump. The deposition thickness is very uniform throughout the chamber and is measured in-situ using a QCM. Two different settings were used to produce two different deposition rates and thicknesses.

Studies of evaporated carbon films suggest they undergo a graphitisation and densification process when annealed [146]. To investigate this effect on AO erosion properties a sample of the thinner carbon films were heat treated to 700 °C for 15minutes, as prescribed by Besold [146]. Post treatment, measurements of electrical conductivity increased by 2 orders of magnitude, as shown in Table 19.

| **Deposition Parameters** | **Annealing** | **Substrate** | **Average Sensor Initial Thickness, $\tau_o$ ($\mu$m)** | **Conductivity ($\Omega^{-1}.m^{-1}$) @ 25°C** |
|---|---|---|---|---|
| 5kV accelerating voltage at 300mA | None | 41-02 | 0.18 | 196 |
| | | 29-01 | 0.18 | 104 |
| | 15mins. @ 700°C in Argon | 28-01 | 0.18 | 58020 |
| | | 27-01 | 0.18 | 59610 |
| | | 26-03 | 0.18 | 55107 |
| 9kV accelerating voltage at 300mA | None | 201-03 | 0.8 | 330 |
| | | 202-03 | 1.00 | 1600 |

**Table 19: Summary of evaporated depositions**

## 8.2 AO Response

### 8.2.1 *Erosion Yield*

Table 20 summarises the theoretical and measured erosion yields of each evaporated film exposed to AO. In many cases, the films eroded completely before the end of the exposure, so the exposure fluence is estimated from the time when $R_0/R=0$ and the average flux measurement of the run. The only successful post exposure thicknesses measurement shows that the theoretical erosion yield (TEY) overestimates the actual erosion yield. The systematic actinometer error (SAE), described in Chapter 3, shows that the erosion yield is overestimated by approximately 28%. A possible reason for this result is that some material inside the film is not electrically conducting but contributing to the bulk thickness.

The range of erosion yields is very broad. The lowest non-zero yield of $2.66 \times 10^{-25}$ $cm^3$/atom lies below the anticipated yield of carbon, whilst the yield of $21.17 \times 10^{-25}$ $cm^3$/atom lies above the anticipated range. Characterisation of these films should help determine what is causing these differences.

| **Substrate** | **Exposure Run No.** | **$R_o/R_{end}$** | **$\tau_{end}/\tau_0$** | **SAE** | **Theoretical Erosion Yield, TEY ($\times 10^{-25}$ $cm^3$/atom)** | **Measured Erosion Yield, Y ($\times 10^{-25}$ $cm^3$/atom)** |
|---|---|---|---|---|---|---|
| 41-02 | 1 | 0 | 0 | - | 2.66 | - |
| 29-01 | 4 | 0.82 | - | - | 6.48 | - |
| 28-01 | 2 | 0 | 0 | - | 15.72 | - |
| 27-01 | 4 | 0.60 | - | - | 14.29 | - |
| 26-03 | 5 | 0 | 0 | - | 21.17 | - |
| 201-03 | 5 | ~1 | 1 | 0% | 0 | 0 |
| 202-03 | 6 | 0.42 | 0.55 | 28% | 8.36 | 6.5 |

**Table 20: Summary of evaporated film erosion yields**

### *8.2.2 Effect of Annealing*

The response from two different sensor substrates is shown together in Figure 42 (with respect to fluence) and Figure 43 (with respect to time). Figure 42 plots an average sensor response, whilst Figure 43 plots the sensor results individually. The differences in lifetime between the annealed and as-deposited films are clearly demonstrated in Figure 42, where the annealed film has an erosion yield nearly 6 times greater than the as-deposited film, assuming the films are the same thickness.

Upon inspection of the results plotted against time, sensor response is not completely linear; it begins with what appears to be a transient ‘settling down’ of sensitivity before a linear second stage, suggesting either the surface of the carbon film is different to the underlying material, or that the AO flux is in a state of decay.

However, the results plotted against fluence show an opposite effect. In the initial stage the rate of change is increasing, therefore suggesting a change in the material.

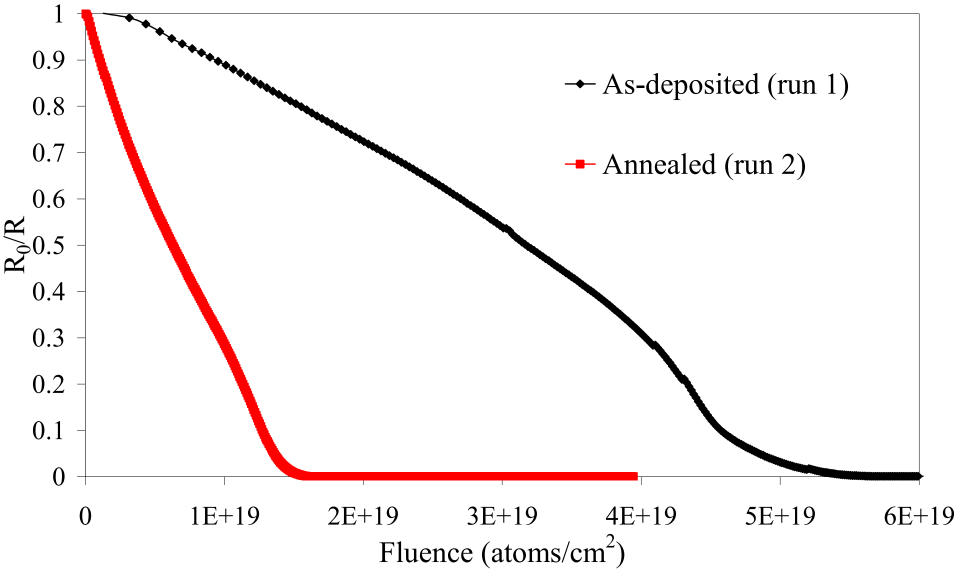

**Figure 42: Evaporated film exposure (versus fluence)**

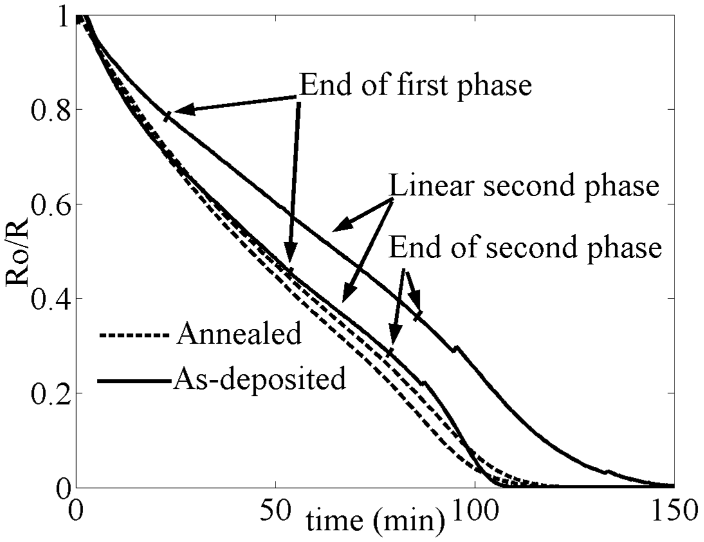

**Figure 43: Evaporated film exposure (runs 1 and 2)**

A third stage is also apparent which again deviates from a linear behaviour. This final stage initiates around Ro/R~0.3→0.4, theoretically equating to a thickness of

54→72nm. This final stage is likely to be the result of increasing resistivity, brought about by the restriction of electron mobility as the film becomes thinner, as discussed in Chapter 3 [17]-[19].

Figure 43 also reveals the variability of the response. For a given Ro/R the time differences between each sensor on the same substrate vary. The as-deposited sensors have a difference that is up to six times that of the annealed sensors.

Comparing the results from runs 1 and 2 with the annealed sensor exposed in run 5, the three-stage response does not appear to exist (Figure 44). The AO exposed sensor appears to have a linear response up to 140 minutes before end effects start to dominate the response, as seen from previous exposures.

Figure 45 highlights the actinometer non-linearity error (ANLE, defined in Chapter 3) of the exposed sensor. The time over which ANLE is calculated is reduced to 140 minutes to omit the final breakdown stage. The error range is ±3.25%, which is significantly greater than the maximum non-linearity error of ±1% from the commercial sensors listed in Table 5.

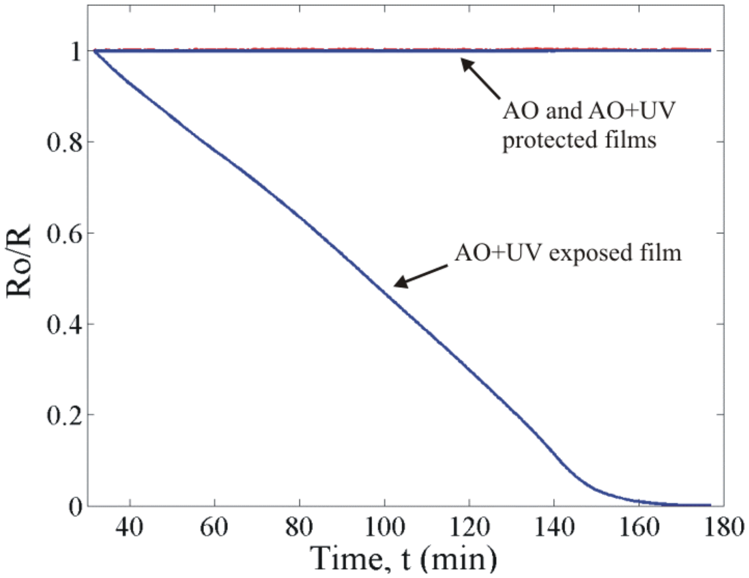

**Figure 44: Evaporated sensor responses to UV and AO+UV (run 5)**

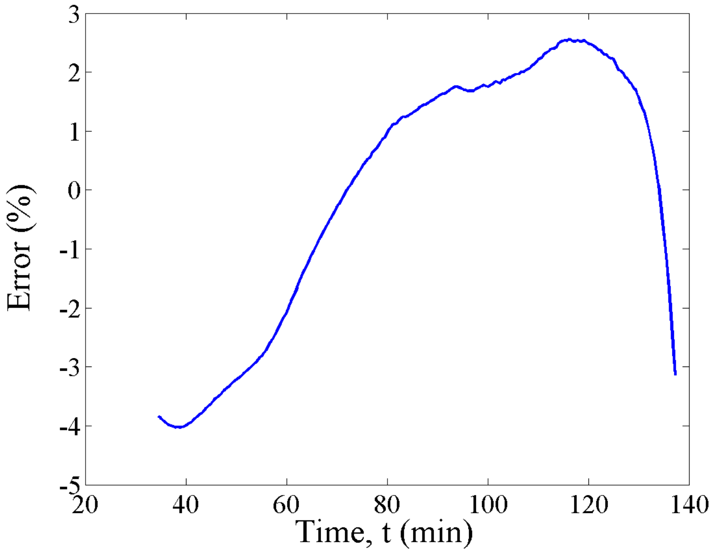

**Figure 45: Evaporated sensor ANLE (run 5)**

### *8.2.3 Effect of UV*

Figure 44 actually shows the normalized resistance of the 3 individual sensors on coupon 26 (an annealed substrate): One sensor was protected from the AO and UV environment generated by ATOX, one protected from the AO but not the UV environment (this coupon was covered with an $MgF_2$ window) and the other exposed to both. The covered sensors are both shown to have the same response, so UV produced by ATOX is not contributing to a resistance change.

### *8.2.4 Effect of Flux*

Flux changes observed by other sensors midway through run 1 (Chapter 10) could not be detected using the evaporated sensors because they had already eroded completely. Filling this knowledge gap, run 4 was principally used to test evaporated sensor sensitivity to changes in flux. Both an as deposited and an annealed sensor were exposed.

During the course of the exposure the sample tray was moved from 55cm, back to 65cm and then forward again to 55cm. Figure 46 shows the normalized resistance of the two evaporated sensors during this run. Indicated are the points when the sample tray was moved. From the results a change in gradient can be seen, suggesting that the evaporated sensors have potential to measure flux.

Moving the sample tray back to 55cm, the gradient is shallower from its original value, meaning either the sensor was detecting the, by then, small AO flux decay or the sensor material was not in a steady erosion regime.

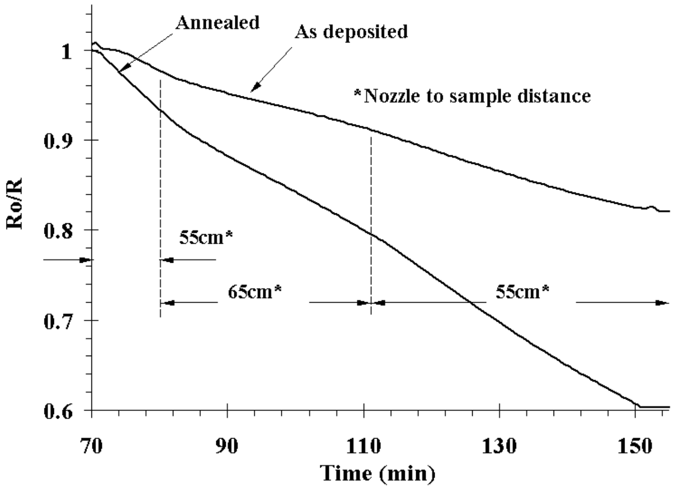

**Figure 46: Evaporated sensor exposures (run 4)**

### 8.2.5 *Effect of Thickness*

Both the coupons of DS2 were approximately 5 times thicker than those fabricated during DS1 and were deposited at a higher rate with no post-deposition annealing. Two very different results were observed. Coupon 201 showed no electrical response to AO, which is thought to be due to contamination, whilst coupon 202 had a decaying response.

Figure 47 shows the response of coupon 202 to be non-linear, thereby creating a relatively large ANLE range of 7% (Figure 48). Chapter 11 will show that the non-linearity of the result could be the result of flux decay during run 6, so the actual ANLE may actually be much smaller than what is shown here.

The response from each sensor is identical, with the gradient of best fits being – 0.0015 min$^{-1}$. The fact that there are no clear discontinuities would also suggest that the erosion-conductivity regime remains the same throughout the thickness eroded here. This means that it should be simple to increase the thickness for increased life.

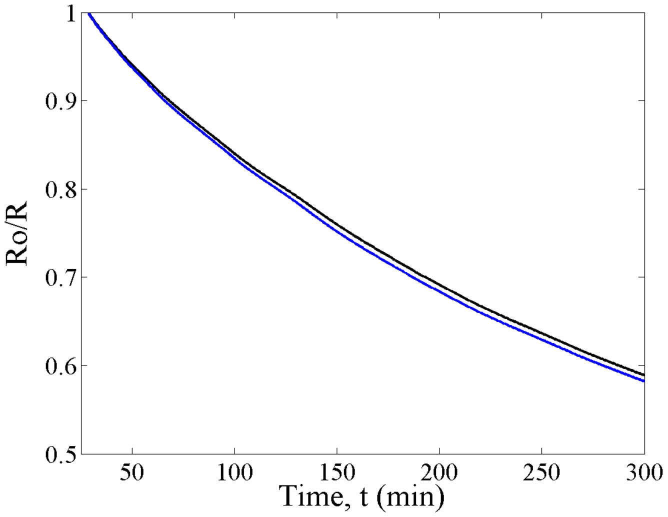

**Figure 47: Evaporated sensor response to AO (Run 6a)**

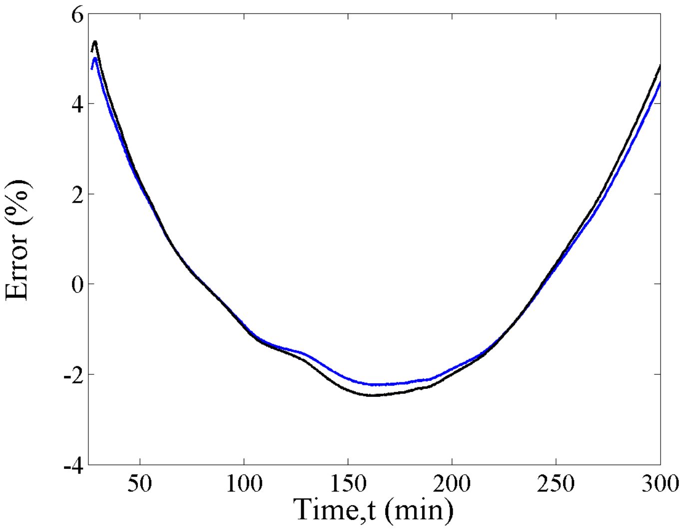

**Figure 48: Evaporated sensor ANLE (run 6a)**

## 8.3 Surface Modification and Bulk Composition

Figure 49 shows that carbon has uniformly coated the underlying alumina substrate. The large grains seen in this figure are from the underlying substrate, whilst the thin carbon layer has conformed to the substrate shape. In most cases, SEM images of the films revealed the carbon material to ablate upon AO exposure. Post exposure (Figure 50), the surface has developed a texture that is common to many different carbon based materials exposed to the same environment, such as the Kapton image shown in Figure 4. One important difference with the texture seen here and Kapton erosion is that the scale of the roughness is much smaller, by at least two orders of magnitude.

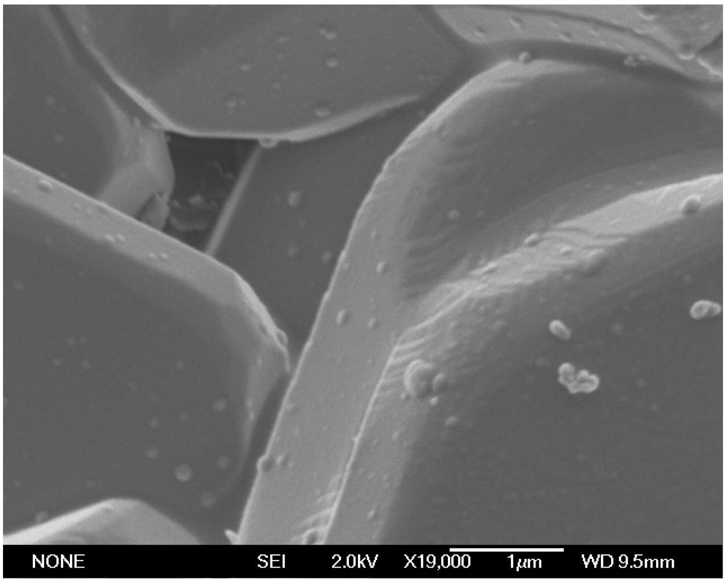

**Figure 49: FEGSEM image of unexposed evaporated sensor**

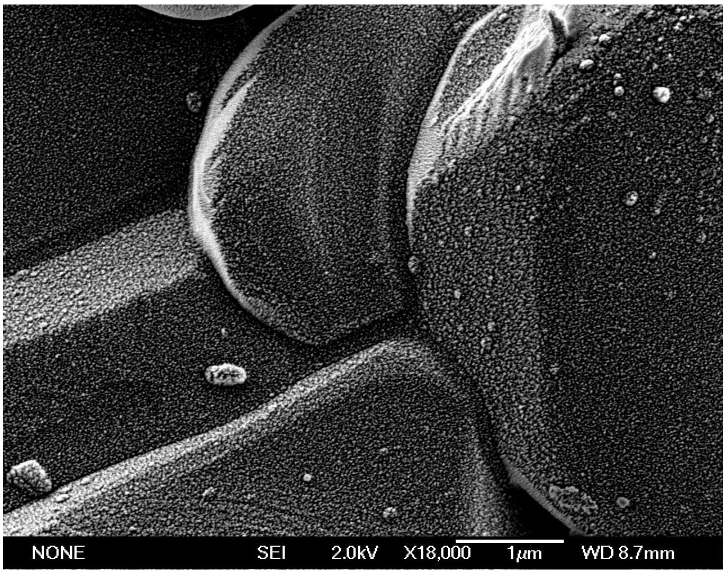

**Figure 50: FEGSEM image of AO exposed evaporated sensor**

When the films had been exposed to sufficient fluence, the films had completely eroded, except in particular protected areas. FEGSEM images of the eroded portion of coupon 26 (Figure 51) reveal that most of the carbon material has eroded away exposing the alumina substrate. Small clusters of carbon are still visible on some surfaces and at substrate grain boundaries.

**Figure 51: SEM image of remaining evaporated carbon exposed to AO**

Coupon 202 also showed signs of AO erosion. Figure 52 shows the SEM image of the unexposed film. Apart from the grains of the underlying alumina substrate, the surface is featureless. It can be seen that the smoother substrate from this coupon has much finer grains than the films of DS1. Post-exposure (Figure 53) the surface has roughened in a similar way to the evaporated films exposed during the first exposure session.

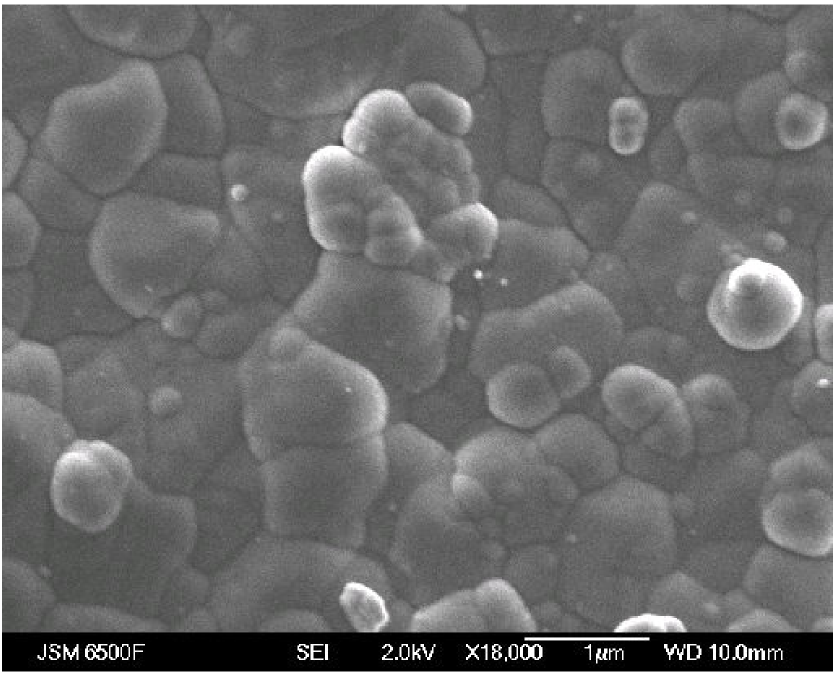

Figure 52: Unexposed evaporated sensor (run 6)

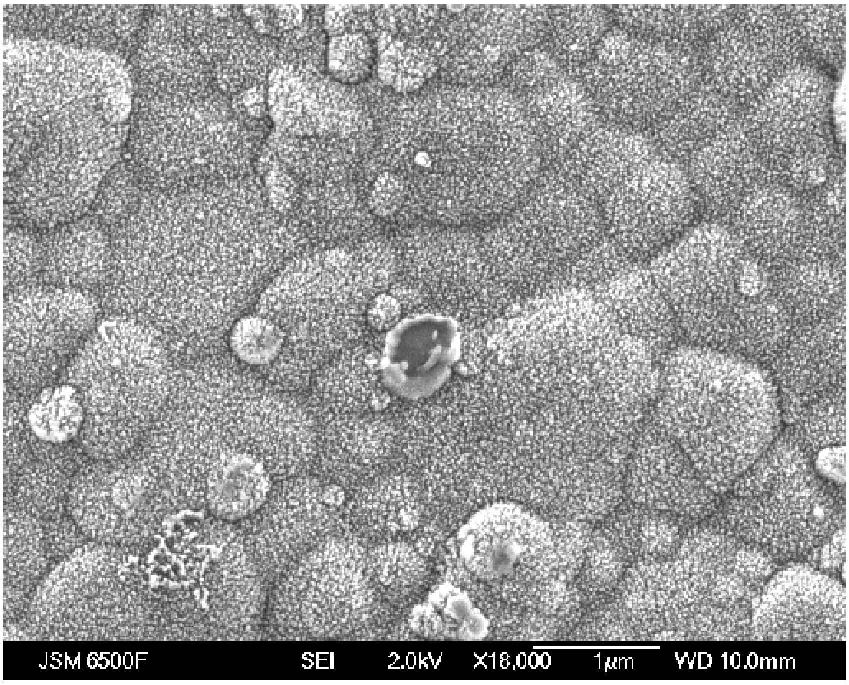

Figure 53: Exposed evaporated sensor (run 6)

Apart from some contaminated samples (that were unresponsive to AO), the EDS spectra for all of the evaporated films were very similar. Table 21 provides an example of the typical content in the exposed and unexposed condition. In both cases EDS has detected carbon as the dominant element, whilst also detecting small quantities of oxygen, aluminium and gold. The EDS beam sampling depth of ~1μm can easily exceed that of the film material and the detection of aluminium suggests the oxygen may not be a part of the carbon film, but that from the alumina substrate.

Although the sensor device does include gold in its construction, the sampled area is in a region where this should not appear. This contamination could have been the result of contact sublimation during the pump down or chamber contamination prior to pump down. Since the film was not exposed to a vacuum environment prior to deposition, it is very possible that residue paste from the screen-printing process is being released by vacuum and condensing onto the substrate surfaces.

| Spectrum | C | O | Al | Au |
|---|---|---|---|---|
| Covered film | 94.70 | 2.25 | 2.38 | 0.68 |
| AO exposed | 97.84 | 0.73 | 0.98 | 0.45 |

**Table 21: Evaporated film content (at. %)**

## 8.4 Raman Spectroscopy

### *8.4.1 Annealed Films*

Figure 54 shows a typical spectrum and curve fit for the annealed evaporated films. A G-peak at ~1582cm$^{-1}$ and a D-peak at ~1403cm$^{-1}$ are fitted, giving a spectrum typical of sp$^{2}$ rich amorphous carbon (a-C) [127]. The spectrum has been extended to show a peak at 2320cm$^{-1}$, which is representative of atmospheric nitrogen, and a broad mound at around 3000cm$^{-1}$ that is indicative of hydrogenation. Unfortunately, due to the thinness of these films it was not possible to collect post AO exposure Raman spectra.

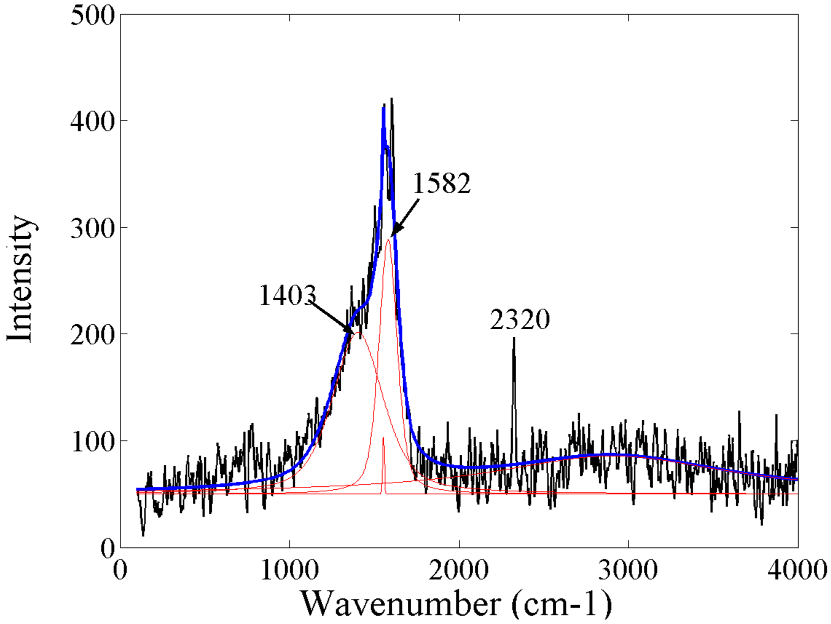

**Figure 54: Curve fit of Raman spectrum for annealed evaporated film (coupon 26)**

### *8.4.2 As-Deposited Films*

Figure 55 shows typical Raman spectra of an evaporated film deposited during the second session (DS2). The general shape is similar to that of an amorphous carbon [127], with the exception that a strong and distinct G-peak at around 1580cm$^{-1}$ exists on some spectra.

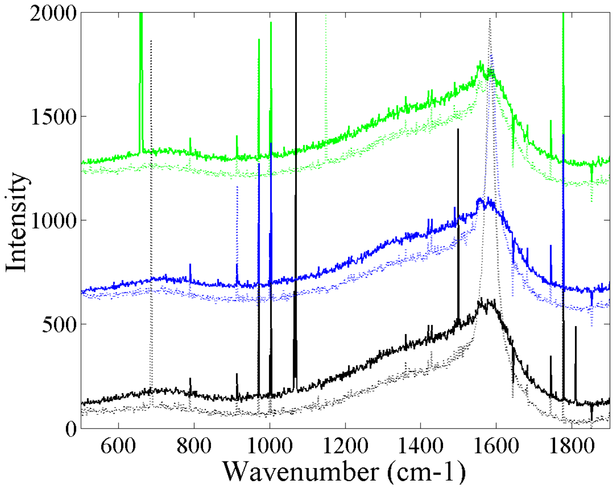

**Figure 55: Raman spectra of evaporated film (coupon 202), covered film spectra are dashed**

Some structural variation appears to be present in the DS1 films. As Figure 56 shows, there are two different kinds of spectra. The first spectrum is one that is similar to glassy or microcrystalline graphite, where two peaks are present. The second spectrum type is one similar to the amorphous carbon spectra shown so far. The exposed material shows the glassy-like spectra to be absent. The slope from 500 cm$^{-1}$ to 900cm$^{-1}$ on the upper most spectrum is a consequence of laser filtering and not film composition.

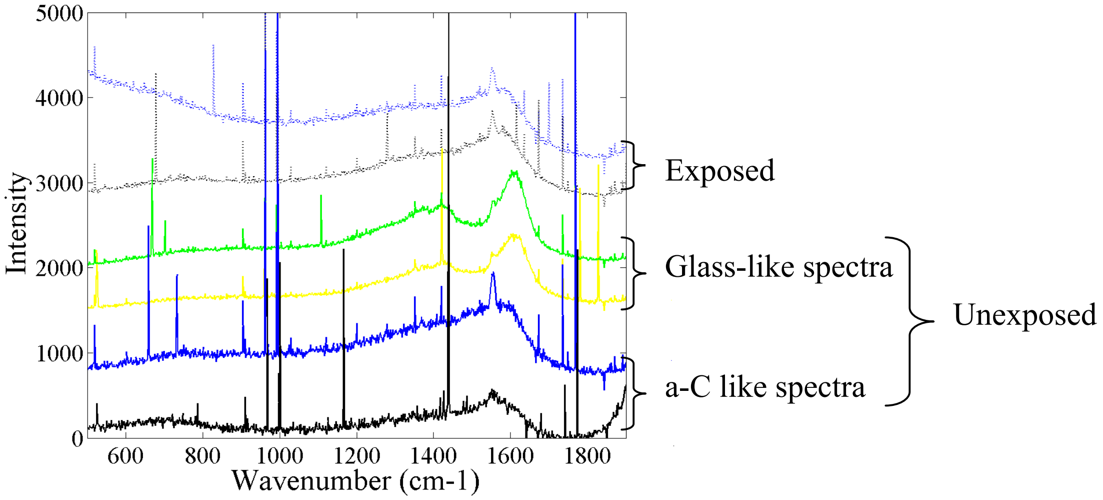

**Figure 56: Raman spectra of untreated evaporated films, exposed spectra is dashed**

Figure 57 shows one of the glassy-like spectrums and the curves fitted to it. The position of the G-peak has moved from around 1580cm$^{-1}$, past 1600cm$^{-1}$ to around 1606cm$^{-1}$. This is usually a good indication that sp$^3$ exists in the film[154]. The peak at 960cm$^{-1}$ was found to be a T-peak, which estimates the sp$^3$ content to no more than 20% [147, 149]. The peaks at 1361cm$^{-1}$, 1426cm$^{-1}$ and a polyacetylene peak at 1248cm$^{-1}$ are consequences of hydrogenation [172].

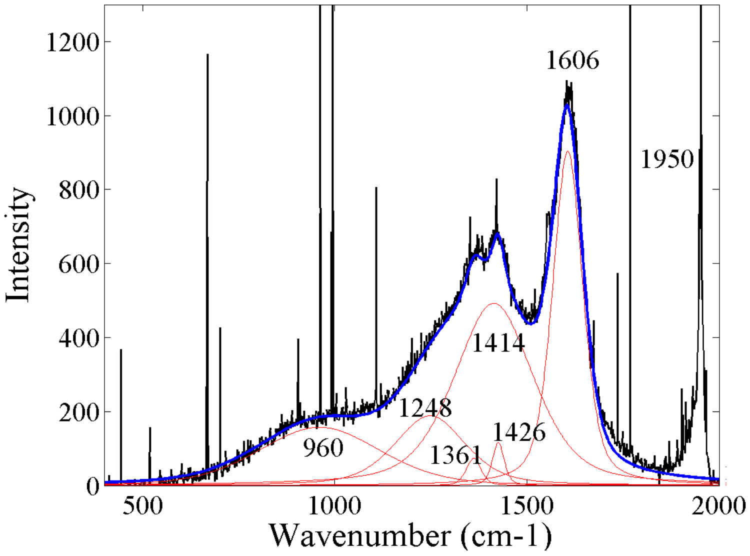

**Figure 57: Curve fit of Raman spectrum for untreated evaporated film (coupon 41)**

It appears from the spectra that the untreated films have large clusters of greater (but by no means large) $sp^3$ content within a mostly $sp^2$ matrix. During annealing these clusters are converted to the bulk $sp^2$ matrix material.

Figure 58 shows the general curve fitting for the DS2 films. The fitted curves become taller and narrower with increasing wavenumber. The feature shown at 1574cm$^{-1}$ is the G-peak, at 1414cm$^{-1}$ the D-peak and at 1245cm$^{-1}$ a polyacetylene feature. Apart from the absence of $sp^3$ and the minor hydrogenation features this spectrum appears very similar to the untreated film of DS1.

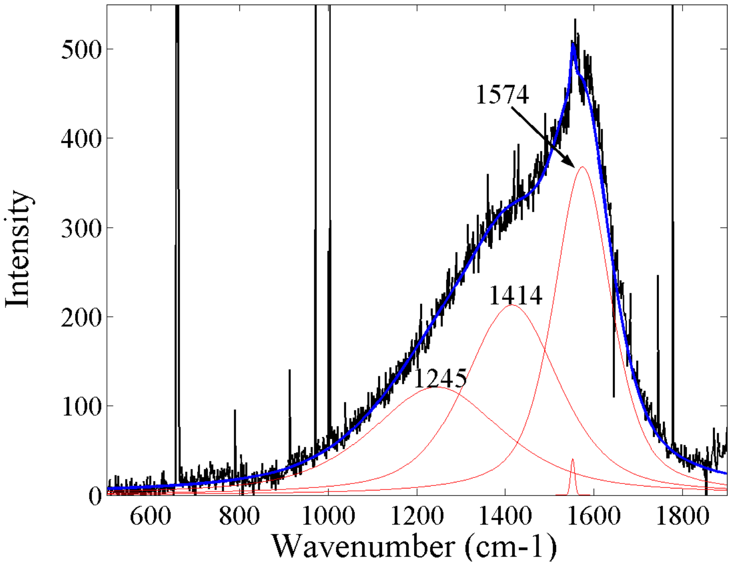

**Figure 58: Curve fit of Raman spectrum for DS2 evaporated film**

A common feature in the Raman spectroscopy of thin films is the presence of a molecular oxygen peak at 1555cm$^{-1}$, which is brought about by absorption from the atmosphere. This feature is present in many of the spectra, suggesting that not all of the oxygen detected in the EDS analysis is that from the alumina substrate.

### *8.4.3 Hydrogenation*

The results from the hydrogenation baseline calculation are shown in Table 22.

| **Coupon I.D.** | **Background Gradient, m** | **I (G)** | **H (at %)** |
|---|---|---|---|
| Coupon 26 (covered) | 750 | 275 | 29% |
| Coupon 26 (uncovered) | 180000 | Negligible | >45% |
| Coupon 202 (covered) | 375 | 215 | 26 |
| Coupon 202 (uncovered) | 375 | 200 | 26 |

**Table 22: Hydrogen content estimates**

The DS1 evaporated film (coupon 26) has an artificially high hydrogen content in the uncovered condition. This is due to an additional photoluminescence (PL) background from the underlying alumina substrate (Figure 59). The thicker DS2 films (coupon 202) do not have this problem and show a consistent content of 26%.

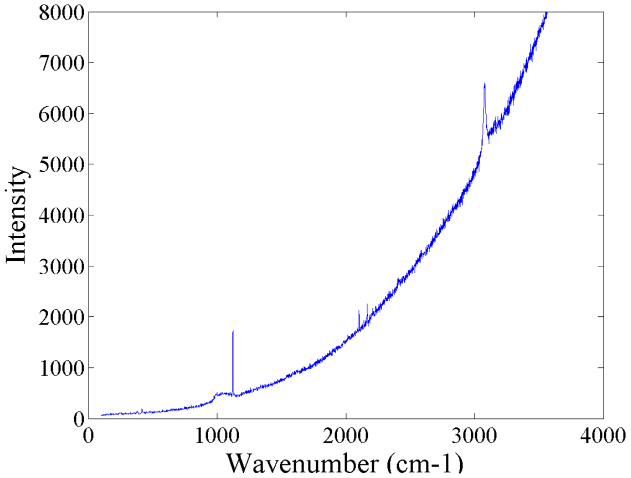

**Figure 59: Raman spectrum of coupon 26 with 510nm excitation wavelength**

### *8.4.4 Polyacetylene Content*

Comparing peak positions with generalised values, the most reasonable assignment of an additional peak at 1245cm$^{-1}$ is that of CH deformations [176]. Ferrari [156] gives details of a string-like polyacetylene (PA) phase present in CVD carbon films. This electrically conducting polymeric phase, which consists of an alternating C-C=C-C chain was found to have an excitation dependence from 1125cm$^{-1}$ for visible Raman to 1200cm$^{-1}$ for UV excitation.

Evidence of a chain-like structure is further strengthened when the UV spectra around 1950cm$^{-1}$ is considered. All the UV spectra from both DS1 and DS2 show a distinct peak in this region. When comparing this to listed tables the only possible assignment is a C=C=C chain [176]. The peak at around 1245cm$^{-1}$ will be referred to as the $PA_1$ peak, to indicate the polyacetylene-like structure. It should be noted that the Raman cross-section for PA is very large, so the quantities present in these films are correspondingly small [178].

### *8.4.5 Preferential Attack*

Table 23 shows a summary of the spectra obtained from coupon 202. Pre-exposure the $I_D/I_G$ ratios vary significantly, from 0.15 to 0.63, whilst post exposure values are very similar at around 0.59.

Assuming similar trends seen in visibly excited samples, the weak $I_D/I_G$ of the pre-exposure films indicate that proportionally less graphitic clustering is present than the post-exposure films. It is proposed here that the non-ring phase, represented by the G-peak is being preferentially attacked by AO.

|  |  |  | **Pre-Exposure** | **Post-Exposure** |
|---|---|---|---|---|
| **Spectrum 1** | G-peak | Position (cm$^{-1}$) | 1579 | 1574 |
|  |  | Height | 401 | 368 |
|  | D-peak | Position (cm$^{-1}$) | 1391 | 1414 |
|  |  | Height | 253 | 213 |
|  | $I_D/I_G$ (Height) |  | 0.63 | 0.58 |
| **Spectrum 2** | G-peak | Position (cm$^{-1}$) | 1580 | 1580 |
|  |  | Height | 1658 | 355 |
|  | D-peak | Position (cm$^{-1}$) | 1449 | 1435 |
|  |  | Height | 250 | 216 |
|  | $I_D/I_G$ (Height) |  | 0.15 | 0.61 |
| **Spectrum 3** | G-peak | Position (cm$^{-1}$) | 1585 | 1579 |
|  |  | Height | 841 | 334 |
|  | D-peak | Position (cm$^{-1}$) | 1396 | 1423 |
|  |  | Height | 226 | 191 |
|  | $I_D/I_G$ (Height) |  | 0.27 | 0.57 |
| **Average** | G-peak position |  | 1581 | 1571 |
|  | D-peak position |  | 1412 | 1412 |
|  | $I_D/I_G$ (Height) |  | 0.35 | 0.59 |

**Table 23: Peak fits of coupon 202**

## 8.5 Summary

The evaporated technique produces amorphous carbon with some potentially significant variation. The same deposition settings have produced films with different levels of disorder and clustering, as well as some degree of sp$^3$ variation. Annealing treatment appears to eliminate any sp$^3$ variation, whilst AO appears to preferentially attack non-ring carbon atoms.

There is evidence of hydrogenation, which has manifested itself as a disordered polyacetylene-like phase. AO erosion occurs evenly across the film surface and the film appears to be sensitive to changes in AO flux.

# 9 SPUTTERED FILM RESULTS

## 9.1 Fabrication

Sputtering was carried out at Cranfield University, using a homemade sputter chamber and magnetron, coupled to a BOC Edwards EO2K diffusion pump. Two different deposition settings were used to provide different content for investigation. Table 24 provides the details of these depositions that were eventually tested in an AO environment.

| **Deposition Parameters** | **Annealing (in Argon)** | **Coupon (Deposition session)** | **Average Sensor Initial Thickness, $\tau_o$ ($\mu$m)** | **Conductivity ($\Omega^{-1}$.m$^{-1}$) @ 25°C** |
|---|---|---|---|---|
| 786V at 600mA. Power Density of 2.6 Wcm$^{-2}$ | 360mins. @ 400°C | 38-01 (DS1) | 2.8±1.3 | 0.003 |
| | 100mins. @ 600°C | 24-03 (DS1) | 2.8±1.3 | 0.012 |
| | | 23-02 (DS1) | 2.8±1.3 | 0.020 |
| | 200mins. @ 600°C | 22-01 (DS1) | 2.8±1.3 | 0.836 |
| | | 21-02 (DS1) | 2.8±1.3 | 0.120 |
| 694V at 1.15mA. | None | 104-03 (DS2) | 0.48 | 0.021 |
| Power Density of 4.4 Wcm$^{-2}$ | | 102-03 (DS2) | 0.80 | 1390 |

**Table 24: Summary of sputtered depositions**

Resistances from the first deposition session (coupons 21 to 38) were measured as open-circuit, so the films were annealed with a view to reducing resistances. The films were heated in an argon furnace for the times and temperatures shown in Table 24, where the subsequent conductivities are also shown. Due to the high resistances of the first depositions, subsequent DS2 films were deposited onto the interdigitated array, described in Chapter 5.

Unlike the evaporated process, in-situ measurements of thickness were not possible, so thicknesses were measured post-deposition. Thicknesses from substrates of DS1 were very difficult to obtain because the surface roughness from the 96%$Al_2O_3$ substrate were greater than the deposited film thickness. The initial thickness measurement is an average of multiple measurements, but there is still a large degree of uncertainty. This issue is resolved for DS2 films by placing atomically smooth silicon-oxide wafers alongside the alumina coupons in the deposition chamber as a thickness reference.

## 9.2 AO Response

### *9.2.1 Erosion Yield*

Table 25 summaries the theoretical erosion yield (TEY) obtained from the normalised resistance measurements and the measured erosion yield. The TEY of coupon 104 is the greatest of all the sensors tested and exceeds typical values for carbon materials (~250% of the maximum erosion yield of graphite [48]), although coupon 102 of the same deposition session had a yield more typical of carbon materials.

Inspection of the systematic actinometer errors (SAE) show that (like the evaporated sensor) TEY can give an overestimate of the actual erosion yield, although the value obtained for that particular sputtered sensor is much less than the evaporated sensor. Substrate 102 had a TEY identical to the measured erosion yield.

The DS1 sensors had the lowest TEY of all the films and in one case appeared negative because the resistance had fallen post exposure. The TEY could not be validated due to the surface roughness of the substrate and the very small erosion that would have taken place if the TEY were correct. The reactions of the DS1 films are discussed in more detail later in this chapter.

| **Substrate** | **Deposition Session** | **Exposure Run No.** | $R_0/R_{end}$ | $\tau_{end}/\tau_0$ | **SAE** | **Theoretical Erosion Yield, TEY ($x10^{-25}$ $cm^3$/atom)** | **Measured Erosion Yield, Y ($x10^{-25}$ $cm^3$/atom)** |
|---|---|---|---|---|---|---|---|
| 38-01 | 1 | 4 | 1.000 | ~1 | - | 0 | ~0 |
| 24-03 | 1 | 2 | 0.981 | ~1 | - | 1.36 | ~0 |
| 22-01 | 1 | 1 | 0.980 | ~1 | - | 0.71 | ~0 |
| 21-02 | 1 | 6 | 1.062 | ~1 | - | -0.62 | |
| 104-03 | 2 | 5 | 0.596 | 0.64 | 6.9% | 22.5 | 21.1 |
| 102-03 | 2 | 6 | 0.15 | 0.15 | 0% | 9.8 | 9.8 |

**Table 25: Comparison of theoretical and measured erosion yields**

### *9.2.2 Sensor Data*

Figure 60 shows the typical AO response of the DS1 sputtered sensors. The response is approximately linear, with slight variations in gradient as temperature is changed (at 50 minutes). The response of each sensor is very similar, with final Ro/R values being within 0.5% of each other. Apart from at the beginning of the exposure, there is no obvious change in rate as the AO flux decays.

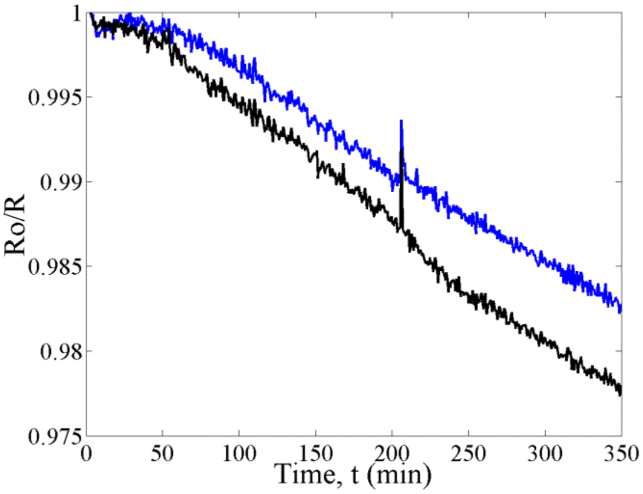

**Figure 60: Sputtered film exposure (run 1)**

The same result plotted against fluence (Figure 61), shows a significant period at the beginning of the exposure where the sensor is insensitive to AO. After a fluence of ~$5x10^{19}$atoms/cm$^2$, the sensor is responding to AO in a linear fashion. Note that the data spike represents the time when temperatures were reduced from 53ºC to 24ºC and the sensor appears insensitive to this change.

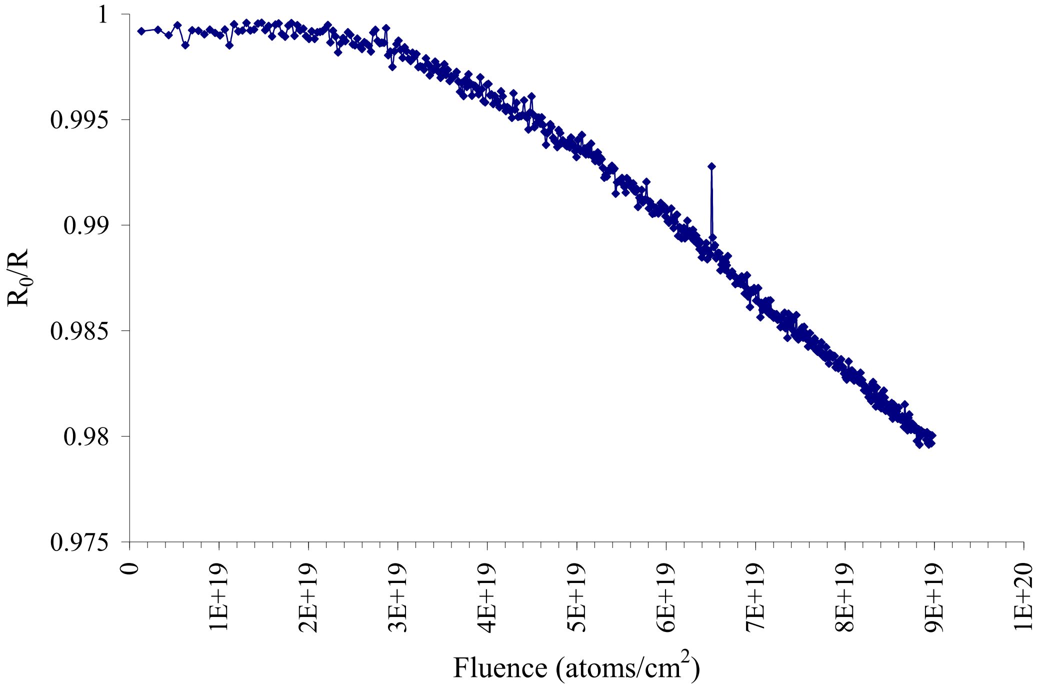

**Figure 61: Sputtered film exposure (run 1) versus fluence**

The DS2 sputtered sensors showed very different responses to those obtained from DS1 sensors. Figure 62 shows the AO response of the sensor exposed during run 5 (coupon 104, DS2). The most obvious difference from the DS1 sputtered sensors is that the carbon film is very responsive to AO.

Over time the response deviates from its initial rate of change, as can be seen by comparing it to a straight line of the same gradient as the initial response. The response of the DS2 sensor deviates from the ideal linear response by approximately 3% (Figure 63). It can be seen that the response from these films is very similar to the DS2 evaporated films (Figure 47).

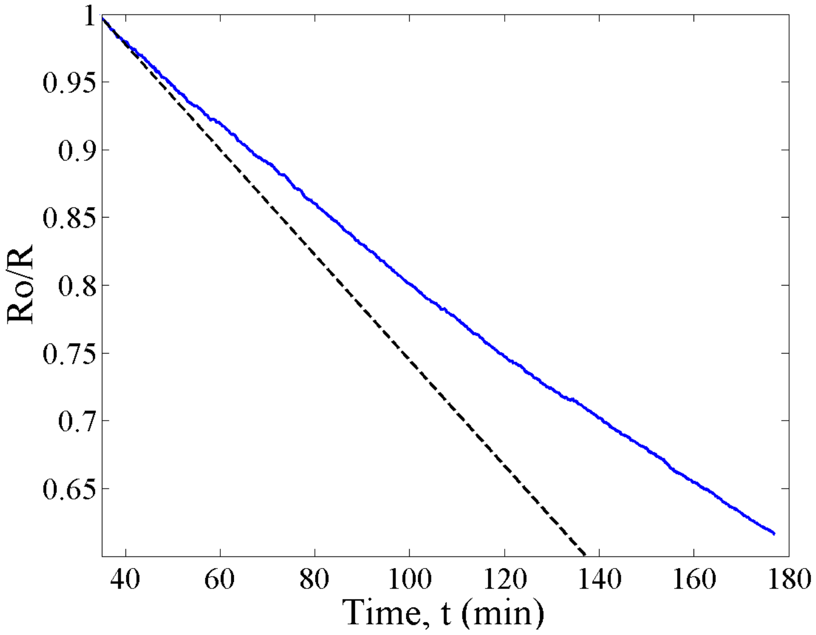

Figure 62: Sputtered sensor exposure (run 5)

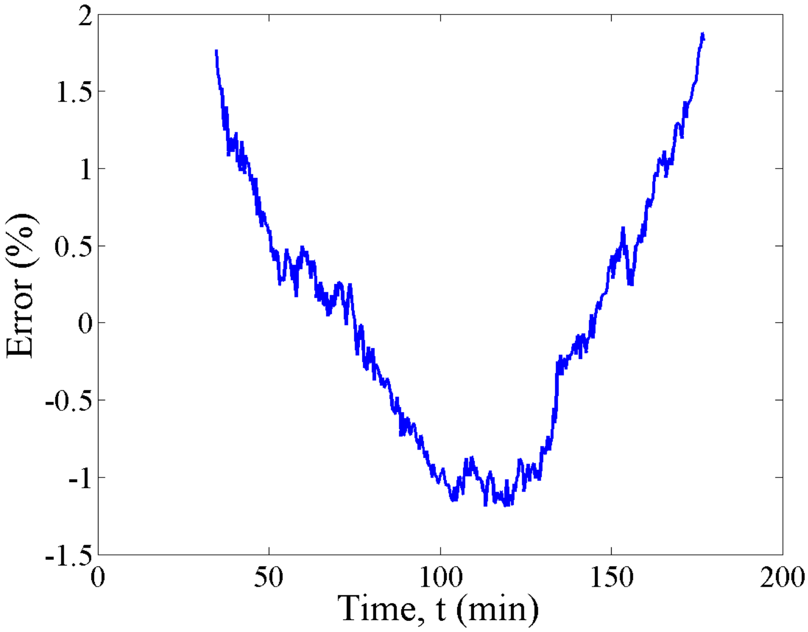

Figure 63: Sputtered sensor ANLE (run 5)

## 9.3 Surface Modification and EDS

SEM of the DS1 samples revealed that those annealed for 100 minutes show a 'brain-like' structure on top of individual alumina substrate grains (Figure 64). As the annealing time is doubled (Figure 65), the structure becomes much finer with narrower boundaries.

The change in microstructure with heat treatment could explain the differences in conductivity. The most segmented 'brain-like' structure with wide boundaries provides the greater electrical resistance of the two annealed samples. It is possible that the 'brain-like' structure has localised or trapped electrons in someway, but determination of the precise mechanisms is beyond the scope of this work.

It is important to know the initial resistance of a film before incorporating it into electrical circuits and this will influence circuit design. The significance of the annealing result is that changes in thickness may not yield the anticipated ohmic change in resistance, so complicate the circuit design process.

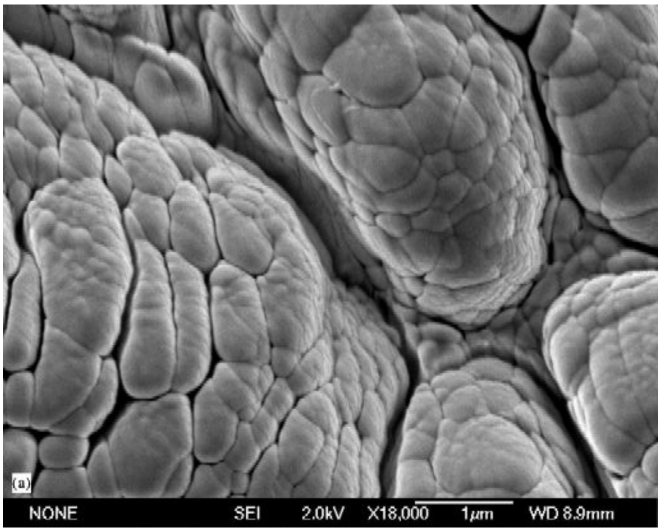

**Figure 64: SEM image of sputtered film annealed to 600°C for 100 minutes**

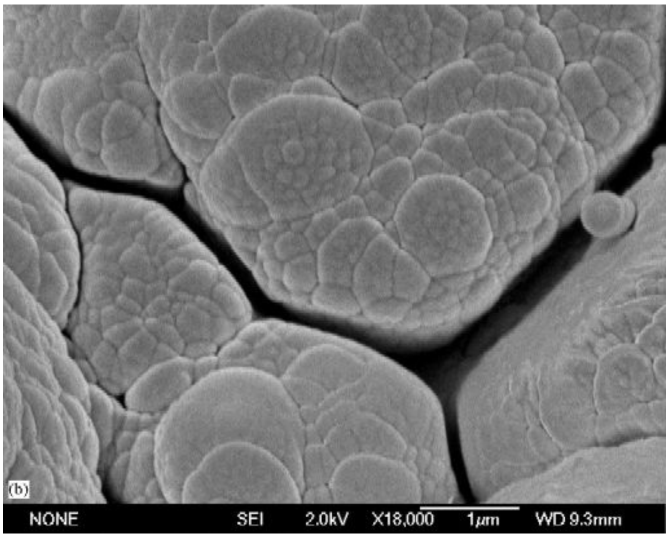

**Figure 65: SEM image of sputtered film annealed to 600°C for 200 minutes**

Images taken post AO exposure revealed no change in topography. Figure 66 and Figure 67 show no obvious materials degradation has taken place at the resolutions shown. If the TEY is representative of film erosion there should be some sign of erosion from the magnification of these micrographs. This is an important result, which is considered in the later discussion.

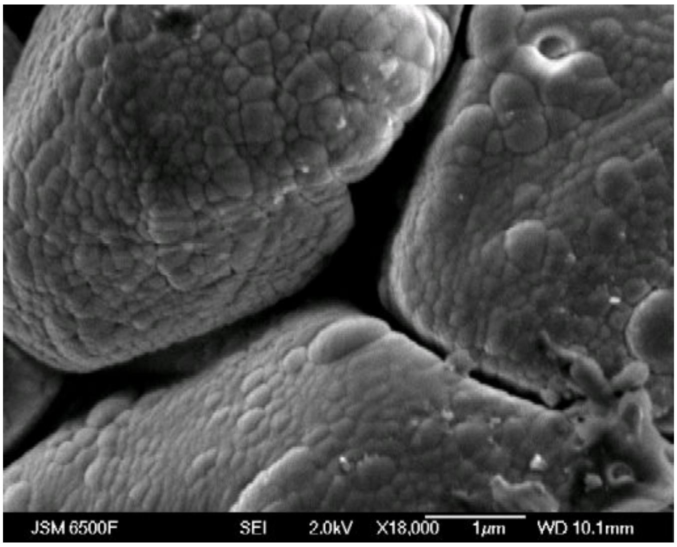

**Figure 66: Unexposed sputtered sensor**

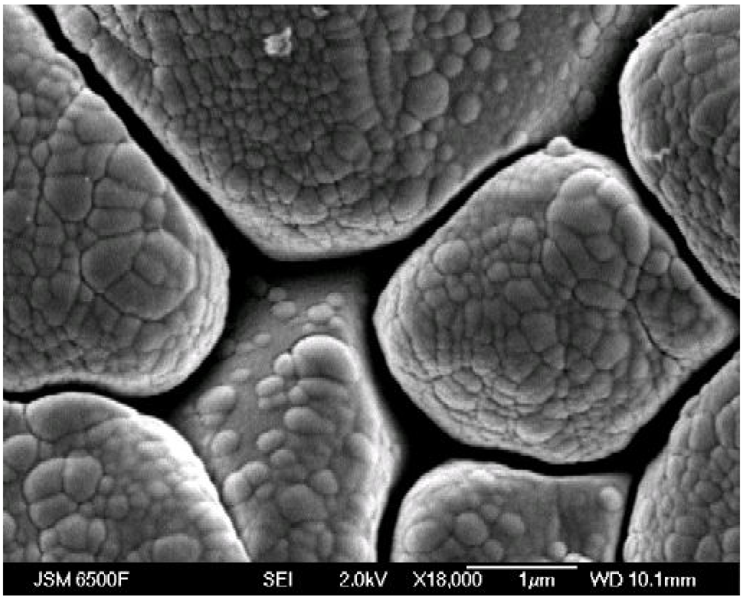

**Figure 67: Exposed sputtered sensor**

Contrasting with DS1, the DS2 films showed that they had eroded, which is in agreement with the greater TEY. The image of Figure 68 shows a debris particle visible in the centre of the image that has shielded some of the underlying material from AO attack. The film is ablating in a very similar manner to many carbon-based materials [179].

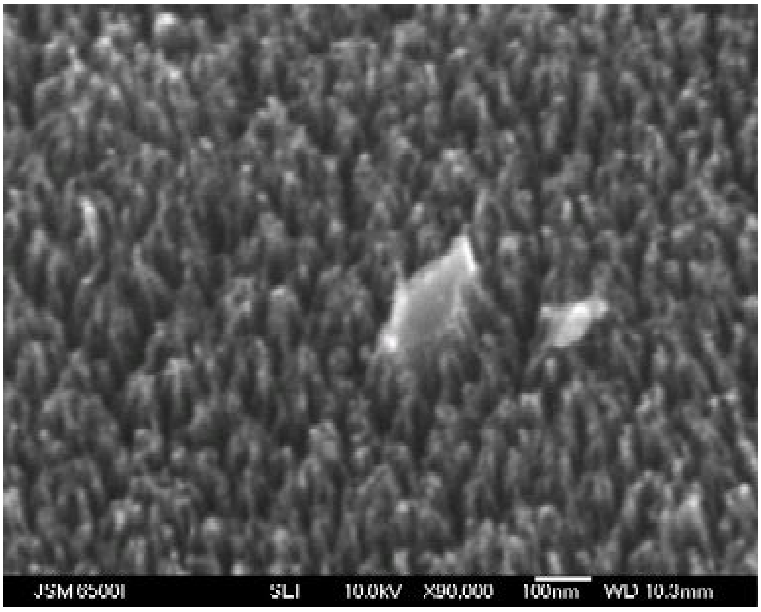

**Figure 68: Sputtered sensor topography after AO exposure (run 5)**

Table 26 shows the EDS spectrum data from a typical DS1 film. Whilst carbon is still the majority constituent, oxygen, aluminium and silicon are also present. The presence of aluminium and oxygen is indicative of the underlying alumina substrate material, whilst the silicon is a contaminant.

| Spectrum | C | O | Al | Si |
|---|---|---|---|---|
| 1 | 58.17 | 33.50 | 1.83 | 6.50 |
| 2 | 56.11 | 34.13 | 3.97 | 5.79 |
| 3 | 55.61 | 30.84 | 9.36 | 4.19 |
| 4 | 59.44 | 28.17 | 6.29 | 6.10 |
| 5 | 59.38 | 29.02 | 5.03 | 6.58 |
| 6 | 55.60 | 31.95 | 4.64 | 7.82 |

**Table 26: Sputtered film content (Atomic percent)**

The results from DS2 reveal the same elemental contents, albeit in different quantities to DS1 films (Table 27), which could be related to the smoother substrates used for this deposition set [177]. Spectra were obtained from regions that were overlying both the alumina substrate and the interdigitated gold contacts. It is probable that the analysis depth is exceeding the thickness of the carbon film, as the underlying material is being detected.

| Spectrum | C | Si | O | Al | Au |
|---|---|---|---|---|---|
| Covered, on alumina | 64.18 | 0.52 | 21.56 | 13.73 | - |
| Covered, on gold | 85.49 | 0.40 | 7.49 | 0.23 | 6.39 |
| Exposed, on alumina | 72.01 | 0.48 | 16.09 | 11.43 | - |
| Exposed, on gold | 88.03 | 0.46 | 6.85 | - | 4.65 |

**Table 27: DS2 Sputtered film content (Atomic percent)**

## 9.4 Raman Spectroscopy

### *9.4.1 Hydrogenation*

Table 28 provides a summary of the hydrogenation estimates for the films.

| **Coupon I.D.** | **Background Gradient, m** | **I (G)** | **H (at %)** |
|---|---|---|---|
| Coupon 21 (covered) | 0 (baseline removed) | - | - |
| Coupon 21 (uncovered) | 8750 | 300 | >45 |
| Coupon 102 (covered) | 4500 | 5200 | 21 |
| Coupon 102 (uncovered) | 1000 | 1500 | 19 |

**Table 28: Hydrogen content estimations**

Unfortunately, the DS1 pre-exposure PL data has been lost so an estimate cannot be made, but the AO exposed spectrum reveals high hydrogen content at above 45%. The DS2 sputtered films (coupon 102) show a consistent hydrogen content pre and post exposure.

### *9.4.2 DS 1 Film Content*

Figure 69 shows the spectra for coupons 21 and 23 pre AO exposure, which appear very similar. Coupon 21 is annealed to 600ºC for 200minutes and then aged, whilst coupon 23 is a coupon that underwent heat treatment to 600ºC for 100minutes before aging. Although SEM has found the topography of the films to change with annealing time, this result suggests the treatment has not had a significant effect on bond type distributions.

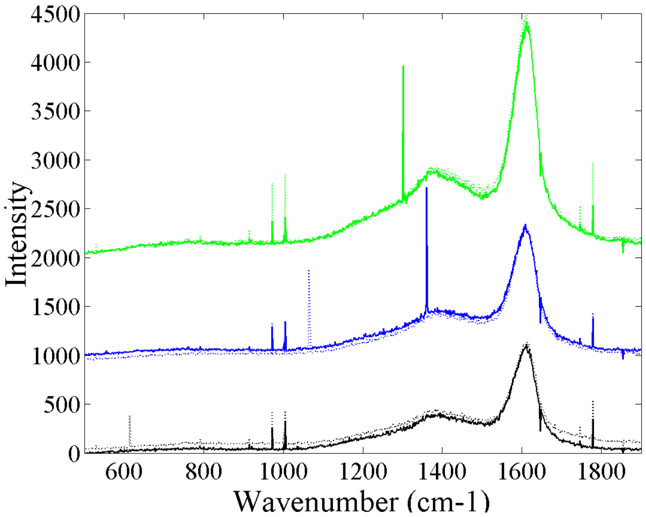

**Figure 69: Raman spectra of coupons 21 and 23 (dashed) before exposure to AO**

Figure 70 shows a typical curve fit for DS 1 sputtered films. Excluding some C=C=C bonding at 1950cm$^{-1}$ there are 5 curves: A G-peak at 1603cm$^{-1}$, a D-peak at 1382cm$^{-1}$, PA features at 1239cm$^{-1}$ (the PA$_1$ peak) and 1546cm$^{-1}$ (the PA$_2$ peak), whilst a curve at around 760cm$^{-1}$ was believed to be a silicon carbide feature. There are no signs of sp$^3$ content in these films.

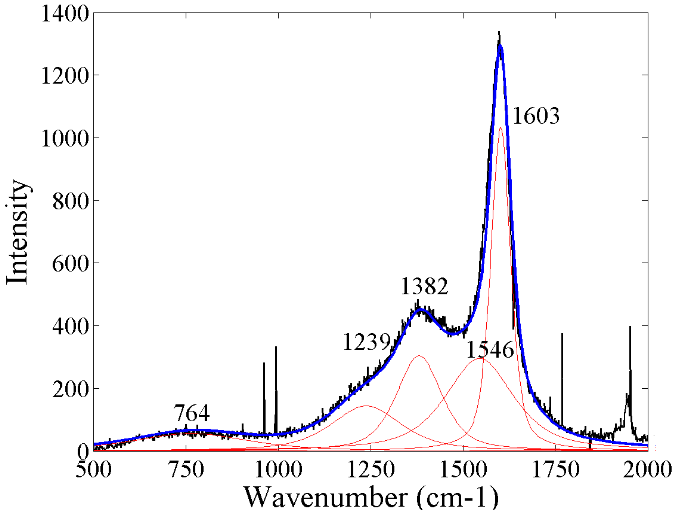

**Figure 70: Curve fit of Raman spectrum for DS1sputtered film**

### *9.4.3 DS1 Changes with AO*

Figure 71 shows the spectra of coupon 21 before and after (dashed) exposure to atomic oxygen. Except for the magnified top spectrum (to highlight general shape), all the spectra pre and post exposure are identical, suggesting that the material remains unchanged. This result is generally replicated by all DS1 films with exception to those of coupon 23.

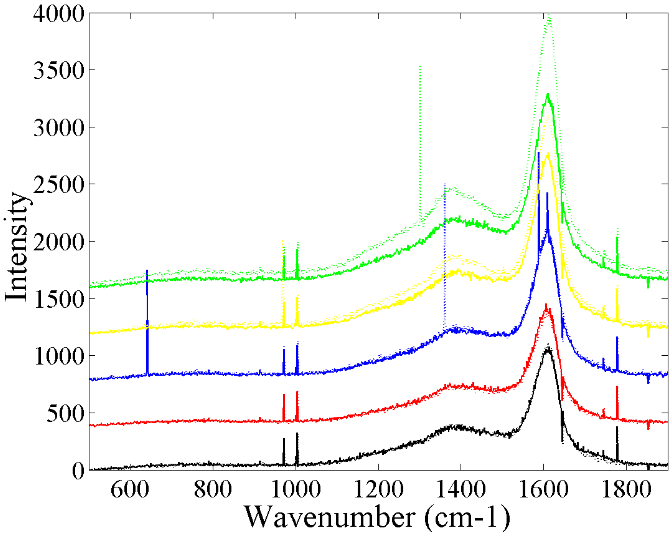

**Figure 71: Raman spectra of coupon 21 films before and after (dashed) AO exposure**

Figure 72 shows the spectra of coupon 23 before and after atomic oxygen exposure. Unlike the previous sample the material seems to have changed slightly, where the wide shoulder appears to be making a small transformation into a secondary peak.

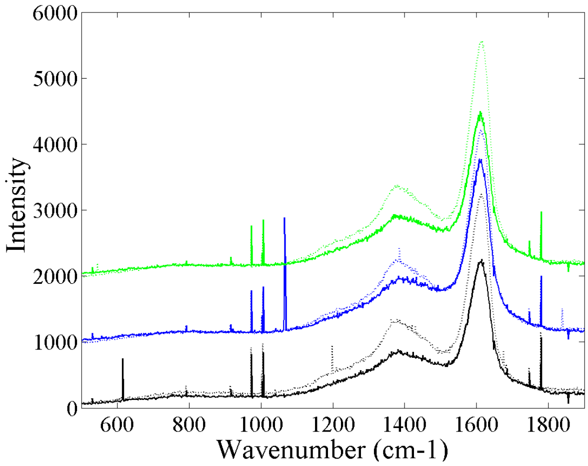

**Figure 72: Raman spectra of sputtered film (coupon 23) before and after AO exposure**

These changes are quantified by taking the ratio of the peak of interest with the G-peak. Table 29 shows the differences between $I_D/I_G$ ratios and the ratio of the $PA_1$ peak with G-peak. The contributions from the $PA_1$ peak remain essentially unchanged, whilst some increase is seen in the $I_D/I_G$ ratio with AO dose, which suggests that graphitic clusters (represented by $I_D$) are more resistant to AO attack than non-ring carbon clusters (represented by $I_G$).

| Fluence (x10$^{19}$ atoms.cm$^{-2}$) | $I_D/I_G$ | Average | $I_{PA1}/I_G$ | Average |
|---|---|---|---|---|
| 0 | 0.34 | 0.287 | 0.09 | 0.090 |
|  | 0.25 |  | 0.1 |  |
|  | 0.27 |  | 0.08 |  |
| 7.8 | 0.38 | 0.387 | 0.08 | 0.093 |
|  | 0.34 |  | 0.1 |  |
|  | 0.44 |  | 0.1 |  |

**Table 29: Spectral change with AO dose for DS1 sputtered sensor**

### *9.4.4 DS 2 Film Content*

The spectra of the DS2 films are provided below in Figure 73. The spectra here resemble a low sp$^3$ amorphous carbon with a sloped shoulder that blends into the main peak. Except for some overall intensity differences that are due to differing thicknesses, all the spectra look very alike regardless of AO exposure or the deposition run. However, as further analysis will show, there are some subtle but important differences.

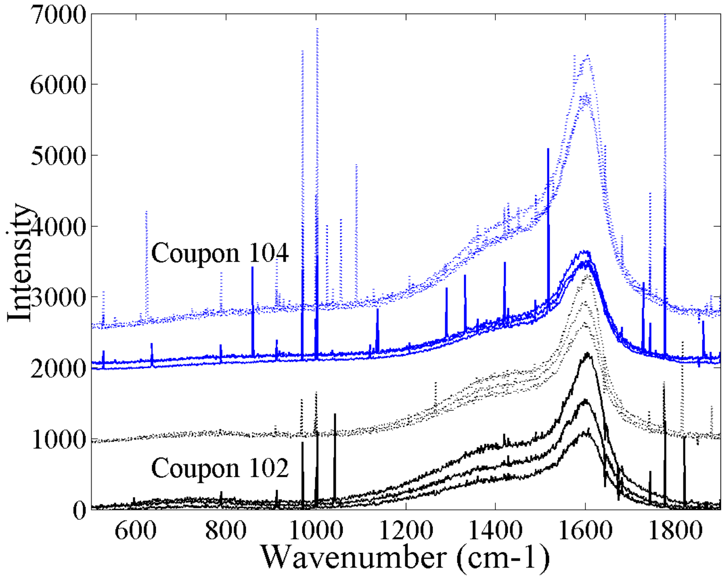

**Figure 73: Interdigitated sensor comparison (AO exposed is dashed)**

A curve fit from coupon 102 is shown in Figure 74. The spectrum has some common features with the films of DS1. For example, the D and G-peaks are in approximately the same positions and there is a low intensity, broad peak at around 760-790 cm$^{-1}$. The differences are that the PA$_1$ peak is not seen and the PA$_2$ peak has shifted ~50cm$^{-1}$ closer to the D-peak.

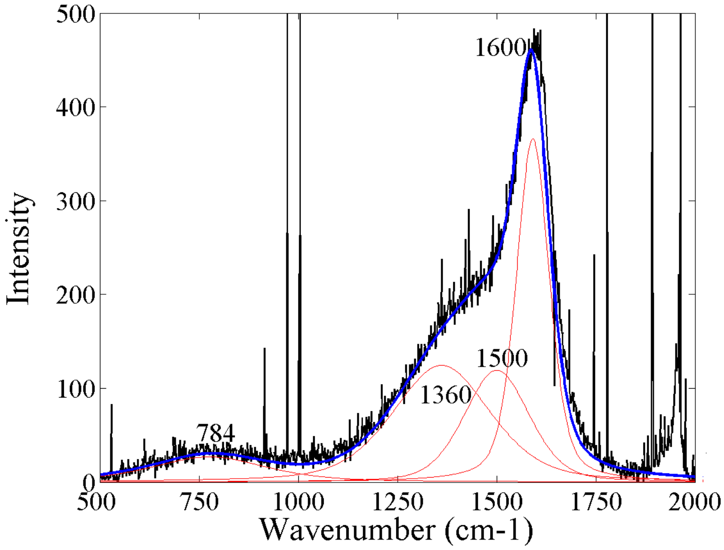

Figure 74: Curve fit of Raman spectrum from coupon 102.

Curve fitting of coupon 104 shows a stronger PA$_1$ curve and an apparent upward shift in the peak found within the 760-790cm$^{-1}$ range to around 990cm$^{-1}$ (Figure 75).

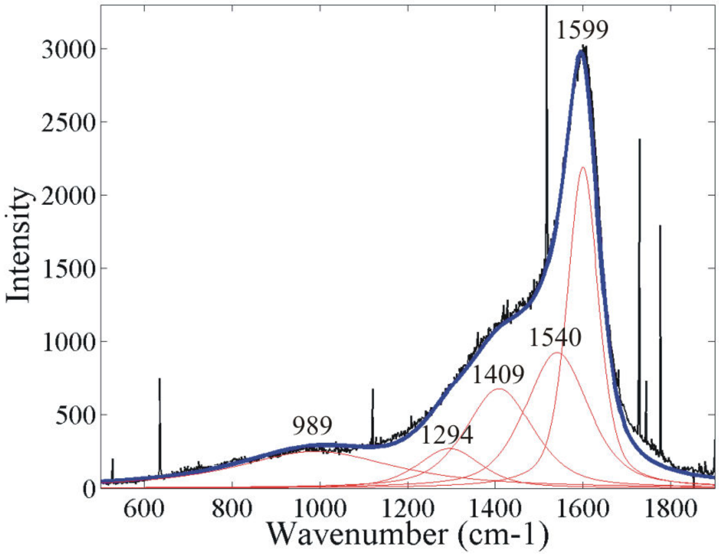

Figure 75: Curve fit of coupon 104 Raman spectrum

The upward shift is not actually a shift, but rather the presence of a more dominant and wider T-peak. Table 30 shows the positions, intensities and relative proportions of this peak for all the spectra obtained from coupon 104. There is a wide spread in the T-peak positions, which is possibly due to dispersal and disorder [124, 154, 180, 181].

| Condition | T-Peak Position | T-Peak Intensity | G-Peak Intensity | $I_T/I_G$ |
|---|---|---|---|---|
| Pre-exposure | 989 | 250 | 2192 | 0.11 |
| | 995 | 78 | 1018 | 0.07 |
| | 1034 | 107 | 979 | 0.10 |
| Post-exposure | 952 | 153 | 2290 | 0.07 |
| | 986 | 234 | 2802 | 0.08 |
| | 970 | 205 | 2487 | 0.08 |

**Table 30: Coupon 104 T-peak positions and intensities**

The peak at 760-790cm$^{-1}$ may still exist, but with a lesser proportion than previous depositions. The ratio of intensity of the 760cm$^{-1}$ peak compared to the G-peak in coupon 102 is ~0.13 and in DS1 films ~ 0.07. Taking the lesser of these ratios, the intensity of a similar peak at 760cm$^{-1}$ in coupon 104 would be 157, which would be barely distinct in the tail of the T-peak. The appearance of the $PA_1$ peak may also be linked to the lesser ratio, but further research is required to validate this result.

### *9.4.5 Discussion*

#### 9.4.5.1 760cm$^{-1}$ Peak Origin

The origin of the ~760cm$^{-1}$ peak has been tentatively assigned to SiC bonding. The feature is sometimes correlated to sp$^3$-bonded vibrations [182] and more commonly to some form of disorder [183-185]. Unlike previous studies, the excitation frequency used for this analysis can directly detect sp$^3$. Given that there was no trace of sp$^3$ when the 760cm$^{-1}$ peaks were detected, it is clear that an sp$^3$ assignment would be false.

The work of Parmigiani was the first to describe the 760cm$^{-1}$ peak as the "L-peak" and associate it to disorder [165]. In the literature, it appears that the L-peak is common to sputtered films, and it is suggested that the peak arises due to the inclusion of the large and heavy ions used to sputter the target material [186]. Inspection of the $I_D/I_G$ ratios suggests there could be a greater degree of disorder in the DS2 films than the DS1 films, so the peak may have different origins between the different deposition sessions. The peak could be attributed to silicon carbide content in DS1 and heavy ion disorder in DS2. It is however, difficult to confirm with certainty, the origins of this peak.

#### 9.4.5.2 DS1 Sputtered Film Response

The absence of change in the topology and only occasional change in Raman spectra casts some doubt that the DS1 films are responding to AO. However, the sensors of run 1 and 2 showed a linear increase in resistance once temperature and pressure effects were compensated.

SiC is known to react with AO to form a stable, non-volatile $SiO_2$ [187]. Given that the DS 1 films were not shown to erode, the most likely explanation is that surface SiC bonds are reacting with AO to form a protective $SiO_2$ layer. $SiO_2$ was not detected in the Raman analysis because the proportions of $SiO_2$ are very small when compared to the bulk material; the study of Raikar detected layers only 1-6nm thick [187].

If the films are not eroding, then the small electrical response must be attributable to some other factor. The most likely explanation is that the surface of the films are behaving in a similar manner to the ZnO sensors reviewed in Chapter 3. As oxygen atoms are chemisorbed onto the surface, surface electrons become trapped, so decreasing conductivity [9, 14, 52].

Unfortunately it is not possible to precisely measure the quantities of the additional elements using the techniques in this study. The work of Chehaidar and others investigated silicon rich SiC films, where the carbon content was increased to as much as 43 at.% [155]. The experimental and theoretical studies undertaken had shown there to be absolutely no sign of either a D or G-peak. This occurred because all of the carbon is used to make SiC bonds. For a similar reason it is perhaps conceivable that no Si-Si bonding was detected in this study because it is used in SiC bonding.

The most significant, yet small, change in spectra was the small post exposure increase in $I_D/I_G$ ratio. This result suggests that small amounts of non-ring carbon atoms that cannot be seen on the SEM images are being preferentially etched. These bonds must be part of a network of linkages incorporating SiC that surround the aromatic clusters. The size of the aromatic clusters can be estimated from experimental fit data (Chapter 7). In the visible spectra, the FWHM of G widens to 120cm$^{-1}$ and the $I_D/I_G$ ratio increases to ~0.5. Comparing this with the data of Schwan, the cluster size is approximately 10Å across [105, 170].

#### 9.4.5.3 Electrical Conductivity

An important aspect of actinometry is the electrical resistance of the films, as this will affect the design of the electronics used to make measurements. Whilst the DS1 films had an initially immeasurable resistance, their electrical conductivities were found to increase with annealing temperature and time.

The Raman spectra from all the films were essentially the same so atomic-scale bonding is not changing with the treatment. The change in conductivity must be purely attributable to morphology, suggesting the brain-like structure cannot be treated as a continuous film. This is perhaps a very significant matter because changes in thickness may not correspond to an ohmic change in resistance.

The two separate depositions of DS2 gave very different conductivities with 5 orders of magnitude differences. This difference may be attributed to differences in sp$^3$ content, but without conducting further studies is hard to prove.

#### 9.4.5.4 DS2 Erosion Yield Differences

Coupons 102 and 104 were found to have large differences in AO yield. The erosion yield of coupon 102 lies within the commonly accepted values for carbon at $9.8\text{x}10^{-25}\text{cm}^3$/atom, whilst coupon 104 showed approximately double these values.

The main structural difference between the films is that one film contains some small, uniform amounts of $sp^3$. Figure 76 plots $sp^3$ content versus erosion yield for the sputtered films and for a DLC film, containing approximately 50% $sp^3$ [134]. Although there are few points, it appears that the erosion yield may increase with $sp^3$ content and then possibly fall at around 50% $sp^3$. There is a great degree of uncertainty in the final point because the film exposed to AO had eroded completely before retrieval. However, it is known that at 100% $sp^3$ the erosion rate will be significantly less.

The critical $sp^3$ content when erosion rates fall is unknown and could potentially occur anywhere from 8% to 100% $sp^3$. If actinometer reactivity is to be reduced by controlling $sp^3$ content, then this parameter must be known.

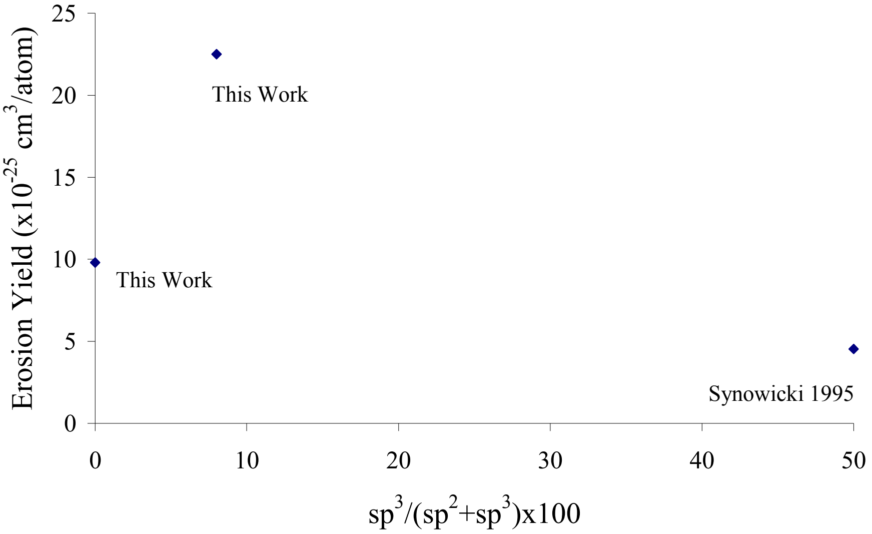

**Figure 76: Erosion yield variation with $sp^3$ content**

# 10 SCREEN PRINTED FILMS

## 10.1 Fabrication

Two different inks were selected for deposition, these being DuPont 4232 and DuPont 4242. Both inks are known to consist of carbon particles in a polymer-based carrier. Differing levels of carbon loading provide conductivity differences. The 4232 ink has more carbon particles than 4242 to give a higher conductivity.

Once deposited, both inks were dried for approximately 3 minutes at a temperature of 170 ºC. The films were then fired for 360 minutes to a temperature of 120 ºC, to polymerise the film. Some of these films underwent a second deposition to provide a double thickness. These films underwent a repeat of the drying and firing process outlined above. Details of the sensor thicknesses, obtained from a Rank Taylor talysurf, and conductivity are shown in Table 31, for sensors that were later tested in an AO environment.

| **Deposition Parameters** | **Annealing** | **Substrate** | **Average Sensor Initial Thickness, $\tau_o$ (μm)** | **Conductivity ($\Omega^{-1}.m^{-1}$) @ 25°C** |
|---|---|---|---|---|
| DuPont 4232 | 3mins. @ 170°C + 360mins. @120°C | 02-01 | 16.63 | 15.41 |
| | | 03-03 | 15.20 | 15.87 |
| | | 05-01 | 14.90 | 15.70 |
| DuPont 4242 | | 14-02 | 13.50 | 0.26 |
| DuPont 4232, Double Deposition | As Above x2 | 09-01 | 27.60 | 12.03 |
| | | 10-03 | 26.75 | 12.90 |
| DuPont 4242, Double Deposition | | 20-02 | 28.75 | 0.20 |

**Table 31: Screen printed depositions**

## 10.2 AO Response

### *10.2.1 Erosion Yield*

| Substrate | Exposure Run | $R_o/R_{end}$ | SAE | Theoretical Erosion Yield, TEY ($\times 10^{-25}$ cm$^3$/atom) | Measured Erosion Yield, Y ($\times 10^{-25}$ cm$^3$/atom) |
|---|---|---|---|---|---|
| 02-01 | 1 | 0.962 | 3.9% | 7.97 | ~0 |
| 02-01 | 3 | 0.953† | 4.9% | 8.51 | ~0 |
| 03-03 | 6 | 0.962 | 3.9% | 7.22 | ~0 |
| 05-01 | Plasma Asher | 0 | - | 34.1 | - |
| 09-01 | Plasma Asher | 0.372 | - | 55.2 | - |
| 10-03 | 3 | 0.976 | 2.5% | 7.27 | ~0 |
| 14-02 | 2 | 0.978 | 2.2% | 7.71 | ~0 |
| 20-02 | 3 | 0.976 | 2.5% | 7.81 | ~0 |

**Table 32: Measured and estimated erosion yields of screen-printed films († treated as a fresh sensor)**

The screen-printed film surface has a peak to trough roughness of approximately 2μm. Since the levels of erosion are small (maximum theoretical change of substrate 02-01 is 0.6μm), thickness changes could not be found using profilometry, as any change will be less than the surface roughness. Erosion rates are therefore inferred from the final resistance changes shown in Table 32.

It is clear that there is a degree of scatter in the ATOX results, so further testing is required to obtain a more accurate assessment of the errors. Comparing substrates 14 and 20 with the other films, changes in film composition do not appear to have a significant effect on the reaction rate for the levels of fluence exposed.

The use of the plasma asher clearly accelerates reaction rates compared to the ATOX facility. This is potentially a consequence of different species in the oxygen beam and changes in the relative erosion yields of the carbon film and the Kapton witness samples used to calibrate the fluence. Erosion yields of the two exposed substrates are very different, although the inks are the same. The reason for this result could be due to flux distributions within the plasma asher. Unfortunately, post exposure thickness was not measured to assess the degree of error.

### *10.2.2 Sensor Data*

Figure 77 shows the sensor response from the 4232 ink of run 1. The data spike evident at approximately 205 minutes represents the switching of the breakdown laser for a C-QCM measurement. Average flux measured by the C-QCM and that observed from the oxygen plasma glow is much reduced after this point. Flux decay is also evident from the carbon films because the data begins to deviate from a line fitted up to the QCM measurement.

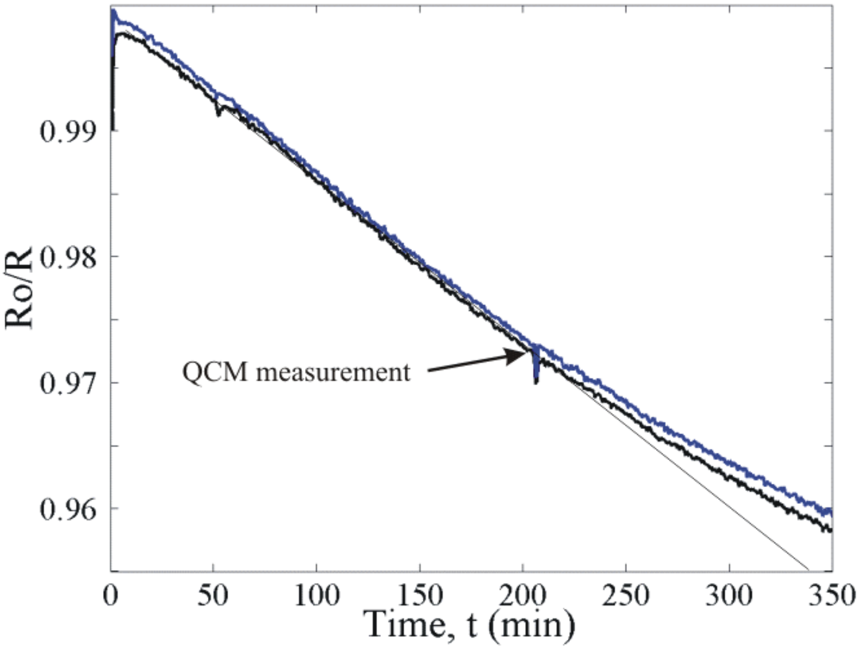

**Figure 77: Screen-printed film exposure (run 1)**

By plotting the same result as a function of fluence, it can be seen that the deviation is most likely a consequence of flux decay rather than any material changes (Figure 78). After a 'burn-in' period of about $4 \times 10^{19}$ atoms/cm$^2$, the sensor response resumes in a linear fashion. The lack of deviation around the QCM measurement point is suggestive that the fluence is well estimated at this point.

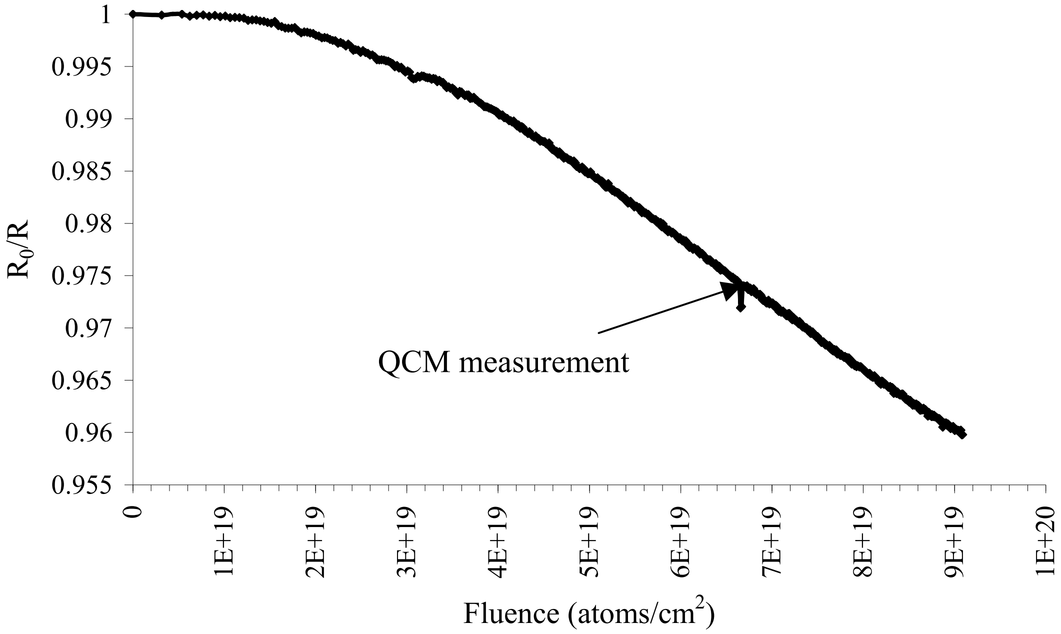

**Figure 78: Screen-printed film exposure as a function of fluence (run 1)**

Comparing the above result with lower carbon content ink, Figure 79 shows the response of two exposed 4242 ink sensors of the same substrate. The slopes for most of the exposure are different even though the material is the same. The difference can be attributed to some extent, but not completely with differences in thickness.

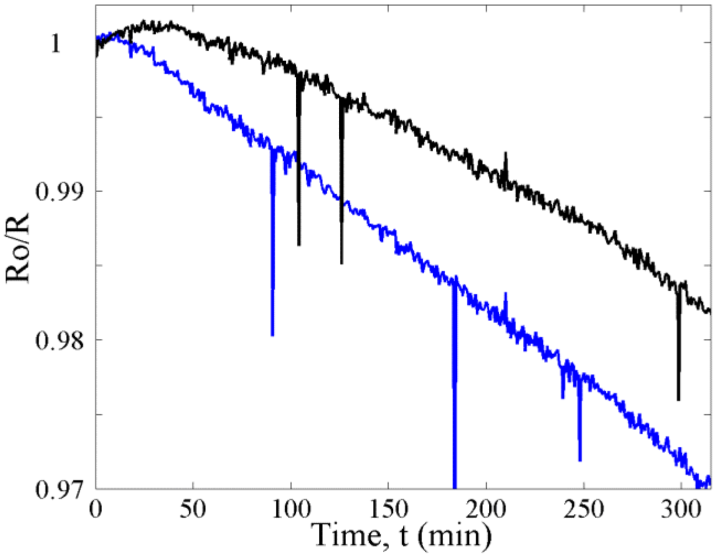

**Figure 79: Thick film exposure (run 2)**

The TEY equation derived in Chapter 3, can be expressed as a function of time and with respect to normalised resistance values as:

$$\frac{Yft}{\tau_0} - 1 = \frac{R_0}{R}$$ **Equation 44**

which can then be differentiated to make:

$$\frac{Yf}{\tau_0} = \frac{\partial (R_0 / R)}{\partial t}$$ **Equation 45**

Gradients of the two fitted response curves are:

$$\frac{\partial (R_0 / R)_1}{\partial t} = -9.0x10^{-5}$$

$$\frac{\partial (R_0 / R)_2}{\partial t} = -5.5x10^{-5}$$

using these values and the measured sensor thicknesses of 12 and 14 microns with the above equation gives:

$$(fY)_1 = 1.0x10^{-9}, (fY)_2 = 7.6x10^{-10}$$

$$\frac{(fY)_2}{(fY)_1} = 0.76$$ **Equation 46**

These values should be identical constants. The fact that they are not suggests that the sensor TEYs are different or each sensor was subjected to a different AO flux. Studies by Tighe [188] suggest flux can vary by as much as 20% across the face of the ATOX sample tray, although the sensors were probably not exposed to such differences, owing to their close proximity.

It is worth noting that although the fluence was still in a state of decay during this run, flux variations were not detected on this occasion. Inspection of the flux decay profile in Figure 32 shows that run 2 and run 3 have almost identical flux levels. This suggests that most decay could have occurred during run 1, after which the flux settled to a steady value.

From Figure 80, both sensors have similar ANLEs over exposure time, which are very small compared with the evaporated and sputtered films, as they do not exceed 0.5%. From this result, it appears that the sensors make accurate measurements, once calibrated. The results from both runs show that for the first few minutes of exposure, the response is not linear. This is thought to be due to composition variations that are discussed later.

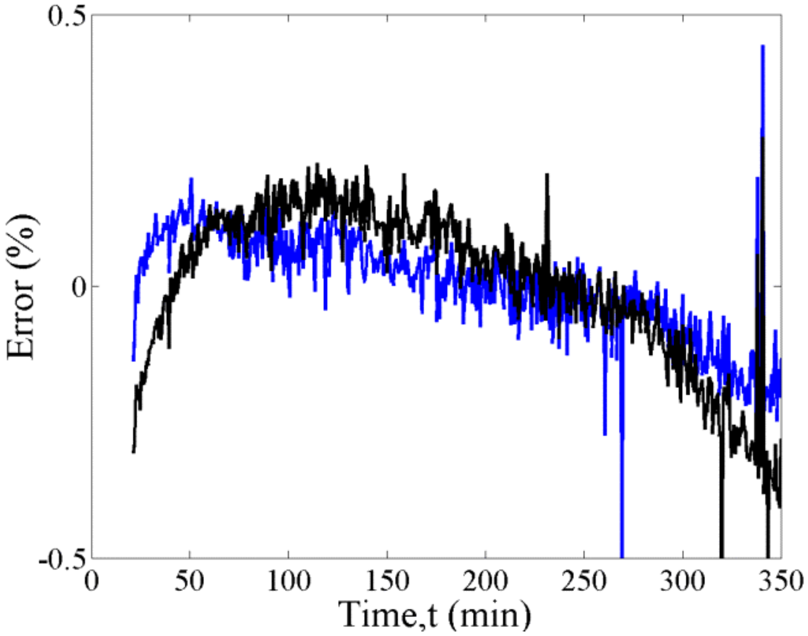

**Figure 80: Thick film sensor ANLE with respect to fitted lines (run 2)**

Run 3 tested a wide variety of thick film sensors with a different sequence of temperature changes when co-incidentally the flux levels had settled to a more steady value. Figure 81 compares the initial (25°C) and final (49°C) gradients of averaged sensor response. From the literature review of Chapter 4, it might be expected that the gradients become steeper as the temperature is increased from 25°C to 49°C, but the gradients become shallower. This could be a consequence of a small flux decay overwhelming any change in reaction rate. Temperature effects are therefore minimal in this range.

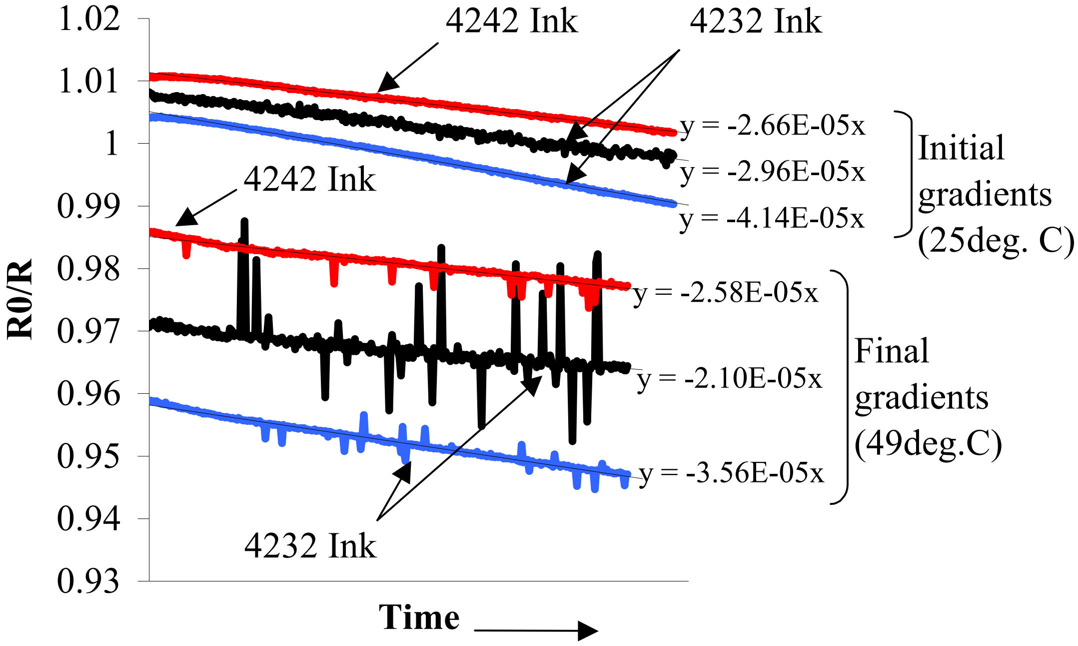

**Figure 81: Run 3 gradient changes**

As part of the CANX-2 experiment some screen-printed films were sent to Integrity Testing Laboratories (ITL) for independent assessment [189]. The main body of this work involved the exposure of the films to an oxygen plasma environment. Oxidation rates for organic materials in these facilities are known to be considerably higher than those replicating a more accurate LEO environment, so the technique is useful for accelerated testing where general, long-term performance patterns need to be assessed [86, 132].

A set of screen-printed films were exposed to the plasma in intervals alongside Kapton witness samples. The results of these experiments (Figure 82) show that the response of the screen-printed films is approximately linear throughout their life and that the thicker carbon film gives a corresponding increase in life.

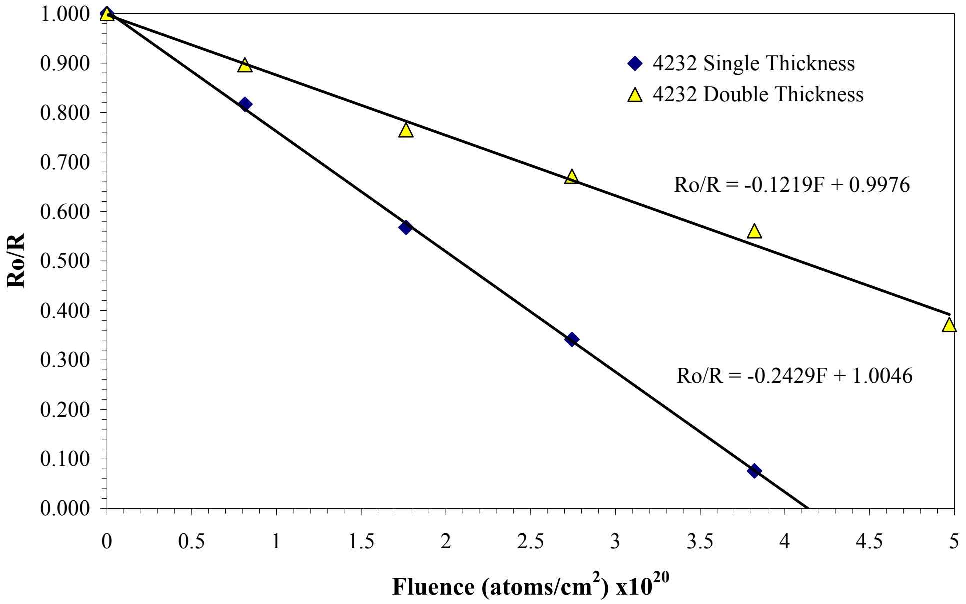

**Figure 82: Screen-printed films exposed to a plasma asher [189]**

## 10.3 Surface Modification and Chemical Content

Figure 83 and Figure 84 show SEM micrographs of a thick film sensor before and after AO exposure respectively. The micrographs reveal an almost featureless surface before AO exposure. Once the film is exposed the surface area appears to increase whilst revealing a sea of plate-like structures. EDS has detected carbon and fluorine in the regions of the plate-like features.

The plates appear to be very resistant to AO erosion because no surface roughening is observed. A common fluorinated polymer that has a significantly low erosion yield is PTFE, with yields in the range of $<0.5\times10^{-24}$ $cm^3$/atom. PTFE consists of a carbon chain backbone, with fluorine terminations, so its presence may be confirmed with Raman spectroscopy.

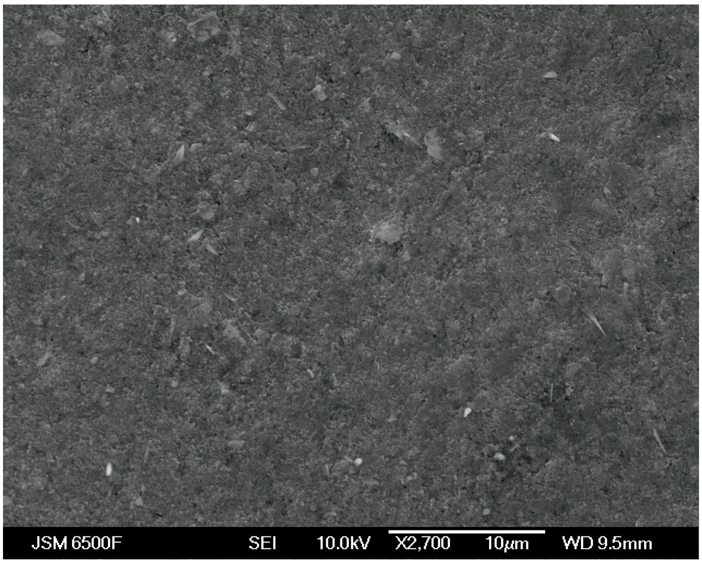

Figure 83: Unexposed thick film sensor

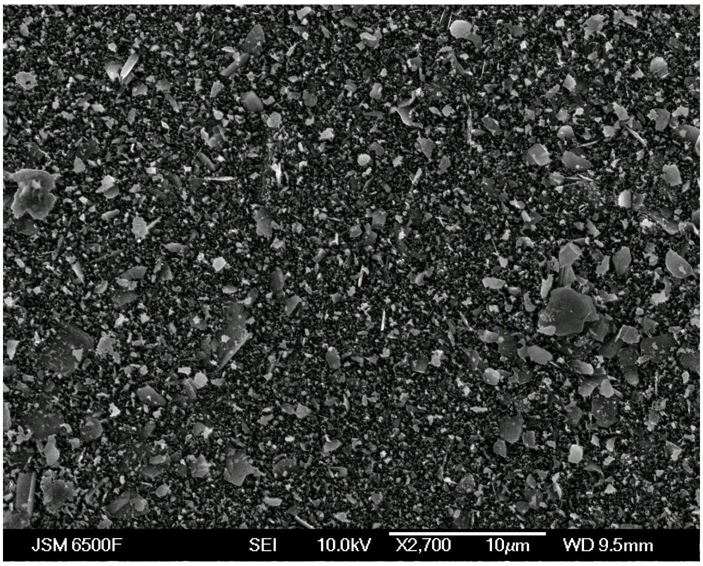

Figure 84: Exposed thick film sensor

All films showed some signs of oxygen content. Its origin is difficult to account for, as the oxygen atoms could be a part of the polymer system or have been absorbed from the atmosphere or the AO exposure environment. It is unlikely that the oxygen is due to the substrate, as the films are relatively thick and there is no aluminium signal.

Table 33 shows that nitrogen was detected. Like oxygen, the nitrogen could have been absorbed from the atmosphere or could be part of the polymer system. Subsequent Raman characterisation should reveal how the oxygen and nitrogen are bonded, which will help determine whether or not these are polymer atoms or merely contaminants. The small amounts of copper are thought to have arisen from the ablation of the copper nozzle in the ATOX facility.

The screen-printed films are a carbon-polymer composite, so the presence of hydrogen must be considered, although it cannot be detected using EDS analysis. Raman spectroscopy gives some indication of hydrogen bonding and is addressed in this chapter.

| Spectrum | C | N | O | F | Cu |
|---|---|---|---|---|---|
| 1 | 83.99 | 5.75 | 7.37 | 2.21 | 0.68 |
| 2 | 75.39 | 17.33 | 5.20 | 2.07 | - |
| 3 | 79.28 | 7.08 | 3.56 | 9.56 | 0.52 |

**Table 33: Screen printed film content (atomic percent).**

## 10.4 Raman Spectroscopy

Figure 85 shows the Raman spectra obtained from a high carbon content thick film (4232) prior to AO exposure. The spectra consist of an intense G-peak at around 1590cm$^{-1}$ on top of a very broad but shallow ‘mound’. On the left of the mound there exists a very small D-peak at around 1380 cm$^{-1}$. It can be seen that the spectra obtained are very repeatable.

The intense G-peak suggests the presence of sp$^2$ stretching, very much like pure graphite. The smaller D-peak suggests a small amount of breathing vibration, so the structure consists of aromatic rings, very much like crystalline graphite or an organic compound.

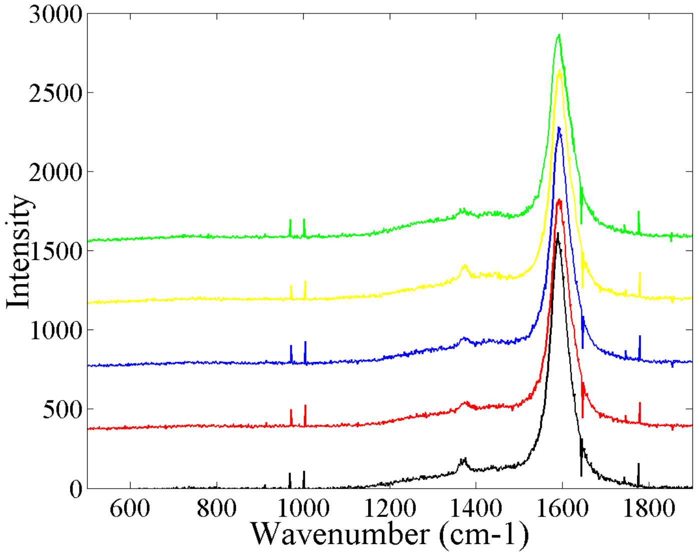

**Figure 85: Raman spectra of unexposed thick film (coupon 2)**

Comparison of the high and low carbon content inks reveal small spectral differences. Figure 86 shows that as carbon content is reduced, the G-peak broadens and the broad mound increases slightly in intensity.

When exposed to AO, the intensity of the small D-peak was found to increase significantly, as shown in Figure 87. There is also a small increase in the G-peak that is attributable to an enhanced cross-section brought about by surface roughening as seen in the microscopy. Overall the response is very repeatable for a given exposure condition.

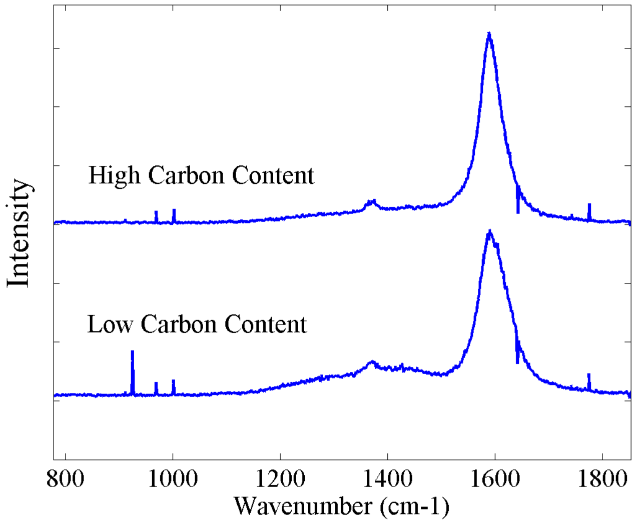

**Figure 86: Raman spectra of unexposed screen-printed films**

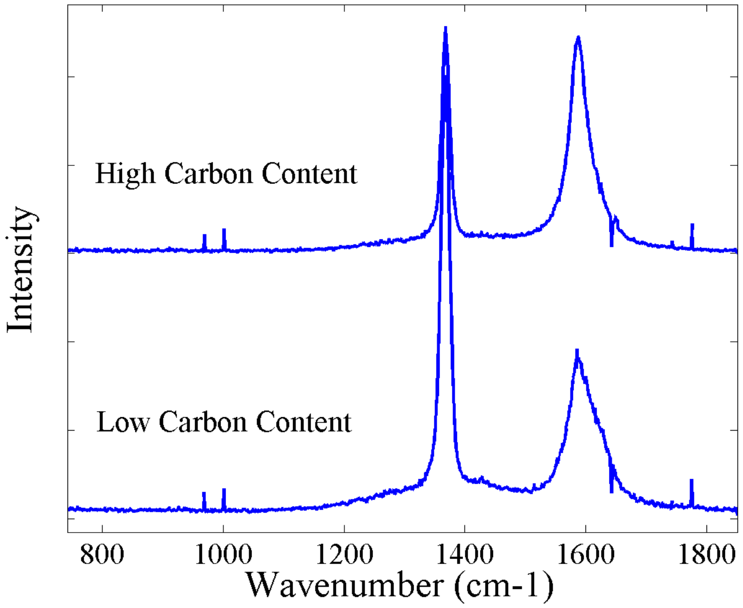

**Figure 87: Raman spectra of exposed screen-printed films**

$I_D/I_G$ for every screen-printed Raman spectrum is plotted against AO fluence to show how the $I_D/I_G$ ratio increases with AO exposure (Figure 88). The $I_D/I_G$ ratio for all films is about the same before AO exposure, but increases once exposed. The films with lower carbon content (coupons 14 and 20) show a greater increase of $I_D/I_G$ with fluence. In both inks, as fluence increases, so does the scatter in $I_D/I_G$ ratio.

These results suggest that the breathing mode before exposure is more constrained than after exposure. The constraining material could be either non-ring carbon atoms or the polymer matrix, both of which will produce an $I_G$ signal [105, 176]. Assuming that the carbon particles used in the different inks are the same and given the faster $I_D/I_G$ growth of the lower carbon content ink, it would appear the constraining material is the polymer matrix, which must be eroding faster than the carbon rings.

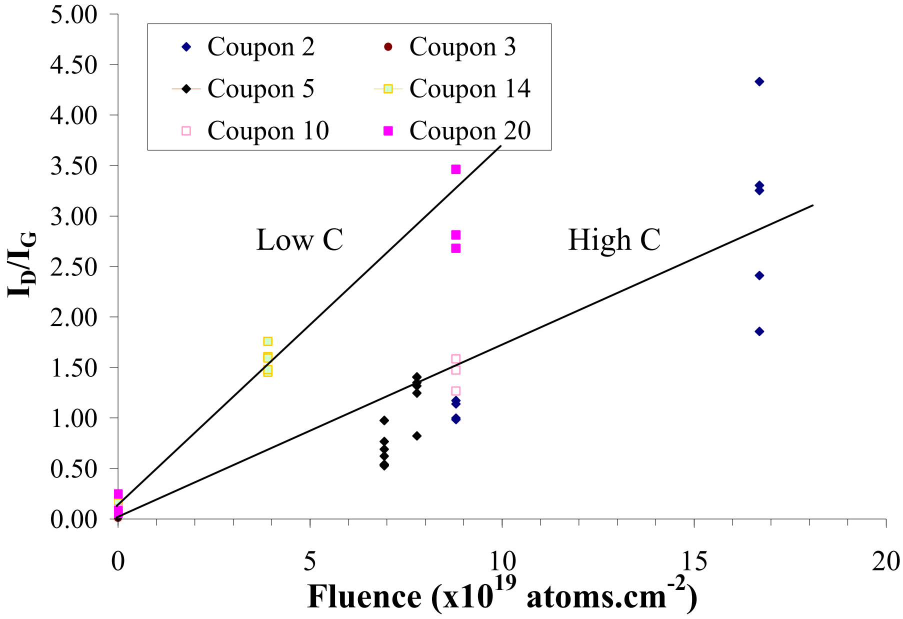

**Figure 88: Variation of $I_D/I_G$ ratio with AO fluence**

A wider spectral analysis shows a feature at around 3000cm$^{-1}$, which is expanded in Figure 89 to reveal two curve fits: one at around 2900cm$^{-1}$ and another at around 3100cm$^{-1}$. The 2900cm$^{-1}$ peak can be assigned to asymmetric $CH_2$ stretching whilst the peak at 3100cm$^{-1}$ can be assigned to an aromatic CH stretch [176].

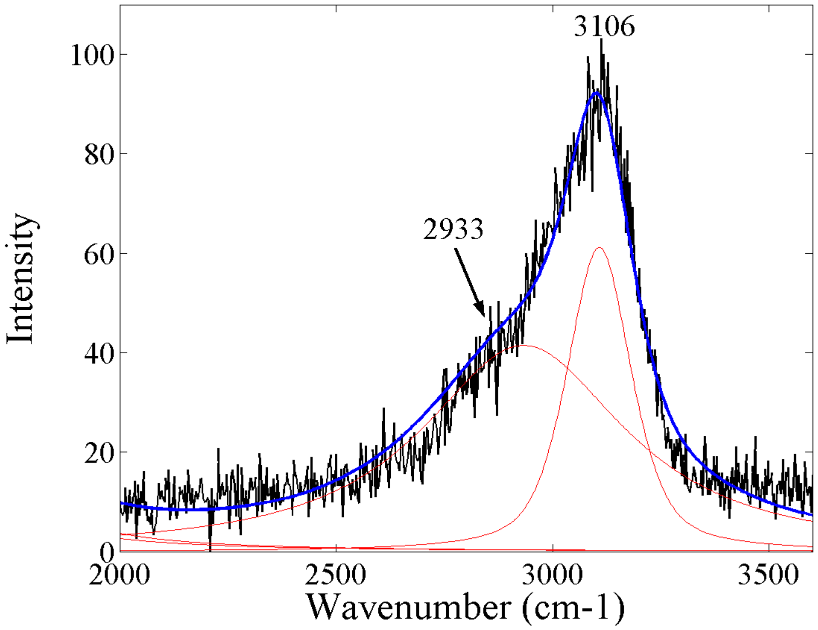

**Figure 89: Curve fit of CH stretching zone found on screen-printed UV spectra**

The broad feature that lies within 1350cm$^{-1}$ to 1423cm$^{-1}$ is assigned to N=C=O symmetric stretching, which agrees with the elemental content detected by EDS. This type of stretching is associated with isocyanates, which are used to react with alcohols to form polyurethanes (PUs).

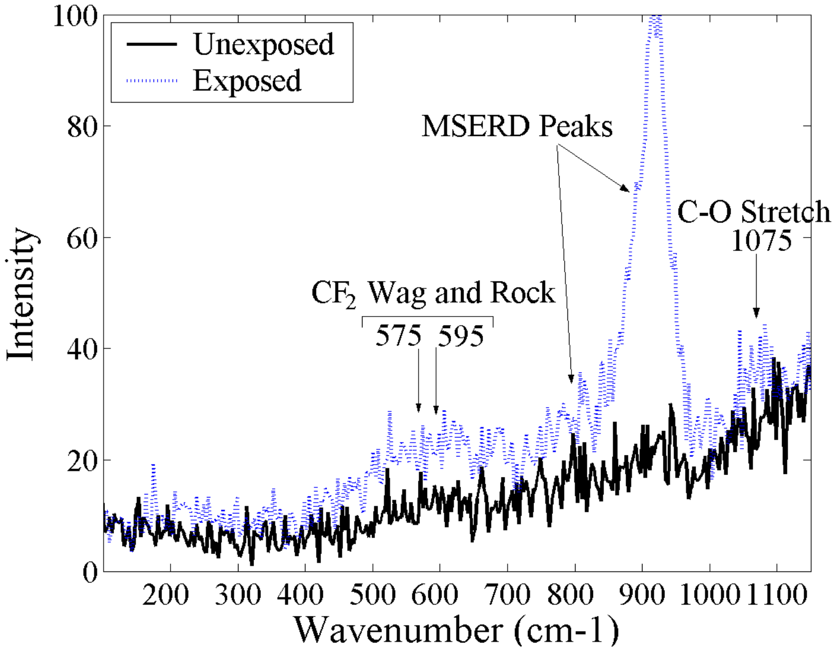

**Figure 90: Screen-printed film lower spectral range**

Many spectra showed a small peak at around 920cm$^{-1}$, which is displayed on Figure 90. This peak is thought to be representative of monosubstituted epoxide ring deformation (MSERD) [176]. Epoxides consist of a triangular arrangement of two carbon atoms and an oxygen atom, usually with other organic molecules bonded to the carbon atoms. There are two MSERD frequency ranges: one lying between 870-970cm$^{-1}$ and another between 750-880cm$^{-1}$, both of which are possible in this example. Polymers made of epoxide units are called polyepoxides (or epoxy) and are commonly used as adhesives [176].

The spectra in Figure 90 also shows some possible C-F features, which are more noticeable, post AO exposure, as are the MSERD peaks. The evidence of C-F bonding post exposure and the broadness of its peak can correlate to the post-exposure occurrence of the dispersed plate like features shown in the SEM imagery of Figure 84 and EDX spectra, although the Raman signal is very weak.

### *10.4.1 Hydrogenation*

Table 34 provides a summary of the hydrogenation estimates in the films. As this is the first incidence of using the hydrogenation estimating technique on thick composite films, much caution should be given to this aspect of the results. Validation of these results is required by further work.

| **Coupon I.D.** | **m** | **I (G)** | **H (at %)** |
|---|---|---|---|
| Coupon 3 (covered) | 500000 | 2000 | >45% |
| Coupon 3 (uncovered) | Noisy | Noisy | <20% |

**Table 34: Hydrogen content estimates**

Hydrogen content could be very high and falls above 45% in the covered condition. The noisy signal from the exposed spectrum means that the hydrogen content is harder to determine, but there is no appreciable gradient and the hydrogen content is thought to be much lower.  This implies that as the film erodes, the polymer components are reducing.

### *10.4.2 Discussion*

Raman spectroscopy has shown the $I_D/I_G$ ratio, which is initially small, to greatly increase as fluence increases, suggesting graphitic clusters are becoming more predominant. Another finding is that the levels of hydrogenation potentially fall when the films undergo AO exposure, although whether or not this continues to fall as fluence increases cannot be determined from the results.

From the current literature, many epoxies are known to erode at a similar rate to carbon, whilst PUs are known to erode faster [48]. These findings suggest that hydrogenated PU or epoxy structures, which restrict small graphite particles, are being removed preferentially during exposure to AO. The removal of this material leaves behind the fluorinated plate like structures and the graphite particles seen in the SEM analysis.

All resistance measurements taken from the screen-printed sensors during exposures show an initial period where the rate of change of resistance is at its lowest, which means fewer particles contributing to electrical conduction (the graphite) are being eroded in this regime. Given the simultaneous change in hydrogenation and the SEM images, it would appear that the non-fluorinated polymers may have a higher concentration at the surface. Table 35 shows some specific gravities of the possible constituents.

| Material | Specific gravity |
|---|---|
| Graphite | 2.2 |
| PTFE | 2.14-2.2 |
| Hylene® PPDI (DuPont Isocyanate) | 1.17 |
| Hylene® CHDI (DuPont Isocyanate) | 1.12 |
| Polyurethane | 1.12-1.24 |
| Epoxies | 1.1-1.4 |

**Table 35: Specific gravities of possible film constituents**

Graphite and PTFE is approximately double the density of the other constituents, which should give graphite and PTFE particles a higher propensity to collect towards the bottom of a film when suspended in the uncured isocyanate/polyurethane paste. These gravitational effects are likely to continue until the film has cured to a solid. If a sufficient amount of carrier ink is used, it is conceivable that the concentration of graphite and PTFE particles is much lower at the surface than at the bottom of the film.

A graphite concentration gradient of any kind would intuitively suggest the film has a thickness dependent erosion yield that would complicate its use as an actinometer. However after a short ‘burn in’ period, resistance measurements appear to form a straight line in agreement with the TEY equation. Graphite is the only substance in the screen-printed films known to conduct electrons, so it appears that the removal of graphite atoms remains constant throughout the exposure.

An important aspect of any actinometer is the need for the response to be repeatable. During run 2, the response of a sensor had ~76% TEY of a film of the same ink and exposed to the same conditions. It should be noted that these differences were the largest obtained; the results from run 1 appear to be very similar and when averaged over all the sensors, the TEY differences are no more than 16% for the same ink. Despite these differences the ANLE was very small, suggesting that the films can make very accurate AO measurements once calibrated.

# 11 FINAL DISCUSSION

## 11.1 Introduction

The previous chapters have discussed the results obtained from each deposition method, but perhaps the most important aspect of this work is to provide actinometers for real spaceflight applications. This chapter provides a discussion of the overall suitability of each deposition method for spacecraft and ground-based simulation sensing. This work has also made extensive use of Raman spectroscopy, so some discussion is made regarding the suitability of the technique for AO research.

## 11.2 Spaceflight Missions

CANX 2 and the ISS are very different in design, which influences the operation of the actinometer. The ISS will remain in a predictable circular orbit with a relatively generous power budget of 1W and a mass budget of 1kg for the entire experiment. This means a degree of thermal control can be built into the experiment by use of the thick film heaters and a separate temperature sensing circuit.

Like many low-cost nano-satellite missions, the CANX 2 design had to be finalised before knowledge of the launch vehicle or orbit. A mass limit of 3.5kg was set for the entire satellite, which includes attitude determination and control devices and a number of other experiments in addition to the AO sensing experiment [21], leaving a mass budget of 100g. The total satellite bus power is variable from 2 to 7W and must supply all systems, so the use of a dedicated temperature control circuit was not possible for this mission. The maximum power budget was set to 150mW for all times during the mission.

Many of the results presented in this thesis have shown the temperature-pressure normalised plots, which have helped isolate the response directly attributable to AO attack. The same method can be used to measure the results from both satellite experiments ensuring that some kind of AO measurement can take place even if temperatures reach levels outside the normal operating ranges.

Looking towards future applications, it is conceivable that the films could be miniaturised and more densely packed than the experiments carried out here. Using fabrication techniques that are common to micro-electromechanical systems (MEMS), the sensor area facing the AO can be significantly reduced.

The simplicity of the actinometer means that multiple devices could be made at low cost and placed over a wide area of a spacecraft, or used on formation flying satellites. The wider area of measurement from such a system will significantly increase knowledge on how can AO concentrations vary within Earth’s atmosphere.

## 11.3 Temperature Dependence

Based on the results of the first exposure run, all of the film deposition methods are capable of measuring fluence up to temperatures of ~75°C. Additionally, temperature variation did not appear to affect the response of the sensors, although the decay of the AO flux in ATOX or small compositional changes may have overwhelmed any small temperature variance that existed. The lack of significant temperature dependence means that the carbon films are well suited to LEO applications, where heating and cooling rates are known to be very high. The CONCAP II mission demonstrated that temperature dependence was minimal up to 45°C with screen-printed and vitreous carbon films [80]. This study has replicated this result for a wider variety of carbon films and extended the temperature to which it happens up to ~75°C.

This observation contrasts greatly with results obtained from a similar simulation facility where the erosion yield increased linearly, over a similar temperature range, to a value approximately four times that at the initial temperature [99]. These results were obtained from ‘microcrystalline carbon’, which may explain the differences, but without more detailed knowledge of the microstructure it is difficult to explain how the differences occur.

The lower energy exposures of Arnold and Peplinski also produced a temperature variable yield [54, 129]. This change in yield may have been brought about their simultaneous changes in AO flux or the lower beam energy. Again, it is difficult to comment on these films as their detailed composition and structure is not described in the literature.

## 11.4 Measurement Errors

Although there was no directly observable flux decay from the ATOX facility during the second exposure session, all of the AO detectors showed decay in the rate of response (Figure 91). From this, it is believed that the observed decay was due to flux changes, although there is no further evidence to strengthen this argument. The ANLEs quoted in this work may not, therefore, be exclusively attributed to sensor errors but also a measure of flux error.

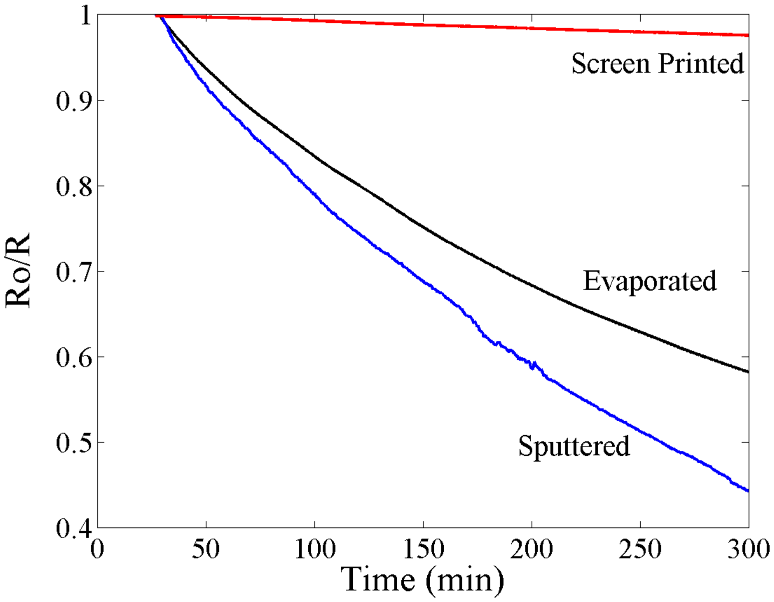

**Figure 91: Response decay during run 6**

One limitation of this work has been that mass loss could not be recorded simultaneously with changes in electrical resistance. In many cases it has not been possible to obtain post-exposure thicknesses either. The systematic actinometer errors (SAEs) that could be assessed were found to vary significantly from 0 to 24%, making it difficult to associate a particular resistance change with a precise AO dose.

Notwithstanding this limitation it appears that, with the exception of the silicon carbide contaminated samples, all the techniques appear to be capable of detecting AO fluence and changes in AO flux. The ANLEs of each deposition method are generally within acceptable sensing limits and in some cases may be attributed to flux changes rather than film error. This means that once calibrated the films are suitable for AO measurement. To make more informed conclusions on the SAE, further testing is required at different fluence levels.

## 11.5 Sensor Lifetime

The most significant advantage of carbon is that the material has a greater useful life for a given thickness of film. Figure 92 compares the results from a silver actinometer from the work of Harris [10] with one of a similar thickness of annealed evaporated carbon. The silver film has a much shorter life because it is limited by the formation of a protective oxide layer. The useful life of the carbon film extends beyond that shown on the figure, to a region at approximately $R_0/R \sim 0.2$.

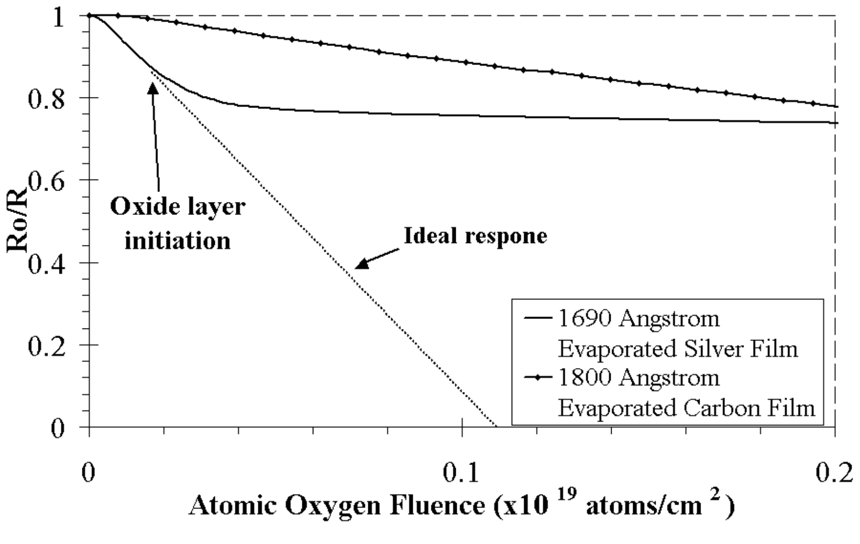

**Figure 92: Comparison of silver and carbon actinometers**

Before this work was started an additional advantage of carbon was thought to be a life that can be tailored to a particular mission by varying the $sp^2/sp^3$ ratio. Whilst this may be possible, any relationships could be very complex, as Figure 76 has already shown. If yield 'tuning' is to be done, the hydrogen content, $sp^2/sp^3$ ratio and degree of order in the film must be carefully monitored and controlled as it is the number of defects in an amorphous network that appears to influence changes in erosion yield.

An apparently easier method of adjusting the sensor lifetime is to 'tune' the thickness of the film. Whilst PVD methods have thickness limitations [106] it has been shown that, by using the screen-printing process, thicknesses can be significantly increased, whilst maintaining carbon-like characteristics.

Whilst it was found that changing the composition of the screen-printed ink did not significantly change the response of the sensor to AO, composition did affect the conductivity of the films. This means that even thicker films can be fabricated, whilst keeping similar values of initial resistance. This will allow the electronics, used to measure the resistance of the films, to be designed and fabricated before the anticipated AO fluence is known.

## 11.6 Film Selection

Taking the fluence estimates from Table 12 and Table 13 enables the construction of a performance map of each tested film (Figure 93). The maximum sensor life ($\tau_0/Y$) is plotted against the erosion yield (or sensitivity) of each material. Superimposed are lines of the anticipated annual fluence of the missions and the erosion yields currently accepted for carbon materials. For comparison, the upper limits of an evaporated silver actinometer are included [10, 139, 140].

Addressing operational requirements, the screen-printed sensors appear to be the most suitable film for an ISS mission, as they are the only film that can be expected to survive a good proportion of an extended stay in orbit.

Many of the carbon films tested are suitable for the CANX 2 mission, as their lifetimes lie within the anticipated fluence range. However, only the DS1 sputtered films (shown as a-C:Si in Figure 93) and screen-printed films will survive the worst case fluence.

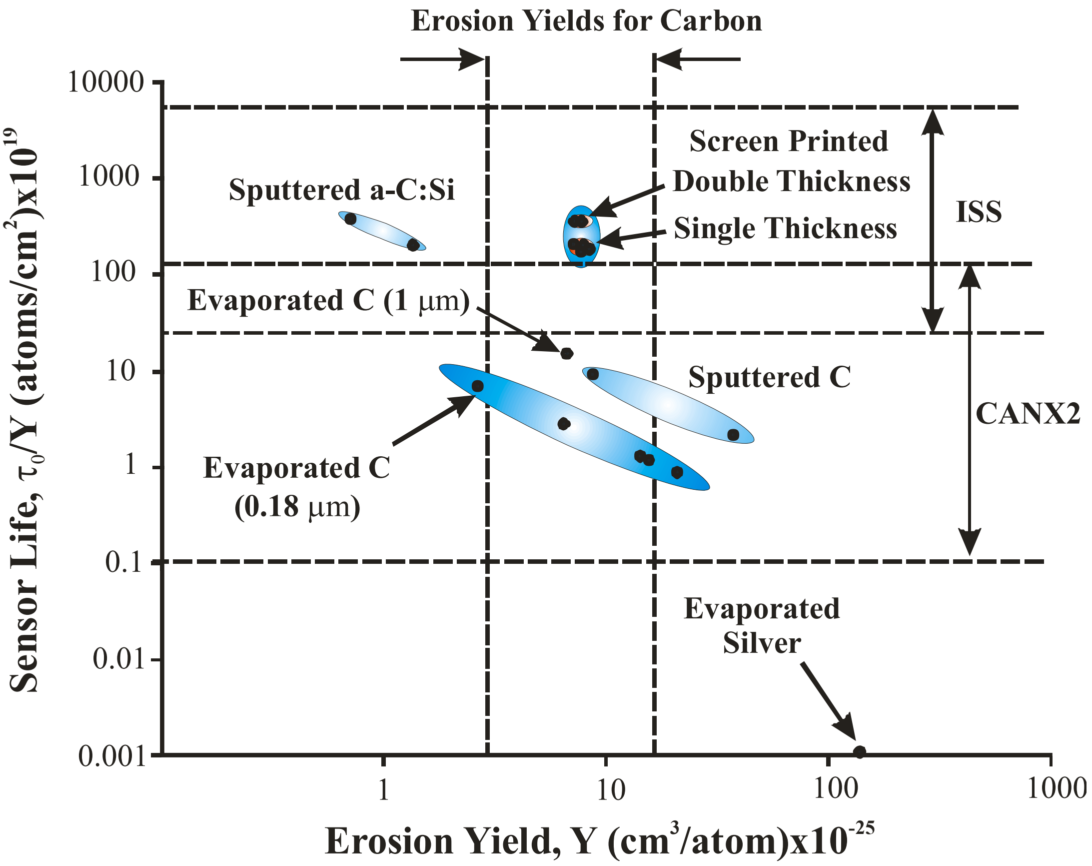

**Figure 93: Lifetime-sensitivity map of exposed materials**

In the tested state, the DS1 sputtered films show a lifetime equivalent to the screen-printed films, but with less sensitivity. However, in their present form, the films are far from an optimal design, because a surface effect is dictating the response and resistance measurements were made across a relatively thick film, on a rough substrate.

Further work should be done to investigate the maximum measurable fluence of these films and the possibility of ZnO like 'regeneration' (Chapter 9) [9]. Assuming the a-C:Si films are not eroding, but responding to AO via an absorption mechanism, films of the same content could be made thinner, on a smoother substrate to improve sensitivity.

Taking all the factors into account, the screen-printed technique appears to be the most appropriate material for both missions. This final selection is in part drawn from the further tests that are required for this material. Whilst plasma asher tests have shown the response to be linear until complete erosion, 5eV AO may yield a different result, owing to the structural complexity of the material.

Following installation of the screen-printed films into CANX2, the orbit was fixed to 600km LEO. This reduces the anticipated fluence range to $6.5\text{x}10^{18}$ to $6.5\text{x}^{20}$ atoms/cm$^2$. Figure 93 shows that both the evaporated and DS2 sputtered sensors would be ideally suited to such an orbit, but it is unfortunately too late to change the carbon film. The screen-printed films have shown good sensitivity in the ground-based experiements, within a similar fluence range, so the chosen film should still be capable of measuring AO fluence in orbit.

## 11.7 Raman Spectroscopy

### *11.7.1 Disorder Dependant Erosion Yields*

The literature review has highlighted that when hydrogenation falls somewhere between 20-35 at.% of the film content, significant variation is present in the erosion yield. From the visible Raman spectra of the evaporated films, it appears that the annealed (coupon 26) and as-deposited (coupon 202) films have approximately the same hydrogen levels (29 and 26 at. % respectively), but the ratio of erosion yields is ~2.6, confirming the erosion sensitivity.

Differences in the Raman spectra may provide a means of determining why the films are so sensitive. The most significant differences between the spectra are that coupon 202, having the lower erosion yield, has a lower, wider G-peak that is indicative of greater disorder [157].

Figure 94 shows how the estimated erosion yield is multiplied versus the average G-position of all non-sp$^3$ evaporated samples in this study. Also included, as a reference is the erosion yield range for HOPG. It appears that as the G-position reduces (indicating greater disorder) the erosion yield of the film also reduces. By adjusting the erosion yield of the annealed films to account for any density change, marked by the crosses (density increase from a-C:H to HOPG is only 150% [120]), still leads to the same general trend. Lines of best fit are given in both cases (density adjusted fit is given by the dashed line).

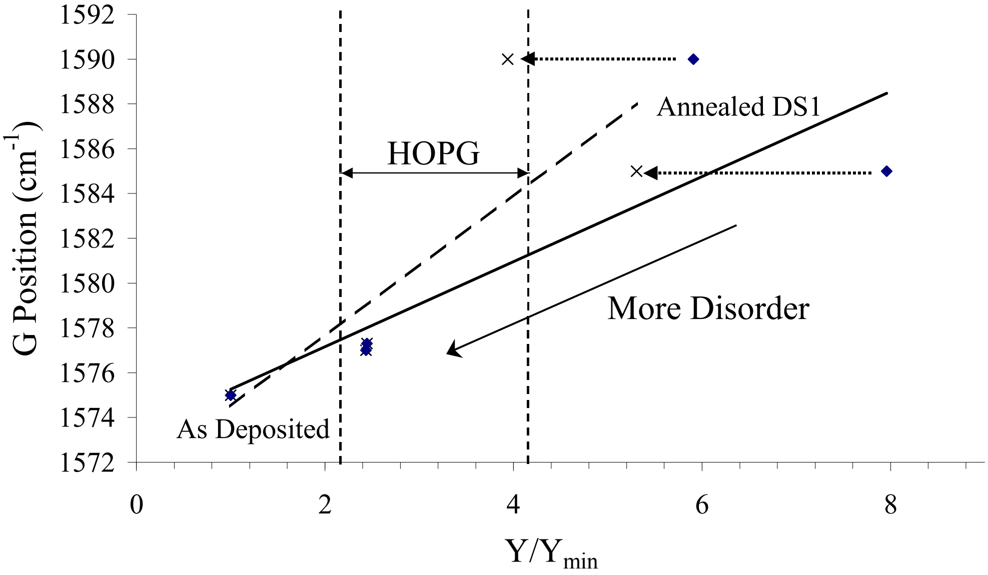

**Figure 94: UV Raman G-position versus sp$^3$ free evaporated film normalised erosion yield. Vector marked by arrows indicates potential error.**

The above result appears to work in the case of the sp$^3$ free evaporated films, but how does this compare with the data from the sputtered films, or the unusual sp$^3$ containing evaporated films?

In Chapter 9, at lower sp$^3$ levels, the DS2 *sputtered* films showed that *less* order gives *more* erosion, which is brought about by the sp$^3$ content. This contrasts greatly with the sp$^3$ free evaporated films, which appear to show *less* order gives *less* erosion. In addressing why there is a switch in trends we have to look at the content difference between the two depositions.

A convenient film to study is the as-deposited evaporated film where two different spectra were obtained. The data from the a-C like spectra showed that the G-peak is the lowest of all the sputtered and evaporated films, whilst the $sp^3$ containing regions have the highest wavenumber. The high position of the G-peak in the $sp^3$ containing segments, suggest that these regions have moved into Ferrari's '3rd stage', describing the transitions from a-C to ta-C [157]. This is where G position increases with disorder. The a-C regions are described by Ferraris '2nd stage' and the low(est) G-peak position is also indicative of high disorder. Based on G-peak positions, this film is the most disordered of the thin films.

According to the sputtered film trend, where $sp^3$ containing films may erode faster, the as deposited evaporated film should erode faster than the annealed film, but it does not. The reason for this could lie in the size of the $sp^3$ clusters, which are found to be large, but not uniformly distributed throughout the film. The $sp^3$ clusters were only detected in the pre-exposure condition; strengthening the possibility that the $sp^3$ erodes faster than the $sp^2$ clusters and that the $sp^2$ disorder increases resistance to AO attack.

From the above discussion, it appears that $sp^3$ induced disorder increases the erosion yield of the carbon film but other sources of disorder, at least for the evaporated films, appear to reduce the erosion yield. The other sources of disorder are variations in bond angle and bond length. Amorphous bonds are known to distort from their crystalline analogies to satisfy bonding requirements so more distorted lattices may be more AO resistant because the concentration of dangling bonds, which should be more reactive, is reduced.

### *11.7.2 Summary*

Raman spectroscopy has an analysis depth much deeper than techniques commonly used to characterise the effects of AO erosion (up to 1 μm)[70, 164] and unlike these techniques can analyse samples in air. Whilst the technique is not as useful in determining surface reactions, it can be used to analyse bulk properties prior to exposure.

This work has shown that disorder is a contributory factor to the reaction rate of amorphous carbon and that Raman spectroscopy could possibly be used to measure disorder. The conjecture requires strengthening by a more controlled experiment that will elucidate the existing data points. With further verification, Raman spectroscopy may become a means of estimating the lifetime of the material non-destructively.

## 11.8 PVD Contamination

Ideally, the sputtered and evaporated films should have consisted of no other element than carbon. As has already been demonstrated in Chapter 7 with ‘ideal’ HOPG samples, a pure carbon film is very difficult to achieve and is costly. This work has used a variety of fabrication techniques that provide a practicable, low cost means to produce carbon actinometers, but unfortunately this has meant that some contaminants were present in the fabricated films. The additional elements must be accounted for, if future attempts to improve the fabrication process are to be made.

The sputtering system employed in this study uses a diffusion pump to evacuate the volume where depositions take place. One major disadvantage of diffusion pumps is the tendency to back stream oil into the vacuum chamber. The oil can contaminate surfaces inside the chamber and contact with hot filaments or electrical discharges resulting in carbonaceous or siliceous deposits.

The presence of hydrogen and oxygen could be the result of air and water vapour trapped inside the deposition chamber, as a consequence of inadequate pump down time [190]. However, it should be noted that there is no evidence of water vapour in any of the Raman spectra, which would have Raman modes centered on 3400cm$^{-1}$ [176], and EDS did not detect nitrogen in the films.

Another possible explanation is that the carbon target was contaminated. The presence of hydrogen in the evaporated films cannot be due to the vacuum pumps used. The evaporation system uses a cryopump to ensure the electron beam works effectively whilst also maintaining high sample cleanliness. The control HOPG sample has shown that even the most idealised carbon samples can have some hydrogenation due to their manufacturing process.

It is conceivable that the target sample used to manufacture the sputtered and evaporated films had a lesser purity than the HOPG sample and contaminants from the target could easily be transferred to the deposited film. Unfortunately, no Raman spectrum of the target material is available.

# 12 CONCLUSIONS AND FURTHER WORK

This work has used three different fabrication methods to produce carbon films for atomic oxygen fluence measurement. The different methods each produced their own carbon content or structure, which in turn has led to different responses to an AO environment. The films have been exposed to a ground-based AO source with a view to using them for the STORM and CANX-2 space missions, which will experience high AO fluences.

For larger fluences, the screen-printed technique appears to offer a useful means of detecting AO. The fluence limit of these films is at least one order of magnitude greater than PVD techniques, without the loss of sensitivity. This fabrication technique has therefore been selected to manufacture films for both the STORM and CANX-2 missions. However, even these films may not survive the full 3-year STORM mission.

Variations in composition have so far not appeared to give a significant variation in life or performance, although they do affect the resistivity of the film. If films are to be made thicker, for greater fluence measurement, then it may be appropriate to find ways of increasing resistivity by changing the composition. This study has provided some indication of the film content, so it may be appropriate to manufacture inks that meet the new thickness requirement. Work with a plasma asher has shown the response of these films to be linear throughout their life and the STORM and CANX-2 flight experiments should eventually reveal if this trend exists in a LEO environment.

Evaporated and sputtered a-C are suitable materials for measuring AO fluences of up to $\sim 10^{20}$atoms.cm$^{-2}$. In principle the sensitivity and erosion yield of these films can be adjusted by changing levels of hydrogenation, sp$^3$ and disorder, although the relationships appear to be very complex and difficult to control.

Amorphous carbon gives uniform erosion across the face of the film, which is a requirement for reliable sensor operation. A potential trend linking the Raman G-peak position (a measure of disorder) with erosion yield has also been discussed, although further experiments are required to confirm this trend.

Whilst the contamination of these films was significant and undesirable, it has led to some interesting findings:

Silicon carbide in the sputtered sensors acted as a passivating layer by forming SiO. This made the films AO resistant, whilst maintaining some degree of electronic sensitivity to the species. By reducing the thickness of the films, sensitivity may be increased. Further work should be carried out to investigate SiC and silicon doped carbon as a sensing material, as it may have the potential of becoming closer to the 'ideal' actinometer on the lifetime-sensitivity map (Figure 93).

Hydrogenation plays an important role in the sensitivity of carbon materials and is difficult to eliminate completely. Future work should focus on controlling hydrogen levels to make yield comparisons easier. Investigations on future films with different hydrogen content would help determine how hydrogenation increases the erosion yield of carbon.

By discounting any end-effects, all of the films produced here had acceptable errors once fitted to a straight-line. Data from each deposition method showed some response to a change in AO flux that will be useful for detecting changes in LEO AO concentration. One limitation of this work has been that the films were calibrated as a function of fluence, so the precise flux levels are harder to ascertain. Further work should attempt to address this issue, perhaps by depositing the same material on a QCM and measuring the in-situ response.

All of the carbon films appear to be capable of measuring AO at temperatures from 25°C to 75°C and there does not appear to be a significant temperature dependence within this range. Whilst this result is useful for AO detection, it differs from previous experiments. Further investigations with different beam energies on microcrystalline carbons may provide an explanation for why this is happening.

Overall, the actinometers have been incorporated into two very different orbital platforms. Their small size, mass and power requirements together with their ability to make uninterrupted flux and fluence measurements mean they are well suited for measuring AO concentrations from small satellites or applications where such an experiment must not significantly intrude on a primary mission.

The size of the actinometers in this study may be made smaller by using Micro-Electro-Mechanical Systems (MEMS) fabrication techniques. Their simplicity means that multiple sensors can be made at low cost, which could make them useful for formation flying missions or large satellites where the flux/fluence distribution must be measured over a wider area.

# 13 REFERENCES

1. P. Fortescue, J.Stark, G. Swinerd, *Spacecraft Systems Engineering (Third Edition)*. 2003. 678 pages.
2. J. Feynman, S.B.Gabriel, *High Energy Charged Particles in Space at One Astronomical Unit.* IEEE Transactions on Nuclear Science, 1996. **43**(2): p. 344-352.
3. S. Deme, G.Reitz, I. Apathy, I. Hejja, E. Lang, I. Feher, *Doses Due to the South Atlantic Anomoly During the Euromir '95 Misson Measured by an On-Board TLD System.* Radiation Protection Dosimetry, 1999. **85**: p. 301-304.
4. G. Drolshagen, *Hypervelocity Impact Effects on Spacecraft.* Proceedings of Meteoroids 2001 Conference, 2001. ESA SP-495: p. 533-541.
5. J.M. Leffler, *Spacecraft External Heating Variations in Orbit.* 22nd Thermophysics Conference, 1987. AIAA-1987-1596: p. 10 Pages.
6. H.B. Garret, *The Charging of Spacecraft Surfaces.* Reviews of Geophysics and Space Physics, 1981. **19**: p. 577-616.
7. D. King-Hele, *Satellite Orbits in an Atmosphere*. 1987: Springer. 304 Pages.
8. B. A. Banks, S.K.Miller, K. K. de Groh, *Low Earth Orbital Atomic Oxygen Interactions with Materials.* NASA TM-2004-213223, 2004: p. 25 Pages.
9. J.J. Osborne, I.L. Harris, G.T. Roberts, A.R. Chambers, *Satellite and Rocket-Borne Atomic Oxygen Sensor Techniques.* Review of Scientific Instruments, 2001. **72**(11): p. 4025-4041.
10. I.L. Harris, Space and Ground Based Studies of Orbital Atomic Oxygen Effects Using Silver Film Detectors. PhD Thesis, 1997. University of Southampton.
11. I.L. Harris, A.R. Chambers, G.T. Roberts, *Preliminary Results of an Atomic Oxygen Spaceflight Experiment.* Materials Letters, 1997. **31**: p. 321-328.
12. I. L. Harris, A.R. Chambers, G. T. Roberts, *A Low Cost Microsatellite Instrument for the In-Situ Measurement of Orbital Atomic Oxygen Effects.* Review of Scientific Instruments, 1997. **68**(8): p. 3220-3228.
13. S.B. Gabriel, J.J. Osborne, G.T. Roberts, A. R. Chambers, *Development of a Renewable Atomic Oxygen Sensor for Low Earth Orbit.* Journal of Spacecraft and Rockets, 1998. **35**(3): p. 413-415.

14. J.J. Osborne, G.T. Roberts, A.R. Chambers, S.B. Gabriel, *Initial Results from Ground Based Testing of an Atomic Oxygen Sensor Designed for Use in Earth Orbit.* Review of Scientific Instruments, 1999. **70**(5): p. 2500-2506.

15. J.J. Osborne, A Study of Semiconductor Based Atomic Oxygen Sensors for Ground and Satellite Applications. PhD Thesis, 1999. University of Southampton.

16. M. Dinguirard, M.van Eesbeek, A. Tighe, C. Durin, S. Gabriel, G. Roberts, A. Chambers, D. Goulty, J.C. Mandeville, *Materials Exposure and Degradation Experiment (MEDET).* AIAA 4th International Conference on International Space Station Utilisation, 2001. AIAA-2001-5070.

17. D. Goulty, C.White, S. Gabriel, G. Roberts, A. Chambers, N. Ross, *The Southampton Transient Oxygen and Radiation Monitor (STORM).* Proceedings of the 10th ISMSE and 8th ICPMSE, 2006: 7 Pages.

18. C. Underwood, G. Richardson, J. Savignol, *SNAP-1: A Low Cost Modular COTS-Based Nano-Satellite - Design, Construction, Launch and Early Operations Phase.* Proceedings of the 15th AIAA/USU Conference on Small Satellites, 2001: 7 Pages.

19. Y. Tsuda, N.Sako, T. Eishima, T. Ito, Y. Arikawa, N. Miyamura, K. Norihide, K. Kanairo, S. Ukawa, S. Ogasawara, S. Ishikawa, *University of Tokyos CubeSat "XI" as a Student Built Educational Pico-Satellite - Final Design and Operation Plan.* Proceedings of the 23rd International Symposium on Space Technology and Science, 2002. **2**: p. 1372-1377.

20. R. Blott, N. Wells, *The Space Technology Research Vehicles: STRV-1A,B, C and D,* Proceedings of the 10th Annual Small Satellite Conference, 1996. **Session I**: p. 8 Pages.

21. K. Sarda, S. Eagleson., E. Caillibot, C. Grant, D. Kekez, F. Pranajaya, R.E. Zee, *Canadian Advanced Nanospace Experiment 2: Scientific and Technological Innovation on a Three-Kilogram Satellite.* Acta Astronautica, 2006. **59**: p. 236-245.

22. J. Sorensen, *CEPF (Columbus External Payload Facility) Environmental Specification.* Prepared for European Space Agency Space Station Utilisation Division (ESA/ESTEC/MSM-GU), 2000: p. 129 Pages.

23. C. Casiraghi, F. Piazza, A.C. Ferrari, D. Grambole, J. Robertson, *Bonding in Hydrogenated Diamond-Like Carbon by Raman Spectroscopy.* Diamond and Related Materials, 2005. **14**: p. 1098-1102.

24. C. Casiraghi, A.C. Ferrari, J. Robertson, *Raman Spectroscopy of Hydrogenated Amorphous Carbons.* Physical Review B, 2005. **72**(085401): p. 1-14.

25. G. Adamopoulos, J. Robertson, N.A. Morrison, C. Godet, *Hydrogen Content Estimation of Hydrogenated Amorphous Carbon by Visible Raman Spectroscopy.* Journal of Applied Physics, 2004. **96**(11): p. 6348-6352.

26. A.C. Ferrari, *Determination of Bonding in Diamond-Like Carbon by Raman Spectroscopy.* Diamond and Related Materials, 2002. **11**: p. 1053-1061.

27. K.W.R. Gilkes, S. Prawer, K.W. Nugent, J. Robertson, H.S. Sands, Y. Lifshitz, X. Shi, *Direct Quantitative Detection of the Sp3 Bonding in Diamond-Like Carbon Films using Ultraviolet and Visible Raman Spectroscopy.* Journal of Applied Physics, 2000. **87**(10): p. 7283-7289.

28. Z. Iskanderova, J. Kleiman, V. Issoupov, A. Chambers, G. Roberts, C. White. *Development of Small Reliable Atomic Oxygen Sensors of Polymeric Carbon Filled Resistor Compositions*. in Proceedings of the 10th ISMSE and 8th ICPMSE. 2006. Collioure, France: ESA Publication SP 616.

29. D.N.O. Goulty, C.B.White, S.B. Gabriel, G.T. Roberts, A.R. Chambers, J.N. Ross. *The Southampton Transient Oxygen and Radiation Monitor (STORM)*. in *Proceedings of the 10th ISMSE and 8th ICPMSE*. 2006. Collioure, France: ESA Publication SP 616.

30. C.B. White, A.R.Chambers, G.T. Roberts. Screen Printed Carbon Films for Atomic Oxygen Measurement. in Proceedings of the 10th ISMSE and 8th ICPMSE. 2006. Collioure, France: ESA Publication SP 616

31. C.B. White, J. Rao, G.T. Roberts, A.R. Chambers, K.J. Lawson, J.R. Nicholls. *The Development of Carbon Based Sensors for the Measurement of Atomic Oxygen*. in Proceedings of the 9th International Symposium on Materials in a Space Environment. 2003. Noordwijk, The Netherlands, p. 137-144.

32. C.B. White, A.R. Chambers, G.T. Roberts. *Carbon Based Atomic Oxygen Sensors*. in Proceedings of the 2nd IEEE International Conference on Sensors. 2003. Toronto, Canada, p. 1287-1292.

33. C.B. White, J.C.Valer, A.R. Chambers, G.T. Roberts. *Atomic Oxygen Source Calibration Issues: A Universal Approach*. in Proceedings of the 7th ICPMSE. 2004. Toronto, Canada.

34. C.B. White, G.T. Roberts, A.R. Chambers, *Measurement of 5 eV Atomic Oxygen using Carbon Based Films: Preliminary Results.* IEEE Sensors Journal, 2005. **5**: p. 1206-1213.

35. I.L. Harris, Space and Ground Based Studies of Orbital Atomic Oxygen Effects Using Silver Film Detectors. PhD Thesis, 1997. University of Southampton.

36. L.A. Teichman, B.A.Stein., *NASA/SDIO Space Environmental Effects Materials Workshop.* NASA CP-3035, 1989. **Part 1**: p. 373 Pages.

37. J.M. Wallace, P.V. Hobbs, *Atmospheric Science: An Introductory Survey*. 1977: Academic Press (NY). 467.

38. J.B. Cross, S.L. Koontz, E.H. Lan, Atomic Oxygen Interaction with Spacecraft Materials: Relationship Between Orbital and Ground-Based Testing for Materials Certification. Proceedings of the 5th International Symposium on Materials in a Space Environment, 1991: p. 369-384.

39. J. Kleiman, Z. Iskanderova., Y. Gudimenko, S. Horodetsky, *Atomic Oxygen Beam Sources: A Critical Overview.* Proceedings of the 9th International Symposium on Materials in a Space Environment, 2003: p. 313-324.

40. R. Collins, J.C. Valer, *Personal Communication.* 2003.

41. M. M. Finckenor, D.L. Edwards, J. A. Vaughn, T. A. Schneider, M. A. Hovater, D. T. Hoppe, *Test and Analysis Capabilities of the Space Environment Effects Team at Marshall Space Flight Center.* NASA Technical Memorandum, 2002. **2002-212076**.

42. D. Dooling, M.M.Finckenor., Material Selection Guidelines to Limit Effects on Spacecraft Surfaces. NASA TP 1999-209260, 1999.

43. G.E. Caledonia, R.H. Krech., B.D. Green, *A High Flux Source of Energetic Oxygen Atoms for Material Degradation Studies.* AIAA Journal, 1987. **25**(1): p. 59-63.

44. E. Grossman, I. Gouzman, V. Viel-Inguimbert, M. Dinguirard, *Modification of a 5eV Atomic Oxygen Laser Detonation Source.* Journal of Spacecraft and Rockets, 2003. **40**(1): p. 110-113.

45. J.B. Cross, Laboratory Investigations: Low Earth Orbit Environment Chemistry with Spacecraft Surfaces. Space Operations Automation and Robotics Workshop, 1989.

46. D. Morrison, R.C. Tennyson, Y. B. French, *Microwave Oxygen Atom Beams Source.* Proceedings of the 4th European Symposium on Materials in a Space Environment, 1988: p. 435-441.

47. R. A. Outlaw, M.R. Davidson, *Small Ultrahigh Vacuum Compatible Hyperthermal Oxygen Atom Generator.* Journal of Vacuum Science and Technology A, 1994. **12**(3): p. 854-860.

48. E.M. Silverman, Space Environmental Effects on Spacecraft: LEO Materials Selection Guide. NASA CP-4661, 1995. **Part 1**.

49. 68 Months in Space: A History of the First LDEF (Long Duration Expsoure Facility) Flown in Space, NASA Langley Research Center. p. 14 Pages.

50. H. B. Garrett, A. Chutjian, S.B. Gabriel, *Space Vehicle Glow and its Impact on Spacecraft Systems.* Journal of Spacecraft and Rockets, 1988. **25**(5): p. 321-340.

51. P. M. Banks, P.R. Williamson, W. J. Raitt, *Space Shuttle Glow Observations.* Geophysical Research Letters, 1983. **10**(2): p. 118-121.

52. J.J. Osborne, A Study of Semiconductor Based Atomic Oxygen Sensors for Ground and Satellite Applications. PhD Thesis, 1999. University of Southampton.

53. I. L. Harris, A.R.Chambers, G. T. Roberts, M. B. J. Van Eesbeek, *The Laboratory Testing of Silver and Polymeric Material in Atomic Oxygen Flows.* Proceedings of the 6th International Symposium on Materials in a Space Environment, 1994. SP-368: p. 195-200.

54. G.S. Arnold, D.R. Peplinski, *Reaction of High Velocity Atomic Oxygen with Carbon.* AIAA Journal, 1986. **24**(4): p. 673-677.

55. A. Gindulyte, L. Massa, B.A. Banks, S.K.R. Miller, *Direct C-C Bond Breaking in the Reaction of O(3P) with Flouropolymers in Low Earth Orbit.* Journal of Physical Chemistry A, 2002. **106**(22): p. 5463-5467.

56. S. Koontz, L. Leger, K. Albyn, J. Cross, *Vacuum Ultraviolet Radiation/Atomic Oxygen Synergism in Materials Reactivity.* Journal of Spacecraft and Rockets, 1990. **27**: p. 346-348.

57. K. Yokota, S. Seikyu, M. Tagawa, N. Ohmae, A Quantitative Study in Synergistic Effects of Atomic Oxygen and Ultraviolet Regarding Polymer

Erosion in LEO Space Environment. Proceedings of the 9th International Symposium on Materials in a Space Environment, 2003. ESA SP-540: p. 265-272.

58. T.K. Minton, Protocol for Atomic Oxygen Testing of Materials in Ground-Based Facilities. NASA CR 95-112589, 1995: p. 40 pages.

59. ASTM, Standard Practices for Ground Laboratory Atomic Oxygen Interaction Evaluation of Materials for Space Application. ASTM E2089-00, 2000: p. 5 Pages.

60. L. Leger, B. Santos-Mason, J. Visentine, J. Kuminecz, *Review of LEO Flight Experiments.* Proceedings of the NASA Workshop on Atomic Oxygen Effects, 1987: p. 1-10.

61. K. Yokota, M. Tagawa, N. Ohmae, *Temperature Dependence in Erosion Rates of Polyimide Under Hyperthermal Atomic Oxygen Exposures.* Journal of Spacecraft and Rockets, 2002. **40**(1): p. 143-144.

62. D.E.Hunton, E.Trzcinski, J.B.Cross, L.H.Spangler, M.H.Hoffbauer, F.H.Archuleta, J.T.Visentine, *Mass Spectrometers and Atomic Oxygen.* Proceedings of the NASA Workshop on Atomic Oxygen Effects, 1987. JPL 87-14: p. 21-28.

63. F. Kaufman, *Reactions of Oxygen Atoms.* Progress in Reaction Kinetics, 1961. **1**(1): p. 1-39.

64. M.A. Butler, A.J. Ricco, Applied Physics Letters, 1988. **53**: p. 1471.

65. M.A. Butler, A.J. Ricco, Sensors and Actuators, 1989. **19**: p. 249.

66. F.J. Grunthaner, Analytical Chemistry, 1995. **67**: p. A605.

67. D.A. Wallace, Use of the Quartz Crystal Microbalance for Outgassing and Optical Contamination Measurements. The Journal of Vacuum Science and Technology, 1971. **9**(1): p. 462-466.

68. G. Drolshagen, M.Van Eesbeek, *Atomic Oxygen Fluence Detector for BREMSAT: Scientific and Technical Description.* Proceedings of the 5th International Symposium on Materials in a Space Environment, 1991: p. 405-408.

69. M. Van Eesbeek, Atomic Oxygen Fluence Detector for BREMSAT Scientific and Technical Result Reporting. ESTEC Working Paper 1921, 1996: p. 95 Pages.

70. H. Kinoshita, J. Ikeda, M. Tagawa, M. Umeno, N. Ohmae, *Hyperthermal Atomic Oxygen Interaction with Highly Orientated Pyrolytic Graphite Studied by Scanning Tunnelling Microscopy.* Proceedings of the 7th International Symposium on Materials in a Space Environment, 1997.
71. H. Kinoshita, M.Umeno, M. Tagawa, N. Ohmae, Hyperthermal Atomic Oxygen Beam-Induced Etching of HOPG (0001) Studied by X-Ray Photoelectron Spectroscopy and Scanning Tunneling Microscopy. Surface Science, 1999. **440**: p. 49-59.
72. J.J. Osborne, I.L. Harris, G.T.Roberts, A.R. Chambers, *Satellite and Rocket-Borne Atomic Oxygen Sensor Techniques.* Review of Scientific Instruments, 2001. **72**(11): p. 4025-4041.
73. R.J. Thomas, A Thin Film Silver Detector for the Direct Measurement of Atomic Oxygen in the Upper Atmosphere. PhD Thesis, 1970. Utah State University: 155 pages.
74. D. B. Oakes, R.H. Krech, B. L. Upschulte, G. E. Caledonia, *Oxidation of Polycrystalline Silver Films by Hyperthermal Oxygen Atoms.* Journal of Applied Physics, 1995. **77**(5): p. 2166-2172.
75. F. Kaufman, Progress in Reaction Kinetics, 1961. **1**: p. 1.
76. W. M. Moore, P.J.Codella., *Oxidation of Silver Films by Atomic Oxygen.* Journal of Physical Chemistry, 1988. **92**: p. 4421-4426.
77. J.B. Cross, Laboratory Investigations: Low Earth Orbit Environment Chemistry with Spacecraft Surfaces. Space Operations Automation and Robotics Workshop, 1989.
78. P.J. Codella, *The Oxidation of Silver Thin Films by Atomic Oxygen.* PhD Thesis, 1977. Utah State University: 173 pages.
79. G.E. Caledonia, R.H. Krech, D.B. Oakes, *Laboratory Simulation of Low Earth Orbit (LEO) Atomic Oxygen Effects.* 18th Space Simulation Conference, 1994. CP 3280: p. 113-120.
80. Y. Asakura, Nippon Kagaku Zasshi, 1967. **90**: p. 987.
81. A.R. Chambers, I.L.H., G.T.Roberts, *Reactions of Spacecraft Materials with Fast Atomic Oxygen.* Materials Letters, 1996. **26**: p. 121-131.
82. A.D. Rooij, *The Degradation of Metal Surfaces by Atomic Oxygen.* 3rd European Symposium on Materials in the Space Environment, 1985. **ESA SP-232**: p. 99-109.

83. A.D. Rooij, *An Approach to the Long Term Predictions of the Atomic Oxygen Effect on Materials.* 4th International Symposium on Materials in a Space Environment, 1988: p. 453-462.

84. W. R. Henderson, H.I. Schiff, A Simple Sensor for the Measurement of Atomic Oxygen Profiles in the Upper Atmosphere. Planetary Space Science, 1970. **18**: p. 1527-1534.

85. W.R. Henderson, Silver Film Atomic Oxygen Sensors: Further Evidence for Utility as an Atmospheric Probe. Canadian Journal of Physics, 1974. **52**: p. 2174-2175.

86. B.A. Banks, S.K. Rutledge, J.A. Brady, *The NASA Atomic Oxygen Effects Program.* Proceedings of the 15th Space Simulation Conference, 1988. NASA CP-3015: p. 51-65.

87. S.L. Koontz, G.King, H.A. Dunnet, T.D. Kirkendahl, R.C. Linton, J. Vaughn, The International Telecommunications Satellite (INTELSAT) Solar Array Coupon (ISAC) Atomic Oxygen Flight Experiment: Techniques, Results and Summary. 5th International Symposium on Materials in a Space Environment, 1991: p. 331-348.

88. J. C. Gregory, G.N. Raiker., *Preliminary Results from the CONCAP-II-01 and EOIM-3 Experiments on STS 46.* LDEF Materials Results for Spacecraft Applications, 1992. NASA CP 3257: p. 439-452.

89. G.P. Miller, P.J. Pettigrew, G.N. Raikar, J.C. Gregory, *A Simple, Inexpensive, Hyperthermal Atomic Oxygen Sensor.* Review of Scientific Instruments, 1997. **68**(9): p. 3557-3562.

90. H.H. Tobben, G.A.Ringel, D.R. Schmitt, P. Weiβbrodt, M. Schrenk, *In-Flight Exposure Experiment SESAM.* Proceedings of the 2nd European Symposium on Utilisation of the International Space Station, 1998. ESA SP 433.

91. F. W. Reynolds, G.R.Stillwell, *Mean Free Paths of Electrons in Evaporated Metal Films.* Physical Review, 1952. **88**: p. 418-419.

92. R. J. Thomas, D.J. Baker, *Silver Film Atomic Oxygen Sensors.* Canadian Journal of Physics, 1972. **50**: p. 1676-1681.

93. J.J. Osborne, G.T. Roberts, A.R. Chambers, S.B. Gabriel, *Thin-Film Semiconductor Sensors for Hyperthermal Oxygen Atoms.* Sensors and Actuators B, 2000. **63**: p. 55-62.

94. A. Jacob, *Detection of Atomic Oxygen and Hydrogen Beams by Semiconductors.* Journal of Applied Physics, 1975. **46**(12): p. 5116-5121.

95. P.N. Peters, J.C. Gregory, J.T. Swann, *Effects on Optical Systems from Interactions with Oxygen Atoms in Low Earth Orbits.* Applied Optics, 1986. **25**(8): p. 1290-1298.

96. P.N. Peters, R.C. Linton, E.R. Miller, Results of Apparent Atomic Oxygen Reactions on Ag, C, and Os Exposed During the Shuttle STS-4 Orbits. Geophysical Research Letters, 1983. **10**(7): p. 569-571.

97. J.C. Gregory, G.P. Miller, P.J. Pettigrew, G.N. Raikar, J.B. Cross, E. Lan, C.L. Renschler, W.T. Sutherland, *Atomic Oxygen Dosimetry Measurements Made on STS-46 by CONCAP-II.* LDEF 3rd Post-Retrival Symposium, 1993. CP-3275: p. 957-970.

98. W. Haenni, H.Baumann, C. Comninellis, D. Gandini, P. Niedermann, A. Perret, N. Skinner, *Diamond-Sensing Microdevices for Environmental Control and Analytical Applications.* Diamond and Related Materials, 1998. **7**: p. 569-574.

99. C.E. Caledonia, R.H. Krech, D.B. Oakes, *Laboratory Studies of Fast Atomic Oxygen Interactions with Materials.* Proceedings of the 6th International Symposium on Materials in a Space Environment, 1994: p. 285-290.

100. J.C. Dawson, C.J.Adkins, *Conduction Mechanisms in Amorphous Carbon Prepared by Ion-Beam Sputtering.* Journal of Physics - Condensed Matter, 1995. **7**(31): p. 6297-6315.

101. L.E. Bareiss, R.M. Payton, H.A. Papazian, *Shuttle/Spacelab Contamination Environment and Effects Handbook.* NASA CP-4053, 1987. **Section 3**: p. 3.1-3.30.

102. R.C. Tennyson, K.G.Balmain, M.R. Wertheimer, D.G. Zimcik, *Evaluation of Plasma-Deposited Protective Coatings for Spacecraft Applications.* 5th International Symposium on Materials in a Space Environment, 1991: p. 385-400.

103. E.B.P. Bourdon, R.H. Prince, W.D. Morison, R.C. Tennyson, *Real Time Monitor for Thin Film Etching in Atomic Oxygen Environment.* Surface and Coatings Technology, 1992. **52**(1): p. 51-56.

104. ESA, *European Space Agency TEAMSAT Web Page.* http://www.estec.esa.nl/teamsat/team/fipex/fipex.html, 2004: p. Last Accessed 19th September 2004.

105. J. Robertson, *Diamond-like Amorphous Carbon.* Materials Science and Engineering, 2002. **R37**: p. 129-281.

106. H.O. Pierson, Handbook of Carbon, Graphite, Diamond and Fullerenes - Properties, Processing and Applications. 1993: Noyes Publications. 399.

107. N.F. Mott, E.A.Davis, *Electronic Processes in Non-Crystalline Materials.* Oxford University Press, London, 1979: 437 Pages.

108. J. Robertson, *Diamond-like Amorphous Carbon.* Materials Science and Engineering, 2002. **R37**: p. 129-281.

109. E.B.D. Bourdon, R.H. Prince, *Growth Mechanisms of Diamond-like Films Formed by Laser Ablation of Graphite.* Applied Surface Science, 1991. **48-9**: p. 50-54.

110. E.B.D. Bourdon, W.W. Duley, A.P. Jones, R.H. Prince, *Characterization of Diamond-like Films Prepared by Laser Ablation of Graphite.* Surface and Coatings Technology, 1991. **47**(1-3): p. 509-516.

111. Y. Lifshitz, *Diamond-Like Carbon - Present Status.* Diamond and Related Materials, 1999. **8**(8-9): p. 1659-1676.

112. A. Grill, *Diamond-Like Carbon: State of the Art.* Diamond and Related Materials, 1999. **8**: p. 428-434.

113. J.E. Field, *Properties of Diamond.* 1993, London: Academic Press.

114. B.T. Kelly, *Physics of Graphite.* 1981, London: Applied Science Publishers.

115. T. Irifune, A. Kurio, S. Sakamoto, T. Inoue, H. Sumiya, *Ultrahard Polycrystalline Diamond from Graphite.* Nature, 2003. **421**: p. 599-600.

116. T. Irifune, A. Kurio, S. Sakamoto, T. Inoue, H. Sumiya, K. Kunakoshi, *Formation of Pure Polycrystalline Diamond by Direct Conversion of Graphite at High Pressure and High Temperature.* Physics of the Earth and Planetary Interiors, 2004. **143-144**: p. 593-600.

117. S. Chattopadhyay, K.H. Chen, L.C. Chen, *Elastic, Mechanical, and Thermal Properties of Nanocrystalline Diamond Films.* Journal of Applied Physics, 2003. **93**(4): p. 2164-2171.

118. S. Mrozowski, Electric Resistivity of Polycrystalline Graphite and Carbons. Physical Review, 1950. **77**(6): p. 838.

119. S. Mrozowski, Semiconductivity and Diamagnetism of Polycrystalline Graphite and Condensed Ring Systems. Physical Review, 1952. **85**(4): p. 609-620.

120. J. Robertson, *Amorphous Carbon.* Advances in Physics, 1986. **35**(4): p. 317-374.

121. G.M. Pharr, D.L. Callahan, S.D. McAdams, T.Y. Tsui, S. Anders, A. Anders, J.W. Ager, I.G. Brown, C.S. Bhatia, S.R.P. Silva, J. Robertson, *Hardness, Elastic Modulus, and Structure of Very Hard Carbon Films Produced by Cathodic-Arc Deposition with Substrate Pulse Biasing.* Applied Physics Letters, 1996. **68**: p. 779-781.

122. D.R. McKenzie, *Tetrahedral Bonding in Amorphous Carbon.* Reports on Progress in Physics, 1996. **59**: p. 1611-1664.

123. P.J. Fallon, V.S.V., C.A. Davis, J. Robertson, G.A.J. Amaratunga, W.I. Milne, J. Koskinen, *Properties of Filtered-Ion-Beam-Deposited Diamondlike Carbon as a Function of Ion Energy.* Physical Review B, 1993. **48**: p. 4777-4782.

124. P. Koidl, C. Wagner, B. Dischler, J. Wagner, M. Ramsteiner, *Properties and Characterization of Amorphous Carbon Films.* Materials Science Forum, 1990. **52**: p. 41.

125. M. Weiler, S.Sattel, K. Jung, H. Ehrhardt, V.S. Veersamy, J. Robertson, *Highly Tetrahedral Diamond-like Amorphous Hydrogenated Carbon Prepared from a Plasma Beam Source.* Applied Physics Letters, 1994. **64**(21): p. 2797-2799.

126. M.F. Ashby, D.R.H. Jones, *Engineering Materials*. 1978, Oxford: Pergamon Press.

127. G.M. Jenkins, K. Kawamura, *Polymeric Carbons-Carbon Fibre, Glass and Char*. 1976, Cambridge: Cambridge University Press.

128. C. Park, *Effects of Atomic Oxygen on Graphite Ablation.* AIAA Journal, 1976. **14**(11): p. 1640-1642.

129. G.S. Arnold, D.R. Peplinski, Reaction of Atomic Oxygen with Vitreous Carbon: Laboratory and STS-5 Data Comparisons. AIAA Journal, 1985. **23**(6): p. 976-977.

130. J.C. Gregory, *On the Linearity of Fast Atomic Oxygen Effects.* LDEF Materials Results for Spacecraft Applications, 1992. NASA CP 3257: p. 193-198.

131. T. Ngo, E.J. Snyder, W. M. Tong, R. S. Williams, M.S. Anderson, *O Atom Etching of Graphite in Low Earth Orbit.* Surface Science, 1994. **314**: p. L817-L822.

132. B.A. Banks, S.K. Rutledge, *Low Earth Orbital Atomic Oxygen Simulation for Materials Durability Evaluation.* 4th International Symposium on Materials in a Space Environment, 1988: p. 371-392.

133. S.L. Koontz, K. Albyn, L.J. Leger, *Atomic Oxygen Testing with Thermal Atom Systems: A Critical Evaluation.* Journal of Spacecraft and Rockets, 1991. **28**(3): p. 315-323.

134. R.A. Synowicki, J.S. Hale, B. Spady, M. Reiser, S. Nafis, J.A. Woollam, *Thin Film Materials Exposure to Low Earth Orbit Aboard Space Shuttle.* Journal of Spacecraft and Rockets, 1995. **32**(1): p. 97-102.

135. A. Joshi, R. Nimmagadda, *Erosion of Diamond Films and Graphite in Oxygen Plasma.* Journal of Materials Research, 1991. **6**(7): p. 1484-1490.

136. L.J. Leger, Oxygen Atom Reaction with Shuttle Materials at Orbital Altitudes - Data and Experiment Status. AIAA Paper 83-0073, 1983.

137. E.B.D. Bourdon, A. Raveh, S.C. Gujrathi, L. Martinu, *Etching of a-C:H Films by an Atomic Oxygen Beam.* Journal of Vacuum Science and Technology A, 1993. **11**(5): p. 2530-2535.

138. B. Singh, L.J. Amore, W. Saylor, G. Racette, Laboratory Simulation of Low Earth Orbital Atomic Oxygen Interaction with Spacecraft Surfaces. AIAA Paper 85-0477, 1985.

139. I.L. Harris, A.R. Chambers, G.T. Roberts, *Preliminary Results of an Atomic Oxygen Spaceflight Experiment.* Materials Letters, 1997. **31**: p. 321-328.

140. I.L. Harris, A.R. Chambers, G.T. Roberts, *A Low Cost Microsatellite Instrument for the In-Situ Measurement of Orbital Atomic Oxygen Effects.* Review of Scientific Instruments, 1997. **68**(8): p. 3220-3228.

141. G.E. Galica, B.D.Green, P.B. Joshi, T. Nakamura, H. Matsumoto, H, Koshiishi, T. Goka, Y. Kimoto, T. Abe, H, Kobayashi. *Atomic Oxygen Monitor Based on Carbon Actinometers for the ISS Japanese Experiment Module*. in *Proceedings of the 10th ISMSE and 8th ICPMSE*. 2006. Collioure, France: ESA SP 616.

142. J. Rao, Personal Communication. 2004.

143. A. Singh, P. Lavigne, Deposition of Diamond-like Carbon Films by Low Energy Ion Beam and D.C. Magnetron Sputtering. Surface and Coatings Technology, 1991. **47**: p. 188-200.

144. M. Gioti, S. Logothetidis, The Effect of Substrate Bias in Amorphous Carbon Films Prepared by Magnetron Sputtering and Monitored by In-Situ

Spectroscopic Ellipsometry. Diamond and Related Materials, 1998. **7**: p. 444-448.

145. J. Luthin, C. Linsmeier, Characterization of Electron Beam Evaporated Carbon Films and Compound Formation on Titanium and Silicon. Physica Scripta, 2001. **T91**: p. 134-137.

146. J. Besold, R. Thielsch, N. Matz, C. Frenzel, R. Born, A. Mobius, *Surface and Bulk Properties of Electron Beam Evaporated Carbon Films.* Thin Solid Films, 1997. **293**: p. 96-102.

147. Z. Zhang, L. Lam, J. Atkinson, C. Maul, Miniature Thick Film Position Sensor for Real Time In-Situ Monitoring at the Contact Point of Automotive Connectors. Measurement Science and Technology, 2005. **16**: p. 1567-1573.

148. Y. Lam, J. Atkinson, *Disposable Screen-Printed Biosensor for Transcutaneous Oxygen Measurement.* Measurement Science and Technology, 2002. **13**: p. 2074-2081.

149. J. Atkinson, *Personal Communication.* 2002.

150. J.J. Osborne, An Investigation of the Effects of Sample Distance and Laser Repetition Rate on the Flux in the Atomic Oxygen Facility at the European Space Research and Technology Centre (ESTEC). ESA/ESTEC D-TOS/QMC Report 98/038, 1998.

151. B. Weihs, M.V. Eesbeek, *Secondary VUV Erosion Effects on Polymers in the ATOX Atomic Oxygen Exposure Facility.* Proceedings of the 6th International Symposium on Materials in a Space Environment, 1994. ESA SP 368: p. 277-283.

152. T.K. Minton, *Personal Communication.* 2004.

153. A. Kailer, K.G. Nickel, Y.G.Gogotsi, *Raman Microspectroscopy of Nanocrystalline and Amorphous Phases in Hardness Indentations.* Journal of Raman Spectroscopy, 1999. **30**: p. 939-946.

154. A.C. Ferrari, J. Robertson, *Interpretation of Raman Spectra of Disordered and Amorphous Carbon.* Physical Review B, 2000. **61**: p. 14095-14107.

155. A. Chehaidar, A. Zwick, R. Carles, Investigation of Structural and Chemical Ordering in Si Rich Amorphous SiC Alloys via Raman Spectroscopy and Numerical Modelling. Journal of Physics - Condensed Matter, 2001. **13**: p. 10743-10755.

156. A.C. Ferrari, J. Robertson, *Origin of the 1150-cm$^{-1}$ Raman Mode in Nanocrystalline Diamond.* Physical Review B, 2001. **63**(121405): p. 1-4.

157. A.C. Ferrari, J. Robertson, *Resonant Raman Spectroscopy of Disordered, Amorphous and Diamond-Like Carbon.* Physical Review B, 2001. **64**: p. 075414 1-13.

158. A.K. Sood, R.Gupta, S.A. Asher, Origin of the Unusual Dependence of Raman D Band on Excitation Wavelength in Graphite-Like Materials. Journal of Applied Physics, 2001. **90**(9): p. 4494-4497.

159. G. Adamopoulos, K.W.R. Gilkes, J. Robertson, N.M.J. Conway, B.Y. Kleinsorge, A. Buckley, D.N. Batchelder, *Ultraviolet Raman Characterisation of Diamond-Like Carbon Films.* Diamond and Related Materials, 1999. **8**: p. 541-544.

160. J. Dong, W. Shen, B. Tatarchuk, *Origin of Strong G' Band in Raman Spectra of Carbon Whiskers.* Applied Physics Letters, 2002. **80**(20): p. 3733-3735.

161. I. Pocsik, M. Hundhausen, M. Koos, L. Ley, *Origin of the D peak in the Raman Spectrum of Microcrystalline Graphite.* Journal of Non-Crystalline Solids, 1998. **227-230**: p. 1083-1086.

162. M. Veres, M. Koos, S. Toth, M. Fule, I. Pocsik, A.Toth, M. Mohai, I. Bertoti, *Characterisation of a-C:H and Oxygen Containing Si:C:H Films by Raman Spectroscopy.* Diamond and Related Materials, 2005. **14**: p. 1051-1056.

163. S. Parnell, K. Min, M. Cakmak, Kinetic Studies of Polyurethane Polymerization with Raman Spectroscopy. Polymer, 2003. **44**: p. 5137-5144.

164. K.T. Nicholson, A. Cisse, T.K. Minton, S.J. Sibener, *A Mechanistic Study of Graphite Erosion by Hyperthermal ($O_3P$) Atomic Oxygen: A Scanning Probe Study.* 9th International Symposium on Materials in a Space Environment, 2003: p. 107-112.

165. F. Parmigiani, E. Kay, H. Seki, Raman Scattering and X-Ray Photoemission Spectroscopy Studies of Carbon Films Sputtered in a Triode System by Ne, Ar, and Xe. Journal of Applied Physics, 1988. **64**(6): p. 3031-3036.

166. J.M. Yanez-Limon, F. Ruiz, J. Gonzalez-Hernandez, C. Vazquez-Lopez, E. Lopez-Cruz, *Characterization of Carbon Films Microstructure by Atomic Force Microscopy and Raman Spectroscopy.* Journal of Applied Physics, 1994. **76**(6): p. 3443-3447.

167. J.G. Grasselli, B.J.Bulkin, ed. *Analytical Raman Spectroscopy*. Chemical Analysis, ed. J.D. Winefordner. Vol. 114. 1991, Wiley. 462.

168. A.C. Ferrari, A. Libassi, B.K. Tanner, V. Stolojan, J. Yuan, L.M. Brown, S.E. Rodil, B. Kleinsorge, J. Robertson, Density, Sp3 Fraction and Cross Sectional Structure of Amorphous Carbon Films Determined by X-Ray Reflectivity and Electron Loss Spectrocopy. Physical Review B, 2000. **62**: p. 11089-11103.

169. A.C. Ferrari, B. Kleinsorge, N.A. Morrison, A. Hart, V. Stolojan, J. Robertson, *Stress Reduction and Bond Stability During Thermal Annealing of Tetrahedral Amorphous Carbon.* Journal of Applied Physics, 1999. **85**(10): p. 7191-7197.

170. J. Schwan, S. Ulrich, V. Batori, H. Ehrhardt, S.R.P. Silva, *Raman Spectroscopy on Amorphous Carbon Films.* Journal of Applied Physics, 1996. **80**(1): p. 440-447.

171. T. Mikami, H. Nakazawa, M. Kudo, M. Mashita, Effects of Hydrogen on Film Properties of Diamond-Like Carbon Films Prepared by Reactive Radio-Frequency Magnetron Sputtering Using Hydrogen Gas. Thin Solid Films, 2005. **488**: p. 87-92.

172. E.B.D. Bourdon, P.Kovarik, R.H. Prince, *Microcrystalline Diamond Phase by Laser Ablation of Graphite.* Diamond and Related Materials, 1993. **2**: p. 425-431.

173. Y. Fan, A.G. Fitzgerald, P. John, C.E. Troupe, J.I.B. Wilson, *X-Ray Photoelectron Spectroscopy Studies of CVD Diamond Films.* Surface and Interface Analysis, 2002. **34**: p. 703-707.

174. S. Gupta, B.R. Weiner, G. Morell, *Spectroscopic Ellipsometry Studies of Nanocrystalline Carbon Thin Films Deposited by HFCVD.* Diamond and Related Materials, 2001. **10**: p. 1968-1972.

175. R.O. Dillon, J.A. Woollam, V. Katkanant, Use of Raman Scattering to Investigate Disorder and Crystallite Formation in As-Deposited and Annealed Carbon Films. Physical Review B, 1984. **29**: p. 3482-3489.

176. G. Socrates, Infrared and Raman Characteristic Group Frequencies. 3rd ed. 2001: Wiley.

177. P.E.J. Flewitt, R.K. Wild, *Physical Methods for Materials Characterisation.* 1993, Bristol: Institute of Physics.

178. P.A. Temple, C.E. Hathaway, *Multiphonon Raman Spectrum of Silicon.* Physical Review B, 1973. **7**(8-15): p. 3685-3697.

179. M.R. Reddy, *Review Effect of Low Earth Orbit Atomic Oxygen on Spacecraft Materials.* Journal of Materials Science, 1995. **30**(2): p. 281-307.

180. M.A. Capano, N.T. McDevitt, R.K. Singh, F. Qian, *Characterization of Amorphous Carbon Thin Films.* Journal of Vacuum Science and Technology A, 1996. **14**(2): p. 431-435.

181. J.W. Ager, *Optical Characterization of Sputtered Carbon Films.* IEEE Transactions on Magnetics, 1993. **29**(1): p. 259-263.

182. A.K.M.S. Chowdhury, D.C. Cameron, M.S.J. Hashmi, J.M. Gregg, *Evidence of Continuous Areas of Crystalline B-C3N4 in Sputter Deposited Thin Films.* Journal of Materials Research, 1999. **14**(6): p. 2359-2363.

183. V. Vorlicek, P. Sirosky, J. Sobota, V. Perina, V. Zelezny, J. Hrdina, *C:N and C:N:O Films: Preparation and Properties.* Diamond and Related Materials, 1996. **5**: p. 570-574.

184. M.Y. Chen, D. Li, X. Lin, V.P. Dravid, Y. Chung, M. Wong, W. D. Sproul, *Analytical Electron Microscopy and Raman Spectroscopy Studies of Carbon Nitride Thin Films.* Journal of Vacuum Science and Technology A, 1993. **11**: p. 521-524.

185. M. Jelinek, W. Kulisch, M.P. Delplancke-Ogletree, V. Vorlicek, V. Studnicka, D. Chvostova, M. Trchova, J. Sobota, *Application Relevant Characterization of Magnetron-Sputtered Carbon Nitride Films.* Diamond and Related Materials, 1999. **8**: p. 1857-1862.

186. G. Messina, A.Paoletti, S. Santangelo, A. Tagliaferro, A. Tucciarone, *Nature of Non-D and Non-G Bands in Raman Spectra of a-C:H(N) Films Grown by Reactive Sputtering.* Journal of Applied Physics, 2001. **89**(2): p. 1053-1058.

187. G.N. Raikar, J.C. Gregory, W.D. Partlow, H. Herzig, W.J. Choyke, *Surface Characterization of SiC Mirrors Exposed to Fast Atomic Oxygen.* Surface and Interface Analysis, 1994. **23**(2): p. 77-82.

188. A. Tighe, *Personal Communication*. 2005.

189. Z. Iskanderova, J.Kleiman, V. Issoupov, A. Chambers, G. Roberts, C. White. *Oxidation Protective Surface Modifiation of Graphite and Polymer-based Carbon Filled Conductive Coatings*. in 5th International Symposium on Polymer Surface Modification. 2005. Toronto, Canada.

190. J. Rao, Personal Communication. 2005.

191. H. Li, T. Xu, J. Chen, H. Zhou, H. Liu, *Preparation and Characterization of Hydrogenated Diamond-Like Carbon Films in a Dual DC-RF Plasma System.* Journal of Physics D: Applied Physics, 2003. **36**: p. 3183-3190.

192. K.W.R. Gilkes, H.S. Sands, D.N. Batchelder, W.I. Milne, J. Robertson, *Direct Observation of Sp3 Bonding in Tetrahedral Amorphous Carbon UV Raman Spectroscopy.* Journal of Non-Crystalline Solids, 1998. **227-230**(1): p. 612-616.

193. B.R. Jackson, C.C. Trout, J.V. Badding, *UV Raman Analysis of the C:H Network Formed by Compression of Benzene.* Chemistry of Materials, 2003. **15**: p. 1820-1824.

194. W. Krasser, A. Fadini, A.J. Renouprez, *The Raman Spectrum of Carbon Monoxide Chemisorbed on Silica-Supported Nickel.* Journal of Catalysts, 1979. **62**(1): p. 94-98.

195. I. Mrozek, C. Pettenkofer, A. Otto, *Raman Spectroscopy of Carbon Monoxide Adsorbed on Silver Island Films.* Surface Science, 1990. **238**(1-3): p. 192-198.

196. T.P. Nguyen, S. Lefrant, *Raman Spectra of Silicon Monoxide.* Solid State Communications, 1985. **57**(4): p. 235-236.

197. B. Racine, A.C. Ferrari, N.A. Morrison, I. Hutchings, W.I. Milne, J. Robertson, *Properties of Amorphous Carbon-Silicon Alloys Deposited by a High Plasma Density Source.* Journal of Applied Physics, 2001. **90**(10): p. 5002-5012.

198. J.R. Shi, X. Shi, Z. Sun, E. Liu, H.S. Yang, L.K. Cheah, X.Z. Jin, *Structural Properties of Amorphous Silicon-Carbon Films Deposited by the Filtered Cathodic Vacuum Arc Technique.* Journal of Physics - Condensed Matter, 1999. **11**(26): p. 5111-5118.

## APPENDIX A1: STORM SENSOR HOLDER

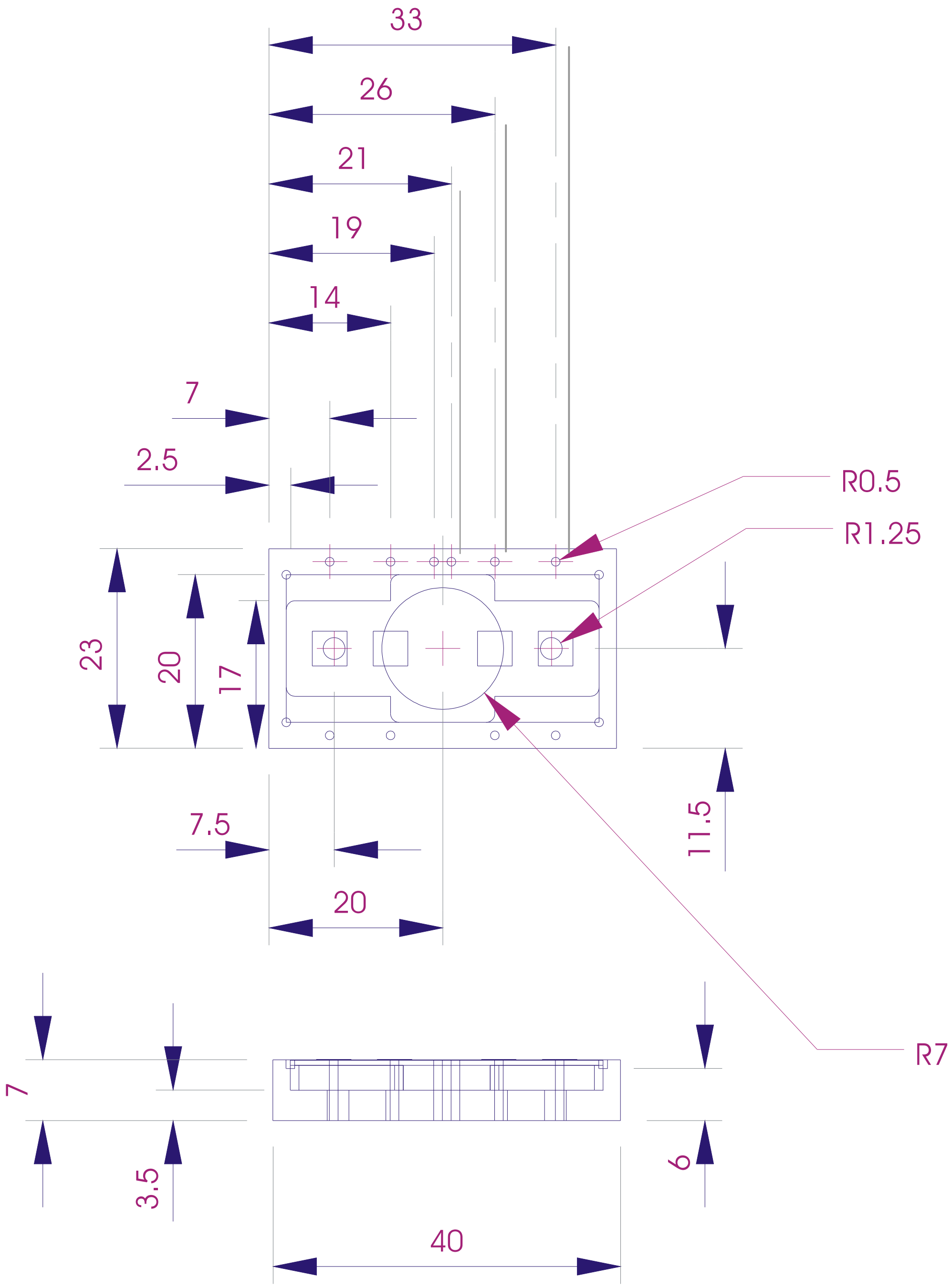

# STORM Sensor Holder

Alumina substrate shown in place
Not to scale
Dimensions in mm
Material: PTFE
Tolerance: +/- 0.25mm

# APPENDIX A2: CHARACTERISATION TECHNIQUES

| Analytical Technique | Typical Applications | Signal Detected | Elements Detected | Depth Resolution | Lateral Resolution |
|---|---|---|---|---|---|
| AFM/SPM | Surface imaging with near atomic resolution | Atomic scale roughness | - | 0.01 nm | 1.5-5 nm |
| FE Auger | Elemental surface analysis, micro-area depth profiling | Auger electrons from near surface atoms | Li-U | 2-6 nm | <15nm |
| Raman | Identification of organics and inorganics | Raman scattering | Molecular chemical identification | 1-2 µm | 1 µm |
| RBS | Quantitative thin film composition and thickness | Backscattered He atoms | Li-U | 2-20 nm | 2 mm |
| SEM/EDS | Imaging and elemental microanalysis | Secondary and backscattered electrons and X-rays | B-U | 1-5 µm | 4.5nm (SEM)<br>1 µm (EDS) |
| FEG SEM | High resolution imaging of polished precision cross sections | Secondary and backscattered electrons | - | - | 1.5 nm |
| SIMS | Dopant and impurity depth profiling, surface and microanalysis | Secondary ions | H-U | 5-30 nm | 1-30 µm |
| TEM | High resolution imaging of thinned cross sections and planar samples | Transmitted electrons | - | - | 0.1 nm |
| XPS | Surface analysis of organic and inorganic molecules | Photoelectrons | Li-U | 1-10 nm | 10 µm – 2mm |
| XRD | Crystal phase identification, orientation and crystallite size | Diffracted X-rays | - | - | 20 µm |

**Summary of Analytical Techniques, adapted from Baumann [194]**

# APPENDIX A3: INTERPRETATION OF RAMAN SPECTRA

## A3.1 Evaporated Films

### *A3.1.1 DS 1 Curve Fitting*

Figure 95 shows the complete UV spectrum and curve fit of an evaporated sensor from DS1. The signal is noisy due to the thinness of the film but some simple features can be extracted. A G-peak at 1582cm$^{-1}$ and a D-peak at 1403cm$^{-1}$ have been fitted with no evidence of a diamond or sp$^3$ T peak. The width of the D-peak confirms that this is an amorphous carbon [105]. A molecular oxygen peak is also fitted at 1555cm$^{-1}$ and the spike at 2320cm$^{-1}$ has been highlighted, as this is the absorption of atmospheric nitrogen. Unfortunately due to the thinness of the DS1 evaporated sensors, it was not possible to collect post AO exposure Raman spectra. Attempts were made, but only the substrate material could be detected.

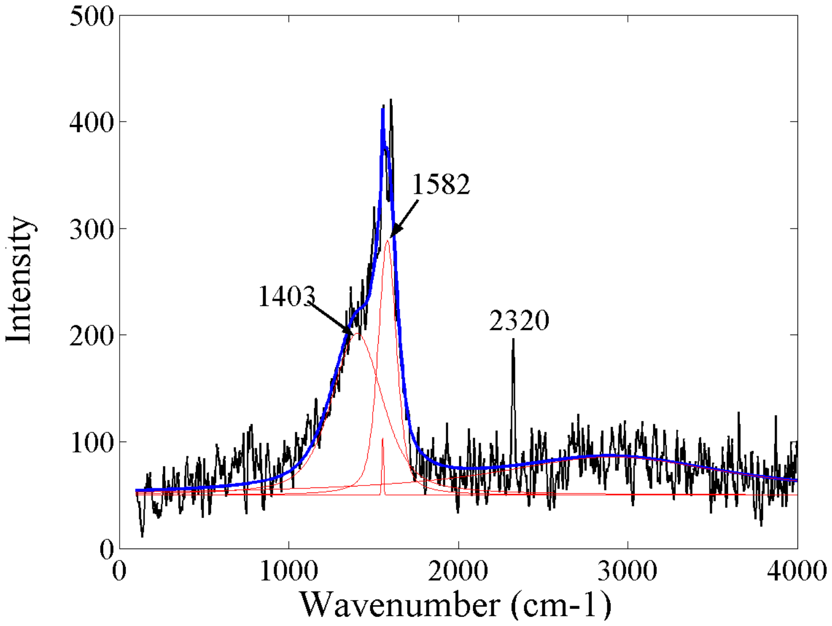

**Figure 95: Curve fit of Raman spectrum for annealed evaporated film (coupon 26)**

The D-peak location at 1403cm$^{-1}$ is high compared to other works, but is within limits of UV excited samples. As already highlighted, a general trend of the D-peak in all carbons is to increase in wavenumber as the excitation wavelength decreases [157]. In

Figure 36 the D-peak lies at around 1450cm$^{-1}$ at the excitation energy of 4.82eV used here. Whilst the D-peak of the film is lower this value, a similar shift can be expected owing to structural differences[191], usually by the size or number of aromatic clusters[154, 158].

The spectral results show two different kinds of spectra in the case of untreated films. Figure 96 shows one of the glassy-like spectrums and the curves fitted to it. The position of the G-peak has moved from around 1580cm$^{-1}$, past 1600cm$^{-1}$ to around 1606cm$^{-1}$. This is usually a good indication that sp$^3$ exists in the film[154], where the position can shift up to 1690cm$^{-1}$ due to short, strained C=C bonded chains[157]. The shift is relatively small and the G-peak has a width comparable to the a-C heat-treated case, which is generally indicative of lower sp$^3$ content [192].

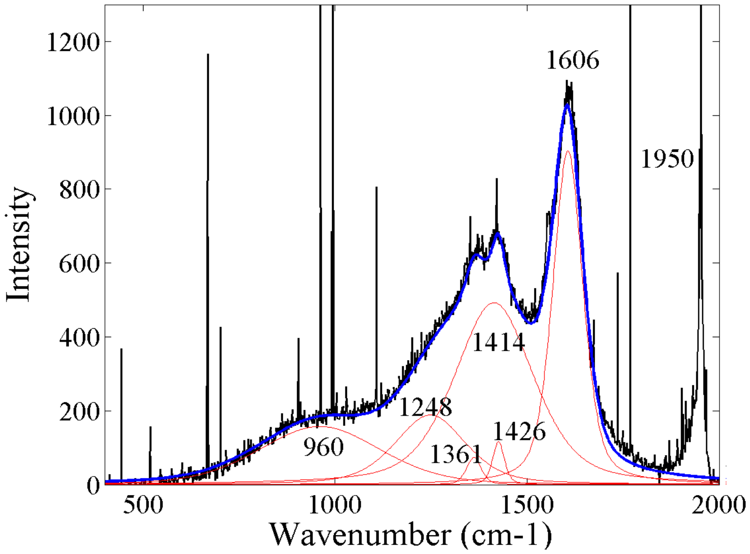

**Figure 96: Curve fit of Raman spectrum for untreated evaporated film (coupon 41)**

The presence of sp$^3$ means that a T peak should be evident in the spectra, which is known to exist between 980cm$^{-1}$ and 1250cm$^{-1}$[157, 159]. There are two possible peak fits for this assignment: the curve at 960cm$^{-1}$ and the other at 1248cm$^{-1}$.

Regardless of peak identity, both peaks have approximately the same height so the sp$^3$ ratio can be estimated from the $I_T/I_G$ ratio. Table 36 shows the G-peak and potential T-peak heights for both the “glassy-like” spectra. Comparing these results with those of Adamopoulos [157, 159] in Figure 34, it can be seen that the $sp^3$ content in these analysed regions can be no more than 20%.

| | **G-Peak Height** | **T-Peak Height** | **$I_T/I_G$** |
|---|---|---|---|
| Spectrum 1 | 960 | 157, 188 | 0.16, 0.2 |
| Spectrum 2 | 674 | 107, 144 | 0.16, 0.21 |

**Table 36: $I_T/I_G$ ratios for DS1 as deposited evaporated sensors.**

Remembering that the double peaked spectrum shown accounts for only 40% of the spectra taken, the overall $sp^3$ content will be much less than this. It appears that the untreated films have large clusters of greater (but by no means large) $sp^3$ content within a mostly $sp^2$ matrix. During annealing these clusters are converted to the bulk $sp^2$ matrix material.

With the exception of the small features at 1361 and 1426cm$^{-1}$ (which are small, separate artefacts of CH bonding[193]) the allocation of the T peak and the origin of the peak at 1950cm$^{-1}$ can be explained by analysing the spectra from the DS2 evaporated films.

### *A3.1.2 DS 2 Curve Fitting*

Figure 97 shows the general curve fitting used for DS2 films. The fitted curves become taller and narrower with increasing wavenumber. The peak shown at 1574cm$^{-1}$ is the G-peak and the peak at 1414cm$^{-1}$ is the D-peak.

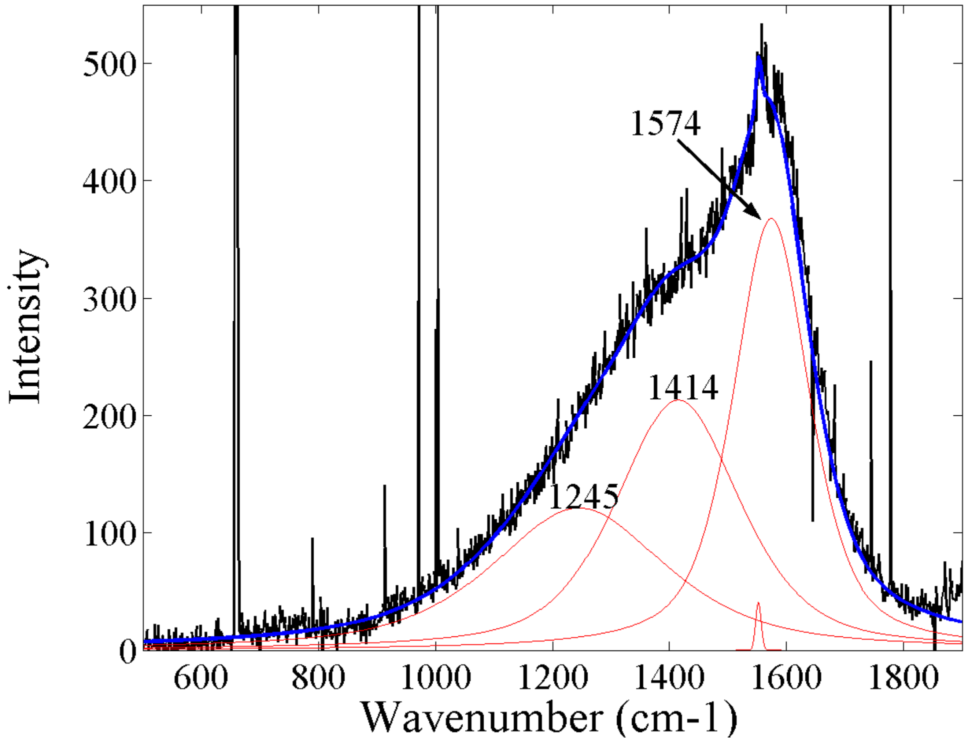

**Figure 97: Curve fit of Raman spectrum for DS2 evaporated film**

The lowest peak, at 1245cm$^{-1}$, is at a very similar position to a potential T peak of the as-deposited film from DS1, but there is no associated shift of the G-peak position, which would be indicative of a true T peak. Instead, the G-peak remains around the same position as for the HOPG control sample, suggesting no sp$^3$ is present.

The same sample was subjected to Raman analysis using a visible wavelength (510nm) that cannot detect sp$^3$ content directly. From this analysis, a third peak located between 1075-1095cm$^{-1}$ was found.

The third peak cannot be a T peak because they are not detectable using visible excitation wavelengths. Given this information and the third peaks relative position with the G and D-peaks, this peak represents the same excitations as the peak at 1245cm$^{-1}$ from DS1. Therefore the peak at 960cm$^{-1}$ from DS1 is the T peak.

## A3.2 Sputtered Films

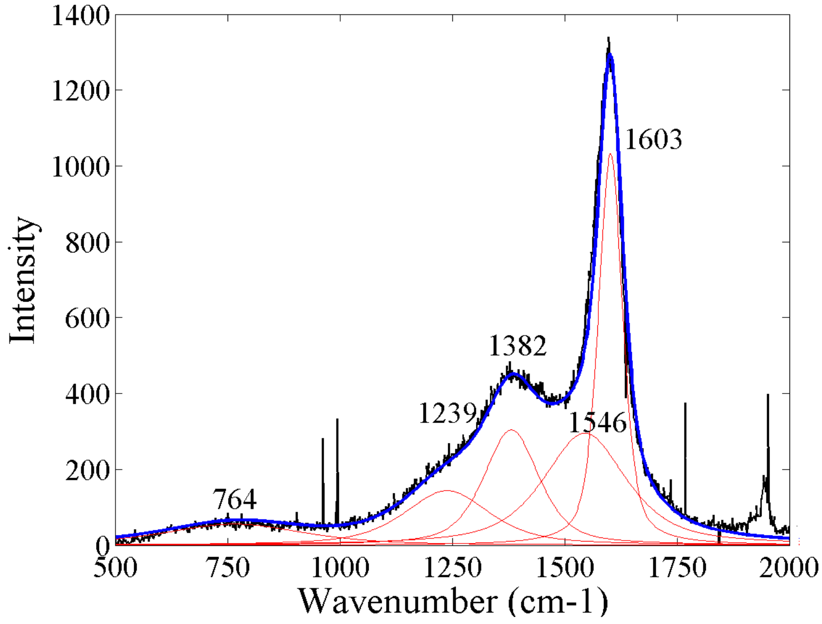

**Figure 98: Curve fit of Raman spectrum for DS1sputtered film**

Figure 98 shows a typical curve fit for DS 1 sputtered films. Excluding some C=C=C bonding at 1950cm$^{-1}$ there are 5 curves: two around the G-peak region, one around the D-peak region, a curve at around 1239cm$^{-1}$ and one at around 760cm$^{-1}$.

A similar analysis to that carried out for the evaporated films was done on the curve at 1239cm$^{-1}$. This curve was found to exist in the visible spectrum, so could not be a T peak and the curve at 760cm$^{-1}$ is too low for this assignment. From this, it can be concluded that there is negligible sp$^3$ content and the peak at around 1240cm$^{-1}$ is a polyacetylene PA$_1$ peak.

The polyacetylene-like phase appears to be very similar to that found in the DS2 evaporated films. A peak at 1950cm$^{-1}$ indicates that C=C=C bonding is present and a PA$_1$ peak strengthens this argument. The second peak in the possible G-peak region (seen at 1546cm$^{-1}$ in Figure 98) is thought to be another peak representing the polyacetylene-like phase. Whenever polyacetylene is present this peak should exist [156]. This peak is not seen in previous evaporated spectra because it is often obscured by the G-peak when it is at lower wavenumbers [156]. This peak will be referred to as a $PA_2$ peak.

### *A3.2.1 DS1 Silicon and Oxygen Bonding*

One notable absence from all the sputtered film Raman spectra was the $O_2$ adsorption band at 1555cm$^{-1}$. This suggests the oxygen detected by the EDS is in some way bonded to the film, if it is not the substrate being detected. It is therefore pertinent to check for oxygen bonded to the other detected elements: carbon, hydrogen and silicon.

Table 37 summarises the general range that these bonds can be found. The most evidence of oxygen bonding occurs at higher wavenumbers that are representative of OH bonding. Unfortunately, within this range of wavenumbers also lie broad fits associated with CH bonding, so associating curves in this region to either CH or OH is very difficult.

| **Bond** | **Range (cm$^{-1}$)** | **Reference** |
|---|---|---|
| C=O | 1700-1900 | [176] |
| C-O-C | 1180-1210 | [176] |
| C-O | 1075-1100 | [176] |
| Chemisorbed CO | 2112-2065, 1940-1770 | [194] |
| Physisorbed CO | 2139 | [195] |
| O-H | 3230-3670 | [176] |
| SiO | 444, 454, 502 | [196] |
| Amorphous $SiO_2$ | 430-490 | [153] |
| Si-O-Si | 480-625 | [176] |

**Table 37: Raman characteristic frequencies of potential oxygen bonding regimes**

From Table 37 it appears that the silicon is generally not bonded to oxygen, leaving the possibility of silicon bonding to hydrogen and carbon. $Si-H_2$ stretching bands are known to exist at 2100cm$^{-1}$ and are absent from all the recorded spectra, but this does not eliminate other Si-H bonding possibilities.

The curve at 764cm$^{-1}$ has so far been unassigned and the more generic SiH$_n$ bending mode is found between 500cm$^{-1}$ and 1000cm$^{-1}$. It should be noted, however, that it is difficult to attribute in disordered films (broad curve fits) because the same region also contains the T peak and Si-C modes[197]. So far the T peak has been eliminated as a significant assignment, leaving the possibility of SiH$_n$ bending (located at ~690cm$^{-1}$) and Si-C stretching (located at ~760cm$^{-1}$ and ~950cm$^{-1}$).

Si-C stretches have a much smaller Raman cross-section in the visible regime than the UV, so a multi-wavelength analysis can prove useful in identifying SiC content. The broad feature was not visible between 500-1000cm$^{-1}$ in the visible, suggesting that the feature seen in the UV regime is SiC. The work of Racine *et al* identifies the need for further investigation into the deconvolution of the 500cm$^{-1}$ to 1000cm$^{-1}$ curve[197] for all different C/Si compositions.

Most of the sputtered films from DS1 showed a G-peak above 1600cm$^{-1}$, which is normally indicative of disorder and some associated sp$^3$ content in a-C films[105]. The presence of silicon changes this trend because the heavier silicon atoms have a damping effect and introduce disorder into the film[198]. This means that as more silicon content is increased, the G-peak decreases. As the silicon atoms are also introducing disorder, a G-peak downward shift represents increasing disorder: the opposite case of a-C films [26, 197]. The work of Ferrari and others has shown that the position of the G-peak can directly measure the silicon content, the results of which are shown in Figure 99 [26, 198].

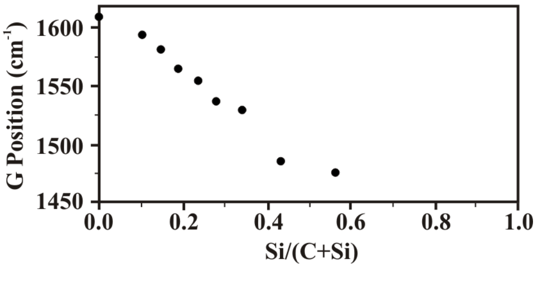

**Figure 99: Variation of G-peak displacement for a-C$_{1-x}$:Si$_x$:H alloys[26]**

The presence of oxygen and hydrogen in these films means that the results from Ferrari cannot be directly applied, but the general trend could still exist because oxygen atoms also have a greater mass than carbon and so damp the material in a similar way. Some work carried out on oxygenated a-C:Si:H films showed that the oxygen can eliminate this trend if Si-O chains are formed, which take out Si atoms from the carbon matrix [162]. However, it has already been shown that this is not the case.

### *A3.2.2 DS2 Films*

The reason for the $PA_1$ peaks' absence is not entirely clear, although a small peak may exist and be lost within the wide D-peak. Since the $PA_2$ peak is as strong as the DS1 films, the ratio between the two PA peak intensities has changed. Unfortunately there is no research into how different ratios effect the composition of the polyacetylene. The peak at 1950cm$^{-1}$ is stronger in these films, so some of the change could be attributed to a greater C=C=C contribution.

From the DS1 spectra, the peak at around 760-789cm$^{-1}$ has been given a possible Si-C bonding assignment. The possibility that the substrate is contributing to the 760cm$^{-1}$ feature has been eliminated because it is present, in equal strength, in films deposited onto both alumina and silicon oxide wafer.

## A3.3 Screen-Printed Films

The broad feature that lies within 1350cm$^{-1}$ to 1423cm$^{-1}$ is assigned to N=C=O symmetric stretching, which agrees with the elemental content detected by EDS. This type of stretching is associated with isocyanates, which are used to react with alcohols to form polyurethanes (PUs).

PU is a polymer with multiple urethane linkages and its basic structure is shown in Figure 100. It is worthwhile to check whether or not the isocyanates are a residue from the production of PU, by checking for other PU bonding assignments. Even if they are very weak features in the spectra, this does not mean they are insignificant in the composition, as the scattering cross section of the important bonds could be very low.

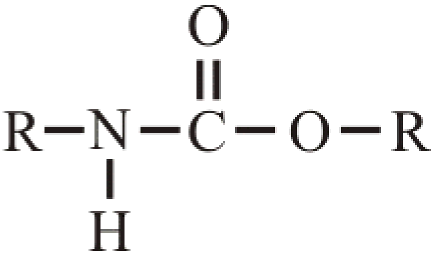

**Figure 100: Urethane Linkage**

Possible peak positions are at 1700-1900cm$^{-1}$ (C=O), 1530 cm$^{-1}$ (C-N) and 1075-1100cm$^{-1}$(C-O). Whilst the broadness of the isocyanate peak and the G-peak hide possible C=O and C-N peaks, a very small peak in the expanded spectra of Figure 90, can be seen at 1075cm$^{-1}$, which correlates to C-O. The absence of a 1550cm$^{-1}$ peak suggests that no oxygen has been absorbed from the atmosphere, so must be included into the film material in some way. The presence of polyurethanes would provide a possible reason for the oxygen content, but their presence is difficult to confirm given the very small intensities being analysed. Future Raman spectra of these films should be taken with significantly longer sampling times to ensure that these smaller intensities can undergo a more thorough analysis.

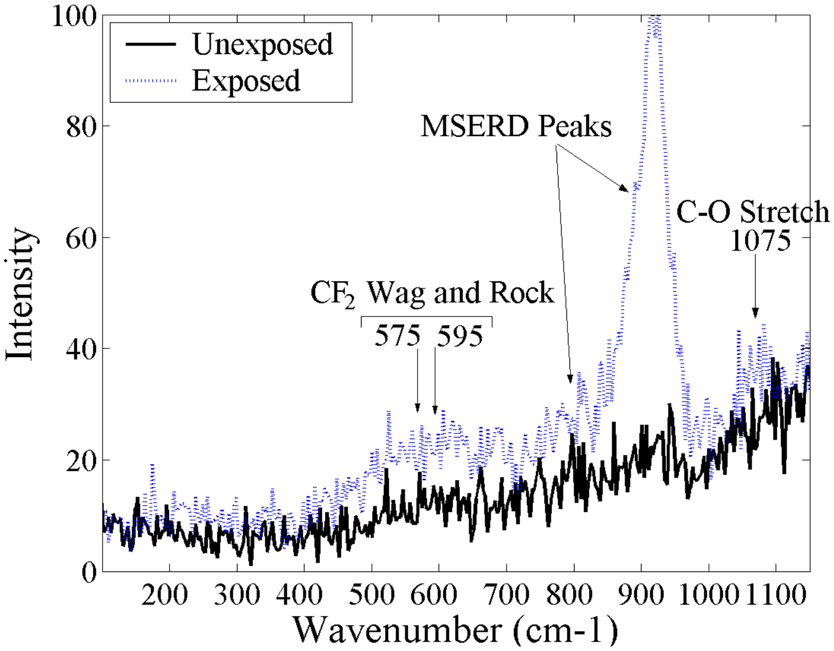

**Figure 101: Screen-printed film lower spectral range**

Many spectra showed a small peak at around 920cm$^{-1}$, which is displayed on Figure 101. This peak is thought to be representative of monosubstituted epoxide ring deformation (MSERD) [176]. Epoxides consist of a triangular arrangement of two carbon atoms and an oxygen atom, usually with other organic molecules bonded to the carbon atoms. There are two MSERD frequency ranges: one lying between 870-970cm$^{-1}$ and another between 750-880cm$^{-1}$, both of which are possible in this example. Polymers made of epoxide units are called polyepoxides (or epoxy) and are commonly used as adhesives [176].

EDS analysis has highlighted the existence of fluorine in all screen-printed films and the possible presence of a fluorinated polymer has been discussed. Bonded fluorine characteristic frequencies lie between 560-580cm$^{-1}$ ($CF_2$) and 1000-1400cm$^{-1}$ (CF). The UV excited spectra show no obvious signs of this kind of bonding, unless CF stretching is a composite component to the broad mound, associated to isocyanates.

# APPENDIX A4: RAMAN SPECTRA DETAILS

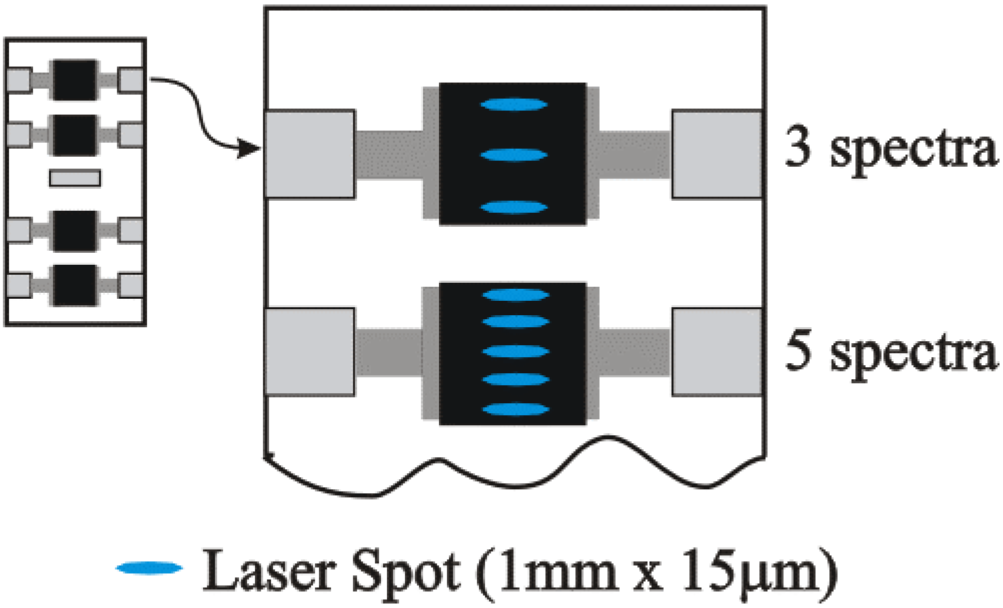

**Figure 102:Schematic of spectra acquisition methodology. Laser spot was equispaced along the centre of each sensor sample.**

| Coupon no. | Deposition | Substrate | Fluence (x$10^{19}$ atoms/cm$^2$) | No. of Spectra | Sample Time (sec) |
|---|---|---|---|---|---|
| 2 | Screen printed, 4232 Ink | Alumina | 16.7 | 5 | 60 |
| | | | 7.9 | 5 | 60 |
| | | | 8.8 | 7 | 60 |
| | | | 0 | 5 | 60 |
| | | | 0 | 2 | 60 |
| 3 | Screen printed, 4232 Ink | Alumina | 0 | 1 | 180 |
| | | | | 7 | 60 |
| | | | 6.9 | 8 | 60 |
| 5 | Screen printed, 4232 Ink | Alumina | 7.8 | 6 | 300 |
| | | | 6.9 | 7 | 300 |
| | | | 0 | 8 | 300 |
| 10 | Screen printed, 4232 Ink | Alumina | 8.8 | 3 | 60 |
| | | | 0 | 3 | 60 |
| 14 | Screen printed, 4242 Ink | Alumina | 3.9 | 5 | 60 |
| | | | 0 | 3 | 60 |

**Table 38: Raman spectra details**

| Coupon no. | Deposition | Substrate | Fluence (x10$^{19}$ atoms/cm$^{2}$) | No. of Spectra | Sample Time (sec) |
|---|---|---|---|---|---|
| 20 | Screen printed, 4242 Ink | Alumina | 8.8 | 3 | 60 |
| | | | 0 | 3 | 60 |
| 21 | DC Magnetron Sputtered | Alumina | 6.9 | 5 | 120 |
| | | | 0 | 5 | 120 |
| 22 | DC Magnetron Sputtered | Alumina | 7.9 | 4 | 120 |
| 23 | DC Magnetron Sputtered | Alumina | 7.8 | 2 | 300 |
| | | | 0.85 | 3 | 300 |
| | | | 0 | 3 | 300 |
| 24 | DC Magnetron Sputtered | Alumina | 3.9 | 3 | 120 |
| 26 | E-Beam Evaporated | Alumina | 6.9 | 6 | 600 |
| | | | 0 | 3 | 1200 |
| | | | 0.85 | 1 | 600 |
| 28 | E-Beam Evaporated | Alumina | 0 | 3 | 600 |
| 29 | E-Beam Evaporated | Alumina | 0.5 | 2 | 1200 |
| 30 | E-Beam Evaporated | Alumina | Unknown, but exposed | 1 | 300 |
| 40 | DC Magnetron Sputtered | Alumina | 0 | 3 | 300 |
| 41 | E-Beam Evaporated | Alumina | 0 | 3 | 600 |
| 102 | DC Magnetron Sputtered | Alumina | 6.9 | 3 | 300 |
| | | | 0 | 3 | 300 |
| 104 | DC Magnetron Sputtered | Alumina | 0.85 | 6 | 600 |
| | | | 0 | 6 | 600 |
| 201 | E-Beam Evaporated | Alumina | 0.85 | 3 | 300 |
| | | | 0 | 3 | 300 |
| | | | 0 | 1 | 600 |
| | | Silicon Oxide Wafer | 0.85 | 4 | 300 |
| | | | 0 | 4 | 600 |
| 202 | E-Beam Evaporated | Alumina | 6.9 | 6 | 300 |
| | | | 0 | 4 | 300 |
| | | Silicon Oxide Wafer | 6.9 | 3 | 300 |
| | | | 0 | 3 | 300 |
| HOPG | - | | 0 | 2 | 60 |
| CVD Diamond | - | | 0 | 2 | 120 |

**Table 39: Raman spectra details (continued)**